Electronic Structure and Chemical Composition Study of MnO$_x$ Catalysts for Water Oxidation using Synchrotron Spectroscopic Techniques

im Fachbereich Physik
der Freien Universität Berlin

eingereichte Dissertation
zur Erlangung des akademischen Grades
der Doktorin der Naturwissenschaften (Dr. rer. nat.)

vorgelegt von

Maryam Nabil Sobhy Shaker

Berlin, Deutschland

2020

Electronic Structure and Chemical Composition Study of MnOₓ Catalysts for Water Oxidation using Synchrotron Spectroscopic Techniques

Maryam N. Shaker

Department of Physics, Freie Universität Berlin, Germany

Institute of Solar Fuels (EE-IF), Helmholtz-Zentrum Berlin für Materialien und Energie, Berlin, Germany

Erstgutachter (First Examiner):

Prof. Dr. Roel van de KROL

Professor at the Department of Chemistry, Technische Universität Berlin, Germany

& Institute Director of Solar Fuels (EE-IF), Helmholtz-Zentrum Berlin für Materialien und Energie, Berlin, Germany

Zweitgutachter (Second Examiner):

Prof. Dr. Holger DAU

Professor at the Department of Physics, Freie Universität Berlin, Germany

Tag der Einreichung (date of submission): 09.11.2020
Tag der Disputation (date of disputation): 03.02.2021

"In the beginning, God created the heavens and the Earth. And the Earth was without form and void, and darkness was upon the face of the deep: and the Spirit of God moved upon the face of the waters. And God said, let there be light: and there was light. And God saw the light, that it was good: and God divided the light from the darkness."

The First Book of Moses, 'Genesis'

"Science without religion is lame; religion without science is blind."

Albert Einstein

"It is not the possession of truth, but the success which attends the seeking after it, that enriches the seeker and brings happiness to him."

Max Planck, Where is Science Going?

"أَسْتَطِيعُ كُلَّ شَيْءٍ فِي الْمَسِيحِ الَّذِي يُقَوِّينِي" (في 4: 13)

"لأَنَّ اللهَ لَمْ يُعْطِنَا رُوحَ الْفَشَلِ، بَلْ رُوحَ الْقُوَّةِ وَالْمَحَبَّةِ وَالنُّصْحِ" (تي 1: 27)

This thesis is dedicated to my darling daughter Anne-Marie and
my husband Mina, who has been a constant source of support,
help, and encouragement during the challenges of studies
and life. I love you very much. I also dedicate this thesis to
my beloved parents, Nabil Sobhy and Attiat Amin, who have always
loved me unconditionally and were very good examples to me.
Thanks for your endless love and support.

Contents

Abstract

Understanding the electronic structure and the chemical composition of a catalyst is of interest, not only for scientific reasons but also for the technological development of catalysts for the (photo) electrochemical production of hydrogen from water, in order to solve the world's steadily growing problems, such as the global warming through CO_2 accumulation in the atmosphere, the increasing energy demand of mankind and environmental pollution. Manganese oxide (MnO_x) catalysts are promising candidates taking advantage of being abundant, non-toxic, and inexpensive for an economically competitive future technology. This thesis reports two aspects of MnO_x: One is to use it as an electrocatalyst, and the other as a cocatalyst, deposited on a semiconducting photoanode.

The first topic of the thesis addresses studies of the electronic structure of MnO_x as an electrocatalyst for water oxidation reaction using absorption spectroscopy and resonant inelastic scattering of soft X-rays at the manganese $L_{2,3}$-edge and the oxygen-K-edge. Two main questions in the first topic were addressed: First, what is the origin of catalytic activity changes in MnO_x films prepared under different pH conditions? The answer is found in the X-ray absorption spectra of seven samples, prepared from highly acidic to (near-)neutral to highly basic electrolytes. The spectra showed a remarkable change in the electronic structure of the pH-dependent MnO_x catalysts. All investigated catalysts include mixtures of Mn_2O_3, Mn_3O_4, and birnessite in different proportions. The highest catalytic active catalyst, prepared under neutral conditions, is composed of birnessite and Mn_2O_3. In contrast, other films are composed predominantly of only one of these phases with a low content of Mn_3O_4. It reveals that the interplay of Mn^{III} and Mn^{IV} species can drastically enhance the catalytic activity, but not a single contribution of any of them alone. This study led to the second significant question of what are the electronic states of MnO_x catalysts during the water oxidation reaction and whether a charge transfer occurs between Mn-metal and O-ligand? Are the Mn valence states increase continuously with increasing the oxidizing potential? The answer has been found after conducting an *in situ* XAS/ RIXS spectroscopic study tracking the electronic state changes happening in the electrodeposited MnO_x catalyst under real reaction conditions (0.75-2.25 V_{RHE}). The *in situ* XAS reveals a full transformation of the MnO_x film into a birnessite state at *ca.* 1.45 V_{RHE} (just before the water oxidation). However, the *in situ* RIXS analysis showed continuous changes in the electronic state of MnO_x up to a potential of *ca.* 1.75 V_{RHE}. More precisely, the Mn $3d$ - O $2p$ hybridization degree increases by applying a more positive potential to the MnO_x films up to 1.75 V_{RHE}. Furthermore, the water oxidation catalysis by MnO_x is facilitated by an O-to-Mn charge transfer, achieved at *ca* 1.75 V_{RHE}, which is believed to be of crucial importance for efficient electrocatalytic water oxidation.

The second topic of the thesis discusses how the MnO_x can enhance the water-oxidation activity of a tantalum-oxynitride (TaON) photoanode when it is coupled as an overlaying co-catalyst to the photoanode. The chemical composition and electronic structure changes at the MnO_x/TaON interface as a function of the thickness of the MnO overlayer (2, 5, 7, and 26 nm) were addressed and studied with hard X-rays photoemission spectroscopy. By depositing ultrathin MnO layers on the TaON photoabsorber, the photocurrent enhances *ca.* 5 times, whereas the amount of Ta_2O_5 at the MnO_x/TaON interface was reduced with increasing MnO overlayer thickness. It implies that the MnO_x co-catalyst reduces the unfavorable Ta_2O_5 at the MnO_x/TaON interface, which in turn facilitates the hole transfer from photoanode to MnO_x surface for water oxidation reaction to occur. Simultaneously, MnO at the interface is oxidized to Mn_2O_3 and birnessite. Our interpretation suggests that $Mn^{II}O$ at the interface consumes oxygen from Ta_2O_5, leading to a reduction of this oxide and oxidation of Mn^{II} to Mn^{III} and Mn^{IV}. A quantitative analysis using SESSA simulations supports the experimental results. In the present dissertation, manganese oxide characteristics as a (co)catalyst for oxygen evolution from water are highlighted. The results are of interest for artificial photosynthesis devices and elucidate some of the missing pieces of the puzzle of the challenging water oxidation reaction.

Kurzfassung

Das Verständnis der elektronischen Struktur und der chemischen Zusammensetzung eines Katalysators ist nicht nur aus wissenschaftlichen Gründen von Interesse, sondern auch für die technologische Entwicklung von Katalysatoren für die (photo)elektrochemische Wasserstoffgewinnung aus Wasser, um die ständig wachsenden Probleme der Welt, wie die globale Erwärmung durch CO_2 Anreicherung in der Atmosphäre, den steigenden Energiebedarf der Menschheit und die Umweltverschmutzung einzudämmen. Manganoxid (MnO_x)-Katalysatoren haben den Vorteil, dass sie reichlich vorhanden, ungiftig sowie kostengünstig sind und werden dadurch zu vielversprechende Kandidaten für eine wirtschaftlich wettbewerbsfähige Zukunftstechnologie. Diese Arbeit befasst sich mit zwei Aspekten von Manganoxiden: zum einen mit der Anwendung als Elektrokatalysatoren, zum anderen mit der Nutzung als Kokatalysator, abgeschieden auf einer halbleitenden Photoanode.

Das erste Thema der Arbeit befasst sich mit Untersuchungen der elektronischen Struktur von MnOx als Elektrokatalysator für die Wasseroxidationsreaktion mittels Absorptionsspektroskopie und resonanter inelastischer Streuung weicher Röntgenstrahlung an der Mangan-$L_{2,3}$-Kanten und der Sauerstoff-K-Kante. Dabei werden zwei wesentliche Fragen behandelt: Erstens, was ist der Ursprung der katalytischen Aktivitätsänderungen in MnO_x-Filmen, die unter verschiedenen pH-Bedingungen abgeschieden wurden. Die Antwort findet sich in den Röntgen Absorptionsspektren von sieben Proben, die aus stark sauren über (fast) neutralen bis hin zu hochbasischen Elektrolyten hergestellt wurden. Die Spektren zeigten eine bemerkenswerte Veränderung der elektronischen Struktur der pH-abhängig abgeschiedenen MnO_x-Katalysatoren. Alle untersuchten Katalysatoren bestehen aus Mischungen von Mn_2O_3, Mn_3O_4 und Birnessit in unterschiedlichen Anteilen. Der Katalysator mit der höchsten Aktivität wurde unter neutralen Bedingungen hergestellt und besteht aus den Phasen Birnessit und Mn_2O_3. Im Gegensatz dazu bestehen andere Filme überwiegend aus nur einem dieser beiden Phasen mit einem geringen Anteil an Mn_3O_4. Es zeigt sich, dass das Zusammenspiel von Mn^{III}- und Mn^{IV}- haltigen Spezies die katalytische Aktivität drastisch erhöhen kann, aber nicht die reine Phase einer dieser Spezies. Dies führt zu der zweiten wichtigen Frage, welche aktiven Oxidationszustände von Mangan im MnO_x-Katalysator während der Wasseroxidationsreaktion vorliegen und ob ein Ladungstransfer zwischen Mn-Metall und O-Ligand des Katalysators stattfindet? Steigen die Mn-Valenzzustände mit zunehmendem Oxidationspotential kontinuierlich an? Die Antwort konnte mittels *in situ* XAS und RIXS-spektroskopie gefunden werden, in der die Transformationen im elektrolytisch abgeschiedenen MnO_x-Katalysator unter realen Reaktionsbedingungen (0,75 bis 2,25 V_{RHE}) beobachtet wurden. Das *in situ*-XAS zeigt eine vollständige Umwandlung des MnO_x-Films in einen Birnessit Zustand bei einem Potential von ca. 1,45 V_{RHE} (kurz vor der Wasseroxidation). Die *in situ*-RIXS-Analyse zeigte jedoch kontinuierliche Änderungen des elektronischen Zustands von MnO_x bis zu einem Potential von ca. 1,75 V_{RHE}, genauer gesagt, erhöht sich der Hybridisierungsgrad von Mn $3d$ - O $2p$ durch Anlegen eines positiveren Potentials. Darüber hinaus wird die Wasseroxidationskatalyse durch MnO_x durch einen O-zu-Mn-Ladungstransfer erleichtert, der bei ca. 1,75 V_{RHE} erreicht wird, was vermutlich von entscheidender Bedeutung für eine effiziente elektrokatalytische Wasseroxidation ist.

Das zweite Thema der Arbeit wird diskutiert, wie MnO_x die Wasseroxidationsaktivität einer Tantaloxynitrid (TaON)-Fotoanode steigern kann, wenn es als Deckschicht-Kokatalysator auf die Fotoanode aufgebracht wird. Die Änderungen der chemischen Zusammensetzung und der elektronischen Struktur an der MnO_x/TaON-Grenzfläche in Abhängigkeit der Dicke der MnO-Deckschicht (2, 5, 7 und 26 nm) wurden mit Photoemissionsspektroskopie mit harter Röntgenstrahlung untersucht. Durch die Abscheidung von ultradünnen MnO-Schichten auf dem TaON-Fotoabsorber erhöht sich der Fotostrom auf *ca.* das 5-fache, wobei sich die Menge an gebildetem Ta_2O_5 an der Grenzfläche MnO_x/TaON mit zunehmender MnO-Deckschichtdicke verringert. Dies legt nahe, dass der MnO_x-Kokatalysator das ungünstige Ta_2O_5 an der MnO_x/TaON-Grenzfläche reduziert, wodurch der Lochtransfer von der Photoanode zur MnO_x-Oberfläche zur Wasseroxidationsreaktion verbessert wird. Gleichzeitig oxidiert MnO an der Grenzfläche zu Mn_2O_3 und Birnessit. Unsere Interpretation geht davon aus , dass $Mn^{II}O$ an der Grenzfläche Sauerstoff aus Ta_2O_5 entzieht, was zu Reduktion dieses Tantaloxids und einer Oxidation von Mn^{II} zu Mn^{III} bzw. Mn^{IV} führt. Eine quantitative Analyse durch SESSA-Simulationen stützt die experimentellen Ergebnisse. In der vorliegenden Dissertation wird die Eignung von Manganoxiden als (Ko-) Katalysator für die Sauerstoffevolutionsreaktion beleuchtet. Die Ergebnisse sind für künstliche Photosynthese von Interesse und liefern einige der fehlenden Puzzleteile zur Aufklärung der herausfordernden Wasseroxidationsreaktion.

Chapter 1

Introduction and Motivation

1.1   Global Energy Demand and Environmental Pollution

Nowadays, the world is facing three main and harsh problems: energy demand, global warming, and environmental pollution.[1] These problems are interdependent and consequential to each other. The increasing global energy demand is expected and in-line with increasing populations, global economic growth, and the industrial revolution. The world population scored 7.8 billion as of July 2020 and is predicted to reach 9.7 billion by year 2050, according to the estimates of the United Nations.[2] In parallel, the world energy council reported that the global energy consumption by the world population in 2020 is 642 EJ (Exajoules = 10^{18} J), which is anticipated to increase to 879 EJ by 2050[3], *i.e.,* the increase of the consumed energy (26%) is even higher than the population increase in the same period. Conventional non-renewable resources like fossil fuels, *viz.* natural gas, coal, and oil, are used to satisfy about 80 % of the global energy demand.[4] Meanwhile, the total world reserves of fossil fuels at present are 1,139 billion tons of coal, and 1,707 billion barrels of Crude oil, 187 trillion cubic meters of Natural gas.[5] While these values seem huge at the current extraction/production rate, it is estimated that we will run out of coal by year 2169, Crude oil in 2066, and Natural gas by year 2068.[5] So, at some point, fossil fuel supplies will not be able to keep up with the steadily growing energy demand by humankind. Therefore, the global community should seriously start producing energy from alternative resources, preferably renewable ones before our fossil fuel supplies run out.

Apart from the inevitable dwindling of fossil fuel reserves in the next centuries, fossil fuels emit about 98% of the carbon dioxide upon fuel combustion.[6] CO_2 is one of the most long-lived greenhouse gases, severely affecting the environment as pollutants, climate change agents, and global warming leading cause.[7] The amount of CO_2 is increasing dramatically in the atmosphere, especially over the last century: In the 19th century, measurements showed that the average growth rate of CO_2 in the atmosphere is 0.13 ppm/year (parts per million/year), which increased to 1.83 ppm/year by the end of year 2000.[8] In the past decade (2010-2019), an increase of 2.4 ppm/year is reported, further-reaching 2.64 ppm over the period from July 2019 to July 2020[9, 10] and is still anticipated to climb further. The steadily increase of CO_2 can have further enormous consequences on the globe, like drought and rising sea level.

For that, many researchers across the scientific community have been tackling the issue to find potential effective solutions to these energy demands and their consequent environmental problems, dedicating their research to developing novel materials and fabricating a new fuel powered by renewable sources. On the one side, taking the advantages of being sustainable energy resources, which is essential to meet the future energy demand, and on the other side, a clean source that can reduce the evolution of global warming or at least keep it at a more manageable level.

1.2   Renewable Energy Resources: A step toward sustainability

Sunlight is a promising candidate to satisfy an enormous part of the growing energy demand. One would, at a glance, recognize the vast capabilities of the sunlight when knowing that the energy-driven by the sun in "one hour" is adequate to support the world's energy consumption of "one year." [11, 12] Thus, the exploitation of solar energy to meet our future demand for clean and sustainable energy is an attractive solution without possessing any negative impacts on the environment.

The key challenge is, however, not the conversion into other energy forms but the storage of solar energy. Solar energy is converted into electricity via photovoltaic cells and solar cells. Effective strategies have been developed for storing solar energy into chemical bonds via hydrogen fuel production devices based on the water-splitting process, *i.e.,* electrolysis.[13] The latter is particularly promising technology due to several advantages of hydrogen use as a fossil-fuel alternative: First, H_2 has a high gravimetric energy density of 143 MJ/kg at 1 bar[14]; second, it is clean energy as it has zero emission (when it burns with oxygen, it releases only water)[15]; third, its source is water which is a sustainable source; and lastly, water-splitting process results also in the by-product of O_2 which is an environment-friendly gas, which can be used in industrial processes.[14-18] Therefore, the approach to artificial photosynthesis via water splitting by sunlight to synthesize hydrogen fuel is considered a significant step toward satisfying a growing global energy demand.

1.3   Artificial Photosynthesis (Water splitting)

Artificial photosynthesis replicates *natural photosynthesis,* as illustrated in Figure 1.1,

mimicking the energy conversion mechanisms in plants to delineate synthetic systems for harvesting solar energy into chemical bonds.[19-21] In *natural photosynthesis*, the plants absorb solar energy, convert CO_2 and H_2O into carbohydrates, and the beneficial by-product of O_2.[21] Thus, to mimic the natural process, synthetic systems in the form of (photo)electrochemical cells were developed, which can similarly split H_2O, producing adequately sufficient electrons and protons needed to synthesize fuel.
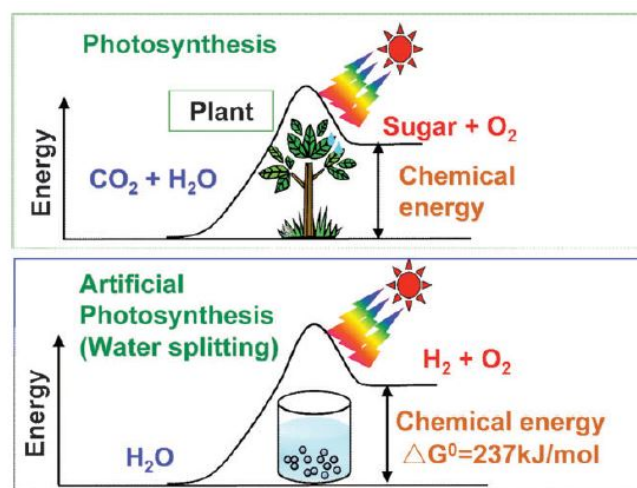
Figure 1.1. "*Natural*" photosynthesis by plants *vs.* "*Artificial*" Photosynthesis through "water-splitting". *Reproduced from [21] with permission from the Royal Society of Chemistry.*

The water-splitting process comprises two half-cell reactions, at which 2 water molecules are oxidized into oxygen, 4 electrons, and 4 protons, which then reduced to molecular hydrogen, as follows:

OER: $2H_2O_{(l)} \rightarrow O_{2(g)} + 4e^- + 4H^+$ +1.23 V *vs.* NHE   (1.1)

HER: $2H^+ + 2e^- \rightarrow H_{2(g)}$ 0 V *vs.* NHE   (1.2)

Overall water-splitting: $2H_2O_{(l)} \rightarrow O_{2(g)} + 2H_{2(g)}$ $\Delta E^o = 1.23$ V   (1.3)
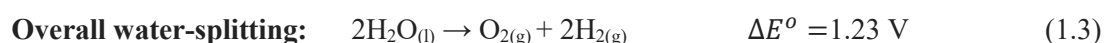
According to the Nernst equation, the water-splitting reaction in equ. (1.3) is thermodynamically uphill (*Gibbs free energy $\Delta G^o = 237$ kJ/mol),* at which a minimum potential of 1.23 V *vs.* Normal Hydrogen Electrode (NHE) at pH 0 is required to split water. The water oxidation reaction in (1.1) is sluggish in terms of kinetics due to four-electron transfer, and various high-energy intermediates are needed for O–O bond formation and O_2 liberation[22, 23], making it challenging

to drive the chemical reaction efficiently without a catalyst. Therefore, significant efforts have been made over the last years to understand this mechanistically complex reaction and improve the catalytic activity of the employed catalyst.[24-27] Thereby, in this thesis, I devote my efforts to better understand and enhance "water oxidation" catalysis for use in energy production.

When aiming at using catalysts for water splitting reaction, two main promising approaches are employed: Electrochemical cell [27, 28] and Photoelectrochemical cell [29-36] as schematized in Figure 1.2(a,b). Both cells host a working electrode acting as an anode, and a counter electrode as a cathode, both immersed in an electrolyte. In the electrochemical cell, the catalyst for oxygen evolution reaction (OER) is loaded onto the anode surface biased by potential from a potentiostat. The catalyst, in this case, is commonly known as an "electrocatalyst." [27, 28] While the catalyst in a photoelectrochemical cell is attached to a light-harvesting electrode (semiconducting photoanode), photogenerated electrons and holes will be produced upon solar irradiation. The catalyst, in this case, is known as "photocatalyst."[14] Practically, due to the sluggish multielectron water oxidation reaction, a potential higher than 1.23 V on the photocatalyst is still required to run the water-splitting reaction efficiently.
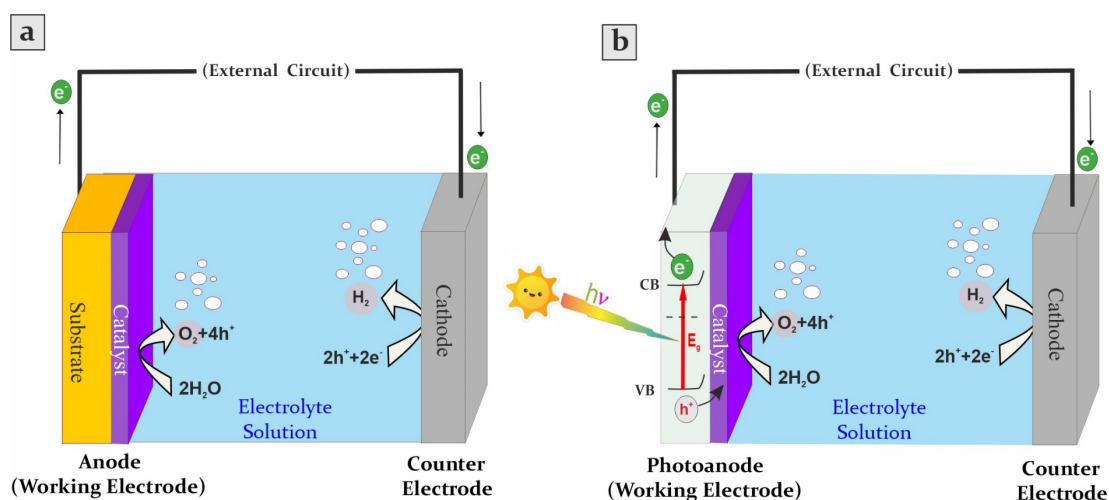
Figure 1.2. Schematic diagram of a) Electrochemical cell and b) Photoelectrochemical cell used for the splitting of water at which the oxidation reaction (H_2O/O_2) occurs at the anode (working electrode) and the reduction reaction (h^+/H_2) at the cathode (counter electrode).

The (photo)electrochemical conversion occurs when the holes and electrons take part in the catalytic reactions at the surface of the anode and cathode, respectively. The holes at the anode oxidize water into O_2, what is known as '*Oxygen Evolution reaction*' (OER) (see equation 1.1), while the electrons arriving at the cathode side undergo a '*Hydrogen Evolution reaction*' (HER)

(see equation 1.2), reducing protons into H_2.[37, 38]

Since the last few decades, various researchers have been addressing the (photo)electrochemical water-splitting systems based on different catalysts, prepared by different methods, which lead to various characteristics and structures.[21, 39-47] However, an efficient and economical catalyst is still not found.[27] When selecting a catalyst (working electrode) in a (photo)electrochemical cell, some factors should be considered for an efficient water oxidation reaction to occur. An active catalyst should be of a novel material in terms of functionality that improves the charge transfer efficiency, has a high concentration of active sites, increases the kinetics of OER reaction.[13, 29-31, 37] Studies showed that the precious-metal-based oxides, such as RuO_2 and IrO_2, are best-known as the 'state-of-the-art' catalysts for the oxygen evolution reaction, exhibiting high catalytic activity and relatively high chemical stability over a wide range of pH conditions.[48-51] Despite the high performance of these precious-metal-based oxides, they are expensive and suffer much scarcity.[52] Thus, the earth-abundant, non-precious transition metal (TM) oxides-based catalysts are then the best suitable candidate to be hired for oxidizing water efficiently.

Within the context of these requirements and among the TM oxides, manganese oxides (MnO_x) were chosen to be the specified material studied in this thesis and of significant interest due to the following advantageous properties:

1. Mn is non-toxic, innocuous, earth-abundant as well as it mimics the natural Mn-based catalyst within photosystem II (PS-II).

2. MnO_x can exist in various oxidation states, 2+, 3+, 4+, 5+, 6+, and 7+, which offers a large degree of flexibility to undergo a range of redox reactions.[27, 53]

3. Mn oxide phases give rise to a wide range of Mn–O moieties that exist in more than 30 crystal structure forms, including polymorphs of the same chemical formula.[54, 55] The concentration of the active sites is affected by the oxide structure (*vide infra*); thus, it is possible to enhance the catalytic activities toward the water oxidation reaction by modulating the structure.[56]

1.4   Manganese Oxide in Nature

Manganese (Mn) element is the third most abundant TM widely spread in see water in the 2+ state (Mn^{II}) at high concentrations.[27] Interestingly, nature has chosen Mn, among other elements, to be the redox-active element for water oxidation in biological PS-II.[27] In the PS-II system, the protein complex located in the thylakoid membranes of biological systems like

plants, algae, and cyanobacteria, is irradiated by sunlight reducing atmospheric CO_2 using electrons extracted from water (*i.e.,* during water splitting) to form energy-rich organic compounds.[57, 58] The active site which is responsible for water oxidation in PS-II is the manganese-calcium-oxo cluster (Mn_4CaO_5) complex stabilized by amino acid residues housed in the membrane protein, as shown in Figure 1.3(a).[58] This Mn complex is known as the "*water-oxidizing complex* (WOC)," or "*oxygen-evolving complex* (OEC)."

The Mn_4CaO_5 cluster exhibits a very high catalytic activity towards the water oxidation reaction. For example, in terms of turnover number (TON), it generates 180,000 molecules of O_2 per site, with turnover frequencies (TOF) of 100-400 s^{-1}, which is much higher than any artificial catalyst.[59, 60] The unique structure of the Mn_4CaO_5 complex is the reason for its high catalytic activity, as confirmed by *Umena et. al.*[58] The high-resolution structure of the Mn_4CaO_5 complex in Figure 1.3(b) reveals the existence of a highly distorted Mn_3Ca Cuban-type cluster connected to a dangling Mn (identified as Mn4 in Figure 1.3) via two oxo-bridges (O4 and O5). This highly distorted structure may provide the essential arrangement flexibility of the Cuban, enabling the state change from Mn^{III} to Mn^{IV}, catalyzing the water oxidation reaction.[27]
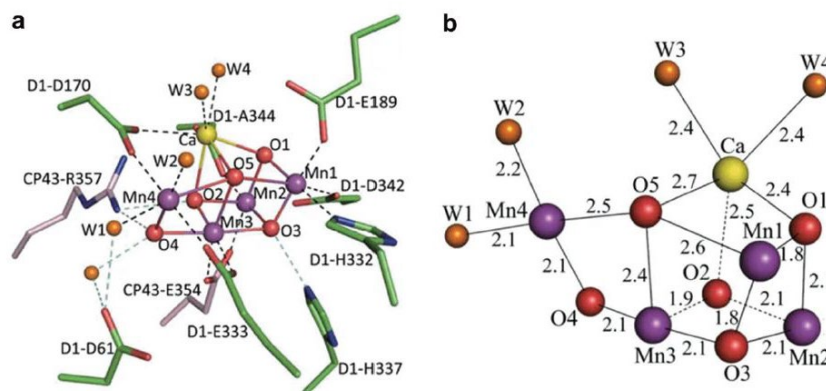
Figure 1.3. The biological Mn_4CaO_5 catalyst within photosystem II. (a) Crystal structure of the Mn_4CaO_5 is surrounded by amino acid residues, (b) a high-resolution structure showing the differences in the bond lengths between metal atoms, water molecules, and oxygen atoms. *Reproduced with permission from* [58]*, Copyright 2011 Nature Publishing Group.*

In an effort toward understanding the WOC mechanisms within the PS-II, *Kok et al.*[61] in 1970, succeeded in proposing the basic principles of water oxidation by the so-called "Kok cycle." The Kok cycle shown in Figure 1.4 reveals the five intermediate states (S_i) of the WOC. The subscript i ($i =0{\rightarrow}4$) represents the oxidation state of the tetranuclear manganese (Mn_4CaO_5) cluster relative to the S_0 state. [61, 62]

In the Kok cycle, the metal ion in the cluster releases electrons upon absorbing light, which results in the oxidation of Mn^{III} to Mn^{IV}, simultaneous to deprotonation of water.[27, 63] In the $S_3 - S_4$ step, the O–O bond is formed. While in the last reaction step, S_4, the oxygen is released under no absorption of light, and the WOC resets again to the lowest state S_0. While Kok cycle succeeded in explaining the basic principle of the WOC in PS-II, great efforts have been made and still ongoing to complete the puzzle and elucidate all aspects behind the water oxidation mechanism, especially in the last step ($S_4 - S_0$) after the O–O bond formation. *Dau et al.* [59, 64, 65] devoted much effort in studying the structural and oxidation state changes of the Mn_4Ca complex in the water oxidation cycle revealed by X-ray absorption spectroscopy. *Glatzel et al.*[66, 67] has employed resonant inelastic X-ray scattering spectroscopy (RIXS) in studying the electronic structure of molecular Mn complexes where they concluded that the electron in the S_1 to S_2 transition is removed from delocalized orbitals in the Mn_4CaO_5 cluster, with ligand taking part in the redox reaction besides the Mn ion.
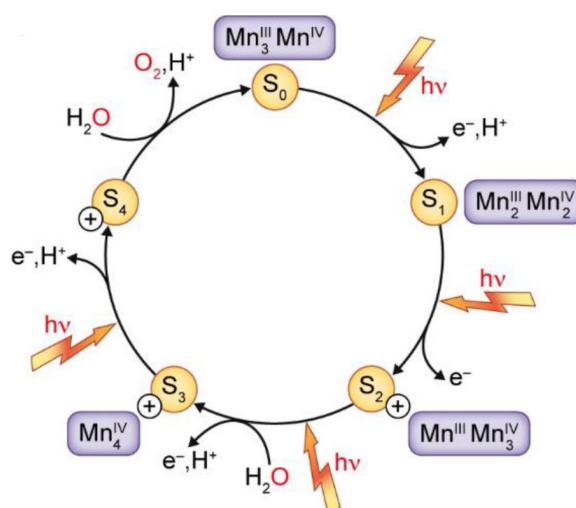
Figure 1.4. The Kok cycle explaining the water oxidation mechanisms in five intermediates oxidizing equivalents. Four light absorption events feed the cycle, by which electrons are extracted from the metal ions. *Reproduced from [62]. Copyright 2019 licensed under a Creative Commons Attribution 4.0 International Licence*

The inspiration to mimic the optimized natural $CaMn_4O_5$ catalyst within PS-II sparked considerable interest in developing the MnO_x catalyst, of near-optimal performance, for water oxidation through artificial photosynthesis.[39, 68-71] However, the search for an optimum MnO_x composition, structure, and morphology is still ongoing.[72, 73] Thus, it is essential to point out the crucial aspects of water oxidation catalysis that are to be considered, in this study, based on previous scientific studies conducted on Mn-based systems.

1.5   Crucial Aspects of Water Oxidation Catalysis

The performance of the OER catalysts is largely dependent on significant parameters like morphology, chemical composition, and electronic structure.[28] These parameters are strongly influenced by factors like particle size, temperature, pH, and potential; thereby, affect the catalytic activity toward the water oxidation reaction.[74, 75] In this section, I will focus on some characteristics of the catalyst related to the main study of this thesis. Indeed I do not exclude other characteristics like the type of supporting electrode, the precursor, and the synthesis method to affect the catalyst performance.

1.5.1   Size and Morphology of the Catalyst

In recent decades, nanotechnology has been developed and succeeded in manufacturing nanostructured catalysts characterized by a large surface area-to-volume ratio, which provides a larger interface between the electrolyte and the catalyst, promoting the catalytic performance.[76, 77] The nanostructured catalysts include most of the active sites at its surface and are more efficient than the microparticles.[78] Consequently, various MnO_x catalysts have also been developed and synthesized from micro-powders to well-defined nanoparticles and more controlled ultra-thin films, even on the atomic scale, like those prepared by atomic layer deposition.[27, 77, 79-83] Since the OER performance is largely dependent on the surface area of the catalysts and the morphology, effective synthesis strategies are developed for preparing catalysts of preferably large surface-to-volume ratio in comparison to bulk, with morphology like nanoflakes, nanosheets, and nanorods.[84-86]

The *Spiccia group* showed that manganese precursor complexes of varying nuclearity and metal oxidation state form different MnO_x nanoparticles sizes when doped in a Nafion matrix, thereby affecting their catalytic activity.[46] Nanostructures with a degree of defects exhibited high electrical conductivity and enhancement toward OER performance, as reported by *Zheng et al.*[87] *Gorlin and Jaramillo* succeeded in preparing MnO_x thin films with a highly nanostructured surface that could exhibit high catalytic activity in alkaline media towards OER, with similar overall oxygen electrode activity to that obtained for precious metal (Pt, Ru, and Ir) nanoparticles.[88] It is concluded that reducing the particle size modifies the surface properties, most probably due to surface distortion.[27, 89] Other studies assigned the high catalytic activity to the Mn^{III} species located at the MnO_x nanoparticle surface.[27, 89, 90] *Jin et al.* reported that post-surface treatment of MnO nanocrystals leads to forming a mixed $Mn^{II/III}$ valency on the MnO surface, which results in a considerable enhancement in the catalytic activity toward OER. [89]

1.5.2 Applied Potential and pH of the electrolyte

Manganese oxides have shown to be promising catalysts toward OER. However, the applied potential and the pH of the electrolyte can influence the MnO_x structure and composition and thereby affect the catalytic activity toward the water oxidation reaction.[72, 75] A typical Pourbaix diagram can provide a guide to the thermodynamically stable regions of several MnO_x phases under anodic potential and over a wide range of pH, as described in Figure 1.5.[91]
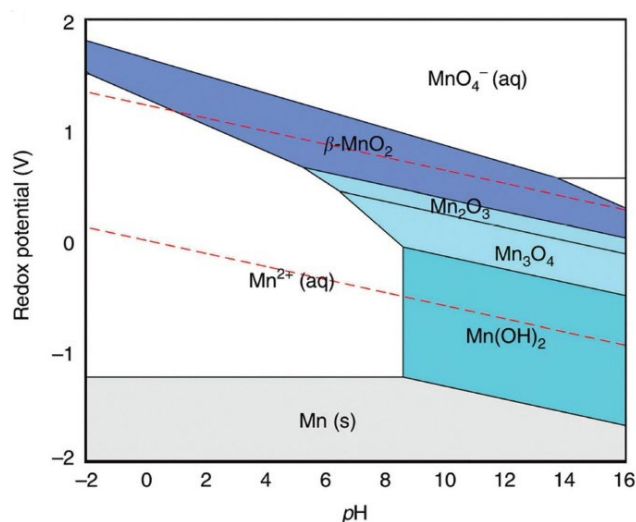
Figure 1.5. Pourbaix diagram of Mn–O–H phases, showing the stability regions as a function of potential-pH. The *red* dashed line indicates the redox stability window of water. *Reprinted with permission from* [91]. *Copyright 2019 Nature Publishing Group.*

Mn-based complexes as an artificial model for WOC were used to show high catalytic activity in alkaline electrolytes and relatively low activity under near-neutral and acidic conditions.[44, 88, 92] However, the natural water oxidation reaction in PS II is performed under near-neutral conditions (at pH 5-6.5).[93-95] *Morita and Tamura* studied the water oxidation activity of a mixture of Mn_2O_3 and β-MnO_2, deposited by thermal decomposition of manganese nitrate, in acidic and basic mediums.[96] The phase mixture could efficiently oxidize water in both acidic and basic electrolytes. They showed that the MnO_x electrode in the basic electrolyte (1 M KOH) could oxidize water for a longer time (~20 h) without any further increase in the overpotential. In contrast, the MnO_x electrode in acidic electrolytes required an increase in the overpotential by 150 mV over the same period due to an increase in the oxygen content in the film.[96] Then *Nakamura's group* reported that the Mn^{III} species, which serve as precursors of active sites of MnO_x and play a key role in the water oxidation reaction, is unstable in the neutral and acidic pH electrolytes as it undergoes disproportionation to form Mn^{II} and Mn^{IV}, which deteriorates the

catalytic activity [44, 97] Hence, the following studies worked on stabilizing the Mn^{III} species, aiming at enhancing the catalytic activity of MnO_x in the (near-)neutral conditions. *Ramirez et al.* showed that the annealing conditions of amorphous MnO_x films control the phases in the films.[98] Therein, they showed that by annealing the anodically deposited amorphous MnO_x films at 773 K in air and 873 K under N_2, the films converted to crystalline films with phases of α-Mn_2O_3 and Mn_3O_4, respectively, resulting in an enhancement in the stabilities and OER performances in both 'neutral' and 'basic' electrolytes. [98] Other studies showed different strategies to improve the catalytic activity under neutral conditions.[44, 75] Table 1.1 includes literature reports on the catalytic performances of manganese-based OER electrocatalysts in different electrolytes and the overpotential applied. The overpotentials arise typically from stray resistance of electrodes in the electrochemical cell, cell interconnections, the energy needed to sustain high rates of electron-transfer processes at electrode/electrolyte interfaces, and electrolyte solution.[99-102] *Indeed*, the overpotential reduces the energy efficiency; for that, enhancing the functionality of the catalysts in the (photo-)electrochemical cell would reduce the overpotential. Table 1.1 demonstrates the efforts employed over the last decade to improve the catalytic performances of MnO_x based OER catalysts under different pH conditions.

Table 1.1 Electrocatalytic performances of manganese-based OER catalysts reported in the literature

Catalyst	Overpotential (mV)	I (mA cm^{-2})	Electrolyte (pH)	Substrate	Source
MnCat	590	1	0.1 M KPi (7)	ITO	*Zaharieva*, 2012 [43]
MnO_x/Au-Si_3N_4	550	10	0.1 M KOH	Au/Si_3N_4	*Gorlin*, 2013 [40]
Crystalline α-Mn_2O_3	520	10	1 M KPi	FTO	*Ramirez*, 2014 [98]
MnO_x/Au-GC	400	0.23	0.1 M KOH	Au/GC	*Gorlin*, 2014 [103]
α-MnO_2	490	10	0.1 M KOH	Graphite carbon	*Meng*, 2014 [104]
α-MnO_2	450	10	1 M KOH	GC	*Huyuh*, 2015 [105]
Activated MnO_x (disordered δ-MnO_2)	470	0.1	0.1 M Pi (2.5)	FTO	*Huyuh*, 2015 [81]
γ-MnOOH	680	10	1 M Pi (7)	GC	*Smith*, 2016 [106]
Mn_2O_3	387	10	1 M NaOH	FTO	*Smith*, 2016 [106]
α-Mn_2O_3	340	10	1 M KOH	FTO	*Kölbach*, 2017 [107]
$CaMn_xO_y$	550	1.5	1/15 M Pi (7)	FTO	*Simchi*, 2018 [108]
MnO_x-10	393	10	1 M KOH	FTO	*Walter*, 2018 [109]
MnO_x	445	1	1M KPi (7)	CFP	*Melder*, 2019 [110]
MnO_x	360	1	1M KPi (12)	CFP	*Melder*, 2019 [110]
4 nm Mn_3O_4 nanoparticles	395	10	0.5 M NaPi (7)	Ni foam	*Cho*, 2020 [111]

Pi=Phosphate, ITO=Indium Tin Oxide, FTO=Fluorine Tin Oxide, GC=Glassy Carbon, CFP=Carbon Fiber Paper.

1.5.3 Structure and Composition

Manganese oxides demonstrate a wide range of Mn-O moieties of different crystal structure phases.[27] Figure 1.6 shows the crystal structures of the biological Mn_4CaO_5 in PS-II (at left) and the most abundant Mn_xO_y compounds of different stoichiometries. The MnO_2 compound exhibits diverse crystalline polymorphism at which the MnO_6 octahedrons are the building blocks of their structures. The structure of each MnO_2 polymorph depends on the arrangements and interconnections of the MnO_6 octahedrons. [27] The MnO_x polymorphs can be classified into three predominantly configurations: tunnel, 2D-layered, and 3D networks (like Haumannite and Bixbyite) structures.[27] The polymorph structure, in general, strongly affects the electrochemical properties of the MnO_x phases. For example, the α-MnO_2 in the tunnel structure promotes the intercalation of ions, which enhances the OER kinetics.[28] The 2D-layered sheets of MnO_6 octahedrons, known as birnessite (δ-MnO_2) polymorph (shown at the right side of Figure 1.6) is widely studied and have been identified as promising catalysts toward water oxidation.[27, 39, 46, 112-114] The Mn^{III} vacancies within the layered sheets of birnessite structure undergo Jahn Teller distortion in $Mn^{III}O_6$ octahedrons, which leads to the elongation of Mn-O bonds.[78, 112, 114, 115] These elongated Mn-O bonds weaken the confinement of MnO_6 octahedron, providing structural flexibility, to which many studies have related to the high catalytic activity toward water oxidation.[27, 68, 112, 115-117]
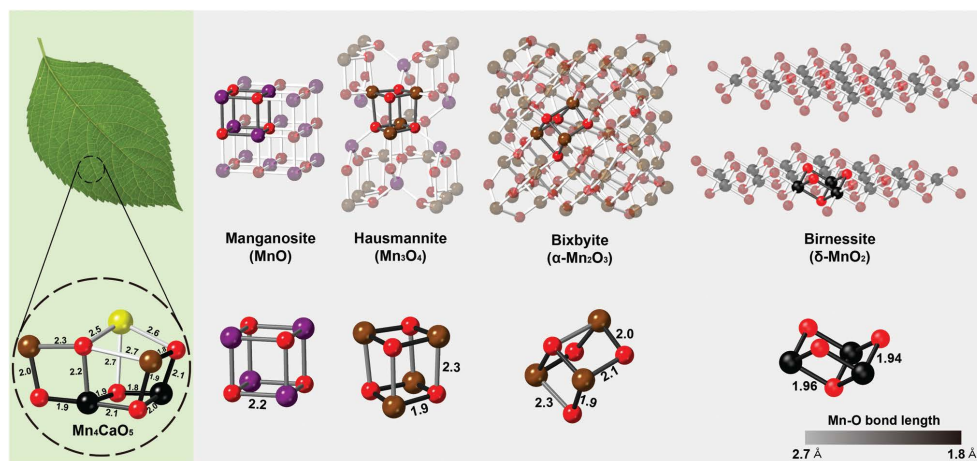
Figure 1.6. Crystal structures of the biological Mn_4CaO_5 cluster (at left) followed by Mn_xO_y compounds of different stoichiometries. Mn^{II} ion in *purple*, Mn^{III} in *brown*, Mn^{IV} in *black*, O in *red*, and Ca in *yellow* spheres. *Reproduced* from [27] *with permission from The Royal Society of Chemistry.*

Figure 1.6 reveals the close similarity between the Cuban structural motif of biological Mn_4CaO_5 cluster and that of Mn_xO_y phases with different Mn-O bond lengths and angles, which promotes

Mn_xO_y likelihood to mimic the optimized natural catalyst in PS-II. *Park et al.*[42] revealed that the catalytic activity is enhanced just by tuning the Mn valency with a negligible change in the crystal framework.

Zaharieva et al.[112] synthesized Mn–Ca oxides catalysts where the Ca^{II} ion was introduced above layer defects in the interlayer space geometry similar to birnessite, resulting in a compound that closely resembles the natural Mn_4Ca complex structurally and functionally. *Zhao et al.*[117] and *Lee et al.*[118] have shown in their recent work that introducing metal cations within the MnO_2 lattice would improve the structural stability and electron transfer, resulting in an enhancement in its electrocatalytic activity toward OER.

Apart from birnessite, other Mn oxide phases are reported to catalyze the OER. Previous studies showed that manganese oxide catalysts of a high concentration of the Mn^{III} oxidation state exhibit a comparably higher catalytic activity toward water oxidation.[42, 56, 97, 119] Other studies reported that the bixbyite exhibit higher catalytic performance than hausmannite and other $Mn^{IV}O_2$ polymorphs.[106] The series of decreasing the catalytic activity within MnO_x film follows an order ($Mn_2^{III}O_3$, birnessite) > $Mn_3^{II/III}O_4$ > $Mn^{II}O$ that mirrors the decrease of the proportion of Mn^{III} in these manganese oxides films.[56, 119, 120] As pointed out in the last section, the Mn^{III} state is unstable in specific electrolytes, *i.e.,* it disproportionate into Mn^{II} and Mn^{IV} in the neutral electrolytes. Hence a significant increase in catalytic activity can be achieved upon stabilizing the Mn^{III} and inhibition of possible disproportionation reaction.[44, 98, 115, 120] *Takashima et al.*[44] revealed that Mn^{III} serves as a vital intermediate state which participates in the water oxidation process regardless of the initial MnO_x phase.

The high catalytic activity of MnO_x catalysts enriched by the Mn^{III} phase might be strongly correlated to the electronic structure of the Mn^{III} ions. The Mn^{III} ion with high spin electronic configuration ($t_{2g}^3 e_g^1$) is bonded to O^{2-} ions in an octahedral arrangement. This configuration undergoes strong Jahn-Teller distortion of the MnO_6 octahedra, which results in two longer and more flexible $Mn-O$ bonds, which likely enhances the formation of $Mn-OH_2$ species at the surface and the cleavage of $Mn-O_2$ bonds, which lead to enhancing the catalytic turnover of the water oxidation reaction.[27, 28, 116]

1.5.4   Co-catalyst/photoanode for PEC

When photoelectrodes are immersed in an electrolyte, the water-splitting process occurs at the photoelectrode surface in three main steps, as illustrated in Figure 1.7. Upon light illumination, (1) charges (electrons and holes) separate, followed by (2) migration of holes to the photoanode

surface and the electrons to the photocathode of the PEC device, and (3) water oxidation and reduction occur at the photoanode and photocathode, respectively.[14] A suitable photoelectrode for water splitting PEC devices should match some characteristics, summarized as following [14, 29-31, 34, 37]:

- Sufficient bandgap ($E_g \geq 1.8$ eV) to generate photovoltage large enough to split water
- Good absorber in the visible light range (400 nm $< \lambda <$ 700 nm).
- High stability in the dark and under light illumination.
- Band position straddle for OER and HER. This occurs when the valence band (VB) edge is more positive than the oxidation potential of (O_2/H_2O), and the conduction band (CB) edge position is more negative than the reduction potential of (H^+/H_2).
- Low overpotential for water oxidation/reduction.
- High charge transfer efficiency.
- Low cost of production and operation for economically competitive devices.
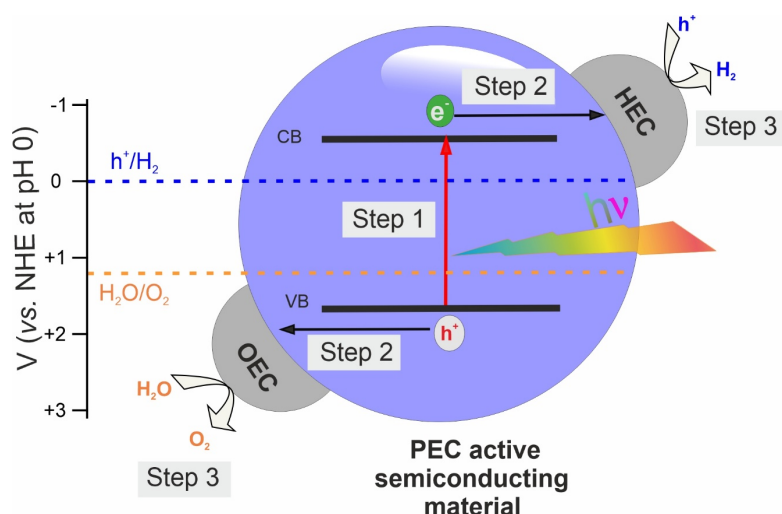
Figure 1.7. Schematic diagram for a typical photoelectrochemical water splitting process. Upon light illumination (hυ), (1) charges (h^+, holes & e^-, electrons) separate, then (2) migrate to the photoelectrodes surface at which oxygen evolution (O_2/H_2O) occurs at the Oxygen Evolution Catalyst (OEC) surface and hydrogen evolution (H^+/H_2) reactions at the Hydrogen Evolution Catalyst (HEC). VB, Valence Band; CB, Conduction Band.

Various semiconductors, like WO_3, [121, 122] Fe_2O_3, [123] $BiVO_4$,[124, 125] and TaON, [126-133] have been developed over the years and utilized as photoanodes for water oxidation. However, they still either suffer poor charge separation/transport processes or exhibit low resistance to photo-corrosion under visible light.[121, 123, 134-136] Poor charge transfer will lead to the hole accumulation

at the photoanode surface, which in turn increases the probability of charge recombination.[34]

Modifying the semiconducting photoanode surface by metal oxide catalysts (also addressed as co-catalysts) can have a synergetic effect toward enhancing water-splitting PEC electrodes. The co-catalyst overlayer has several advantages: on the one hand, it protects the semiconductor from (photo-)corrosion, which leads to an improvement in stability and overall efficiency [34, 130, 137], and on the other hand, it assists in the kinetics of the interfacial charge transfer, *i.e.,* reduce the activation barrier to be required for charge transfer.[14, 34, 138] Furthermore, the co-catalyst can modify the photoanode's surface chemistry via band bending and passivating recombination centers, which increase the charge separation efficiency.

Various MnO_x based materials have been studied in the literature for the aforementioned advantages as a co-catalyst to several photoanodes. *Irani et al.* investigated the role of ultra-thin MnO_x co-catalyst films on the photoelectrochemical performance of $BiVO_4$ photoanodes as a function of MnO_x thickness. [139] Therein, at up to 4 nm thick MnO_x, the photocurrent increased due to a band bending at the interface of $MnO_x/BiVO_4$ while very thick MnO_x (> 4 nm) on $BiVO_4$ will lead to charge recombination, deteriorating the photoactivity.[139] *Cao et al.* demonstrated an enhancement in the WO_3 photoanode activity after loading MnO_x by photodeposition.[140] *Gujral et al.* reported a 7-fold enhancement in the oxidative photocurrent densities for MnO_x electrodeposited on a TiO_2–TaON photoanode in near-neutral solutions (pH 6).[130] *Liu and co-workers* reported that $Mn_3O_{4+\delta}$ co-catalysts coated on α-Fe_2O_3 photoanode enhanced the photoelectrochemical OER performance due to the improved charge separation and the enhanced interfacial charge transfer, reporting the most prominent enhancement to be attributed to the Mn valency of ~3.4+.[141]

Based on these crucial aspects related to MnO_x as a catalyst or co-catalyst for OER, the various composition and structural characteristics of MnO_x-based systems are reported to offer a significant degree of freedom to formulate efficient catalysts. However, at the same time, the pathways to achieving such a goal are becoming more complicated. Therefore, significant development steps are being made to better understand the underlying mechanism of water oxidation catalysis by MnO_x through three commonly synergistic ways: (i) kinetics studies for unraveling the water oxidation reaction mechanism,[142] (ii) Theoretical calculations to understand and elucidate feasible reaction mechanisms,[143] and (iii) spectroscopic analysis to identify the changes happening to the catalytic materials.[40, 73, 113, 144-148] For the latter, X-ray spectroscopic techniques fundamentally characterizing the structural and electronic properties of the catalytic materials are primarily adopted for studies reported in this dissertation. The theoretical background of the X-ray spectroscopic techniques used in this dissertation is highlighted in detail in *Chapter 2*.

Among various X-ray techniques, soft X-ray absorption spectroscopy (XAS) and resonant inelastic X-ray scattering (RIXS) measured at the Mn $L_{2,3}$-edge and O K-edge enable mechanistic probe into the electronic structure of the metal-ligand, *i.e.,* (Mn—O) sites. Precisely, these techniques provide information on the $3d$ electronic valence states, which are responsible for the redox reaction.[149] Furthermore, RIXS is a technique that probes the valence excitations and enables analysis of the *d-d* excitations and the charge transfer transitions.[150, 151] While interpreting the O K-edge XA spectra, two main regions can be found: The first is the pre-edge region with well-defined peaks, which originate from the hybridization of O $2p$ and Mn $3d$ states. This pre-edge offers information about the Mn oxidation state and Mn-O bonding.[72, 152-154] The molecular orbitals are hybridized, and features arise from manganese and oxygen in the ligand manifest in the measured spectra. *Ex situ* and *in situ* soft XAS and RIXS studies on electrodeposited MnO_x catalysts are reported in *Chapter 4* and *Chapter 5*.

While XAS and RIXS probe the unoccupied and occupied valence states, the X-ray photoemission spectroscopic (XPS) technique, being based on the ionization of core-electron, is thereby probing the core levels, providing information about the chemical and electronic properties of the material. Multiplet splitting is a characteristic behavior for some transition metals, with manganese included. All Mn oxidation states except Mn^{VII} give rise to multiplet splitting in Mn $2p$ XPS spectra with distinguishable peak structures that provide a useful quantitative assignment of Mn oxidation states present in the catalyst.[155] This is shown later in section 6.3.2.2. In *Chapter 6*, we used hard XPS or the commonly known "*hard X-ray photoelectron spectroscopic* (HAXPES)" measurement to study the chemical composition and electronic structure changes at the interface between MnO_x as a co-catalyst and TaON photoanode, as a function of MnO_x overlayer thickness.

1.6   Scope and Thesis Outline

This dissertation focuses on elucidating the chemical composition and the electronic structure of the manganese oxide system either in the form of a catalyst or as a co-catalyst coupled to tantalum oxynitride photoanode, aiming to find an optimal MnO_x structure for the (photo)electrochemical device. Also, another objective of this thesis is to lay a proof-on-concept on the feasibility of *in situ* investigation at the manganese-electrolyte interface in an electrochemical cell under a high vacuum probed by soft X-rays. Working on our project, we focused on getting answers to the following scientific questions:

➢   What is the origin of catalytic activity changes in MnO_x films prepared under different pH conditions? How does the Mn oxide oxidation state change as a function of pH?

-    This question was addressed by conducting a soft X-ray absorption investigation on MnO_x films electrodeposited from acidic, neutral, and basic electrolytes using the LiXEdrom endstation of BESSY II. Measurements were recorded at Mn $L_{2,3}$-edge and O K-edge. A linear fitting algorithm, coupled with the experimental results, was used to identify the amount of MnO_x phases in each film. [Details in *Chapter 4*]

➢   Which oxidation state(s) present during the water oxidation reaction, and whether the MnO_x states increase continuously with increasing potential? Are there any changes in the bandgap of the material? Role of charge transfer between metal-ligand during OER?

-    In an effort toward getting concrete answers to those questions, *in situ* XAS/RIXS spectroscopic studies under electrocatalytic conditions were conducted to track the transformations and electrochemical analysis happening in the electrodeposited MnO_x catalyst. Moreover, the active states of the MnO_x catalyst were identified before, during, and beyond the water oxidation reaction under real working conditions. [Details in *Chapter 5*]

➢   How can MnO_x be an efficient co-catalyst to the TaON semiconductor? Is the thickness of the MnO_x as an overlayer will change the chemical composition and structural properties at the MnO_x/TaON interface? Is there any enhancement in the photoactivity after depositing ultra-thin MnO_x films (even 0.5 nm) on the TaON photoanode?

-    Hard X-ray photoemission spectroscopy was employed at the HIKE endstation of BESSY II to tailor the compositional and structural changes at the MnO_x/TaON interface as a function of increasing the MnO_x thickness. The experimental results were supported further with numerical simulation using SESSA software to better understand the HAXPES experimental measurements. [Details in *Chapter 6*]

This dissertation comprises seven chapters with the following outline:

   Chapter 1, "Introduction," introduces the current energy problem, including climate change and global warming, caused by the dependence on fossil fuels as the primary energy source. A solution is to produce clean fuel from renewable and sustainable energy sources based on sunlight, precisely, hydrogen formed in artificial photosynthesis by the water-splitting reaction. I elaborate on the particular selection of manganese oxide to be the catalyst studied in this thesis, as a water oxidation (co)catalyst. This chapter provides comprehensive literature on the manganese oxide system, pointing out the crucial aspects that can influence its catalytic activity toward OER.

Chapter 2, "X-ray Spectroscopies," gives an overview of X-ray interaction with core/valence levels of the material, resulting in photoemission/absorption excitation processes. It covers the theoretical fundamentals of the X-ray spectroscopic techniques employed in this thesis, such as "*X-ray absorption spectroscopy* (XAS)," "*resonant inelastic X-ray scattering* (RIXS)," "*X-ray photoelectron spectroscopy* (XPS)," and "*hard X-ray photoemission spectroscopy* (HAXPES)." Besides, an understanding of the principle concepts behind the measurements and the information we can gain.

Chapter 3, "Experimental Methods and Setups," provides an overview of the experimental methods and setups used. It covers the technical descriptions of the experimental endstations and beamlines used for data acquisition. I start by describing the experimental endstations and the electrochemical flow cell in which the samples were hosted and measured in (ultra-)high vacuum. Then I described the synchrotron facility of BESSY II, highlighting the technical parameters of the beamlines. A brief overview of sample preparation methods is presented, followed by ways of XAS/RIXS data correction.

The main Ph.D. study on manganese oxides is reported in *Chapter 4*, *Chapter 5,* and *Chapter 6*, where each chapter includes parts from articles either published or under preparation.

Chapter 4, "Electronic structural Insight into Formation of MnO$_x$ Phases in Electrodeposited Catalytic Films of different pH," starts with an introduction about MnO$_x$ as a promising catalyst for water oxidation reaction, with the motivation of studying the electronic structure for MnO$_x$ catalysts of different pH. Conventional electrodeposition was used to deposit the MnO$_x$ films from ionic liquids under different pH conditions. Soft XAS was employed in this study to understand the electronic structures for each catalyst and relate it to their catalytic activity. In the Experimental section, a description of the sample preparation and the experimental parameters used to collect the XAS spectra are presented, followed by the radiation damage study used to find out the optimum experimental settings to collect XA spectra free of any damage. The Results and Discussion section include the spectroscopic results at the Manganese L$_{2,3}$-edge and Oxygen K-edge. Then, I introduced the linear fitting algorithm in the following section, which was used to fit the experimental spectra in order to identify the amount of MnO$_x$ phases quantitatively in each film. Finally, a conclusion section summarizes the results at the end of the chapter. Further details are included in Appendix A.

Chapter 5, "An in situ Study of the Electronic States of the MnO$_x$ Catalyst During Water Electrooxidation," is organized analogously to the previous chapter: the introduction motivates toward understanding the functionality of MnO$_x$ catalyst under real water oxidation reaction condition. More precisely, the main goal of this study is to apply an *in situ* spectroscopic study on electrodeposited MnO$_x$ films under electrocatalytic conditions in order to monitor and track

the structural changes happening in the metal oxides electronic states of MnO_x at various catalytic cycle stages. Manganese $L_{2,3}$-edge XAS and RIXS were measured in this study as a function of applied positive potential under turnover conditions. It also includes the previously reported literature and our elaborated approach to measuring it. In the Experimental section, a detailed description of the sample electrodeposition is given, and the characterization of the samples is presented together with the specific experimental parameters used in XAS and RIXS. A damage study for the samples measured with X-ray simultaneously applied to potential (*i.e., in situ*) are also reported. The experimental Results and Discussion section is divided into (i) cyclic voltammetry of MnO_x, (ii) XAS spectra, and (iii) *In situ* RIXS spectra of MnO_x films. The samples in this study were investigated *in situ* and *ex situ* for comparison. Lastly, I presented some of the theoretical calculations related results. Lastly, the conclusion is drawn in the last section. Further details are included in Appendix B.

Chapter 6, "Chemical Composition and Electronic Structure of the MnO_x/TaON Interfaces," starts with an introduction and motivation toward enhancing the catalytic activity of photoanodes by adding an efficient overlayer (*i.e.,* co-catalyst). In this study, the MnO_x is acting as a co-catalyst to the TaON photoanode. This study aims to understand the phase composition and electronic structural changes at the MnO_x/TaON interface as a function of the thickness of the MnO_x overlayer. The "Sample Preparation" section describes the method used to synthesize the MnO_x/TaON films. The "Experimental Methods" sections include all the specific experimental parameters used for collecting HAXPES spectra, and a description of the HAXPES experimental geometry used is provided. The experimental Results and Discussion section is divided into two main subsections (i) sample characterization and (ii) HAXPES results measured at the core levels of Ta $4f$, O $2s$, Mn $2p_{3/2}$, Mn $3s$, Ta $4p_{3/2}$, N $1s$, C $1s$, and the valence band, analyzed and studied in detail. This is followed by the Numerical Simulation section, using the SESSA software applied on the MnO_x/TaON system as a multi-layered sample of different thicknesses to understand the experimental results better. The "Conclusion" section follows afterward. More details are reported in Appendix C.

Chapter 7, "Summary and Outlook," summarizes the most significant results of the reported studies and this dissertation's outcome with my perspective on future experiments.

Chapter 2

X-ray Spectroscopies

Different spectroscopic techniques are used as probing methods to investigate the electronic structure in materials. In this dissertation, spectroscopic techniques encompassing "*X-ray absorption spectroscopy* (XAS)," "*resonant inelastic X-ray scattering* (RIXS)," "*X-ray photoemission spectroscopy* (XPS)," and "*hard X-ray photoemission spectroscopy* (HAXPES)" are used to investigate the electronic structure and the chemical composition of manganese oxide-based catalysts for water oxidation. These techniques are element-sensitive, providing insights into unoccupied, and occupied valence states in the investigated material. This chapter presents a theoretical background on X-ray spectroscopies, starting with X-ray properties, and a description of the interaction of X-rays with matter, followed by the fundamental aspects of the employed X-ray spectroscopic techniques used in this thesis.

2.1   Introduction to X-ray Spectroscopies

Wilhelm Conrad Röntgen initially discovered the X-ray or X-radiation in 1895 while he was running experiments using a high-voltage discharge tube.[156, 157] He named it "**X-ray**s" because of the unknown nature of the discovered radiation. The electromagnetic X-rays serve as the best tool to study materials since it has wavelengths, ranging from tens of nanometer to Ångstrom, which is about the same order of magnitude as the atomic distances in the matter. The energy of the incident photons (E) can be determined by Plank's law, as follow,

$$E = h\upsilon = \frac{hc}{\lambda} \tag{2.1}$$

where h is the Planck's constant (6.626×10^{-34} J.s), υ and λ denote the frequency and wavelength of the wave, respectively, c is the speed of light (3×10^8 m/s). X-rays are divided according to their energies into two ranges: **'Soft' X-rays** (between 0.1-2 keV) and **'Hard' or 'Tender' X-rays** (between 2-10 keV).

X-ray radiation can be generated either by a laboratory-based anode source with fixed photon energy, like Al K_α (1486.6 eV) and Mg K_α (1253.6 eV) anodes or by synchrotron radiation source (like BESSY II in Germany). The latter offers particular advantages: (1) it provides a highly collimated X-ray beam with high brilliance, (2) the tunability of photon energies allows for local probing of core resonances of elements in the material and can probe the surface or bulk of the sample based on the incident photon energy.[151, 158, 159] In the last few decades,

synchrotron-based spectroscopic techniques have become remarkably a powerful tool to study and investigate the properties and structure of materials to the most delicate details. BESSY II synchrotron radiation is used in this dissertation as the primary energy source for all measurements (details in section 3.2).

Core-level X-ray spectroscopies can give direct access to probe detailed electronic structure. In X-ray absorption (XA) or X-ray photoemission (XP) experiments, a core-hole is created upon X-ray excitation, leaving the system in an excited state. The core-hole is considered an essential ingredient of core-level spectroscopy.[159] Then, an electron in a higher-lying energy level relaxes to fill the core-hole within the core-hole lifetime (typically femtoseconds) with possible rearrangements through radiative (*i.e.,* emit photons) and/or non-radiative decay processes.[159, 160]

Figure 2.1 shows core-level spectroscopies at which various electronic excitations are presented based on X-photon interaction with core-electron in a molecular system. Electronic excitation processes can be classified into two dominant processes as follow:

(i)   "***Non-Resonant Excitation***": It occurs when the energy of the incident photon is higher than the binding energy of the core-electron; thereby, ionization of the core-electron occurs, as represented in Figure 2.1(a). It is commonly known as "*X-ray photoemission spectroscopy (XPS)*" or "*photoionization.*" The photoemitted electrons can be measured by an electron analyzer, which discriminates the emitted electrons energetically. After photoionization, the core-hole is subsequently filled through two decay mechanisms: The first is the "*non-resonant X-ray emission* (XE)" shown in Figure 2.1(b), where a valence electron fills the core-hole, and photons are emitted (*i.e.,* radiative decay). While the other decay process in Figure 2.1(c) is the "*normal Auger-electron emission,*" where it is nearly like the non-resonant X-ray emission, but instead of emitting some photons, there is photoionization of Auger electrons from a valence level (*i.e.,* non-radiative decay).

(ii)   "***Resonant Excitation***": It involves tuning the incident photon energy resonantly to match a specific electronic excitation from the core level to an unoccupied valence level as schematized in Figure 2.1(d). This process is known as "*X-ray absorption spectroscopy* (XAS).*" After the X-photon absorption, two subsequent decay processes can occur. The first is a radiative decay, where a valence electron fills the core-hole, and photons are emitted, as shown in Figure 2.1(e) and known as "*X-ray fluorescence emission*" or "*resonant inelastic X-ray scattering* (RIXS)." The second decay process is a non-radiative emission, where no photons are emitted but electrons. In this process, the Auger electron is emitted either through the "*participator Auger electron emission*" in Figure 2.1(f) or

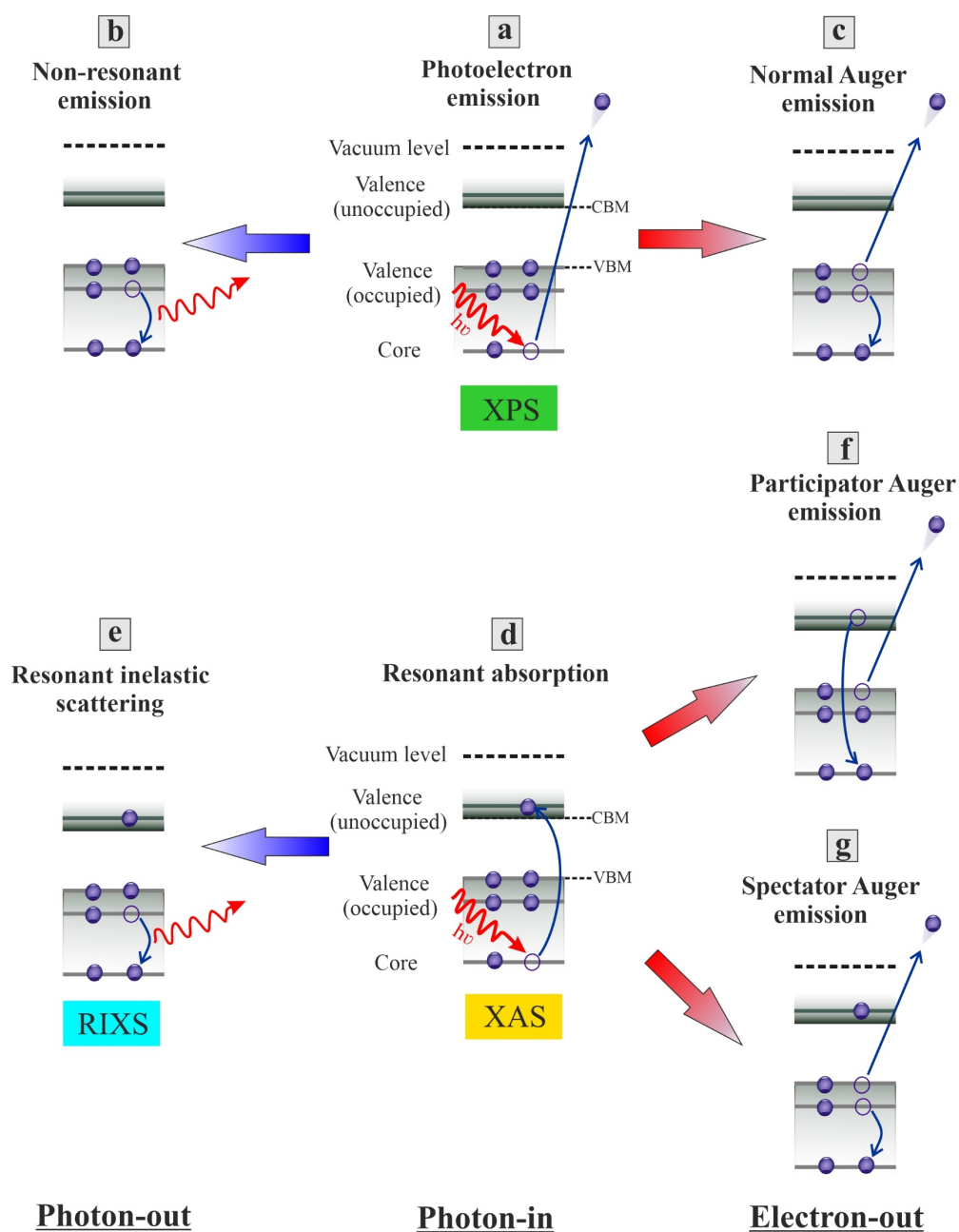"*spectator Auger emission*" in Figure 2.1(g).

Figure 2.1. Schematic representation of core-level spectroscopies (XPS and XAS), depicting the excitation processes in a molecular system and their subsequent decay processes. *The blue* arrows yield a radiative decay (*i.e.,* photon-out) while the *red* arrows to a non-radiative decay (*i.e.,* electron-out). A detailed explanation of these processes is described in the text.

Here in this thesis, I used three main spectroscopic techniques, XAS, RIXS, and HAXPES, as a probing tool to study the MnO_x as a water oxidation (co-)catalyst. HAXPES technique is based

on XPS but using hard X-rays as the probing source instead of soft X-rays. The electronic excitations involved in the three above-mentioned spectroscopic techniques are schematized in Figure 2.2 on the MnO_x molecular system. In this specific system, the core level represents $2p$ orbitals, and the occupied valence level represents the $3d$ (t_{2g}) orbitals of manganese. The unoccupied valence level represents the manganese $3d$ (e_g) orbitals. Each of the above-mentioned spectroscopic techniques (also referred to in Figure 2.2(b)) will be discussed more in detail in the next sections, 2.2 - 2.5.
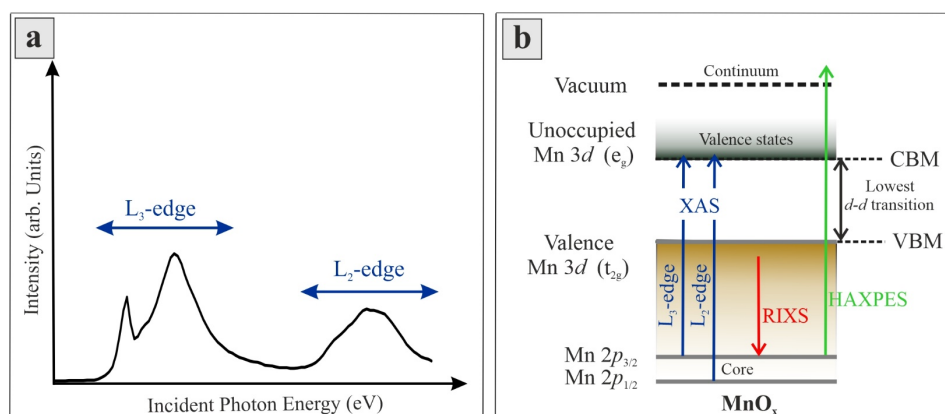

Figure 2.2. (a) Typical $L_{2,3}$-edge absorption spectrum for a transition metal oxide (birnessite $Mn^{III/IV}$ is chosen here as an example) with well-defined separated multiplet splitting peaks, and (b) Schematic representation of the electronic transitions for XAS in *blue*, RIXS in *red*, and HAXPES in *green* in the MnO_x system.

2.2 X-ray Absorption Spectroscopy

The "*X-ray absorption spectroscopy* (XAS)" is a powerful spectroscopic technique used to investigate the electronic structure of the materials. In XAS, the incident energy of X-rays is tunned resonantly to match the excitation of an electron from the core level to unoccupied valence states above the Fermi level of the element under investigation. A typical XA spectrum is displayed as a plot of the intensity of outcoming photons *vs.* incident photon energy, as shown in Figure 2.2(a). The characteristic sharp peaks in any XA spectrum are assigned to the transition from the core to unoccupied valence levels (*i.e.,* absorption edges).[161]

X-ray absorption edges are denoted by the letters K, L, M, .. starting this sequence with the edge of the highest energy. Each edge represents an excitation from a specific energy level. For example, the K-edge is assigned to the excitation from the $1s$ level into the empty $2p$ level;

whereas the L_1- edge assigns a transition from $2s \rightarrow 3d$ level; L_2- and L_3-edges are assigned to $(2p_{1/2})^2 \rightarrow 3d$ and $(2p_{3/2})^4 \rightarrow 3d$ transitions, respectively, and so on for M_1, M_2, .., M_5.

Like any other optical transitions, transitions upon X-ray excitations are usually electric dipole transitions, which are governed by selection rules. Therefore, transitions between electronic energy levels are allowed when the selection rules ($\Delta l = \pm 1$, $\Delta s = 0$) are obeyed where l is the *angular momentum quantum number* ($l = 0$ for *s-orbital*, $l = 1$ for *p-orbital*, $l = 2$ for *d-orbital*, …) and $s = $ *spin quantum number* $= \pm 1/2$. [162]

The intensity of each absorption peak in a typical XA spectrum (Figure 2.2(a)) depends on the transition probability or the absorption cross-section of the electronic transition between the core and unoccupied valence levels involved. The XA transition probability ($W_{g \rightarrow f}$) between a system in an initial ground state $|\psi_g\rangle$ and final state $|\psi_f\rangle$ upon absorbing photon of energy ($\hbar\omega$) can be expressed by Fermi's golden rule: [159]

$$W_{g \rightarrow f} = \frac{2\pi}{\hbar} \left| \langle \psi_f | \hat{T} | \psi_g \rangle \right|^2 \delta(E_f - E_g - \hbar\omega) \qquad (2.2)$$

Here $\hat{T}$ represents the transition operator. The $\langle \psi_f | \hat{T} | \psi_g \rangle$ describes the matrix element between the ground and final states. Dirac delta (δ) function ensures the conservation of energy and identifies the density of states.[163] E_g, and E_f are the energies of the ground and final states, respectively. Based on the dipole selection rule, the $2s^2 \rightarrow 3d$ transition is electric dipole forbidden ($\Delta l \neq \pm 1$). In contrast, the dipole transitions from $2p$ state into an unoccupied $3d$ valence orbital are allowed and manifested in a typical L-edge XA spectrum for the first-row TMs in the form of two multiplet splitting well-separated intense peaks, shown in Figure 2.2(a). These two peaks arise due to the spin-orbit interaction of the excited metal $2p$ core level. The $2p$ level splits according to *total angular momentum j* ($j = |l \pm s|$) into $\frac{3}{2}, \frac{1}{2}$ with an intensity ratio of 2: 1.[164] For that, the first peak at the low energy range originates from $2p_{3/2} \rightarrow 3d$ transition and is known as "L_3-edge", while the second absorption feature "L_2-edge" on the higher energy side is assigned to the $2p_{1/2} \rightarrow 3d$ transition, as shown in Figure 2.2(a,b). The energetic separation between the L_3 and L_2-edges originates from spin-orbit splitting, which differs for different elements.[165] *E.g.*, the L_3 and L_2-edges are separated by ~ 6.65 eV for vanadium, while 11 eV for manganese.[166] Since the MnO_x is the specified material studied in this thesis; therefore I focused on measuring the absorption spectra reported in *Chapter 4* and *Chapter 5* at the dipole-allowed manganese L_2 and L_3-edges ($2p_{1/2} \rightarrow 3d$, and $2p_{3/2} \rightarrow 3d$ transitions, respectively) and oxygen K-edge ($1s \rightarrow 2p$) transitions.

Different acquisition modes can be considered to collect an XA spectrum (see Figure 2.3). One can use the *direct transmission mode,* at which the incident and transmitted X-ray intensities (I_o and I) can be measured through a thickness (z) in a material under investigation, as shown in Figure 2.3(b).
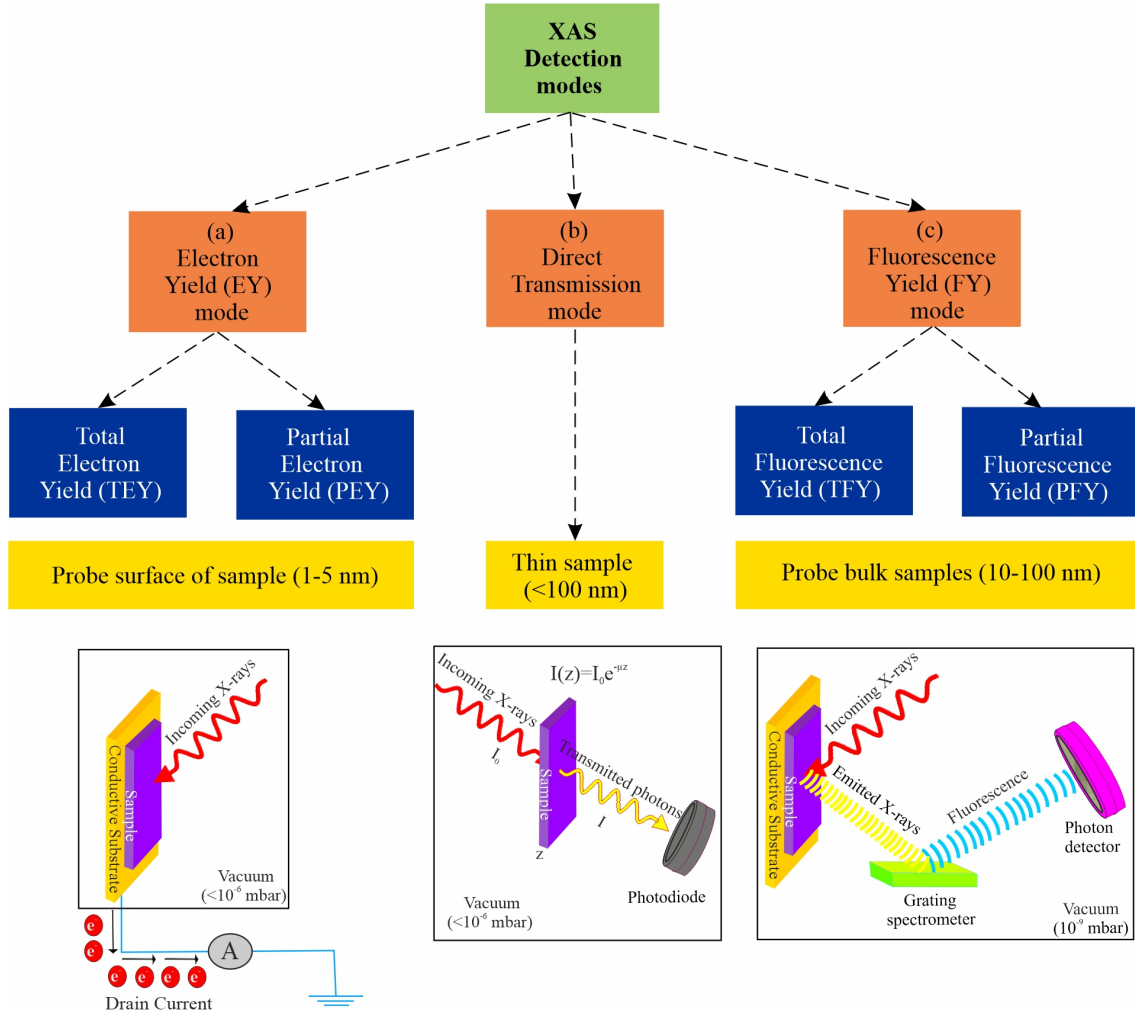

Figure 2.3. Detection modes of X-ray absorption spectroscopy

Hence, the absorption coefficient (μ) can be calculated from the Beer-Lambert equation (2.3)

$$I(z) = I_0 e^{-\mu z} \tag{2.3}$$

Where z is the thickness of the material, and μ is the absorption coefficient.

The *absorption coefficient* (μ) is a sign of the electron density in a material and is directly related to the *absorption cross-section* of the element (σ_a) through [162]

$$\mu = \frac{ln\left(\frac{I}{I_0}\right)}{z} = \rho_a \sigma_a = \left(\frac{\rho_m N_A}{A}\right)\sigma_a \tag{2.4}$$

where ρ_a is the atomic number density, ρ_m, N_A, and A, are the mass density, Avogadro's number, and the atomic mass, respectively. Although the *absorption cross-section* (σ_a) can be known, soft X-photons are attenuated strongly within a few micrometers, which results in a very weak transmitted intensity.[167] Therefore, XA spectra collected with *transmission mode* require extremely thin (<100 nm) samples, which is challenging for some sample preparation techniques, like electrodeposition.

Yield mode is an alternative way to measure the XA spectrum without facing sample restrictions and X-ray limitations as in the transmission mode. There are two aspects of yield modes; "*Electron yield* (EY)" and "*Fluorescence yield* (FY)" modes (Figure 2.3). Both detection modes rely on creating a core-hole upon X-ray absorption, followed by a subsequent energy release during the relaxation process. On the one hand, in EY mode, the released energy is transmitted to a second electron, which results in the ejection of an auger electron.[162] This is shown in Figure 2.1(f,g) and Figure 2.3(a). EY is a surface-sensitive method due to the short escape depth of electrons from the material.[168] On the other hand, the released photons in the FY mode are directly measured, as in Figure 2.1(e) and Figure 2.3(c).

Since the amount of core-holes being filled by some higher-lying valence electrons in the sample is equal to the number of emitted particles (electron or photon), the absorption cross-section can be measured by detecting such particles. Most of the emitted particles are electrons representing more than 95% of the total decay.[169] When one collects all the electrons flowing out of the sample, this is known as the "*total electron yield* (TEY)" mode. The TEY intensity is dominated by secondary electrons created upon scattering as the Auger electron leaves the sample.[170] It can be practically measured by recording the drain current flowing from the solid sample holder, as initially investigated by *Gudat and Kunz*.[171, 172] The drain current is measured using the Keithley ammeter, which can measure extremely low currents down to 50 pA. The kinetic energies of the emitted electrons can be collected and measured by an electron analyzer. When the data acquisition is restricted to a specific range of kinetic energies, this is known as the "*partial electron yield* (PEY)" method. [167]

In contrast to EY mode, the *fluorescence yield* (FY) mode or *X-ray emission* (XE) are bulk sensitive methods (*ca.* 10-100 nm) since it is based on collecting photons instead of electrons.[169] The photons have a high penetration depth in the material (in the range of micrometers). A photodiode or a grating spectrometer is used to detect the emitted photons. In case the photodiode detects all the photons without discriminating their wavelengths, this method is known as the "*total fluorescence yield* (TFY)" mode. However, when the grating spectrometer is adjusted to detect photons within a specific range of energies, this is called the "*partial fluorescence yield* (PFY)" method.[167] Among all, the TEY and PFY acquisition modes were

used to collect XA spectra in the experiments reported in *Chapter 4* and *Chapter 5*.

The XA spectroscopy is element-specific since the edge energy varies with each element (or atomic number), as shown in Figure 2.4(a).[173] In the soft X-ray regime, the fluorescence probability is significantly weak, which deteriorates the signal to noise ratio of the measured spectra.[174, 175] On the downside, the FY method also suffers distortions due to self-absorption and saturation effects due to the high penetration depth of photons within the sample. [169] This can also lead to a further reduction in the intensities of an FY spectrum. This phenomenon occurs mainly for highly concentrated samples.[176] The FY and the Auger emission quantum yield *vs.* the atomic number of elements are shown in Figure 2.4(b). The Auger processes compete with the fluorescence yield in a way that the probability for Auger emission is much higher for light elements (small Z) than the fluorescence.[177, 178] For example, in the soft X-ray regime, the fluorescence yield signal for manganese (Z=25) at L_3-subshell ($2p_{3/2}$) represents only *ca*. 1%.
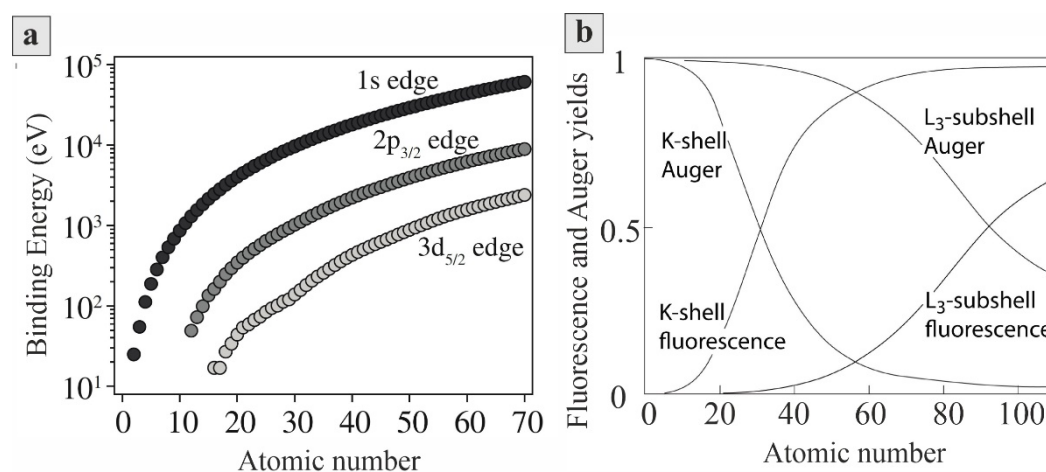

Figure 2.4. (a) Binding energy of the $1s$ (K-edge), $2p_{3/2}$ (L₃-edge), and $3d_{5/2}$ (M₅-edge) levels as a function of the atomic number. *Reproduced from* [173], *Copyright 2018 Springer Nature Switzerland AG* (b) Fluorescence and Auger yield probabilities as a function of atomic number. *Reproduced from* [178]. *Copyright 1999 Cambridge University Press.*

2.3   Resonant Inelastic X-ray Scattering

Resonant inelastic X-ray scattering (RIXS) is a photon in/photon out spectroscopy, which is also known as '*resonant X-ray emission spectroscopy* (RXES)'.[150, 179, 180] 'Resonant' of RIXS means that the incident X-ray energy match well with one of the core-electron excitation thresholds (*i.e.,* absorption edges). While 'Inelastic' means that the incoming photon energy

which enters the sample is not equal to the emitted photon energies ($E_{in} \neq E_{out}$). RIXS technique is a bulk sensitive method, which gives element-specific information. While XAS is a first-order optical process which probes an unoccupied state as an intermediate state, RIXS act as a second-order optical process which probes the occupied valence states in the final state.[159, 181-183] I elaborate on explaining this using an example in Figure 2.5(a) for a typical d^4 TM ion, like Mn[III]. In XAS, core-electron is resonantly excited upon photon absorption of energy ($\hbar\omega_k$) to unoccupied valence state $[2p_{3/2} \rightarrow 3d(e_g)]$ followed by a relaxation of a lower-lying valence electron to fill the core-hole $[3d(t_{2g}) \rightarrow 2p_{3/2}]$ which can be probed by RIXS technique. The energy difference between the incident and emitted photons (*i.e.,* energy loss) is transferred to the material in the form of low-energy elementary excitations.[150, 151]
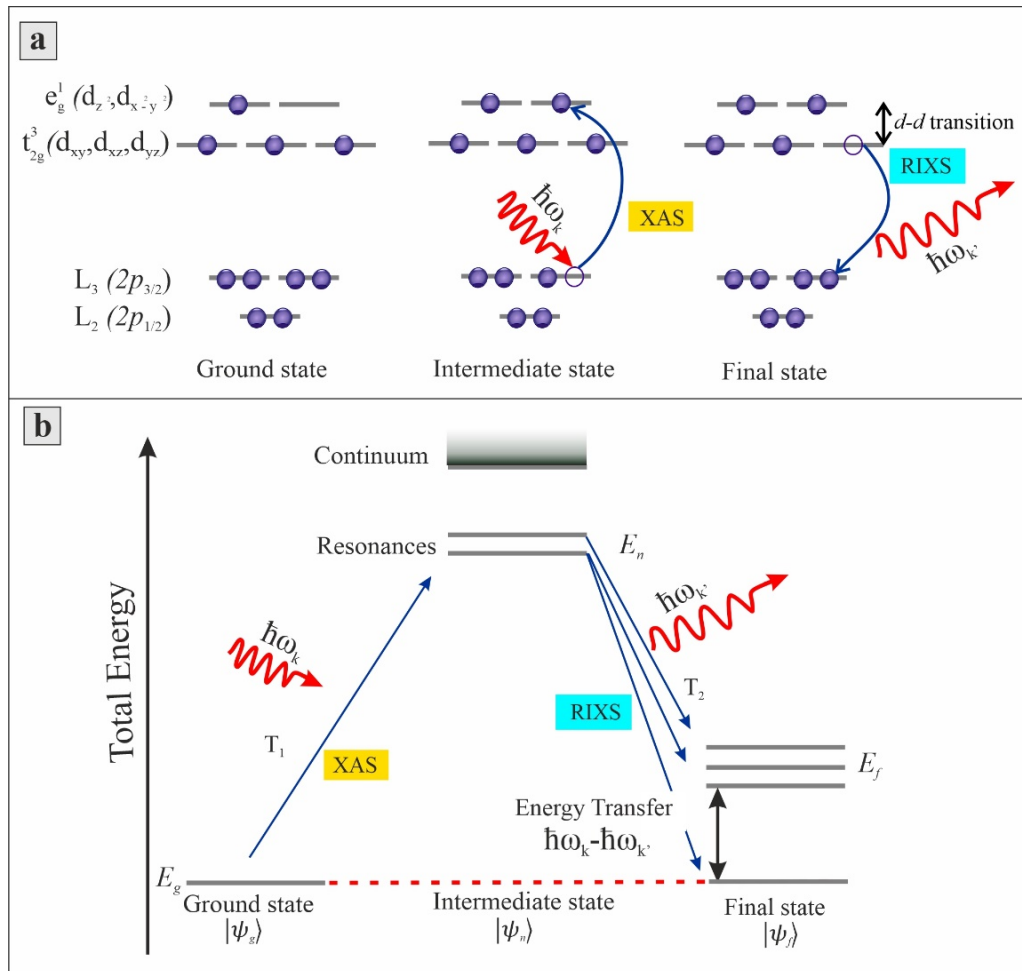

Figure 2.5. Schematic representation of the XAS/RIXS process: (a) The electronic transitions at the L$_3$-edge (*2p$_{3/2}$*) for a typical d^4 transition metal ion like Mn[III] in an octahedral symmetry, and (b) its corresponding energy scheme at which T$_1$ and T$_2$ are the transition operators between the states. More details are described in the text. *Figure (b) is adapted from [183] with permission from Elsevier.*

(b) shows a schematic energy diagram for the states involved in XAS/RIXS processes.[183] A core-electron in the ground-state system of wave function $|\psi_g\rangle$ and energy E_g absorbs incoming photon energy of ($\hbar\omega_k$), close to the core-electron excitation threshold, then excited to an unoccupied valence state above Fermi level, leaving a core-hole behind; this now represents the intermediate state with wave function $|\psi_n\rangle$ and energy E_n. Then an electron in a lower-lying valence state relaxes to fill the core-hole, emitting photon of energy ($\hbar\omega_{k'}$) and reach a final state represented by $|\psi_f\rangle$ and energy E_f. The final state may not necessarily be the electronic ground state.[183]

The one-step Fermi's Golden rule in equ. (2.2) cannot describe transitions in RIXS since it is a two-step process, so it needs a higher-order treatment, incorporating the resonant second-part of the Kramers-Heisenberg equation[184, 185],

$$W(\omega_k, \omega_{k'}) \, \alpha \sum_f \left| \sum_n \frac{\langle\psi_f|\widehat{T_2}|\psi_n\rangle\langle\psi_n|\widehat{T_1}|\psi_g\rangle}{E_g + \hbar\omega_k - E_n - i\Gamma_n/2} \right|^2 \times \frac{\Gamma_f/2\pi}{(E_g - E_f + \hbar\omega_k - \hbar\omega_{k'})^2 + \Gamma_f^2/4} \quad (2.5)$$

where, $\widehat{T_1}$ and $\widehat{T_2}$ represents the optical transition operators for the photon absorption and electron relaxation processes, respectively; Γ_n and Γ_f are the core-hole lifetime broadening of the intermediate and final states, respectively. The energy transferred to the system is equal to the difference between the incoming and emitted photons (*i.e.,* $\hbar\omega = \hbar\omega_k - \hbar\omega_{k'}$), which is also equivalent to the energy difference between the ground and the final state of the atom. Interestingly, as the dipole operator acts twice ($|\psi_g\rangle \rightarrow |\psi_n\rangle$ followed by $|\psi_n\rangle \rightarrow |\psi_f\rangle$), there is no necessity that the ground-final transition is dipole allowed. In other words, transitions at which the change in angular momentum equal to zero ($\Delta l = 0$) are thereby accessible.[150, 183] Therefore, RIXS can access the dipole forbidden *d-d* transition between the 3*d* states in TM oxides.

The RIXS spectrum is typically a plot of intensity versus energy-loss scale (*i.e.,* the incident energy minus the emitted energy). The energy calibration used for plotting RIXS spectra is described in section 3.4.2. Compared to other spectroscopic techniques like XAS and XPS, RIXS has a much lower intensity signal, but simultaneously it provides valuable information about elementary excitations near the Fermi level, which manifest in the RIXS spectrum as energy-loss (Raman) features such as [150, 159, 180]

(1) *Elastic Peak*: This peak appears at zero energy loss ($\hbar\omega = 0$) at which the final state energy in Figure 2.5(b) matches the initial state energy. In other words, the excited electron in the intermediate state refills the core level, and no energy is transferred into

the system. This process is known as "*Resonant Elastic X-ray scattering* (REXS)."

(2) ***d-d Excitations***: it originates when there is an energy difference between the initial and the final states, so energy ($\hbar\omega$) is transferred to the system. It is commonly known as "*d-d transition*" excitation. The intensity and energetic position of the *d-d* excitation feature can give direct information of the occupied density of states relative to empty states ($3d$ in the case of first-row TMs). Thereby it provides information on the bandgap in case of semiconductors.[113] For TM complexes, the *d-d* transition is in the range of 1-5 eV. This *d-d* excitation can also be monitored using the conventional UV-Vis spectroscopy; however, RIXS is a much superior technique. It is an element selective and orbital specific technique with relaxed selection rules and provides a relatively higher energy resolution than UV.[186]

(3) ***Charge Transfer Excitations***: it originates when a neighboring electron in the ligand participates in the decay of electron in the metal or vice versa. Here this excitation often appears as a broad peak in the range of 4-15 eV.[187, 188]

(4) ***Fluorescence***: it originates when a core-ionized atom is created, followed by an electron relaxation from the occupied valence orbitals to fill the core-hole, and photons are emitted, as shown in Figure 2.1(b). Fluorescence is also known as "*Normal X-ray Emission.*" This fluorescence feature scales linearly with the excitation energy.

(5) ***Magnons and Phonons Excitations*** appear energetically below 1 eV energy loss. The detection of such excitations requires a high-resolution RIXS spectrum.

Among these, we focused on studying *d-d* excitations and charge transfer (CT) excitations, as described (*vide infra)* in section 5.3.3. Therein, I elaborate on an *in situ* RIXS study done on the MnO_x catalyst, showing changes that evolve in the elastic feature, *d-d* excitations, and charge transfer excitations as a function of applied potential to the MnO_x.

The RIXS data can be plotted as a map in the incident photon energy (horizontal) *vs.* the emitted photon energy (vertical), and colors discriminate the intensity changes, as shown in Figure 2.6. By integrating the emitted intensities for every incident energy, *i.e.,* a vertical line in the RIXS map will result in an XA spectrum with absorption edges, as shown in the bottom panel of Figure 2.6. RIXS maps can also be plotted *vs.* energy-loss instead of the emitted energy scale. In such a plot, the elastic features will be seen as a vertical line, while the fluorescence features as diagonal traces, as shown later in Figure 5.10.
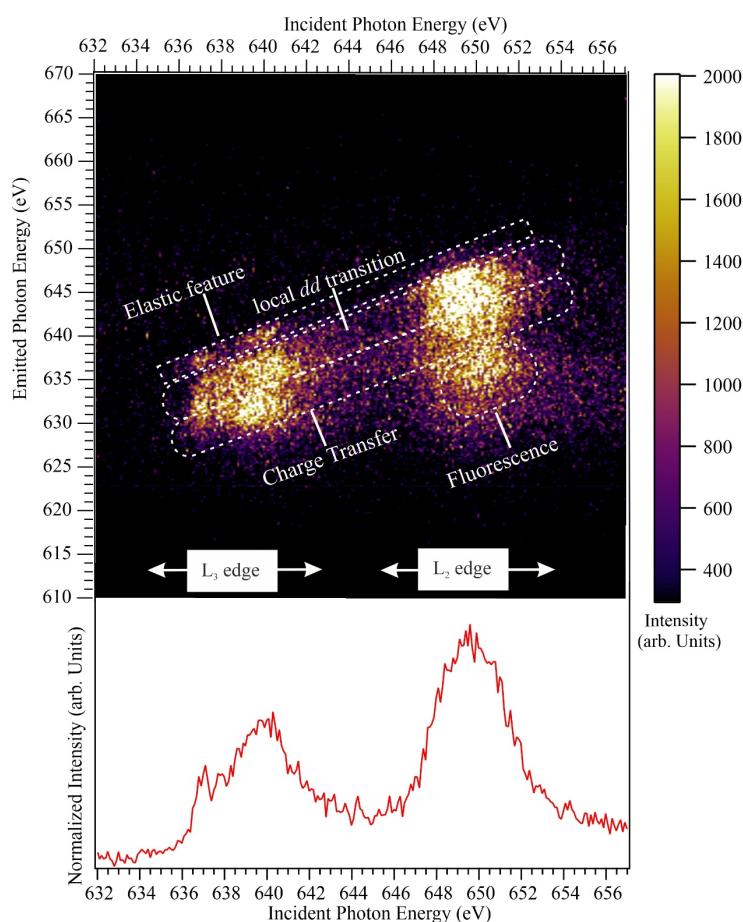
Figure 2.6. The top panel shows a 2D RIXS map with different excitation features, collected experimentally for a MnO_x thin film. The bottom panel shows an XA spectrum collected in the partial fluorescence yield mode, at which the intensity of emitted photons is integrated as a function of incident energy. The experimental details are discussed in *Chapter 5*.

2.4   X-ray Photoelectron Spectroscopy

The "*X-ray Photoelectron Spectroscopy* (XPS)" is a well-established technique to measure the binding energies of electrons and identify the chemical composition of materials. This spectroscopic technique is based on the photoelectric effect explained by Albert Einstein in 1905 [189] and developed later by K. Siegbahn in 1981.[190] A three-step model can precisely describe the direct photoemission process, as schematized in Figure 2.1(a):[191] (1) Photon excites an electron in a sample, (2) electron travels within the sample to the surface, then (3) escapes from the sample surface with kinetic energy into the vacuum, leaving the system in an ionized state.

An electron analyzer can discriminate the kinetic energy of the photoemitted electrons. Depending on the incident X-photon energy, an electron in valence orbitals or core level can be

excited. For that, two emission channels exist; *"valence photoemission,"* and *"core-level photoemission."*

Since the energy is conserved, the excitation energy of the incident photons ($\hbar\omega$) is used to overcomes the binding energy of the electrons (BE) and the rest of energy is given as kinetic energy (KE) to the ejected electron, as follow,

$$KE = \hbar\omega - BE, \quad \hbar\omega > BE \tag{2.6}$$

Since the binding energy of the electrons of an atom under investigation is an intrinsic property, thus, the KE of photoelectrons can be known if $\hbar\omega$ and BE are known. But if the sample is electrically connected with a spectrometer (Figure 2.7), it is necessary to include the work function of the spectrometer (Φ_{spect}) in equation (2.6). Then, equation (2.7) is taken the vacuum level (E_v) as a reference and can be written as follow,

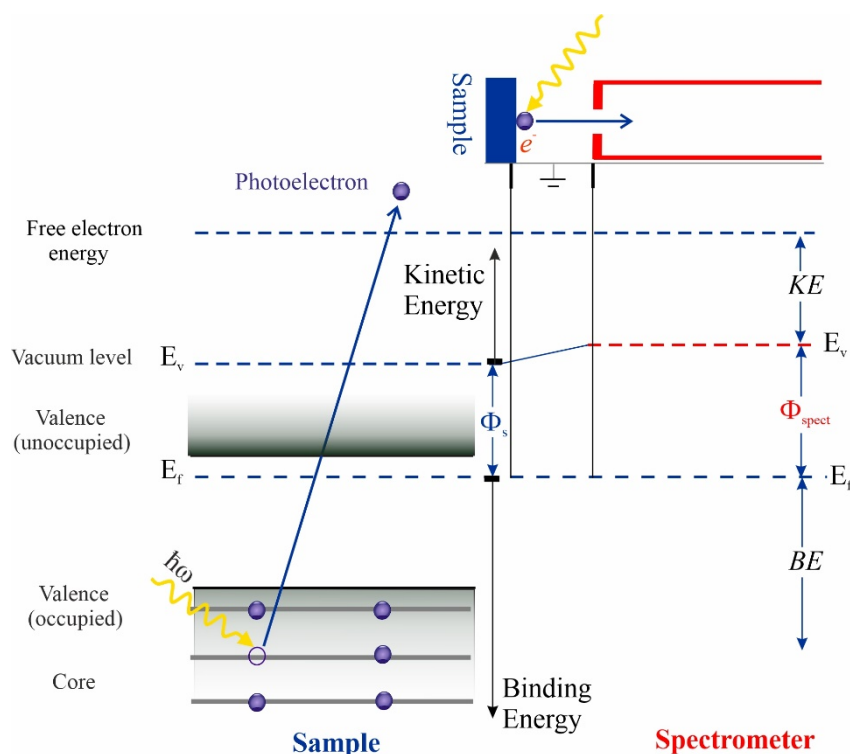$$KE = \hbar\omega - BE - \Phi_{spect} \tag{2.7}$$

Figure 2.7. Energy Diagram of a sample that is electrically connected to a spectrometer (electron analyzer) used for the XPS experiment. X-ray photons will excite and liberate electrons at a specific core level against its binding energy (BE) and work function (Φ_s), and the rest energy will be given as kinetic energy (KE). *Adapted from* [192] *Copyright 2015 Springer-Verlag Berlin Heidelberg.*

In contrast to PFY-XAS and RIXS processes, the X-ray photoemission process is a surface-

sensitive technique where the photoemitted electrons originate from the very top surface layers (*i.e.,* few nms underneath the sample surface). The reason is that electrons have a short escape depth, generally in the order of Angstroms, whereas the attenuation length of X-rays (or penetrating power of X-photons) is much deeper in the sample, *e.g.,* $1 - 10$ μm for a soft X-ray beam.[193, 194] Those electrons emitted from the sample provide direct information about the electronic structure.

In the *photoemission* process, an electron is removed upon absorption of photon energy $\hbar\omega$ from the N-electron ground state $\left| {}^{N}\psi_g \right\rangle$ with occupied spin-orbital of energy $E_g(N)$ to the $(N-1)$-electron final ionized state $\left| {}^{N-1}\psi_i \right\rangle$ of an energy $E_i(N-1)$ where (i refer to "ionized"). The transition probability between the ground $E_g(N)$ and the ionized state $E_i(N-1)$ is like any state transition, governed by Fermi's Golden Rule, so equation (2.2) will be modified to equation (2.8), to give an expression of the transition probability ($W_{g\rightarrow i}$):[195, 196]

$$W_{g\rightarrow i} = \frac{2\pi}{\hbar} \left| \langle {}^{N-1}\psi_i \left| \hat{T} \right| {}^{N}\psi_g \rangle \right|^2 \delta(E_i - E_g - \hbar\omega) \qquad (2.8)$$

After the *core-electron photoemission* process, an electron from the valence level decays to fill the core-hole, and a photon or an electron is emitted. The decay processes are known as "*non-resonant X-ray emission*" or "*normal Auger electron emission*" processes. In the *normal Auger-electron emission* (Figure 2.1(c))*,* an electron from a high-lying valence level fills the core-hole, transferring its energy to a third electron (Auger) to ionize it, and the system is left in a doubly ionized state. The KE of the Auger electrons is determined by the energy difference between the electronic states involved in the process and independent of the incoming photon energy in contrast to the photoelectrons.[197] The Auger electrons can also be emitted during relaxation via non-radiative channels, known as "*participator Auger emission*" and "*spectator Auger emission,*" illustrated in Figure 2.1(f) and (g), respectively. It is known as *resonant photoelectron spectroscopy* (RPES) since the Auger emission occurs under resonance conditions. In other words, photon energy is tuned resonantly (like XAS) with unoccupied valence states just above the Fermi edge, then the relaxation of an electron from the valence band to fill the core-hole resonantly promotes the emission of Auger electron from the same valence band.[151] The resonant Auger electrons give rise to the intensity of the emitted photoelectrons due to the coherent superposition between resonant Auger electrons and direct photoemitted electrons.[191] However, it also makes it difficult to distinguish between the final states of resonant Auger electrons and the direct photoelectrons in the XPS spectrum.

The XPS spectrum describes the intensity I_{ij} of the emitted photoelectrons as a function of

their binding energies. I_{ij} is the intensity of the photoelectron peak j from element i, which describes the number of photoelectrons that hit the detector per unit time and per unit energy, and can be described by the following equation [189, 198]:

$$I_{ij} = e^{-\frac{z}{\lambda_X \sin\vartheta}} (\rho(z)dxdydz) \left(\frac{d\sigma_{nl}(\alpha)}{d\Omega}\Omega\right) I_o e^{-\frac{z}{\lambda_e \sin\theta}} D_o(KE) \tag{2.9}$$

Where the first exponential term ($e^{-\frac{z}{\lambda_X \sin\vartheta}}$) describes the X-ray intensity attenuation during its way from the surface of the sample to the volume element $dxdydz$ (supposing that an angle ϑ is the angle of incidence at the sample surface or the angle between the X-ray trajectory and the normal to the sample surface), λ_X is the *inelastic X-ray attenuation length*, $\rho(z)dxdydz$ is the local material density of the infinitesimal volume element $dxdydz$ at a depth z from the sample surface; $\left(\frac{d\sigma_{nl}(\alpha)}{d\Omega}\right)$ is the differential scattering cross-section, which describes the probability of the photoelectrons emitted from a xy plane forming an angle θ between the analyzer and the sample surface (*i.e., take-off* angle) into the *analyzer acceptance solid angle* (Ω).[199] Under the assumption of dipolar approximation and for 100% linearly polarized light with low photon energies in the soft X-ray regime, the differential scattering cross-section can be expressed as follows:[199-201]

$$\frac{d\sigma_{nl}(\alpha)}{d\Omega} = \frac{\sigma_{nl}}{4\pi}\left[1 + \frac{1}{2}\beta_{nl}.\,(3cos^2\alpha - 1)\right] \tag{2.10}$$

where σ_{nl} is the *total photoionization cross-section* for a core level described by n-principal and l-angular momentum quantum number. It can be defined as the ratio of the number of electrons emitted to the incident photons per unit time and unit surface area. β_{nl} is the corresponding asymmetry parameter, which describes the anisotropy of the photoelectron angular distribution, α is the angle formed between the photon polarization vector $\vec{\varepsilon}$ and the photoelectron momentum direction $\vec{P}$.[201, 202] Figure 2.8 schematizes the photoemission experimental geometry describing the aforementioned angles. The value of the anisotropy parameter (β) varies between -1 and 2;[201] however, when $\alpha = 54.7°$, the anisotropy parameter can be eliminated. This angle is commonly referred to as the '*magic angle*'.

The second exponential term in equation (2.9) defines the attenuation of the photoelectron intensity I_o, during its way to the surface of the sample within a thickness (z) as a result of inelastic scattering collisions as described in equ. (2.11):

$$I(z) = I_o e^{-\frac{z}{\lambda_e \sin\theta}} \tag{2.11}$$
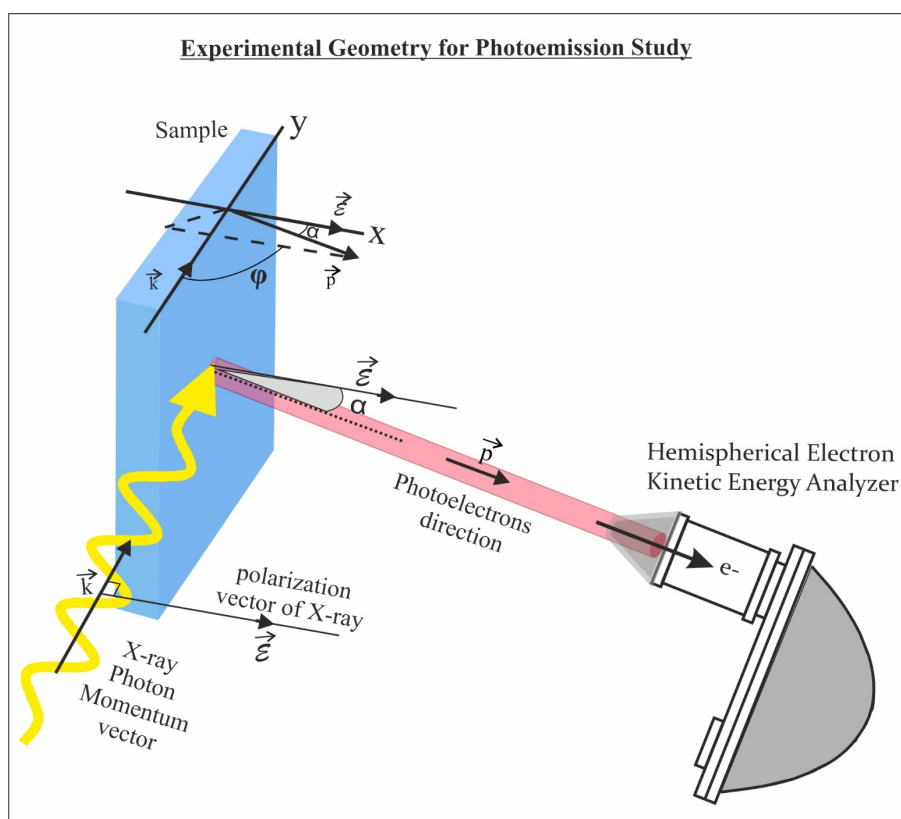
Figure 2.8. Schematic illustration of the X-ray photoelectron spectroscopy (XPS) experimental geometry, using the aforementioned angles in equation (2.10).

λ_e is the *inelastic mean free path,* which is the average path length traveled by the photoelectron before it is inelastically scattered; θ is the *take-off* angle to the sample surface ($\theta = 90 - \alpha$). For constant θ, the signal detected at a depth of $\lambda_e, 2\lambda_e$, and $3\lambda_e$ is about 64%, 87%, and 95%, respectively.[198, 203] In general, electrons have a rather short "*inelastic mean free path* (IMFP)" in materials. The probed depths depend on three main factors: (1) the inelastic mean free path, which is highly dependent on the KE of the photoelectrons or the photon excitation energy (illustrated further in next section 2.5), (2) the probed material, and (3) the detection angle of the photoelectrons with respect to the sample surface (θ, *take-off* angle). By increasing the angle θ, the photoelectrons have to move longer in the material, so it becomes less surface sensitive, and the probing depth increases.

$D_o(KE)$ in equation (2.9) is the electron analyzer detection efficiency.

In a typical XPS spectrum, the photoemission peaks are commonly represented as "nl_j", where the *principal quantum number* "n" refers to the orbital at which the photoelectrons have been emitted ($n = 1, 2, 3 ...$); while "l" resembles the "*orbital angular momentum quantum*

number and j is the total angular momentum $(j = l \pm s)$. The *full width at half maximum* (FWHM) of a typical XPS peak is determined mainly by the *natural line width* (Γ) and the instrumental resolution. On the one hand, the *natural line width* (Γ) depends on the lifetime of the excited core-hole (τ) while on the other hand, the instrumental resolution is determined by the X-ray beamline resolution (ΔE_{x-ray}), and analyzer resolution ($\Delta E_{analyzer}$). By convoluting these components, the FWHM (Λ) of a typical XPS peak can be written as [198, 203]:

$$\Lambda = \sqrt{\Delta E_{x-ray}^2 + \Delta E_{analyzer}^2 + \Gamma^2} \tag{2.12}$$

The linewidth ΔE_{x-ray} is affected by slit widths and the spot size of the incident X-rays; whereas $\Delta E_{analyzer}$ is affected by the analyzer pass energy. The micro-focusing monochromator with a small spot size provides a proper instrumental resolution. The core-hole lifetime τ generally describes the spectral broadening; it decreases as the core-hole is deeper (*i.e.,* closer to the nucleus). In that instance, the deep core-hole will have a higher chance of being filled by more higher-lying electrons, so smaller lifetime.[195, 196] For example, the FWHM for Au 4*f* is smaller compared to a deeper core level like Au 4*d*. The reason for that returns to the Heisenberg uncertainty principle ($\Delta E \cdot \Delta t \sim \hbar$) such that as Δt decreases, ΔE should increase.

2.5   Hard X-ray Photoemission Spectroscopy

As pointed out in the last section that typical XPS is well-known to be surface-sensitive due to the low KE of the photoelectrons, which is related to the low excitation energy as described by equ. (2.7). It becomes clear that when the excitation energy increases, the KE of photoelectrons increases and surface sensitivity decreases. To do so, high energy X-rays ("Hard" or "Tender" X-rays) in the energy range of *ca.* 2–12 keV probe more in-depth into the samples (*i.e.,* bulk sensitive). This technique is developed and known as "*Hard X-ray photoemission spectroscopy* (HAXPES)." It is an appropriate technique used to increase the probing depth into a sample (*i.e.,* buried layers or interface) without removing the surface layers.[201] On the downside, the photoionization cross-section decreases rapidly with increasing the excitation energy, which deteriorates the photoemission signal. Therefore the high brilliance synchrotron radiation would be suitably used for the HAXPES technique. Compared to the grating monochromator used for delivering soft X-rays, the crystal monochromator typically delivers energies in the hard X-ray regime.

For hard X-rays, the differential scattering cross-section in equ. (2.10) should be corrected to include the first-order non-dipole approximation expressed in the second square parenthesis

beside the dipole approximation as follow: [199-201]

$$\frac{d\sigma_{nl}(\alpha)}{d\Omega} = \frac{\sigma_{nl}}{4\pi}\left\{\left[1 + \frac{1}{2}\beta_{nl}.\ (3cos^2\alpha - 1)\right] + (\delta + \gamma.cos^2\alpha)\ sin\alpha cos\varphi\right\} \tag{2.13}$$

φ is the angle between the photon momentum vector $\vec{k}$ and the plane containing $\vec{P}$ and $\vec{\varepsilon}$ (as illustrated in Figure 2.8). While β_{nl} is a dipolar parameter, the δ and γ are non-dipolar parameters. The parameters $\sigma_{nl}, \beta_{nl}, \delta$, and γ are functions dependent on the excitation energy.[200]

In photoemission experiments, some significant parameters are closely related to each other and are used in this thesis: "The *inelastic mean free path (IMFP)*," "*mean escape depth (MED)*," and the "*information depth (ID)*." These parameters depend on the configuration of the experimental instruments used (*i.e.,* beamline and analyzer) and the sample under investigation (amount of (in)elastic-scattering events within the material, which affect the trajectories of the detected photoelectrons).[201] These parameters are defined according to the International Organisation for Standardisation (ISO) as follows: [204]

"Inelastic mean free path (IMFP): *average distance that an electron with given energy travels between successive inelastic collisions.*"[194] The universal curve in Figure 2.9(a) shows the dependence of the IMFP (λ_e) on the KE of the emitted photoelectron and IMFP value can be estimated using equation (2.14).[151] [KE is expressed in eV]

$$\lambda_e = \frac{1430}{KE^2} + 0.54\sqrt{KE} \tag{2.14}$$

"Mean escape depth (MED): *it is the average depth normal to the surface from which the specified particles or radiation escape.*" [194]

"Information depth (ID): *maximum depth, normal to the surface, from which useful information is obtained.*"[194] It is also commonly termed as "*probing depth*". One should remember that this information is based on a thickness, from which 95% or 99% of the detected signal originates.[205]

The higher the kinetic energy of the photoelectrons, the higher the IMFP, so higher the probing depth ($\sim 3\lambda_e$). When increasing the excitation photon energy from 2 to 12 keV, the IMFP of the photoelectrons in the matter will be generally increased from approximately 3 nm to 15 nm. [206]
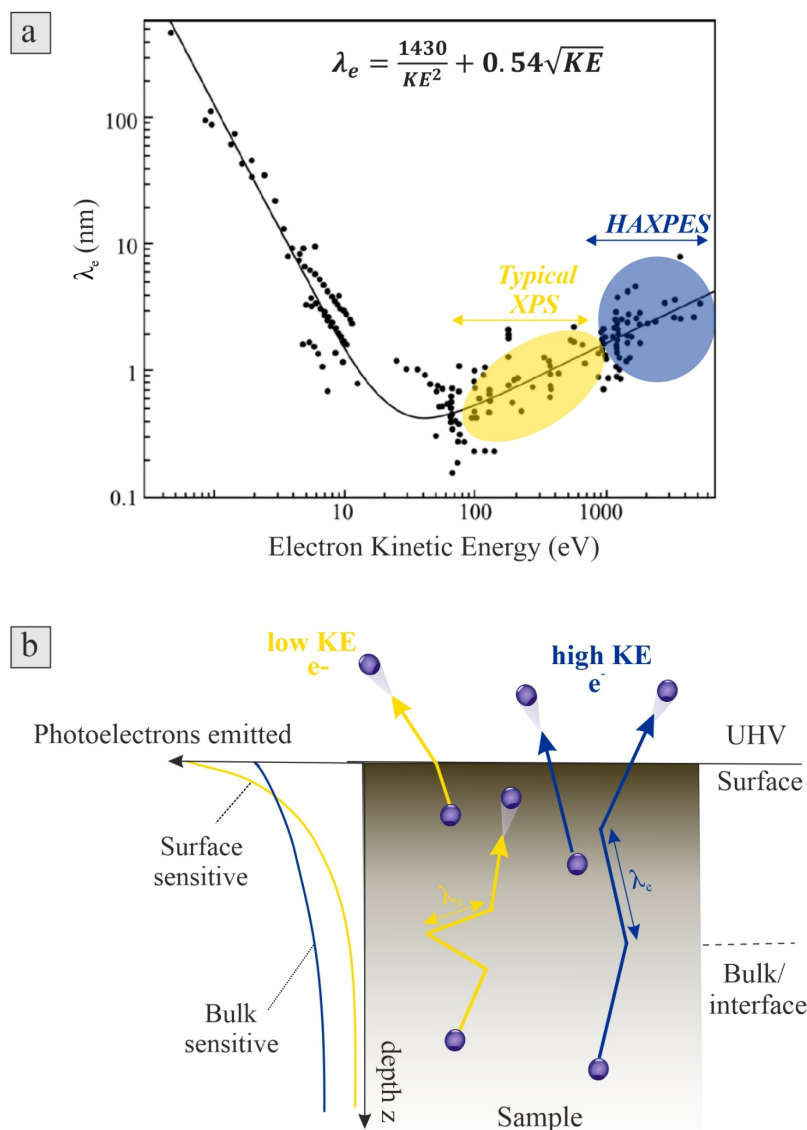
Figure 2.9. (a) Electron inelastic mean free paths (λ_e) trend as a function of photoelectron kinetic energy. *Adapted from* [207] *with permission from John Wiley.* (b) Schematic illustration of the photoelectron emission with high- (*blue*) and low- (*yellow*) kinetic energy electrons. The left-side in (b) graph simplifies the probing sensitivity through the exponential attenuation of the emitted photoelectron intensity as a function of sample depth for the low and high kinetic energy electrons.

Figure 2.9(b) schematically illustrates how electrons in solids with low and high kinetic energy are emitted from the surface and bulk. The low kinetic energy photoelectrons, shown in *yellow*, have a high probability of undergoing inelastic scattering, so they have shorter IMFP compared to photoelectrons with high kinetic energy (shown in *blue*). As a result, the low KE electrons in bulk will scatter away before reaching the sample surface, and only those close to the surface can be emitted and detected by the electron analyzer. Meanwhile, the high KE electrons can

escape from the bulk and interfaces between inter-layers. The left-hand side of Figure 2.9(b) illustrates the exponential attenuation of the emitted photoelectron intensity. It shows that most of the information depth for the low KE photoelectrons will be from the surface and least from bulk in contrast to the high KE photoelectrons.

For that, the relatively bulk sensitive HAXPES spectroscopic technique is employed in this thesis in *Chapter 6* as a probing tool to study structural and compositional changes at the interface between MnO_x and TaON photoabsorber as a function of increasing the MnO_x overlayer thickness.

Chapter 3

Experimental Methods and Setups

This chapter provides an overview of two experimental setups (LiXEdrom and HIKE) we used to perform spectroscopic measurements, together with using various beamlines of the synchrotron facility of BESSY II in Berlin, Germany. The absorption and resonant inelastic spectra were collected using the LiXEdrom setup, while the hard X-ray photoemission study was explored with the HIKE setup. In this chapter, I describe the characteristics of both experimental setups and the electrochemical flow cell used to host the sample under investigation for the XAS/RIXS study. In the subsequent section, I present some fundamentals of the synchrotron radiation, which is used in this thesis as the primary probing tool, including the beamlines used—followed by describing sample preparation methodologies and data analysis consideration. The chapter is concluded with a brief description of the "*simulation of electron spectra for surface analysis* (SESSA)" software I used to perform numerical simulation, which supported the hard X-ray photoemission measurements.

3.1   Experimental Setups

3.1.1   LiXEdrom Experimental Setup

The LiXEdrom is a mobile experimental endstation at the BESSY II facility used to measure high-resolution absorption and emission measurements for solid or liquid samples.[208] This setup was used to collect the XAS/RIXS measurements reported in this thesis in *Chapter 4* and *Chapter 5*. Figure 3.1 shows a schematic diagram of the LiXEdrom endstation. The LiXEdrom setup is comprised of three sections: **(1) The main chamber,** in which the X-ray beamline passes along the y-direction, interacting with the sample. The solid samples can be mounted on a sample holder while liquid samples flow either in a liquid jet[209] or electrochemical flow cell.[148] The sample holder or flow cell is mounted on a motorized micrometer-precision manipulator, which can move by submicron steps in XYZ directions with rotation around the z-axis (φ) required for proper sample alignment with the spectrometer and the beamline. The vacuum pressure inside the main chamber can reach 10^{-7} mbar for a solid sample holder and

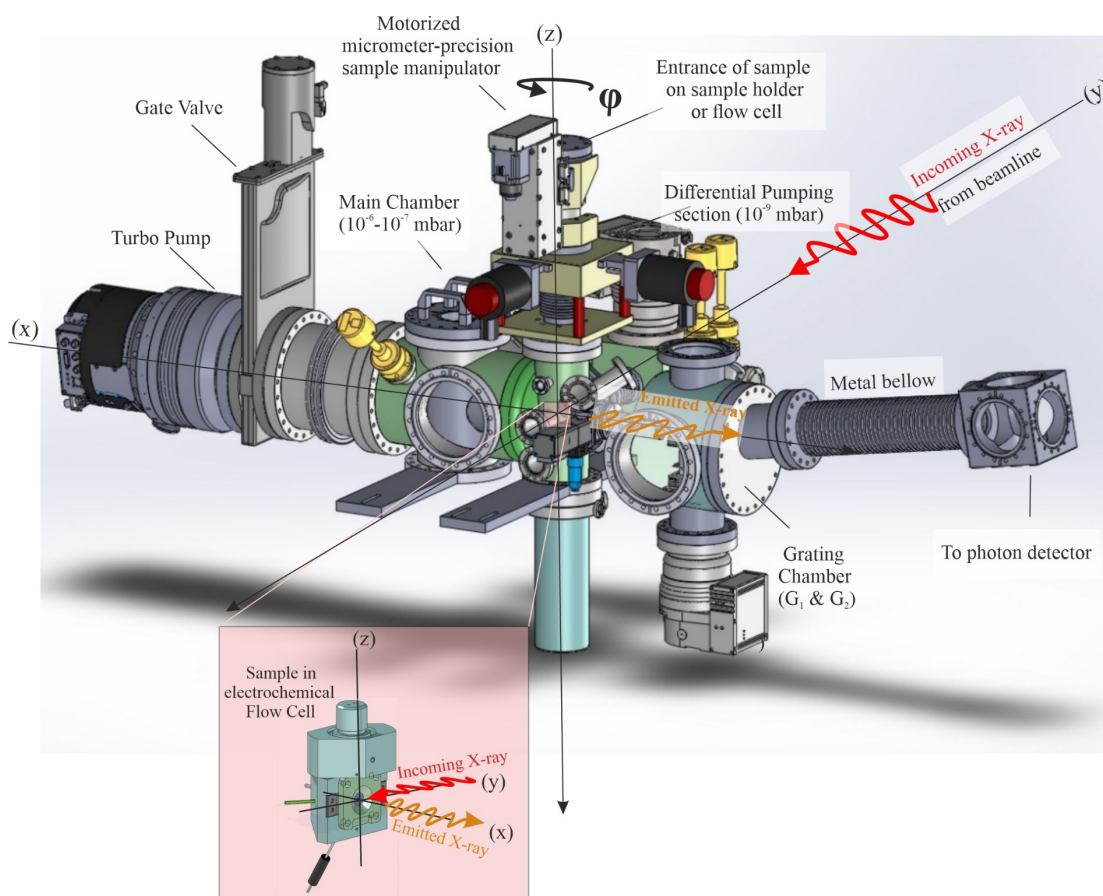10^{-6} mbar in the case of the flow cell.

Figure 3.1. A 3D schematic drawing of the LiXEdrom experimental setup, encompassing the main chamber, differential pumping, and the spectrometer section. The spectrometer section includes the grating chamber and the photon detector. *The 3D drawing is adapted from* [208].

(2) a differential pumping section is placed behind the main chamber. Its function is to differentiate the pressure between the main chamber and the beamline and to the spectrometer section. A pinhole is used to separate these sections, which allows the pressure inside the differential pumping and the spectrometer section to reach 10^{-9} mbar. **(3) the Spectrometer** consists of a grating serving as a dispersive element and a photon detector. The gate valve between the main chamber and the spectrometer is left open during XA spectra measured in FY mode and RIXS measurements; however, it should be closed during collecting XA spectra measured in EY mode or when the sample is inserted or removed from the main chamber to preserve the vacuum pressure. The LiXEdrom spectrometer in the current version includes two variable-line-spacing (VLS) spherical gratings. One is a low-energy grating (G_1) with line density 1200 I/mm, which covers energies of 200 – 500 eV, while the high-energy grating (G_2)

with 2400 I/mm line density is optimized for covering energies of 400 – 1200 eV.[208] Both gratings are connected to the photon detector via a metal bellow (right of Figure 3.1) and placed on a motorized manipulator. The LiXEdrom spectrometer (*i.e.,* gratings and detector) is arranged in a Rowland circle geometry, as illustrated in Figure 3.2, aiming at minimizing aberrations from spherical grating as suggested by Henry Rowland.[210] The grating radius defines the diameter of the Rowland circle. [210] The photons emitted out of the sample are focused on the spherical grating, which allows for wavelength dispersion, then the signal is subsequently detected by a rotatable photon detector (Figure 3.2).
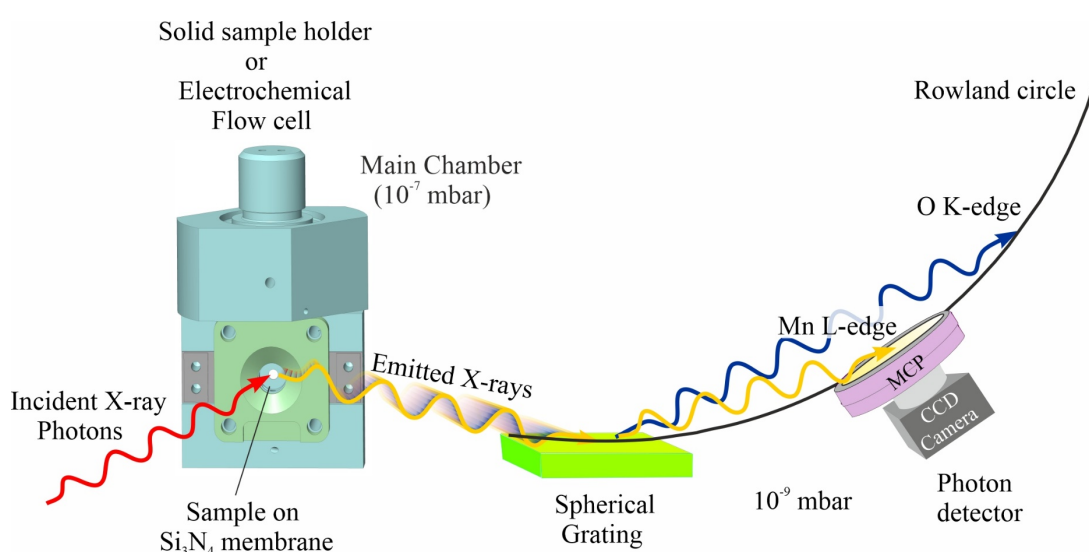
Figure 3.2. Schematic drawing of the LiXEdrom spectrometer arranged in a Rowland circle geometry. The incoming X-ray beam interacts with the sample (here as an example, the sample is deposited on a membrane in a flow cell); then, the emitted photons are focused on a spherical grating and energetically resolved toward a photon detector. A rotatable photon detector then collects the fluorescence light in the form of XAS/RIXS.
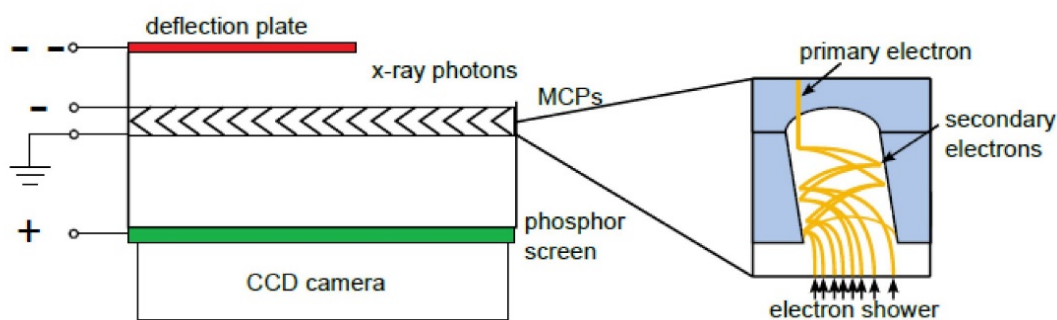

Figure 3.3. Photon detector assembly of the LiXEdrom. The electron avalanche process happening in the MCP is shown on the right side. *This figure is reproduced from reference* [211].

Figure 3.3 shows an assembly for the photon detector placed in the spectrometer section of the LiXEdrom setup. It consists of a deflection plate, a microchannel plate (MCP), a phosphorous screen, and a charge-coupled device (CCD) camera.[208] Once the photons are received from the grating and incident on the MCP surface, electrons will be emitted. Every single electron enters a small tube known as a *microchannel* of the MCP, in which they are accelerated under high voltage.[167] As schematized on the right-hand side of Figure 3.3, the primary electron emits a shower of secondary electrons, known as *electron avalanche*, upon collision with the microchannel walls.[167] The electron shower will subsequently impinge on the phosphorous screen, producing a fluorescence image on the CCD camera, which can be measured, corrected, and converted to RIX spectra, as illustrated in section 3.4.

The XA spectra are measured in PFY mode (abbreviated as PFY-XA spectra) using the rotatable photon detector with a relatively low signal to noise ratio compared to XA spectra measured in TEY mode (abbreviated as TEY-XA spectra). Hence relatively longer data acquisition time should be considered when collecting PFY/TFY spectra to improve the signal to noise ratio.

3.1.1.1 Electrochemical Flow Cell – Liquid in Vacuum

The flow cell is an intelligent way to investigate liquids in a vacuum with X-rays, at which a membrane acts as a barrier between liquid and vacuum and simultaneously allows transmission of X-rays. [167, 212] The flow cell is specially designed for the LiXEdrom endstation and used to conduct *in situ* soft X-ray spectroscopic (XAS/RIXS) measurements together with electrochemical analysis, as reported in *Chapter 5*. The flow cell is mounted on a manipulator to adjust its position with respect to the X-ray beam and the grating. The flow cell body is made of polyether ether ketone (PEEK). It includes an O-ring of Viton, which has high chemical resistance, prevents electrolyte leakage, and secures the membrane against the mechanical force applied from the cell body.[167] The small amount of electrolyte (*ca.* 5 mL) needed to conduct measurements with the flow cell is an advantageous feature, which distinct it over other techniques, like micro-jet. Since conductive substrates are needed for XAS/RIXS measurements, a 20 nm thick layer of gold (Au) is sputter-coated on the 100 nm Si_3N_4 membrane. Details on the Si_3N_4 membrane is reported in section 3.3.1.2.

The electrochemical flow cell (in the middle of Figure 3.4) is fitted with 3-electrodes: platinum (Pt) wire used as a counter electrode, Ag|AgCl|3.4 M KCl electrode (sourced from Innovative Instruments, Inc., USA) as the reference electrode, and the Si_3N_4 membrane (sourced from Silson Ltd, UK) served as the working electrode. The flow cell is connected to a peristaltic pump (REGLO ICC- 75-0514), which is used to pump the electrolyte from the electrolyte reservoir to

the flow cell under a controlled flow rate, as shown in Figure 3.4. The potentiostat and the peristaltic pump are placed outside the LiXEdrom setup, connected to the flow cell in the vacuum chamber via feedthrough. Before conducting the *in situ* X-ray spectroscopic measurements, the sample is first deposited on the smooth side of the Au/Si_3N_4 membrane (attached to the electrolyte).
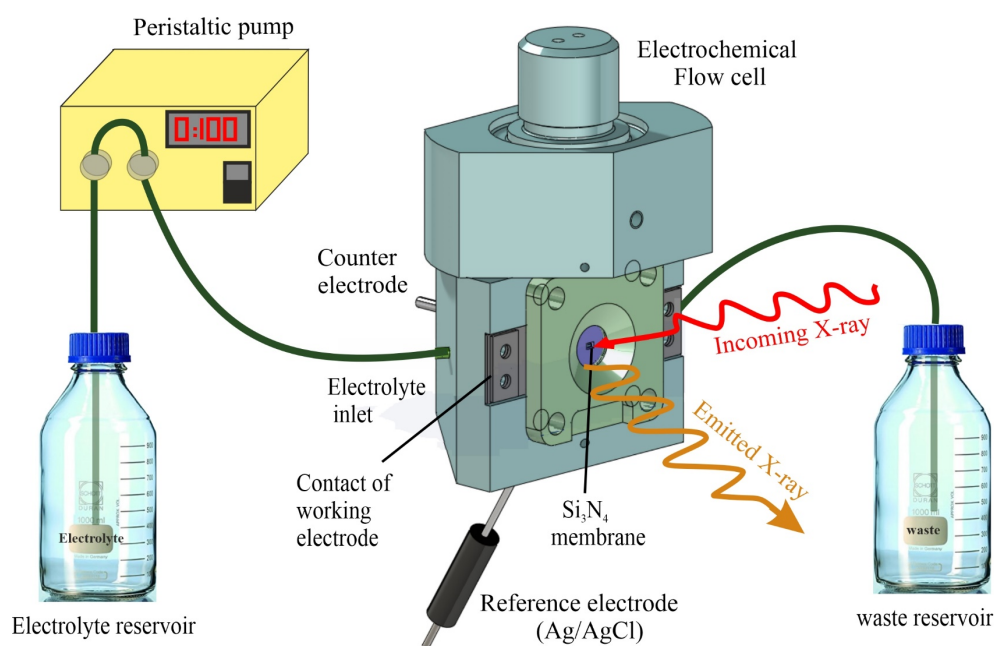

Figure 3.4. A schematic diagram for the electrochemical flow cell connected to a peristaltic pump. The electrolyte is pumped into the flow cell via a peristaltic pump under a controlled flow rate. The electrolyte is flushed in a small area behind the Si_3N_4 membrane then flushed out to the waste reservoir.

The Au/Si_3N_4 membrane should be relatively thin to allow the transmission of photons through the membrane to interact with the sample. At the same time, the membrane should sustain the difference in the pressure (~1 bar). Figure 3.5 shows the calculated X-ray transmission curves of Si_3N_4 (100 nm) membrane with and without a gold overlayer (20 nm). It reveals that X-ray transmission is reduced by 25-40 % through the Au/ Si_3N_4 membrane in the energy range (500-660 eV). This specified energy range mainly covers the oxygen and the manganese absorption edges needed in our investigations. It should be mentioned that the transmission is further reduced by 10-20 % when the flow cell is tilted by 45º with respect to the X-ray direction.[167]
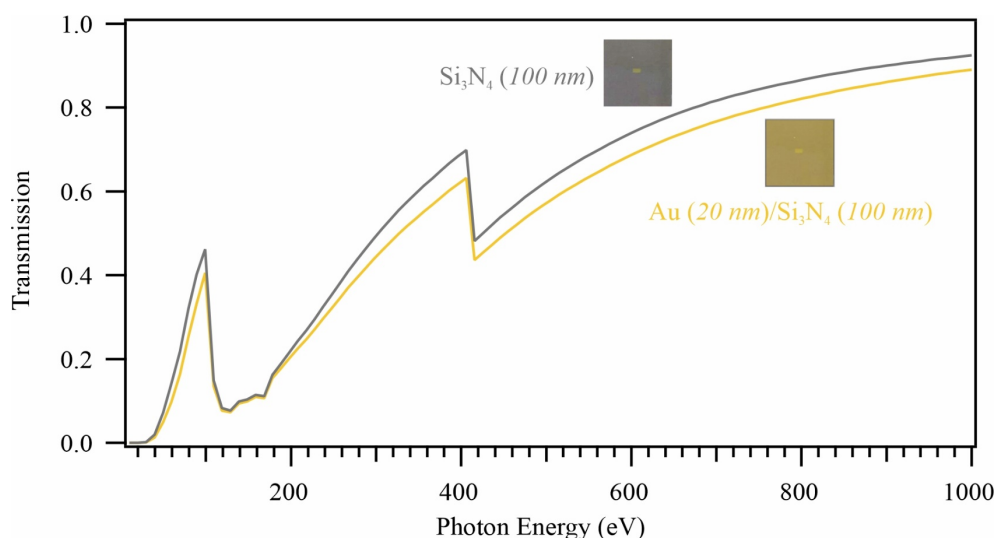
Figure 3.5. The X-ray transmission curve through 100 nm Si_3N_4 membrane window in *gray* and 20 nm Au overlayer on 100 nm Si_3N_4 membrane in *orange*. Data obtained from http://henke.lbl.gov/optical_constants/filter2.html

3.1.2   HIKE Experimental Setup

The ***High Kinetic Energy*** (HIKE) photoelectron experimental setup is designed for HAXPES experiments, optimized for electron kinetic energies of 2 – 10 keV.[213] This setup was used to collect the HAXPES measurements presented in *Chapter 6*. A schematic diagram of the HIKE endstation is presented in Figure 3.6. This experimental setup has three sections: **(1) The load lock** is necessary for mounting the samples. It can store up to 6 samples. The pressure inside the load lock section is down to 10^{-6} mbar. **(2) The preparation chamber** allows for heating the samples up to 800 °C and is also equipped with a diamond scraper. **(3) The analysis chamber** includes the solid sample holder, a hemispherical electron analyzer (Scienta R4000), and a photon detector. The analyzer is fixed at an angle of 90° with the X-ray beam and used for photoemission experiments, while the photon detector is used for performing the absorption (NEXAFS/EXAFS) measurements. The sample holder is mounted on a motorized 5-axis VG Scienta-manipulator, which adjusts the sample's position with respect to the electron analyzer and X-ray beam. The pressure inside the analysis chamber and near the hemispherical electron analyzer reaches 10^{-9} mbar. The analysis chamber is separated from the load lock by a gate valve, which is necessary to preserve the pressure in the analysis chamber.

The load-lock and the analysis chamber are mounted on a motorized chamber stand to allow

further alignment of the analyzer with the sample and the X-ray beam. This alignment can be translational in x, y, and z-direction and rotational through tilting (φ) or rolling (θ) the frame, as indicated in Figure 3.6. Further adjustment is possible using a hand-crank.
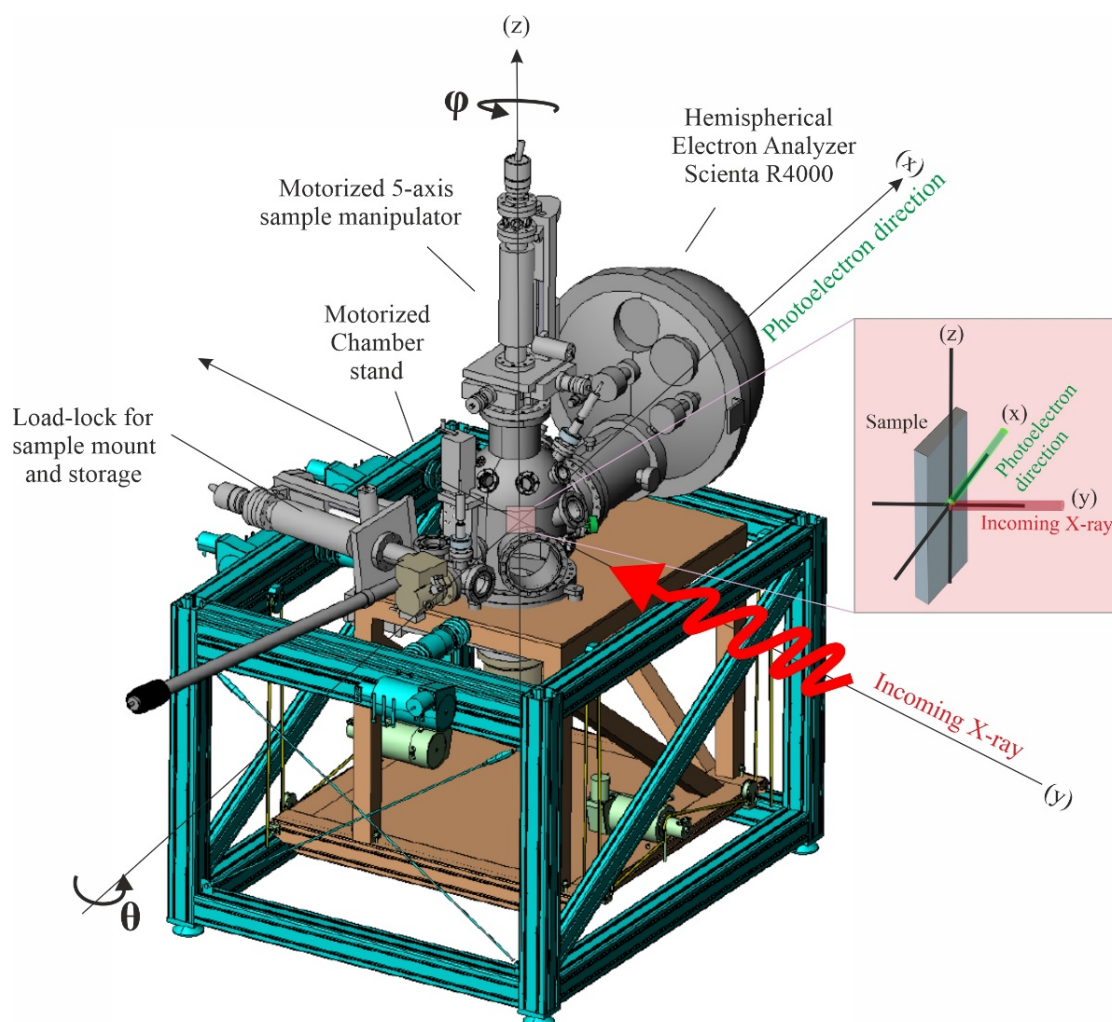

Figure 3.6. A schematic view of the HIKE experimental station.
The zoom-in on the right side shows the manipulation of the sample inside the analysis chamber (at the *rose* square). *The figure is adapted from* [213], *with permission from Elsevier.*

As pointed out, the photoionization cross-section of the photoelectrons decreases with increasing the X-photon kinetic energies. This problem is mitigated by performing the HAXPES experiment using hard X-rays of synchrotron storage rings. Hence, the HIKE endstation is mounted at the KMC-1 beamline at BESSY II, Berlin, Germany. More details about the specification of the KMC-1, which makes it well-matched with the HIKE setup, will be mentioned in the following section 3.2.3.

3.2   Synchrotron Facility - BESSY II Storage Ring

Synchrotron radiation is electromagnetic radiation that propagates nearly at the speed of light (0.99C) in a closed circular path. This radiation is produced along the tangential trajectory of the charged particles when deflected by strong magnetic fields. The BESSY II "*Berliner Elektronenspeicherring-Gesellschaft für Synchrotronstrahlung*" is one of the advanced research facilities established for producing the synchrotron radiations at the Helmholtz-Zentrum Berlin (HZB), Germany. All the spectroscopic experiments reported in this thesis were performed at BESSY II. In 2014, BESSY II operated the 3rd generation synchrotron light facility, at which electrons are accelerated at an energy of 1.7 GeV before injection into the storage ring.[214] One of the best characteristics of synchrotron radiations is its high brilliance. Brilliance is defined as "*the number of photons emitted per second per unit source area, and per solid angle of the radiation cone.*"[151] BESSY II provides an ultra-bright photon beam ranging from long-wavelength Terahertz region to hard X-ray, with full control of the radiation polarization of the radiation.[214]   With BESSY II capabilities, various researches like medical, energy material, biological researches, and industrial applications can be conducted.[214-216]
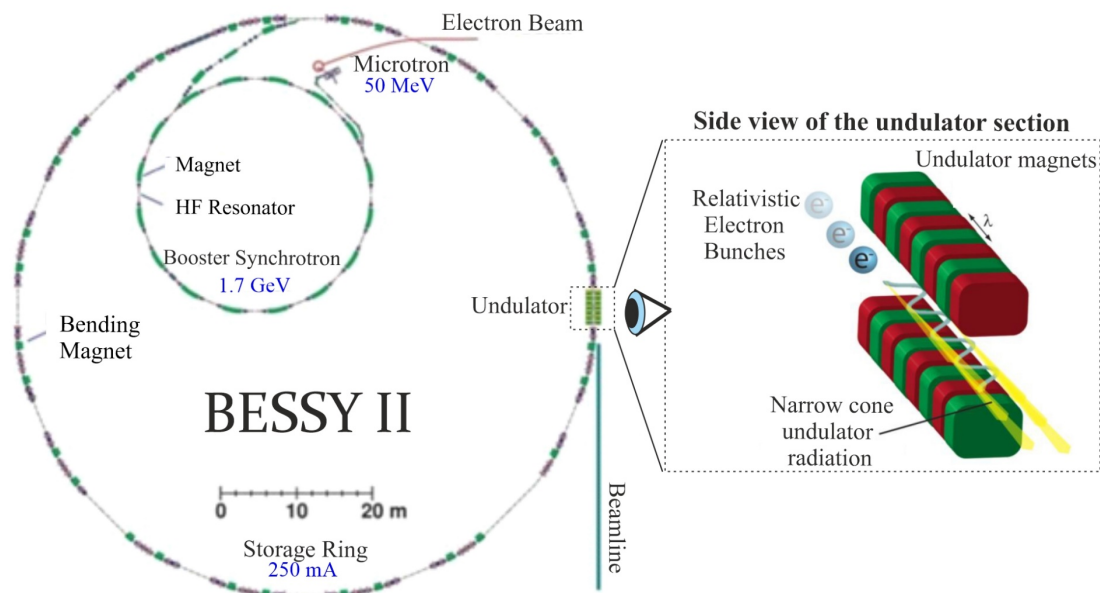

Figure 3.7. A schematic layout of the BESSY II synchrotron facility. The storage ring has several linear connections of bending magnets and insertion devices, viz. undulators and wigglers. Taken from [217]. The inset on the right-hand side is a zoom-in of a side view for a periodic arrangement of undulator magnets needed to accelerate and produce the synchrotron radiation. The figure is taken from [218].

Figure 3.7 shows a schematic diagram of the electron trajectory at BESSY II. Electrons at its core are emitted by an electron gun (hot cathode) and accelerated by the anode voltage up to 100 keV. Before shooting into the so-called 'booster synchrotron' of 96 m circumference, they are further accelerated over the microtron orbit to 50 MeV with the help of a high-frequency linear accelerator. In the booster synchrotron, 16 dipole magnets produce a large magnetic field, which subsequently increases the electron energy to reach 1.7 GeV.[214] These high energy electrons – packed in bunches – are then injected into a larger storage ring of 240 m circumference. In the storage ring, electrons pass through bending magnets and insertion devices (IDs), *viz.* undulators and wigglers, at which they are decelerated upon deflection losing energy, known as "Bremsstrahlung radiation." Thanks to the high-frequency resonators implemented over the storage ring path for compensating the energy loss due to the Bremsstrahlung process. Bending magnets produce a fan of radiation round the arced section with lower brilliance than that provided by IDs.[151] As shown schematically in the inset of Figure 3.7, an undulator consists of a periodic arrangement of closely spaced magnets of alternating polarity. The alternating magnetic field of the undulator will change the electron trajectory to a confined circular path until light in the form of narrow cones tangential to the storage ring is produced. Wigglers are analogous to undulators but with stronger magnetic fields giving rise to a broader radiation cone with higher brilliance.[151] Bremsstrahlung radiation passes in a straight line, commonly known as "beamline," tangential to the storage ring, as shown in Figure 3.7. The beamline comprises an insertion device, a monochromator, focusing optics, and ending up with an experimental endstation. Experiments at more than 50 beamlines of the BESSY II can be operated independently in the top-up mode [219] at a constant ring current close to 300 mA.

This thesis contains experiments performed at two plane grating monochromators (PGM) soft X-ray beamlines (U41/PGM and U49/PGM1) and hard X-ray beamline (KMC-1). The U41 and U49 beamlines provide the required microfocus beam size with tunable X-rays, accordant with the absorption and resonant inelastic X-ray studies on manganese oxide presented in this work. Moreover, the high energy beam offered by the KMC-1 beamline is essential for conducting HAXPES studies needed to investigate the interface of the MnO_x/TaON system. Details of experiments are reported in *Chapter 4*, *Chapter 5*, and *Chapter 6*.

3.2.1   Beamline U41/PGM

The undulator U41 beamline is mounted in a low beta section of the BESSY II storage ring orbit, which delivers a soft X-ray beam at a low current of 100 mA.[220] The microfocus beamline U41/PGM with the reduced photon flux meets the requirements needed to conduct the XAS

measurements presented in this thesis in *Chapter 4*.[72] The layout of the U41/PGM beamline is shown in Figure 3.8(a). Along the beamline, the linearly polarized X-ray photons received from the undulator are collimated by a gold-coated toroidal mirror (M_1). Monochromatization of X-ray is subsequently achieved using the combination of a plane grating monochromator (G) and a plane mirror (M_2). Thanks to the 600 l/mm grating (G) for delivering a photon flux between 10^{12} and 10^{13} photons/s over the $170 - 1500$ eV energy range, and for resolving the energy by varying the '*fixfocus*' constant (C_{ff}). The *fixfocus* constant $C_{ff} = cos\beta/cos\alpha$ where α and β are angle of incident and diffraction relative to the grating normal, respectively. [220] Based on the experimental requirements, the C_{ff} value can be varied over a wide range with values less than 1 to get either a high energy resolution or a high photon flux (*i.e.,* by increasing the C_{ff} value, the energy resolution increases and the flux relatively decreases).
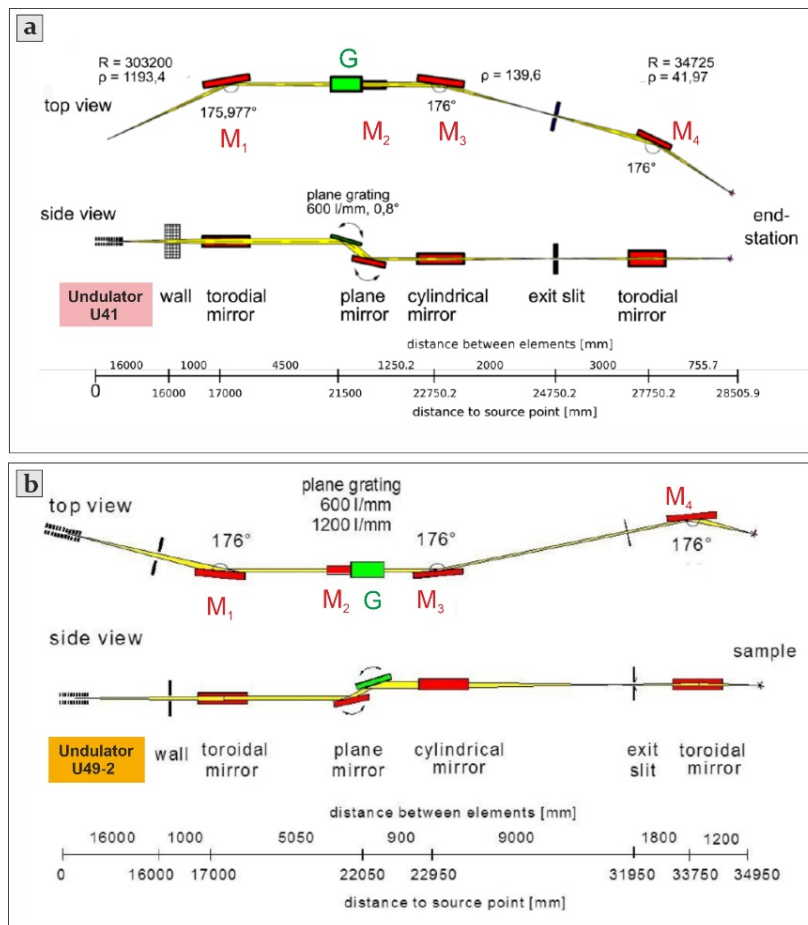

Figure 3.8. Schematic top and side view of the optics along a) the U41/PGM and b) U49-2/PGM1 beamlines of the BESSY II storage ring. taken from [221, 222].

The monochromatic, collimated light is then focused vertically by a cylindrical mirror (M_3)

toward an exit slit with different sizes (20, 40, 100, 200, 500, 2000, and 3000 µm). By decreasing the exit slit size, the energy resolution enhances. For that, all the absorption spectra reported in *Chapter 4* were measured using 20 μm slit to obtain a maximum energy resolution. Another toroidal mirror (M_4) is placed behind the exit slit to refocus the beam toward the experimental endstation. The U41/PGM has been upgraded and is currently dedicated to XPS/RIXS studies using the fixed 'PEAXIS' endstation. The technical parameters of the U41 beamline are summarized in Table 3.1.

3.2.2   Beamline U49-2/PGM1

The undulator U49-2/PGM1 provides a linearly polarized soft X-beam with photon energies ranging between 85 and 1600 eV in the form of a microfocus beam with high flux.[222] Figure 3.8(b) shows the schematic top and side view of the U49-2/PGM1 beamline displayed parallel to the optics of U41 for better comparison. The U49-2/PGM1 beamline optics looks analogous to the optics of the U41 beamline; however, minor and significant updates exist. For example, in the U49-2/PGM1 monochromator section, the plane mirror (M_2) is located in front of the plane grating (G) and equipped with an additional 1200 lines/mm plane grating beside the 600 lines/mm plane grating to achieve a better resolution. The high photon flux soft X-beam with a high energy resolution and microfocus spot meet the requirement needed to conduct the XAS/RIXS measurement for liquids in the flow cell, as reported in *Chapter 5*. The experimental endstation attached to this beamline is the LiXEdrom setup (*vide supra* in section 3.1.1). The technical parameters of the U49-2/PGM1 beamline are summarized in Table 3.1.

3.2.3   Beamline KMC-1

The bending magnet KMC-1 beamline delivers hard X-rays, optimized in the energy range from 2.003 to 12 keV, monochromatized using different sets of double crystals.[223] A top and side view of the KMC-1 beamline is shown in Figure 3.9. The beamline in the current version is installed with three sets of crystals, Si(111), Si(311), and Si(422), highly optimized at 2, 6, and 8 keV photon energy to achieve high energy resolution.[213] The flux of the KMC-1 beamline (10^{11}–10^{12} photons/s) concentrated in a focus size of 400 µm × 600 µm, together with the high energy accordant with the requirements needed to conduct experiments using the HIKE experimental endstation. HAXPES measurements in *Chapter 6* were carried out at the KMC-1 at two excitation energies, 2003 and 4000 eV, using Si(111) and Si(311) crystals, respectively. Table 3.1 summarizes all the technical parameters of the U41, U49-2, and KMC-1 beamlines of the BESSY II.

Table 3.1 Technical parameters of the U41/PGM, U49-2/PGM-1, and KMC−1 beamlines of the BESSY II storage ring, used in this thesis.

|	U41/PGM	U49-2/PGM1	KMC−1
Energy Regime	Soft X-rays	Soft X-rays	Hard X-rays
Energy range	170 – 1500 eV	85 – 1600 eV	Si(111): 2 – 12 keV Si(311): 4 – 12 keV Si(422): 6 – 12 keV
Source	Undulator	Undulator	Bending Magnet (dipole)
Monochromator	PGM	PGM	Double Crystal
Energy resolution $\left(\frac{E}{\Delta E}\right)$	6300 (at 400 eV)	25,000 (85 – 500 eV) 15,000 (500 – 1500 eV)	1000 at 4 keV at Si(111) 5700 at 4 keV at Si(311)
Photon Flux	10^{12} - 10^{13} photons/s	10^{13} photons/s (85 – 500 eV) 10^{12} photons/s (500 – 1500 eV)	10^{11} photons/s at 4 keV
Polarization	Linear (Horizontal)	Linear (Horizontal)	Linear (Horizontal)
Divergence	1.2 mrad (horizontal) 0.5 – 2.5 mrad (vertical)	2 mrad (horizontal) 2 mrad (vertical)	3 mrad (horizontal) 0.2 mrad (vertical)
Focus size (hor. x vert.)	36 μm × 12 μm	100 μm × 22 μm	400 μm × 600 μm
Focus distance from the last valve	504 mm	959 mm	670 mm
Focus height from floor level	1376 mm	1417 mm	1728 mm
Fixed end station	Yes (currently PEAXIS endstation)	NO	NO
Reference	[214, 220]	[222]	[224]
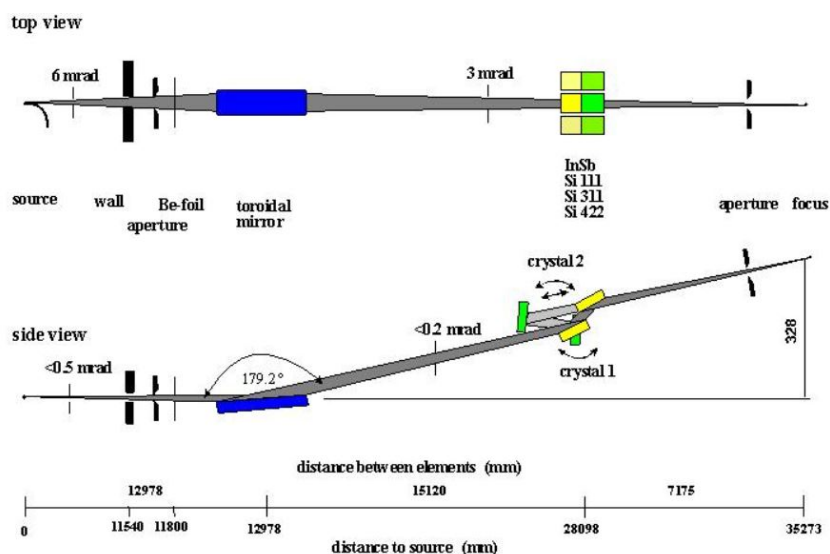
Figure 3.9. Schematic top and side view of the bending magnet KMC−1
double crystal monochromator beamline at the BESSY II synchrotron facility taken from [223].

3.3   Sample Materials and Preparation

3.3.1   Substrates

3.3.1.1   FTO and quartz substrates

Fluorine-doped tin dioxide (FTO) substrates (sheet resistance 115 Ω/m^2, TEC-15, Pilkington) are cleaned by ultrasonication in an aqueous bath containing detergent. Subsequently, the FTO is rinsed several times with deionized water then sonicated again in ethanol to remove any detergent traces. This cleaning procedure was previously tested and published elsewhere in [75].

Quartz substrates (polished, Spectrosil 2000, Heraeus) are cleaned by ultrasonication for 15 minutes in ethanol then rinsed several times with Millipore water. Then the substrates are dried in air at room temperature before sample electrodeposition or sputtering.

3.3.1.2   Silicon nitride membranes

Silicon nitride membranes (100 nm thickness, Silson Ltd., United Kingdom) are supported on silicon frames ($10 \times 10 \times 0.38$ mm^3) with a window in the center of the frame with a dimension of 1.0 mm × 0.5 mm. Prior to use, Si_3N_4 membranes were first cleaned with isopropanol, then dried in the air, then sputter-coated with a 20 nm thick layer of Au in an in-house cleanroom. The time for Au sputtering was set to 11 s at 400 W with a flow rate of Argon gas at 17 sccm

(standard cubic centimeters per minute). After sputtering, the sputtered gold layer thickness was measured using Dektak 150 Surface Profiler at the Helmholtz Institute in Berlin. For better adhesion between Au and Si_3N_4 surface, a Chromium interlayer is included at the Au/Si_3N_4 interface. Thus, Si_3N_4 membranes were also purchased with 3 nm Cr layer in between 20 nm Au and Si_3N_4 membranes. Both substrates are used in the study of *Chapter 5* and produce identical spectroscopic results.

3.3.2   Electrolyte Preparation

3.3.2.1 Preparation of borate buffer solution

According to the recipe in [225], the borate buffer solution was prepared in-house and used as a supporting electrolyte in the flow cell during XAS/RIXS measurements of *Chapter 5*. There are two essential parameters in the buffer preparation: the solution pH and concentration. To ensure that both parameters are at the desired values, the pH of the electrolyte was adjusted before reaching the final electrolyte volume.

Preparation of borate buffer, 500 mL, 0.1 M, pH 9.2
First, an accurate mass of high purity $B(OH)_3$ pellets (Sigma-Aldrich, 99.99%) is weighed out into a vial or small beaker for convenience. For a 500 mL solution, 3.092 g of $B(OH)_3$ (61.83 g/mol) is dissolved first in approximately 300 mL of deionized water, with stirring. Heating is not be required and non-ideal as pH is dependent on temperature. Once the $B(OH)_3$ is dissolved, the pH of the solution is measured with a glass pH electrode (pH meter). A pH value of 3-4 is expected. The solution is subsequently stirred with the pH electrode tip immersed and measuring. Then aqueous NaOH ($\sim$ 1 M, $\sim$ 25 mL) is added carefully while monitoring the pH until the desired pH of 9.2 is reached. The addition of NaOH should be done by careful pouring in the initial stages and using a Pasteur pipette. After pH adjustment, more deionized water is added to the beaker to reach $\sim$ 420 - 450 mL volume based on the volume guide on the beaker. This solution is then poured into a volumetric flask, 500 mL, and deionized water is further added until the final volume reaches 500 mL. After multiple inversions of the flask, the final pH of the solution is confirmed.

3.3.2.2 Preparation of Mn^{II} acetate in a borate buffer

The Mn^{II} solution buffered by borate [*i.e.,* 0.5 mM $Mn(CH_3COO)_2$ in 0.1 M borate buffer (pH 9.2)] is used in the electrodeposition of MnO_x film on Au/Si_3N_4 membranes in the flow cell, which used in the study of *Chapter 5*.

Preparation of 0.5 mM manganese acetate in 0.1 M borate buffer

First, prepare 1 mM concentration of Mn^{II} acetate [$(Mn(OAc)_2$, molecular weight 173.03 g/mol] by adding, *e.g.,* 30 mL of deionized water to 5.19 mg of $Mn(OAc)_2$ on a magnetic stirrer for proper dissolution without heating. Second, equal masses of 1 *mM* Mn acetate solution and 0.2 M borate buffer (*vide supra* in section 3.3.2.1) are added together to give a final solution of 0.5 mM manganese acetate in 0.1 M borate buffer.

3.4 RIXS Data Processing

Data processing of the experimentally measured RIXS data should be executed before any analysis or interpretation. Data processing stages include image correction, background correction, and energy calibration.

3.4.1 RIXS image/background correction

As pointed out in section 3.1.1, the grating in the spectrometer section of the LiXEdrom endstation has a spherical shape, which leads to the dispersion of the fluorescence photons hitting the detector in many vertical dimensions. As a result, the produced and measured RIXS image recorded by the CCD camera will be curved on the outer edges, as shown in Figure 3.10(a). Curve correction is consequently applied. Figure 3.10(c) shows the RIXS image after applying curve correction.
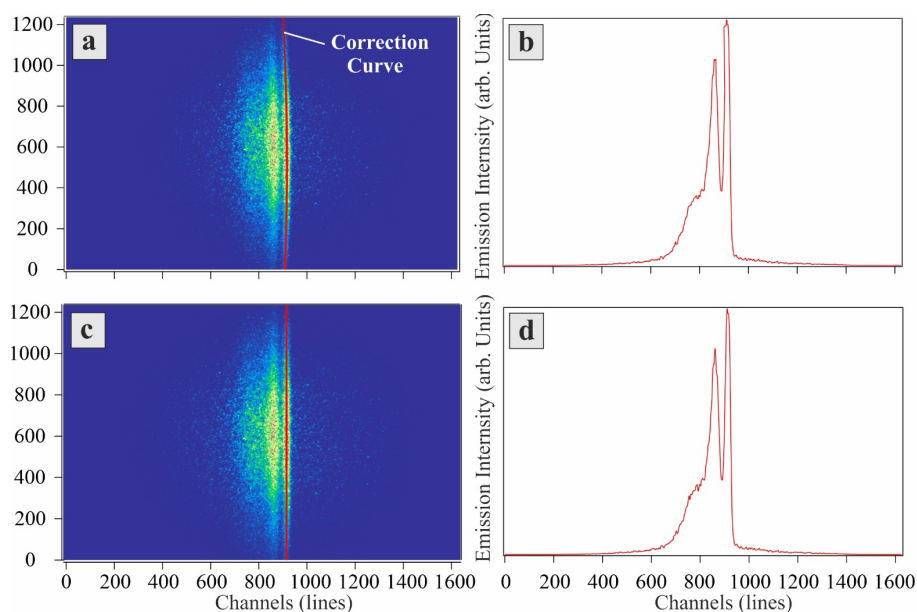
Figure 3.10. A 2D RIXS image collected by the CCD camera for a MnO_x catalyst. The image is a matrix of 1625×1235 channels. (a) and (c) are images before and after applying curve correction (*red*). (b) and (d) shows their corresponding spectra, respectively. Each spectrum is collected after summing up intensities at every channel line.

RIXS spectrum can be obtained by summing up the intensities at every channel line of the detector (vertical column). The curved feature in the RIXS image of Figure 3.10(a) leads to a slight broadening of the peaks of the RIXS spectrum in Figure 3.10(b) compared to the spectrum after curve correction in Figure 3.10(d).

Before obtaining an energy scale to these RIXS spectra, all the spectra should be corrected from the noise background by subtracting the non-linear baseline noise signal of the detector (so-called "dark spectrum") measured in the absence of X-ray irradiation.

3.4.2 Energy calibration

The RIX spectrum obtained after the curve correction (Figure 3.10(d)) is plotted versus the channel number. Figure 3.11(a) shows the background-corrected RIXS spectra plotted versus the channel number measured for Mn^{II} acetate (as a reference) at different excitation energies.
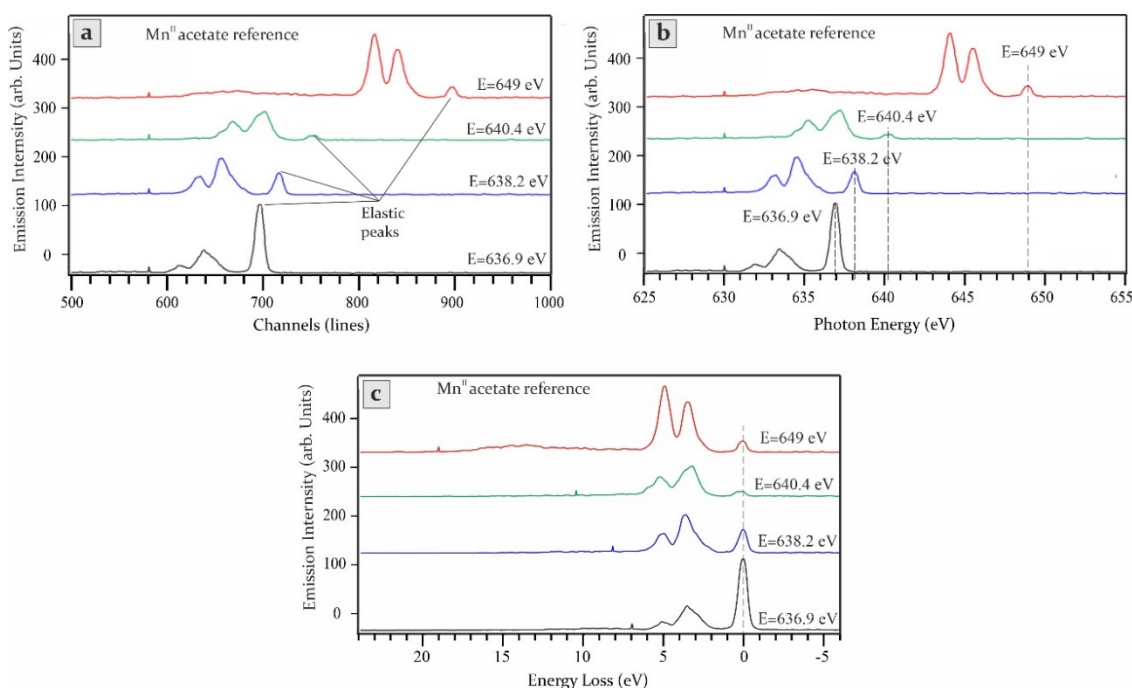
Figure 3.11. RIXS spectra (a) plotted *vs.* Channels (before energy calibration), (b) plotted *vs.* emitted photon energy (after energy calibration). The emitted energy at the elastic peak is equal to its corresponding excitation energy, as indicated by the dashed lines, (c) plotted as energy loss features.

It can be shown that as the excitation energy increases, the elastic feature appears at higher

channel lines. The elastic feature in any RIXS spectrum refers to that the incident photon energy is equal to the emitted photon energy, and no energy is transferred to the system (*i.e.,* $E_{in} = E_{out}$). For that, the energy position of the elastic peak in the RIXS spectra can be used for energy calibration. For example, the elastic peaks for the RIXS reference spectra of Mn^{II} acetate at different excitation energies are used for calibration, as shown in Figure 3.11(a,b). This calibration method is applied for the RIXS data in section 5.3.3. To plot the RIXS spectra as energy loss features, the emitted photon energy scale is subtracted from the excitation energy (*i.e.,* energy loss = $\hbar\omega_k - \hbar\omega_{k'}$), as shown in Figure 3.11(c).

3.5 Theoretical calculation of HAXPES spectra

In order to interpret the experimental data carried out using the HAXPES technique and generate useful insights about the chemical properties at the manganese oxide/tantalum oxynitride interface, additional theoretical calculations were needed. These calculations were done using the software, "*simulation of Electron Spectra for Surface Analysis* (SESSA)" provided by the "National Institute of Standards and Technology (NIST)," Gaithersburg, MD, USA. [226, 227] The SESSA software can provide a quantitative analysis of the photoemission spectra based on a database implemented in the software that contains all the physical parameters required. The crucial physical parameters provided by the database are the IMFP values for electron energies up to 20 keV, and the photoionization cross-sections which are significant resources, especially for HAXPES studies.[228] It is possible in SESSA to model the sample as a planar layer(s) or layered spheres (*e.g.,* nanoparticles) with or without a degree of roughness.[227] A good agreement between the experimental and the simulated spectra can only be achieved upon implementing accurate experimental parameters. These parameters include the sample specification (composition, morphology, atomic density, and layer(s) thicknesses) and setup parameters.[227] The setup parameters include the X-ray source (energy and polarization) and the experimental geometry of the setup components, as identified in Figure 2.7, based on equation (2.14). The simulated spectra using the Monte Carlo algorithm can provide a good estimation for the peak intensities, peak energy, and the angular distribution of the emitted electrons.[226, 227]

Numerical simulations of the HAXPES studies on the MnO$_x$/TaON system were performed using SESSA software version 2.1.1 and shown in this thesis in *Chapter 6*. In this study, the MnO$_x$ is deposited on the top of the TaON photoanode. The HAXPES experimental results showed the presence of the Ta$_2$O$_5$ layer at the surface of TaON with an oxidized MnO$_x$ layer (*i.e.,* MnO$_2$ and Mn$_2$O$_3$) at the interface facing the Ta$_2$O$_5$ layer. Experimental results showed that by increasing the thickness of the deposited MnO on the top of Ta$_2$O$_5$/TaON, the Ta$_2$O$_5$ thickness

reduces, whereas the oxidized MnO_x layers (MnO_2 and Mn_2O_3) increases. SESSA simulation was thereby performed in order to quantify the thicknesses of the multilayers when the experimental and simulated peak intensities are well-matched. Then, the number of oxygen atoms in the reduced in Ta_2O_5 could be calculated and compared to that in the oxidized MnO_x layers. The results could help to elucidate the chemical properties at the MnO_x/TaON interface. The simulation results are reported in detail in section 6.5.

Chapter 4

Electronic structural Insight into Formation of MnOₓ Phases in Electrodeposited Catalytic Films of different pH

This chapter is taken from the following publication

"Insight into pH-Dependent Formation of Manganese Oxide Phases in Electrodeposited Catalytic Films Probed by Soft X-ray Absorption Spectroscopy."

Maryam N. Shaker, Shannon A. Bonke, Jie Xiao, Munirah Khan, Rosalie K. Hocking, and Marc F. Tesch. *Chempluschem* (2018) 83, 721-727. **DOI**: 10.1002/cplu.201800055
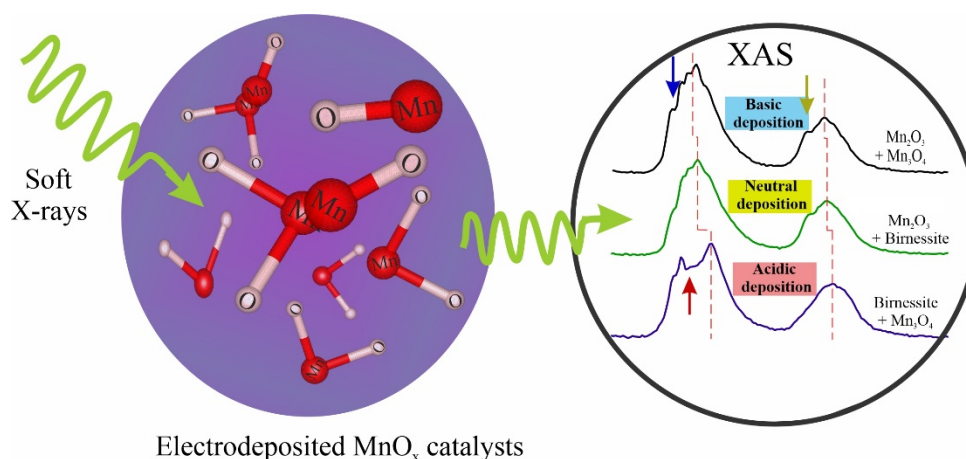
Exploring the MnOₓ phases in the catalytic MnOₓ films electrodeposited under different pH conditions using soft XAS measured at Mn L$_{2,3}$-edge and O K-edge.

# 4.1	Introduction

Manganese oxides catalysts have been widely studied and showed to be promising catalysts for water oxidation reaction.[27, 28, 39-43] As pointed out in the introduction chapter of this thesis, MnO_x being a transition metal oxide composed of earth-abundant and innocuous elements, mimics the natural $CaMn_4O_5$ catalytic complex in PS II.[45, 68-71] Despite the great interest in MnO_x as a water oxidation catalyst, their catalytic activity differs according to their structure, namely the oxidation number of Mn^{n+} in the oxide, affecting the crystalline phase, giving each its electronic properties. [56, 75, 229, 230] Studies have been conducted to understand the electronic structure of MnO_x catalysts and how it affects the water oxidation mechanisms.[44, 231, 232] It was found that the MnO_x catalytic performance is primarily affected by the Mn oxidation state and the Mn-to-O atomic arrangement.[56] Preparation methods under different conditions can significantly influence the formation of MnO_x in various Mn-to-O ratios of particular morphology and structure, which in turn, would affect their catalytic activity. Several techniques have been used to deposit MnO_x thin films, aiming at improving their catalytic performance.[74, 75] Among several deposition methods, electrodeposition is an attractive method since it allows creating films in a controllable fashion.[233-236] Despite its promise, it remains very challenging to develop efficient MnO_x catalysts because of the formation of a broad range of disordered mixed Mn oxides with various Mn oxidation states formed from the soluble ions during electrodeposition, leaving the oxide structure susceptible to changes in temperature and pH. [74, 75, 98, 237, 238] These factors affect the water oxidation catalytic functionality of MnO_x, rendering it even more complicated to study and understand.[44, 56, 237, 238] A Pourbaix diagram provides a guide to indicate the most thermodynamically stable MnO_x species as a function of pH and potential; however, as a drawback of this method, it takes into consideration neither the kinetic barriers nor the potential importance of structural disorder. Also, studying and quantifying the prevalent Mn oxidation state, as a particular structural motif within a largely amorphous film, can be very challenging and remains a target for further investigation.

Soft X-ray absorption spectroscopy (XAS) is sensitive to differences in redox states and electronic structure. Thereby, it is employed in this study to determine the structural motifs formed by the electrodeposition of MnO_x films from ionic liquid under systematically varied pH conditions. The ionic liquid (IL) is a salt solution composed of only anions and cations. The electrolyte used in electrodeposition is a mixture of ionic liquid (90%) and water (10%). Electrodeposition from IL is promising since it allows deposition at high temperatures, exceeding the boiling point of water, allowing atom diffusion on the surface during the growth, which can positively influence the quality of the films.[75, 239]

The MnO_x films in this study were synthesized by electrodeposition onto a fluorine-doped tin oxide (F:SnO_2; FTO) substrate from an IL electrolyte composed of Mn—precursor (Mn^{II} acetate), ethylammonium nitrate ($EtNH_3NO_3$), and deionized water at 120°C. The pH of the electrolyte was varied during electrodeposition by adding either nitric acid or ethylamine for acidic or alkaline MnO_x films, respectively. This preparation approach is described in a previously conducted study.[75] Therein, the morphology and chemical composition of the electrodeposited samples were characterized utilizing voltammetry, X-ray diffraction (XRD), scanning electron microscopy (SEM), and energy-dispersive X-ray (EDX). The dominant structural motif within the films was estimated by comparing the Mn K-edge X-ray absorption spectra of samples with fingerprints of reference spectra (X-ray absorption near-edge structure and extended X-ray absorption fine structure). By this means, it could be determined that electrodeposition under different pH conditions significantly influences the film morphology, the formation of MnO_x phases, and the catalytic activity towards OER. In particular, the previous hard XAS results at the Mn K-edge could be interpreted in terms of the presence of multiple MnO_x structural phases within the electrodeposited samples.[75] However, the exact subtle varieties in the MnO_x films and the mixtures of different structural motifs could not be fully examined. Also, the surface compositional analysis of the studied samples was limited, despite their importance for catalysis. Thus, the underlying reason for the surface-area-normalized catalytic differences between the samples remained unclear.

Herein, we employed soft XAS to identify the compositional changes in MnO_x films electrodeposited at different pH to better understand their effect on the catalytic activity of every particular pH-deposited film. The XA spectra were measured in the surface-sensitive total electron yield (TEY) method, which allows identifying the MnO_x structural motifs within the samples and gives a more detailed picture of the sample composition and structure. We measured the Mn $L_{2,3}$-edge to uncover changes in the $3d$ valence electronic structure. Compared to hard X-rays, which address the deep Mn K-edge, Mn L-edge spectroscopy is much more sensitive to the $3d$ valence electronic structure, which plays a vital part in the catalytic activity. It provides distinct and unique spectral features for different oxidation states and, to some extent, can identify changes in the chemical environment.[240] Additional O K-edge XAS analysis provides complementary information about the samples.

4.2 Experimental Section

4.2.1 Sample Preparation

MnO_x thin films were electrochemically deposited on the FTO glass substrate using a

conventional three-electrode electrochemical cell. Prior to electrodeposition, the FTO was cleaned, as described in section 3.3.1.1, and used as a working electrode. Titanium (Ti) foil was used as a counter electrode, whereas a Ti wire as a pseudo-reference electrode. The Ti electrodes provide reproducible and relatively stable potential at the high temperature of 120 °C needed for the MnO_x electrodeposition. The MnO_x samples are divided into three groups: acidic 'A', neutral 'E0', and basic 'B', according to the pH of the electrolyte used in electrodepositing the samples. The neutral 'E0' sample was electrodeposited directly from the precursor electrolyte containing 90% ethylammonium nitrate (EAN), 10% water, and 10 mM Mn^{II} acetate [$Mn(CH_3COO)_2$]. The acidic 'A' and basic 'B' samples were electrodeposited from the same precursor but with different pH by adding different amounts of nitric acid and ethylamine, respectively. The concentration of acid and base added to the E0 electrolyte are tabulated in Table A.1 in Appendix A. For highly concentrated ILs, the concentration of acid and base is more reliable than the pH values measured by the pH meter. The oxidative electrochemical deposition for all the catalysts was performed at 120 °C at a constant current density of 200 $\mu A.cm^{-2}$ for 10 min. Seven samples in total were electrodeposited from electrolytes at different pH, A3, A2, A1, E0, B1, B2, and B3, ordered from the samples prepared under highly acidic 'A3' to – neutral 'E0' – to highly basic 'B3' conditions. After electrodeposition, the films were rinsed with deionized water, then purged with nitrogen gas. A more detailed description of the sample preparation, along with catalytic testing for water oxidation, has been published.[75]

4.2.2   XAS Measurements

The X-ray absorption spectroscopic measurements were recorded at room temperature using the LiXEdrom experimental endstation mounted at the U41-PGM beamline of the BESSY II synchrotron facility in Berlin, Germany.[208] Details on the LiXEdrom setup and the U41-PGM beamline are described in sections 3.1.1 & 3.2. respectively After electrodepositing the MnO_x catalysts on FTO anodes, the samples were mounted on a solid sample holder via adhesive Cu tapes then inserted in the main chamber (10^{-6} mbar) of the LiXEdrom setup for spectroscopic investigation. To assure the reproducibility of the collected XA spectra and to test for sample homogeneity, spectra were measured at various spots several times on the same sample. The reported spectra are an average of those damage-free spectra taken at the same/various positions. This was also a way to improve the signal-to-noise ratio of the spectra.

All the spectra of the investigated samples were collected within the same beamtime, except for sample B1 measured later at beamline U49-2/PGM1 with a comparable setting (*i.e.,* similar resolution and photon flux). The energy range of the XA spectrum of sample B1 was corrected

according to a reference MnO_x sample, which was measured at the two beamlines. Nonetheless, an instrumental energy shift of 0.1 eV was required to correct for the spectrum of the B1 sample. All the XA spectra were calibrated and normalized to the L_2 edge intensity to compare changes of the spectral features.

4.2.3 Radiation Damage Study

Under the intense flux of X-rays, samples are susceptible to undergo photo-reduction.[241] Manganese oxides are particularly susceptible to reduction by high flux X-ray illumination.[241, 242] At a glance, one can think that sample damage would be prevented below a particular photon flux. However, fluxes acquiring photoreduction can differ from one sample to another. Hence, the best way to avoid radiation damage is to precisely perform a systematic radiation damage study to adjust the best experimental settings that would keep the sample intact. In this study, XA spectra were measured at several sample spots for different photon flux densities. For all the manganese oxide samples, increasing the synchrotron beam flux acquires changes in the relative intensity of spectral features, indicating that all samples are susceptible to beam damage.

Radiation damages were severe in the case of MnO_2, as well as for samples A1-A3. In order to test the impact of radiation damage, all XA spectra were collected at least twice at the same spot then compared to those collected of fresh spots under lower photons flux. Figure A.1 shows XA spectra measured at a fresh spot with a subsequent measurement with lower flux. This was done for each sample at different photon fluxes.

To reduce the photon flux, the spectroscopic measurements were conducted in the low-alpha mode of BESSY II, where the ring current is low (< 100 mA injection current). Additionally, the opening of the primary beamline aperture located directly after the insertion device was stepwise decreased from the conventional values of 2.4 mm × 2.4 mm down to the least possible values that allowed to collect the XA spectra. The photon flux was further reduced by changing the beamline order of diffraction from 1st to 4th order. Figure A.2 shows XA spectra collected at the same spot on MnO_2 and Mn_2O_3 samples with increasing the photon flux by increasing the aperture size to identify the best beamline settings for measuring damage-free spectra.

4.2.4 MnO$_x$ references

The XA spectra at the Mn $L_{2,3}$-edge and O K-edge for a set of well-characterized MnO_x references (Mn^{II} resembling the spectra of MnO, Mn_3O_4, Mn_2O_3, and birnessite)[56] were collected using the same experimental settings as for the investigated samples. The MnO_2

reference spectrum was measured later at the beamline UE56-2 PGM-2 with settings that were chosen to resemble the resolution of the previously collected reference spectra, and the energy scale was corrected accordingly.

The manganese oxides references, $Mn_3^{II/III}O_4$, $Mn_2^{III}O_3$, and $Mn^{IV}O_2$, were commercially bought from Sigma-Aldrich and measured as received in the form of powder on double-sided adhesive Cu tapes attached to the sample holder. $Mn^{II}O$ is very unstable and quickly oxidize in air and could not directly be measured as a reference sample. Therefore, Mn $(ClO_4)_2 \cdot 6H_2O$ (Sigma-Aldrich, 99%) was dissolved in acetonitrile and doped into a Nafion film (*i.e.,* polymer matrix). This method was previously proven to be a valid technique to obtain absorption spectra that resemble the Mn $L_{2,3}$-edge spectrum of crystalline MnO.[56, 113, 240] As a drawback, the additional O sites present in the Nafion membrane would distort any O K-edge spectrum. Therefore, the O K-edge spectrum for MnO-like reference was not incorporated in the fitting process to avoid any distraction.

The K^+ birnessite reference material was synthesized according to [243] by high-temperature decomposition of potassium permanganate ($KMnO_4$) at 800 °C for 12 h, followed by a filtration process to remove any residual unreacted $KMnO_4$. As previously established,[243, 244] this yielded a highly ordered K^+ birnessite as characterized by X-ray diffraction. Due to its relatively complex structure and non-unique average oxidation state[245, 246], birnessite prepared differently is expected to show deviations in spectral shape.

The Mn $L_{2,3}$-edge and the O K-edge XA spectra for all MnO_x reference samples were measured in the energy range (636 - 661 eV) and (525 - 550 eV) as displayed in Figure 4.1(b) and Figure 4.3(b), respectively. More details are found in Appendix A. All reference XA spectra resemble existing data in the literature.[240, 247]

4.3   Experimental Results and Discussion

4.3.1   Mn $L_{2,3}$-edge absorption spectra of MnO_x films

A series of MnO_x catalysts electrodeposited on FTO under different pH conditions, ranging from acidic to alkaline, have been investigated intensively with soft X-ray absorption spectroscopy to elucidate the electronic and compositional phase structure of the catalysts. The investigated samples are nominally indicated as A3, A2, A1, E0, B1, B2, and B3 in order of increasing pH. Upon normalizing the catalytic activity to all the samples, it was shown that the sample prepared under neutral condition (E0) was reported to be the optimal catalyst over other catalyst samples deposited under slightly acidic and basic conditions (A1 and B1, respectively). Although lower

than the aforementioned samples, the catalytic activity for samples prepared under acidic conditions was higher than those prepared under alkaline conditions.[75]

In order to understand the deviation in the catalytic activity for these pH-deposited MnO_x films, the samples were investigated in an element-selective fashion, setting the incoming X-ray photons energy to the Mn $L_{2,3}$-edge (635 - 663 eV) then recording the drain current emitted from the sample (*i.e.,* surface TEY mode). The XA spectra of the investigated samples in the top panel of Figure 4.1 show two multiplet structures that arise from core electron transitions to unoccupied valence states induced by the incident soft X-rays. The first multiplet structure from 639-648 eV originates from Mn $2p_{3/2} \rightarrow 3d$ transitions (L_3-edge), while the second absorption structure in the energy range between 650 eV and 658 eV are attributed to the Mn $2p_{1/2} \rightarrow 3d$ transition (L_2-edge). The XA spectra in Figure 4.1(a) are separated, according to the pH conditions, into three sets: basic (group 'B', top), neutral ('E0', middle), and acidic (group 'A', bottom); though all these spectra are also overlaid in Figure 4.2 for a better comparison of the changes happening in the absorption features. Figure 4.1(b) shows the XA spectra for the MnO_x references of a well-defined structure to facilitate the comparison with the XA spectra of the investigated samples in the top panel.

XAS, being sensitive to the local electronic structure of the Mn oxides, is less influenced by sample morphology. Thus, although the morphology of the samples within groups 'A' and 'B' was shown to be quite diverse[75], their respective XA spectral shape is quite similar, indicating similar MnO_x composition in each group.

Although the spectral shape of samples of group 'A' and group 'B' is quite similar, some distinct differences can be noticed. On the one hand, the L_3 main peak of group 'B' exhibits a broad feature over the energy range 639-649 eV with several high- and low- energetic shoulders, while the L_2 main peak is shown to have a separated shoulder over the lower energy side. On the other hand, the spectra of group 'A' are shown to be double-peaked at the L_3-edge, with the L_2-edge exhibiting no distinguishable low-energy shoulder. Compared to the samples of group 'A' and 'B', sample E0 appears to have an intermediate structure. Besides the changes in the spectral shape, there are shifts in the energetic positions of the most pronounced features of the three groups, marked by red dashed lines in Figure 4.1(a). The main peak energy at the L_3-edge shifts from approximately 641.8 eV (group 'B'), over 642.2 eV (E0) to 643.3 eV (group 'A') while the L_2-edge peak shifts from approximately 652.7 eV, over 652.9 eV, to 653.4 eV. When comparing this energy shift to the energetic position of the main spectral features of the MnO_x references in Figure 4.1(b), a change in the ratio of the coexisting phases within the investigated pH-deposited MnO_x samples is revealed. Typically, for Mn in a higher oxidation state, the $L_{2,3}$ main features occur at higher excitation energies, as seen in Figure 4.1(b). Therefore, it can be

concluded that the overall average oxidation state of Mn in the MnO$_x$ films increases with increasing the acidity of the electrolyte used in electrodeposition. This is further confirmed by the disappearance of the clear shoulder at the L$_2$-edge for the group 'A' samples.
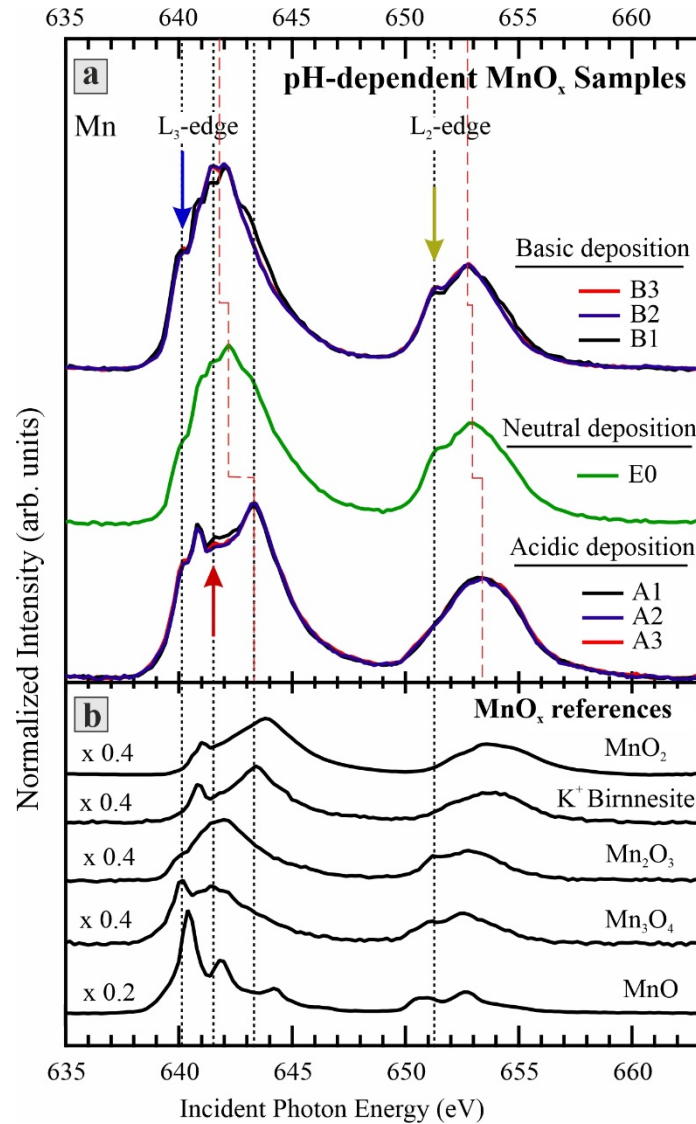

Figure 4.1. Mn L$_{2,3}$-edge TEY-XA spectra arising from $2p \rightarrow 3d$ transition, measured for a) the MnO$_x$ samples electrodeposited under basic ('B', top), neutral ('E0', middle), and acidic ('A', bottom) conditions, and b) the MnO$_x$ references of well-defined structures, which are added to facilitate assigning features to specific MnO$_x$ phases at the dashed lines and the colored arrows as referred to in the text.

The absence of the clearly separated shoulder at the L$_2$-edge indicates the presence of a high Mn oxidation state resembling the spectrum of MnO$_2$ in the 4+ state. According to the literature in

[240, 247], and the measured XA spectra of MnO_x references, a low energy shoulder at the Mn L_2-edge position (*yellow* arrow in Figure 4.1) is manifested for MnO_x reference samples with a high amount of Mn^{III} (*i.e.,* Mn_2O_3 or Mn_3O_4) while being absent in MnO_x samples with a high amount of Mn^{IV} (*i.e.,* birnessite and MnO_2). This reveals that the group 'A' samples contain a high proportion of Mn^{IV}, while group 'B' samples contain more Mn^{III}.

Interestingly, the shoulder appearing at the lowest excitation energy at 640.2 eV has its lowest intensity for sample 'E0', as clearly seen at the blue arrow in the inset of Figure 4.2, where the spectra are plotted on the same axis and normalized to the same L_2-edge intensity. The energetic position of that feature coincides with the main peak position of the MnO_x references with a considerable amount of Mn^{II} phase (MnO and Mn_3O_4), as indicated in the lower panel of Figure 4.1. This indicates that sample E0 has the least amount of this oxidation state. A detailed discussion untangling the contributions of Mn phases in every sample using a quantitative analysis will be given later in section 4.4.

The previous study revealed that the samples A1, B1, and E0 are the most active catalysts among other samples.[75] This result is obtained after normalizing the catalytic activity to the electroactive area, where the influences of the sample morphology play a minimal role in comparisons of activity for OER catalysis. Interestingly, the XA spectra of samples A1 and B1 are compatible with samples in their respective groups rather than being similar to each other. Thus, the origin of the catalytic enhancement should arise from the differences in the electronic structure of the samples within the same group. For that, the absorption spectra must be examined more closely to reveal variations in the sample composition. Indeed, the A1 and B1 catalysts show weak but distinctive spectral differences compared to the other two catalysts in their respective groups. These differences appear mostly at the L_3-edge, at ~641.6 eV (*red* arrow in Figure 4.1 & Figure 4.2). At this energy, the spectrum of sample B1 reveals a lower absorption compared to the spectra of sample B2 and B3. While sample A1 showed a higher absorption in this energy region than the other two samples of the same group. Comparable changes occur at the L_2-edge. These subtle but continuous spectral changes reflect a continuous change in the formed MnO_x phases. Moreover, this implies that the enhancement of the catalytic activity for samples A1, E0, and B1 is not due to the existence of a specific MnO_x phase but an interplay of mixed phases in the MnO_x film. In addition to the spectral change at 641.6 eV, the spectrum of sample 'B1' reveals a slight increase in the high energy shoulder at approximately 643.0 eV that does not occur in the spectra of group 'A', indicating that the samples of group 'B' contain a different set of MnO_x phases than the samples of group 'A' (*vide infra*).
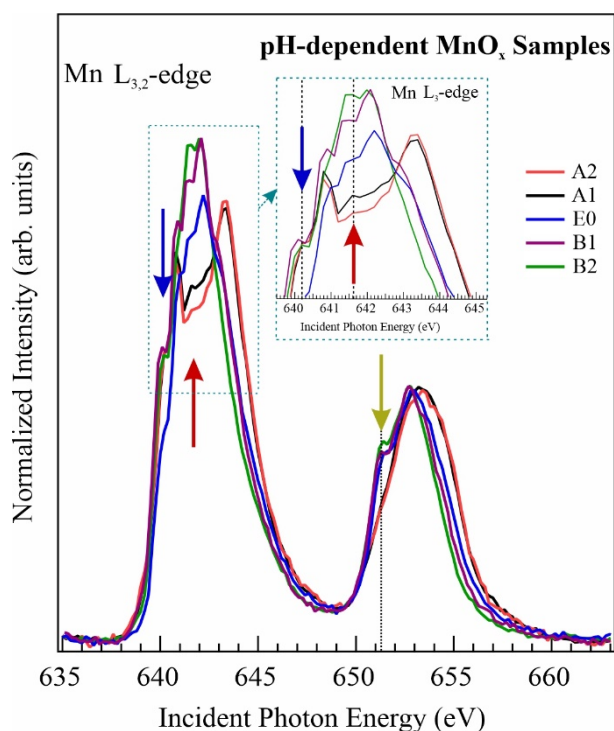
Figure 4.2. Comparison of Mn $L_{2,3}$-edge X-ray absorption spectra for the MnO_x samples electrodeposited under acidic (A1 and A2), neutral (E0), and basic (B1 and B2) conditions. All spectra are plotted on the same axis to facilitate comparison and emphasize the differences. The dashed rectangle highlights the main spectral differences at the Mn L_3-edge and is further enlarged as an inset to identify better the unique features. The dashed lines and the arrows indicate changes in the features, as referred to in the text.

4.3.2   O K-edge absorption spectra of MnO_x films

The XA spectra at the oxygen K-edge were investigated in order to get a more comprehensive picture of the changes in the MnO_x electronic structure. The O K-edge spectra for all samples are shown in Figure 4.3 in the energy range of 525-550 eV. Two regions can be separated when interpreting the O K-edge spectra in terms of electronic contributions: The first is the pre-edge region from approximately 528 to 534 eV of well-defined peaks, originating from the electron transition from $1s$ state to the hybridized state of O $2p$ and Mn $3d$ orbitals.[152, 248] This pre-edge region is attributed to an interaction between O with the metal atom. It can provide complementary information about the Mn oxidation state, ligand field, and ligand-metal bond covalency.[248] The main absorption edge above ~535 eV, comprising broad and less defined structures, is attributed to the transition to the hybridized orbitals of O $2p$ with Mn $4s$ and $4p$ states.[152-154]
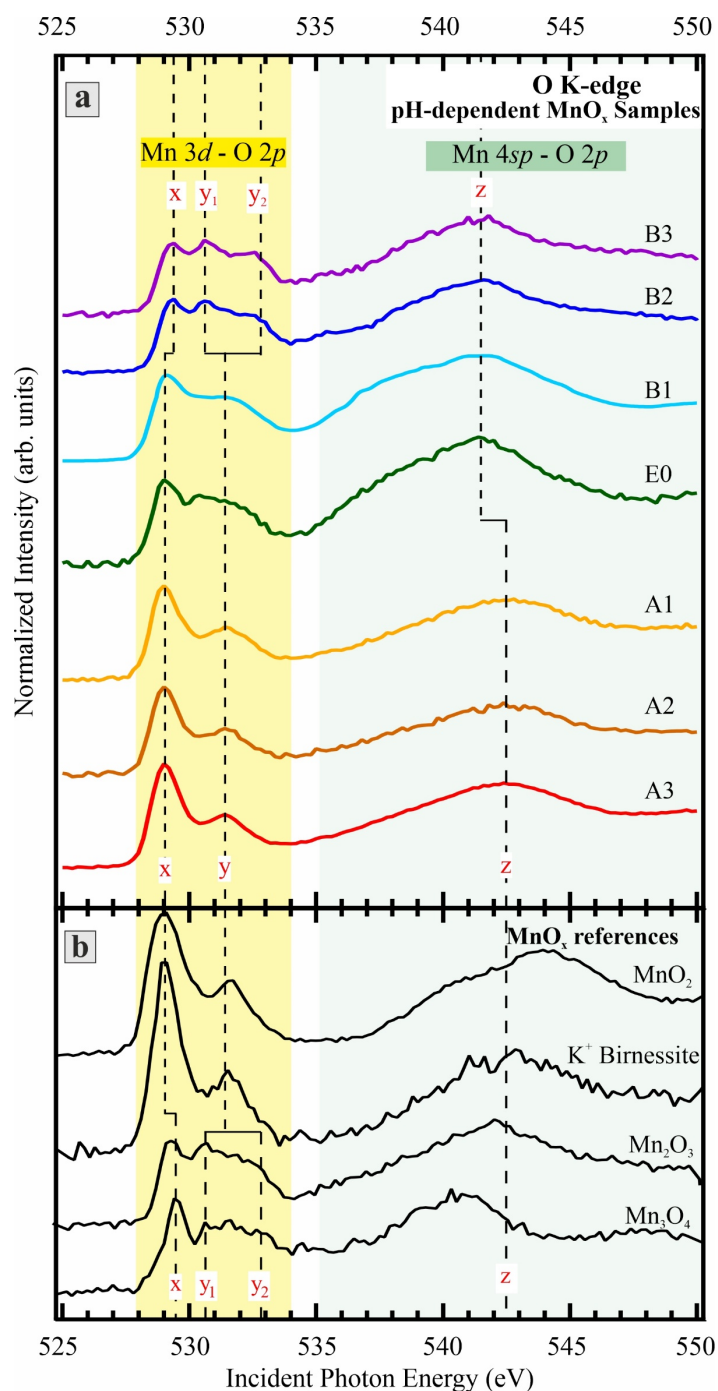
Figure 4.3. Oxygen K-edge TEY-XA spectra measured for a) MnO_x samples electrodeposited from basic ('B', top spectra), neutral ('E0', middle spectrum), and acidic ('A', bottom spectra) electrolytes. b) MnO_x references (Mn_3O_4, Mn_2O_3, K^+ Birnessite, and MnO_2). By going downwards, the pH of the electrolyte during electrodeposition gradually decreases. The background shading shows the spectral regions assigned to electronic transitions, as indicated in the text.

By interpreting the spectra in Figure 4.3(a), the energetic shift of the pre-edge main feature (black dashed line at 'x') to lower energies indicates an increase of the Mn average oxidation state, ligand field, and bonding.[240, 248] A further indication of the MnO_x phase changes can be noticed from the ratio of the first two peaks (peak 'x' and 'y' in Figure 4.3). According to the literature[240] and the XA spectra of the MnO_x references in Figure 4.3(b), a clear dominance of peak 'x' compared to peak 'y' can be seen for birnessite and MnO_2, containing Mn^{IV}. Furthermore, the $3d$ pre-peak intensity (*i.e.,* area under the peak in the yellow highlighted range minus the background) increases when the valence increases from +2→+3→+4.[249] Increasing the oxidation state means more O character in the metal $3d$ band, which would appear as a higher intensity in the O pre-peak. The $4sp$ broad peak (above 535 eV) will also gain some intensity with an increasing oxidation state; however, it would be less pronounced compared to the $3d$ pre-peak because the $4s$ and $4p$ orbitals are mostly delocalized orbitals with less overlap than the $3d$ orbitals.[249]

By comparing the XA spectra of the investigated samples with the MnO_x references in Figure 4.3(a and b), on the one hand, the spectra for the samples prepared from acidic electrolyte 'A' show the highest area under the peaks at x and y positions, which indicates the presence of Mn^{IV} in these samples. While on the other hand, samples B2 and B3 exhibit a 1:1 ratio with a lower peak area. Furthermore, peak 'y' split into two separate features (y_1 and y_2 in Figure 4.3) resembling the O K-edge spectra of Mn_2O_3 and Mn_3O_4, comprising Mn^{III}, which indicates that samples B2 and B3 have a considerable amount of Mn^{III}. The samples of B1 and E0 have an intermediate ratio of the features at 'x' and 'y' and a broadening of peak 'y' indicating an intermediate oxidation state between the acidic or more basic samples. These findings agree well with the spectra at the Mn $L_{2,3}$-edge (*vide supra*), indicating that the MnO_x films electrodeposited from electrolytes of low pH value (high proton activity) favor the formation of MnO_x in a higher oxidation state.

The second region of the O K-edge spectra (*i.e.,* above ~535 eV) also reveals an apparent change between the acidic 'A' and basic 'B' groups. The energetic position of peak 'z' for the samples of group 'B' is shifted about 1 eV to lower energy compared to the samples of group 'A', reflecting a higher localization of the underlying electronic transitions to the hybridized O $2p-$Mn $4sp$ states. Interestingly, this shift already sets in for sample E0 that – together with sample B1 – more closely resembles the pre-edge region of the spectra of the group 'A'. Moreover, peak 'z' appears much broader for these two samples compared to the other samples. This broadening is caused by changes in electronic structure, which is sensitive to the Mn—O bond length.[240] These findings suggest changes of Mn—O bond lengths in the catalyst, which may be explained by a stronger mixing of different MnO_x phases and a higher rate of crystalline

distortion in samples B1 and E0.

In the conclusion of this part, the analysis of the Mn $L_{2,3}$-edge and the O K-edge absorption spectra show that the sample with the highest catalytic activity deposited from the neutral electrolyte, namely, sample E0, exhibits evident characteristics of both Mn^{III} and Mn^{IV} along with low content of Mn^{II}. However, the pure analysis of the Mn oxidation state cannot explain by itself the origin of the high catalytic activity of samples A1 and B1, which is still less than that of sample E0. Therefore, it is necessary to quantify the concentration of a particular phase in each sample. This is done by employing a linear combination fitting method of the XA spectra of the investigated pH-electrodeposited MnO_x samples as a superposition of the XA spectra of reference MnO_x samples with a well-known structure (*vide infra*).

4.4 Fitting Algorithm of XA spectra

4.4.1 Linear Combination Fitting Procedure

The Mn $L_{2,3}$-edge XA spectrum has distinctive and unique features for each Mn oxide phase. Therefore, the linear combination fitting (LCF) procedure can be employed to provide quantitative analysis for the amount of different MnO_x phases present in every catalyst.[113] The LCF method is the most applicable fitting method, especially in the case of mixed oxidation states and multiple phases, where it allows for a linear combination of the reference spectra that strongly resemble the spectra of the investigated samples.[250] Thus, it can track the amount and composition of MnO_x phases within the pH-deposited MnO_x catalysts, which can be the leading cause of the differences in the catalytic activity of the films. The fitting procedure utilizes XA spectra of MnO_x references of well-characterized MnO_x structure, nominally Mn^{II} resembling the spectrum of MnO, Mn_3O_4, Mn_2O_3, birnessite, and MnO_2 (Figure A.3 and Figure A.4), which are measured with the same settings as the XA spectra of the pH-deposited MnO_x samples.

Prior to the fitting procedure, three steps regarding the spectra should be done. First, all the Mn XA spectra were normalized to the off-resonant background to enable a direct comparison and ensure that a fluctuation in the signal strength does not influence the spectra, *i.e.*, by photon flux variations between measurements. Secondly, the XA spectra were corrected by linear background subtraction to emphasize the resonant spectral features. Thirdly, data interpolation for the spectra was needed to eliminate experimentally caused small deviations in the energetic position of the individual data points, *i.e.,* to unify the energy range/step for all the spectra.

The Mn $L_{2,3}$-edge spectra of the investigated samples in Figure 4.1(a) were then fitted by linear

combinations of the Mn $L_{2,3}$-edge MnO_x reference spectra in Figure 4.1(b) using the following function:

Fitted spectrum = α x sp(MnO) + **β** x sp(Mn_2O_3) + **γ** x sp(Mn_3O_4) + **δ** x sp(MnO_2)
$$+\, \boldsymbol{\varepsilon} \text{ x sp(birnessite)}$$

Where the sp(MnO) to sp(birnessite) denotes the XA spectra of the MnO_x references from MnO to birnessite spectra, respectively, and the parameters $\alpha, \beta, \gamma, \delta, \varepsilon$ denote the fraction of the reference spectra needed to the fit every spectrum. These parameters were fitted in an iterative process using the Levenberg-Marquardt-algorithm and the Igor Pro software. The fitting procedure was performed several times, varying the starting parameters to obtain the best possible fit. The obtained fitting parameters are a measure for the relative contribution of the MnO_x reference spectra, which reflect the amount of Mn existing in different chemical environments, *i.e.,* in different phases. The fitting results for Mn $L_{2,3}$- and O K-edges are reported in the following subsection.

4.4.2   Fitting Mn $L_{2,3}$-edge and O K-edge

Figure 4.4 shows the superposition of the Mn $L_{2,3}$-edge XA spectra of the MnO_x references using the LCF method for the **pH-deposited MnO_x** samples, whereas the quantitative contributions of MnO_x species in each sample are presented in Figure 4.5 and Table A.2 in the Appendix. The fittings results indicate that the samples composed predominantly of mainly three MnO_x structural motifs – Mn_3O_4, Mn_2O_3, and birnessite, while the contribution of $Mn^{II}O$ and $Mn^{IV}O_2$ is less than 10%. The samples electrodeposited from acidic electrolyte "group A" consist predominantly of a birnessite-like phase (δ-$Mn^{III/IV}O_2$) and $Mn_3^{II/III}O_4$, with percentages of 58-62% and 31-33%, respectively, as shown in Figure 4.5 & Table A.2; while samples electrodeposited from basic electrolyte "group B" consist of a mixture of $Mn_2^{III}O_3$ with a low proportion of $Mn_3^{II/III}O_4$ (57-79% and 21-29%, respectively).

The concentration of the birnessite-like structure gradually decreases with increasing the pH value of electrolytes during electrodeposition. At the same time, an abrupt increase in the amount of Mn_2O_3 was found for samples prepared at neutral and basic conditions. Apart from the highly acidic or highly basic samples, the samples electrodeposited (near-)neutral conditions, namely A1, E0, and B1, have a different composition compared to the other two samples of their respective groups. Moreover, the best catalytic active sample electrodeposited from the neutral electrolyte (*i.e.,* E0) has the highest concentration of birnessite and Mn_2O_3, with only 4% Mn_3O_4.
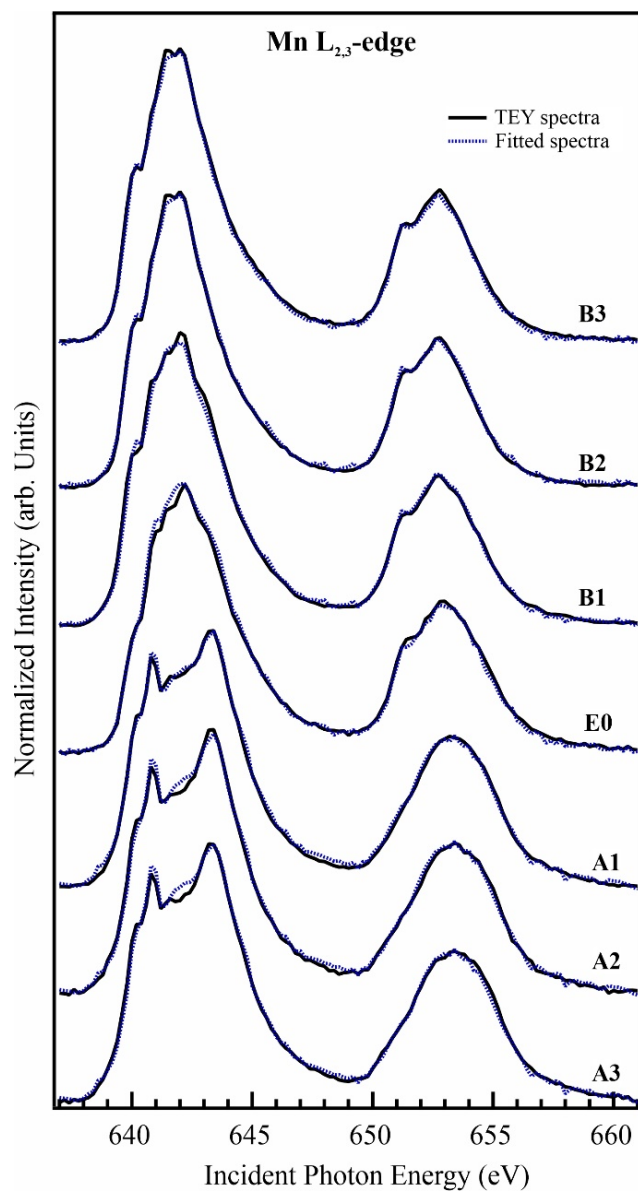
Figure 4.4. Mn $L_{2,3}$-edge TEY-XA spectra of the MnO_x samples electrodeposited from electrolytes at different pH (solid *black* lines) and their corresponding linear fittings as a superposition of the MnO_x reference spectra (dotted *blue* lines).
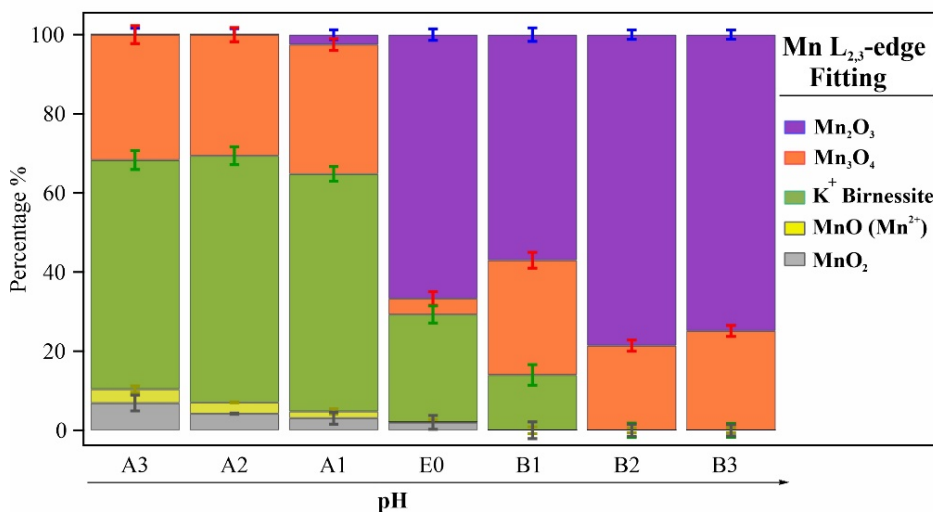
Figure 4.5. Percentages of different MnO$_x$ phases found by a linear fitting procedure for the pH-deposited samples, from highly acidic 'A3' to neutral 'E0' to highly basic electrolytes. The measured and fitted spectra are displayed in Figure 4.4. The contribution of K$^+$ Birnessite (light *green*), Mn$_2$O$_3$ (*violet*), and Mn$_3$O$_4$ (*orange*) are shown for each sample. The contribution of MnO$_2$ (*gray*) and MnO (*yellow*) was found to be below 10% in all samples. The percentages are plotted with an error ±1 standard deviation. However, total accuracy is estimated to be approximately ±5%. The numerical values are tabulated in Table A.2.

To cross-check the reliability of the fitting parameters obtained from fitting the Mn L$_{2,3}$-edge XA spectra, a linear superposition of O K-edge reference spectra (Figure A.4) was carried out using the parameters found for the Mn L$_{2,3}$-edge spectra (Table A.2). Interestingly, the superimposed O K-edge XA spectra of the samples can be well reproduced (blue dotted lines in Figure 4.6) and matched the XA spectra of the pH-deposited MnO$_x$ samples (solid *black* lines in Figure 4.6).

The parameters were then varied, aiming to find the best fit using the same fitting algorithm as for the Mn spectra but using the O K-edge reference spectra. The fitting results obtained for O K-edge spectra show a minimal deviation compared to that for Mn L$_{2,3}$-edge. *I.e.,* the standard deviation error is higher for the O K-edge fitting (around 5-10 %). This might be due to possible O contributions of adsorbed or intercalated water in the substrate that manifested in the spectra or due to less accuracy which arises from the low signal to noise ratio of the O K-edge reference spectra. To avoid this, only the pre-edge region from approximately 525 to 534 eV was used. The features in this region are well defined and arise predominantly from transitions to the hybridized state of O 2p and Mn 3d orbitals. Besides, it should be mentioned that it was not

possible to use a spectrum of MnO in the fitting of the O K-edge spectra as detailed in the MnO_x references experimental section. This, however, is not suspected to affect the fitting results since the amount of MnO is negligible (~2-3 %) for all the samples, as revealed by the Mn $L_{2,3}$-edge fitting; therefore, the omission of the MnO spectra in the O K-edge fitting procedure is not expected to affect the results significantly. Moreover, the close resemblance of the O K-edge XA spectra between MnO_2 and birnessite-like structure hinders the accurate linear fitting to the O K-edge XA reference spectra.
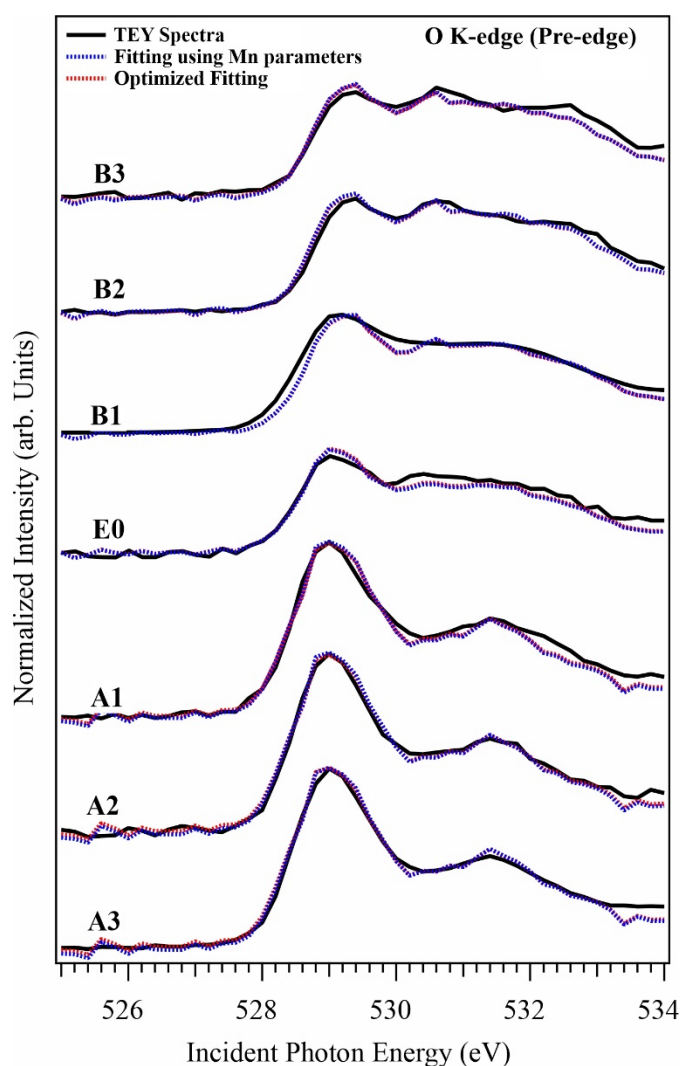
Figure 4.6. O K-edge TEY-XA spectra of the investigated samples (solid *black* lines), and the corresponding linear fittings as a superposition of the reference spectra measured at the O K-edge using the fitting parameters resulted from fitting the Mn $L_{2,3}$ edge - (dotted *blue* lines) and after further optimization with free fitting parameters (dotted *red* lines).

Further parameter optimization did not show a major enhancement in the fitting quality (red dotted lines in Figure 4.6), suggesting that the resulted parameters are consistent for Mn $L_{2,3}$-edge and O K-edge. The quantitative contributions based on further parameter optimization are represented in the histogram in Figure 4.7, and numerical values are tabulated in Table A.3.
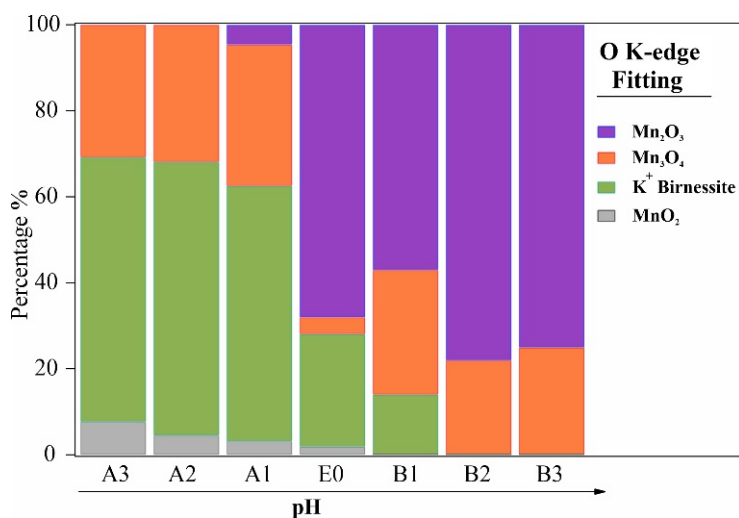
Figure 4.7. Percentages of MnO_x species in the samples deposited at different pH, identified by the linear fitting procedure for O K-edge spectra after further optimization of the parameters used to fit the Mn $L_{2,3}$-edge XA spectra. The contribution of K^+ Birnessite (light *green*), Mn_2O_3 (*violet*), Mn_3O_4 (*orange*), and MnO_2 (*gray*) are shown for each MnO_x catalyst. Numerical values for the MnO_x contributions are tabulated in Table A.3.

Overall fitting findings show that the amount of $Mn_3^{II/III}O_4$ is nearly constant for the acidic 'A' and the basic 'B' samples, while almost no contribution was found in the 'E0' sample. The absence of Mn_3O_4 in the sample 'E0' may explain being the best catalytic active sample since Mn_3O_4 shows the least catalytic activity among the other MnO_x phases for OER.[75, 251] Nonetheless, this cannot explain why samples A1 and B1 show higher catalytic activities among the other two samples in their respective groups, all of which contain a similar proportion of Mn_3O_4. The fitting approach herein demonstrates that both samples A1 and B1 have contributions from birnessite and Mn_2O_3, although in different proportions (30:1 and 1:4, respectively; Table A.2). Meanwhile, the best catalytic activity film E0 includes birnessite and Mn_2O_3 phases in a ratio of about 1:2.5.

This finding is consistent with studies on the natural water-splitting process, where the interplay between these two Mn oxidation states (Mn^{III} and Mn^{IV}) was identified to be the key to the function of the oxygen evolution center in photosystem II (see, *e.g.,* Refs. [59, 252]). Previous

studies of other groups showed that Mn^{III} represents a crucial intermediate state in the artificial water-splitting process.[40, 42-44, 68, 97] It is believed that the Mn^{III} vacancies within the layer sheets of the birnessite structure lead to the elongation of Mn-O bonds as perceived by Jahn Teller distorted $Mn^{III}O_6$ octahedra. [78, 112, 114, 115] A higher concentration of Mn^{III} can lead to a larger degree of distortion in the local structure, which might favor catalytic activity by providing structural flexibility. [42, 113] However, the presence of a high concentration of a single Mn^{III} oxide in the film does not lead by itself to high catalytic activity; otherwise, one would expect the highest catalytic activity for the samples B2 and B3 that consist of nearly 80% Mn_2O_3 while in fact, they have the least catalytic activity. However, our findings on the continuous change of the oxidation state suggest that besides the oxidation state of the Mn, the interplay between different Mn phases (Mn_2O_3 and birnessite) within the deposited catalyst also plays a crucial role in the efficiency of electro-synthesized MnO_x catalysts. It should also be noted that this study is restricted to an *ex situ* analysis of the samples, *i.e.,* without applying any potential, and further phase transition may occur when a potential is applied (see the *in situ* study later in *Chapter 5*).

For amorphous MnO_x, it is predicted that high catalytic activity toward OER is related to a variety of Mn—O bond lengths.[98] This is confirmed by the broad features in the region denoted 'z' within the O K-edge spectra herein (Figure 4.3), which are sensitive to changes in the electronic structure correlated to the Mn—O bond lengths, especially for the E0 and B1 samples. It can be hypothesized that a greater number of structural distortions may occur as a result of local fluctuation in the pH of electrolyte during electrodeposition. It might either be caused by a local distortion of the birnessite structure or a structural reorganization at the phase boundaries. As shown, the XAS technique could provide vital information about the total contribution of MnO_x phases present in the sample. However, it is not possible to state a definite correlation toward a catalytic activity while evaluating the MnO_x species ratios within the sample series since other properties such as spatial phase distribution, adjacent phases, and grain size are believed to play a role. The determination of those parameters is beyond the capabilities of the specific experimental technique used herein. Such properties may affect the extent of structural disorder, which is also often essential for catalysis. The findings may still be tentatively linked to MnO_x properties suggested as important for OER catalysis.

4.5   Conclusion

Soft X-ray absorption spectroscopy has been employed to examine a series of MnO_x films electrodeposited at 120 °C from Mn^{II} acetate in ionic liquid electrolytes with varying pH. The

films – ranging from highly acidic 'A3' to highly basic 'B3' (namely, A3, A2, A1, E0, B1, B2, B3) – showed previously different electrocatalytic activity toward water oxidation. The study herein focused on elucidating the compositional changes of different MnO_x phases as a function of pH and correlation with the previously identified catalytic activity of the samples. The analysis of the absorption spectra at the Mn $L_{2,3}$-edge and the O K-edge revealed the following:

- a gradual increase of the mean Mn oxidation state with decreasing pH during the electrodeposition process.

- All pH-deposited samples include three MnO_x phases with different proportions: Mn_3O_4, Mn_2O_3, and Birnessite, while the contribution of MnO and MnO_2 is less than 10%.

- The contribution of Mn_3O_4 is almost the same for the acidic and basic samples while being negligible for the highest catalytic active sample electrodeposited from the neutral electrolyte.

- The samples with the least catalytic activity showed a dominant contribution of either a birnessite-like structure (for A2/A3 samples) or Mn_2O_3 (for B2/B3 samples). The next better catalytic activity was found for the samples A1 and B1 (deposited near-neutral conditions), composed of a mixture of the birnessite-like structure and $Mn_2^{III}O_3$ with one of the phases dominating.

- Finally, the sample with the highest catalytic activity (E0), electrodeposited in neutral conditions, showed a composition of nearly equal amounts of the birnessite-like structure and $Mn^{III}_2O_3$.

These results did not reveal an isolated single MnO_x structural composition responsible for the optimally achieved catalytic activity. However, the interplay of birnessite and Mn_2O_3 structural motifs could drastically enhance the catalytic activity and not due to a single contribution of any of them. Other factors, such as structural disorder and Mn—O bond length distortions, may play a crucial role in the catalytic activity. This study revealed that the contribution of both phases is continuously tunable by a careful choice of the preparation conditions. Hence, these findings can be used for future studies on creating efficient catalysts solely based on MnO_x in desired ratios of structural composition.

Chapter 5

An *in situ* Study of the Electronic States of the MnOₓ Catalyst During Water Electrooxidation

This part of the thesis is taken from the following publication.

"Evolution of Oxygen-Metal Electron Transfer and Metal Electronic States During Manganese Oxide Catalyzed Water Oxidation Revealed with *In Situ* Soft X-ray Spectroscopy"

Marc F. Tesch, Shannon A. Bonke, Travis E. Jones, **Maryam N. Shaker**, Jie Xiao, Katarzyna Skorupska, Rik Mom, Jens Melder, Philipp Kurz, Axel Knop-Gericke, Robert Schlögel, Rosalie K. Hocking, and Alexander N. Simonov. *Angewandte Chemie International journal* (2019) 131, 3464-3470. **DOI:** 10.1002/anie.201810825
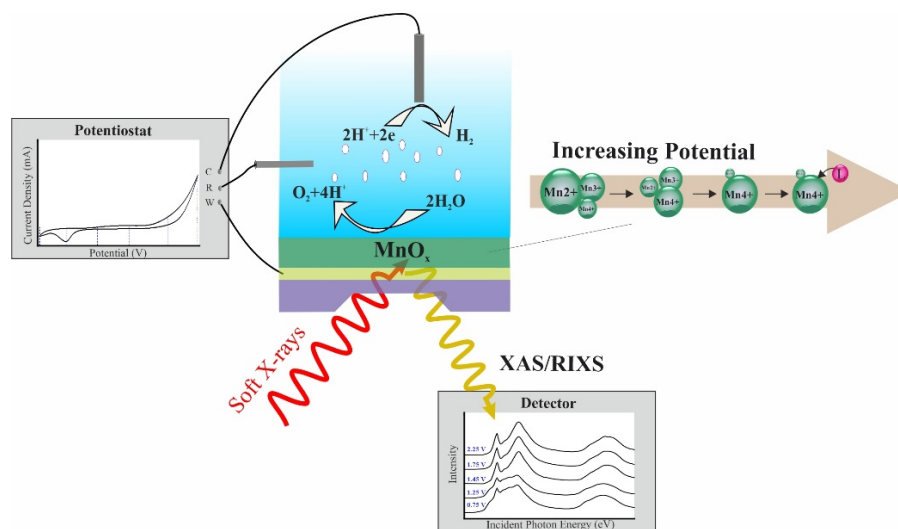
Deciphering the electronic states of MnOₓ electrocatalyst *in situ* under applying potentials and screening changes in the Mn states, including oxidations and charge transfer process between Mn in the metal and O in the ligand.

5.1   Introduction

Ex situ studies have been reported on MnO_x water oxidation catalysts using both soft X-ray absorption spectroscopy, as shown in *Chapter 4* (also in ref. [56, 72, 113]) and hard X-ray absorption spectroscopy (see scientific review in [147]). However, analyzing the catalyst after electrolysis does not give the exact structural changes like that under real reaction. For that, to develop an efficient water splitting electrocatalyst, a comprehensive understanding of the catalytic mechanism of water electrooxidation and transformations occurring in the catalytic material is indispensable. Thereby, *in situ* investigation has become inevitable to identify the actual MnO_x active phase besides monitoring and tracking the structural changes during water oxidation reaction under real-time electrocatalytic conditions. Such investigations on Mn-based catalysts are limited.[73, 145, 253, 254] All the previous *in situ* investigation on manganese oxide has been performed utilizing "hard" XAS at Mn K-edge, which probe the transition of an electron from the deep-lying $1s$ to $4p$ states.[147] It has proven to be a potent tool to investigate the MnO_x structure and identify the mean oxidation state. However, the pre-edge intensity, arising from the electron transition from $1s$ to empty $3d$ valence states, is very weak because it is dipole forbidden, which makes it difficult to probe the $3d$ electronic valence states, which are responsible for the redox reaction.[149] Thus, "soft" XAS measured at the Mn $L_{2,3}$-edge and resonant inelastic X-ray scattering (RIXS) have spurred much interest as a promising technique to probe the unoccupied and occupied $3d$ valence states and is sensitive to the metal-ligand (Mn—O) sites. [159, 181-183] Besides, XAS at Mn L-edge can provide more detailed spectral features, which are not observed at the K-edge due to the ultra-short lifetime of $1s$ core-hole that is created in the absorption process.[255] Furthermore, Mn L-edge has a narrow natural line width of 0.32 eV compared to 1.12 eV for Mn K-edge, so the ratio of the edge shift for L-edge is higher (*i.e.,* shifts are more pronounced), which makes it favorable to decipher mixtures of oxidation states.[247] Moreover, the energy-resolved distribution of the emitted photons in the RIXS process serves as a measure of different excitation processes that occur by valence electrons, like local *d-d* transition and charge transfer (CT) excitations[113], which are fundamental characteristics closely related to the catalytic properties.

In this chapter, this fundamental knowledge is obtained *in situ*, for the first time, for the MnO_x water oxidation catalysts over a wide range of applied positive potential from 0.75 to 2.25 V *vs.* reference hydrogen electrode (RHE), which help to define the state of the catalyst at different catalytic stages. Measurements at high potentials are necessary to uncover higher Mn oxidation states that might involve in catalytic water oxidation.

While X-rays require high vacuum conditions, the MnO_x catalyst has to be biased while being

in contact with the electrolyte during X-ray investigation. To conquer the challenging requirements needed for the *in situ* XAS/RIXS experiment, the LiXEdrom endstation installed at the BESSY-II synchrotron facility accommodates a custom-made electrochemical flow cell (Figure 5.1), in which a gold-coated silicon nitride (Au/Si_3N_4) membrane is placed.
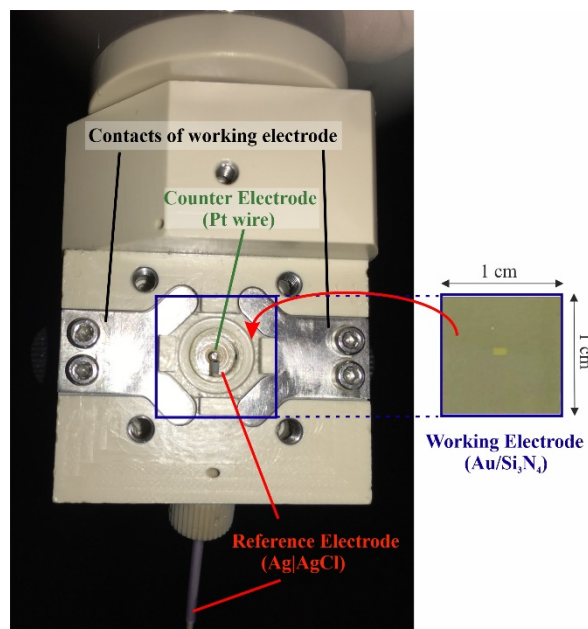

Figure 5.1. A real picture of the electrochemical flow cell used in the electrodeposition of MnO_x films and for XAS/RIXS measurements. The cell is fitted with 3-electrodes at which the counter electrode (Pt wire) and the reference electrode (Ag|AgCl) are embedded in a small volume where the electrolyte flows interacting with the working electrode (MnO_x on Au/Si_3N_4). The working electrode lay on two conductive contact Y-pieces for electrochemical analysis.

The Au/Si_3N_4 membrane has two significant functions: (1) act as a substrate for the MnO_x sample under investigation, (2) separates the liquid from the vacuum. Details about the LiXEdrom endstation and BESSY-II synchrotron facility are presented in sections 3.1.1 and 3.2. Technical details on the flow cell are reported in section 3.1.1.1.

5.2 Experimental Section

5.2.1 Materials

$Mn(CH_3COO)_2$, $B(OH)_3$, NaOH, and HNO_3 were purchased from Sigma-Aldrich and used without additional purification. In all sample preparations, high-purity deionized water (Milli-Q; 18.2 MΩ.cm at 25°C) was used. Reference manganese oxide powders (MnO, Mn_3O_4, Mn_2O_3,

and MnO_2) were obtained from Sigma-Aldrich, except for birnessite. Potassium-rich birnessite (K-birnessite) was synthesized according to [243] and donated by Dr. R. K. Hocking from Swinburne University of Technology, Australia. The Mn^{II} reference XA spectrum exhibiting the typical spectral features of undamaged MnO was taken from the previous study.[72]

Si_3N_4 membrane (100 nm thickness) supported on silicon frames ($10 \times 10 \times 0.38$ mm^3) with a window in the center of the frame with a dimension of 1.0 mm $\times$ 0.5 mm is used as a substrate in this study. As conductive substrates are needed for XAS/RIXS measurements, Si_3N_4 membranes were sputter-coated prior to use with a 20 nm thick Au film, as described in section 3.3.1.2. The Ag|AgCl|3.4 M KCl electrode, from Innovative Instruments Inc., is used as a reference electrode.
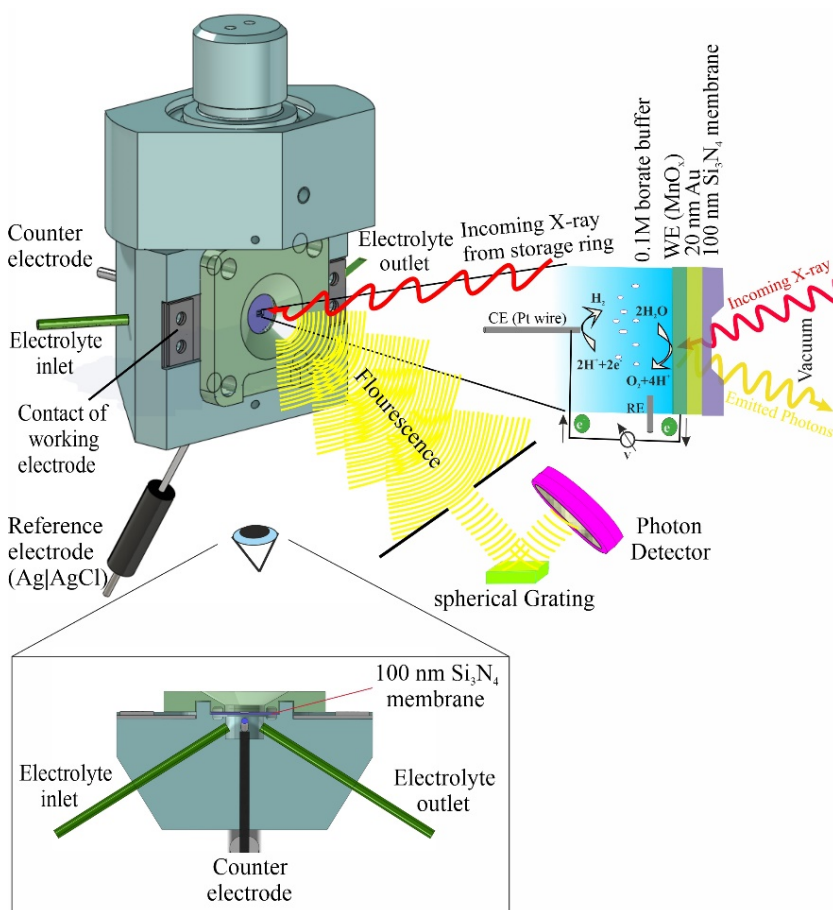
Figure 5.2. Schematic drawing of the electrochemical flow cell used for the *in situ* absorption/emission experiments. The zoom in on the right side shows the electrochemical reaction happening at the MnO_x catalyst screened by XAS/RIXS techniques. Incident X-rays (*red* wave) penetrate the Au/Si_3N_4 membrane and interact with the MnO_x sample, then the emitted fluorescence (*yellow* waves) is collected by a spectrometer (spherical grating + photon detector). The bottom scheme is a bottom view of the flow cell.

5.2.2   RIXS/XAS Electrochemical Flow Cell Design

The electrochemical flow cell (Figure 5.1 & Figure 5.2) used for all measurements is fitted with 3-electrodes, *viz.* Pt wire was used as a counter electrode (CE), Ag|AgCl electrode was used as the reference electrode (RE), and the Au/Si_3N_4 substrate served as the working electrode (WE). As depicted in Figure 5.1 and the bottom view of the flow cell in Figure 5.2, the CE and RE are embedded in a small volume in which the electrolyte flows, interacting with the $MnO_x/Au/Si_3N_4$. The flow cell is not only used for electrodeposition of MnO_x on Au/Si_3N_4 but can also be implemented in the LiXEdrom main chamber for XAS and RIXS measurements.

X-rays (*red* wave in Figure 5.2) coming from the synchrotron beamline will penetrate the 120 nm thick Au/Si_3N_4 membrane, interact with the MnO_x catalyst, then the spectrometer, *viz.* spherical grating and detector collect and detect the scattered light in an energy-resolved fashion, as illustrated in Figure 5.2. Simultaneously to RIXS/XAS measurements, potentials were applied to the MnO_x catalyst attached to the electrolyte solution through a potentiostat (EmStat3+ series from PalmSens company) connected to the three-electrodes configuration.

5.2.3   Electrodeposition of MnO_x

Prior to the electrodeposition of MnO_x film on the Au/Si_3N_4 membranes, it was necessary to clean the Au/Si_3N_4 membrane. Our approach was to perform cyclic voltammetry cycles (0.75 − 2.25 V_{RHE}; sweep rate of 0.020 V s^{-1}) on the unmodified Au/Si_3N_4 membrane in contact with the supporting electrolyte solution of borate buffer (0.1 M, pH 9.2) until a stable cyclic voltammogram was achieved. This preliminary cleaning step was done before each MnO_x deposition. All potentials in this chapter are given *vs.* reversible hydrogen electrode and written as V_{RHE}).

As just pointed out, the supporting electrolyte of 0.1 M borate buffer at pH 9.2 was used not only in the cleaning step but also for all XAS/RIXS measurements. The electrolyte is prepared according to the recipe in [225] and described more precisely in section 3.3.2.1. The pH value of the borate buffer was checked regularly before each experiment using a calibrated pH meter. All the potentials were measured versus Ag|AgCl then recalculated versus the RHE scale according to the relationship $E (V_{RHE}) = E (V_{Ag|AgCl} + 0.210 + 0.059 \times pH)$, where pH = 9.2. The electrolyte used in the deposition of MnO_x was prepared by mixing 0.5 mM $Mn(CH_3COO)_2$ and 0.1 M borate buffer (pH 9.2) [*i.e.,* Mn^{II} solution buffered by borate], as described in section 3.3.2.2. The MnO_x film was electrodeposited on the Au/Si_3N_4 membrane via chronoamperometry mode at a potential of 1.95 V_{RHE} at 25°C.

Electrodeposition of the MnO$_x$ was done using five, two-minute-long depositions without flow, separated by *ca.* 2 min periods, which were needed to change the deposition solution in the cell with a fresh solution (flow rate *ca.* 15 µL s^{-1}). However, this deposition protocol yielded unstable MnO$_x$ film at potentials more positive than 1.75 V$_{RHE}$ during spectroscopic analysis under X-ray irradiation, and film detachment from the Au/Si$_3$N$_4$ membrane was seen. For that, a second deposition protocol was applied and lead to the preparation of more stable and relatively thicker catalyst films as needed for the spectroscopic analysis at potentials more positive than 1.75 V$_{RHE}$. In the second electrodeposition protocol, MnO$_x$ film is formed by a 4 mins continuous electrodeposition without any interruption with a flow rate of 13 µL s^{-1}. Except for the improved stability, no other differences in the XAS/RIXS or electrochemical characteristics of the MnO$_x$ films produced were revealed via the two different deposition protocols. Prior to and after each experiment, the internal cell tubing was cleaned by flowing 1 M HNO$_3$ for at least 15 min, then flushed with de-ionized water at a flow rate of 15 µL s^{-1} for 20 min to remove any acid/MnO$_x$ traces.

5.2.4   Scanning Electron Microscopy of electrodeposited MnO$_x$ films

Scanning Electron Micrographs (SEM) were obtained using a HITACHI S-4100 scanning electron microscope. Images were taken in several areas of each sample to ascertain the morphological homogeneity. Figure 5.3 shows the SEM images obtained for the MnO$_x$ film in the as-deposited state and after biasing the same film at 1.75 V$_{RHE}$.
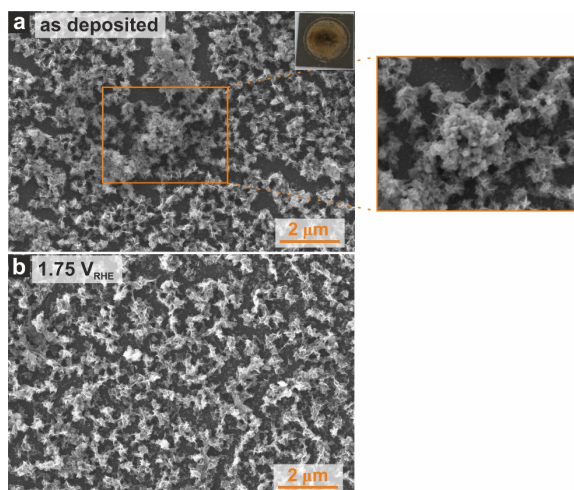

Figure 5.3. Scanning electron micrographs of freshly deposited MnO$_x$
(a) before and (b) after applying potential for 15 min at 1.75 V$_{RHE}$ in 0.1 M borate buffer (pH 9.2). The top right picture of (a) is a real picture of the as-deposited MnO$_x$ film as a brownish area on the Au/Si$_3$N$_4$ substrate. The inset on the right side shows random nanostructured particles in the as-deposited MnO$_x$ film.

The potential was applied *ex situ* for 15 min in 0.1 M borate buffer (pH 9.2) directly before SEM measurement. Both images revealed the formation of uniform distribution of the MnO_x on the Au/Si_3N_4 substrate. The as-deposited film reveals two different structures; porous nanoflakes and interconnected grains which strongly resembling the birnessite structure [256], with some regions which contain irregular, random nanostructured particles, as shown in the inset of Figure 5.3(a), which resembles Mn in lower oxidation states, like Mn_3O_4.[257] After applying a potential of 1.75 V_{RHE} to the same MnO_x film, the nanostructured particles are likely transformed, and the nanoflakes are uniformly covering the substrate, which may enhance better access of electrolyte into the catalyst.

5.2.5   Mn L-edge XAS/RIXS spectroscopy

The XAS/RIXS experiments were performed at the U49-2/PGM1 beamline of the BESSY II synchrotron facility in Berlin, Germany. The LiXEdrom endstation was used to host the electrochemical flow cell in a high vacuum chamber (10^{-6} mbar), allowing the electrolyte to enter and exit the flow cell via feedthroughs. Moreover, the LiXEdrom setup includes the photon detector by which the energy of the emitted photons can be detected in an energy-resolved fashion probing specific excitations in the catalyst. The emitted photons (*yellow* waves in Figure 5.2) were detected in the energy range 632-660 eV, which allows probing the transitions from the Mn $2p$ to unoccupied $3d$ valence state.

The X-ray absorption (XA) spectra were measured herein in two acquisition modes: *total electron yield* (TEY) and *partial fluorescence yield* (PFY) modes. Both acquisition modes are discussed in section 2.2. The TEY-XA spectra were collected *ex situ*, at which a potential was applied to the MnO_x film substrate in the electrochemical flow cell for 15 mins; then, the substrate is mounted on a solid sample holder and transferred directly afterward to be measured with X-rays. While the PFY-XA spectra were collected *in situ*, at which the potential is applied to the MnO_x film simultaneously to X-ray illumination. The *in situ* PFY-XA spectra were measured at different positions at least twice on the sample and compared to each other to check for the homogeneity of the MnO_x film and identify any beam damage. Then the overall detected intensity of the spectra was summed up to increase the signal to noise ratio when no sample damage was detected. The PFY-XA spectra were reproducible for freshly prepared MnO_x samples. An advantage of our experimental setup is that a RIXS measurement can be carried out simultaneously with the PFY-XA measurement. This is done by recording the energy-resolved spectrum for each excitation energy as a 3D map. The emitted photons were collected at each incident energy for *ca.*10 sec for every single scan. *I.e.,* one PFY-XA spectrum in the range of

632-658/0.1 eV takes *ca.* 43 minutes with a moderate signal to noise. However, 10 sec acquisition time at each excitation energy of the energy range was not enough to collect high resolved RIXS spectra. Hence, to obtain a more detailed RIXS spectrum with a better signal to noise ratio at selected energy, it was collected in 30 min, as triplicate RIXS measurements of 10 minutes each. The RIXS spectra were then compared to each other to identify possible sample damage and subsequently summed up.

All the experimental raw RIXS spectra were corrected from the noise background, and energy was calibrated, as described in section 3.4. In order to compare relative amounts of scattered photons (*i.e.,* intensity) into the various channels, all the experimental and theoretical spectra were normalized to an intensity of 1. It should be mentioned that this normalization does not change the relative intensities of the RIXS features, as shown in Figure B.1 in Appendix B.

5.2.6   Sample Damage Study

As previously pointed out, samples investigated with soft X-rays of a high photon flux are highly prone to sample damage.[258] Hence, one should pay special attention to the verification and elimination of sample damage during the spectroscopic investigation. A sample damage study protocol similar to that applied in *Chapter 4* was followed for the *in situ* and *ex situ* measurements of this study.

Absorption/Emission spectra for MnO_x were recorded using different X-ray intensities under applied potentials to identify any undesired processes that may happen. It is found that sample damage is possible to occur for the *in situ* PFY-XA spectra as well as the *ex situ* TEY-XA spectra. Figure 5.4 reveals that the induced spectral changes in the TEY-XA spectra measured *ex situ* follow those obtained *in situ* in the PFY mode.

For the *in situ* PFY-XA measurements conducted at potentials up to 1.75 V_{RHE}, the opening of the beamline aperture located directly after the insertion device was adjusted to (1.6 mm × 1.6 mm) and exit slit size of 50 μm, which results in a reasonable signal to noise ratio with no indication for sample damage by the X-rays. However, this photon flux yielded a substantial reduction of electrodeposited MnO_x to the state dominated by Mn^{II} upon collecting the PFY-XA spectra at potentials equal to or above 1.75 V_{RHE} (Figure 5.4(b)). Therefore, it was necessary to stepwise decrease the beamline aperture down to 0.8 mm × 0.8 mm, at which the flux decreased by approximately a factor of 4. As a result, no beam damage was obtained as checked at different sample positions. It reveals that the reduction of the MnO_x was predominantly arising from the relatively high photon flux. In the case of *ex situ* TEY-XA measurements up to 1.75 V_{RHE}, the

beamline aperture was adjusted to the least value (0.2 mm × 0.2 mm) that would allow collecting undamaged spectra (black in Figure 5.4(a)).
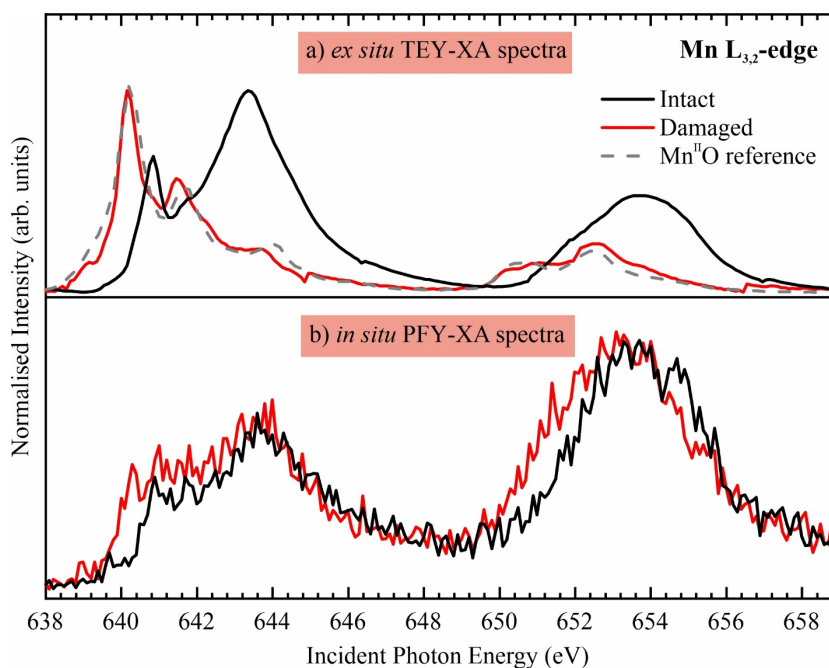

Figure 5.4. Mn L-edge XA spectra for intact (*black*) and X-ray damaged (*red*) electrodeposited MnO_x film obtained (a) *ex situ* in TEY mode after polarization at 1.45 V_{RHE} for 15 min, and (b) *in situ* in PFY mode during biasing at 1.75 V_{RHE}. Potentiostatic treatment was performed using a 0.1 M borate buffer solution (pH 9.2). The TEY-XA spectrum of $Mn^{II}O$ reference (*gray*) was plotted in the top panel for comparison.

All spectra were obtained multiple times at various sample spots to detect undesired changes due to sample damage and to evaluate spectral reproducibility using different low photon fluxes. The spectroscopic data were perfectly reproducible in all, but in a few cases, some spectra were found to include some spectral changes due to X-ray induced sample damage. Those spectra were excluded from the analysis, and only spectra that include no sample damage were eventually addressed, and therefore were used for analysis.

5.3 Experimental Results and Discussion

5.3.1 Cyclic Voltammetry of MnO_x films

Cyclic voltammetry (CV) is used to investigate the redox process happening at the MnO_x

catalyst. Figure 5.5 shows the cyclic voltammograms for Au/Si₃N₄ substrate before and after the MnOₓ electrodeposition, with both exhibiting a combination of redox processes.
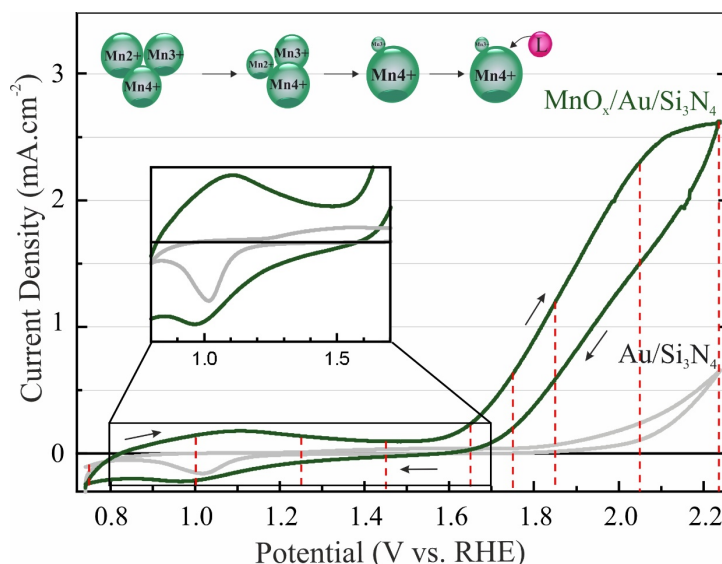

Figure 5.5. Cyclic voltammograms for unmodified Au/Si₃N₄ substrate (*gray*) and electrodeposited MnOₓ on Au/Si₃N₄ substrate (*green*) in 0.1 M borate buffer (pH 9.2). Currents were normalized to the geometric surface area of the electrode. The plot region of the Mn redox transformations is enlarged as an inset in the figure. The top scheme illustrates the potential-induced changes of the Mn oxidation states, initiated from spectroscopic results (*vide infra*). The *in situ* XAS/RIXS spectroscopic measurements (*vide infra*) are collected at nine potentials at the dashed (*red*) lines.

All the CV curves were undertaken using the same electrochemical flow cell used for the MnOₓ electrodeposition with a Ag|AgCl reference electrode and a platinum wire counter electrode. CVs were measured in 0.1 M borate buffer (pH 9.2) in the potential range (0.75 - 2.25 V_{RHE}, starting and terminating at 0.75 V_{RHE}, sweep rate of 0.02 V s⁻¹). During the spectroscopic analysis, the potential of the electrode was kept constant. All electrochemical and spectroscopic studies were undertaken at 23 ± 2°C. Before the MnOₓ electrodeposition, the Au-coated Si₃N₄ support exhibits typical features of gold substrates, *viz.* surface oxidation starts at *ca.* 1.2 V_{RHE}, and their reduction as a well-defined peak at *ca.* 1.0 V_{RHE} (*gray* curve in the inset of Figure 5.5). This value is close to that reported in the literature.[259] By electrodepositing MnOₓ on the Au-coated Si₃N₄ support, the Au redox features are suppressed as expected, while the redox features of MnOₓ catalyst are pronounced along with water oxidation at potentials >1.6 V. In the potential range of 0.8-1.4 V, at least two redox transformations of Mn can be seen, [142] as shown in the inset of Figure 5.5.

5.3.2   XAS measurements of MnO$_x$ films

In situ X-ray absorption spectroscopy measurements were carried out at nine potentials (*red dashed lines in* Figure 5.5), addressing different catalytic regions of MnO$_x$. The initial as-deposited state of the freshly deposited MnO$_x$ catalyst was examined with no potential applied (*i.e.,* at open circuit potential (OCP)). The OCP allows the MnO$_x$ catalyst to equilibrate after the cyclic voltammetric analysis.

Figure 5.6(a) shows the *in situ* PFY-XA spectra measured at the Mn L$_{2,3}$-edge in the energy range 636 - 658 eV. The spectra reveal typical multiple structures, arising from the electronic transitions of 2p core – 3d conduction band (unoccupied valence states) upon soft X-ray absorption. The first multiplet structure in the energy range of *ca.* 639-647 eV originates from Mn 2$p_{3/2}$ → 3d transitions (L$_3$-edge), and the second absorption features between 650 eV and 658 eV are attributed to the Mn 2$p_{1/2}$ → 3d transitions (L$_2$-edge). After excitation, there is a relaxation process via electron/photon emission.

In situ PFY-XA spectra were collected simultaneously while applying potentials from 0.75 to 2.25 V$_{RHE}$ to the electrodeposited MnO$_x$, as displayed vertically in Figure 5.6(a). The application of increasing potential induces significant changes in the spectral features: On one hand, the peaks at 640.2 eV and 641.6 eV in the L$_3$ edge regime arise mainly from Mn^{II} and Mn^{III}, respectively, are notably suppressed, while a significant increase in the intensity of spectral features located at 640.8 and 643.7 eV (fingerprints of Mn^{IV}). On the other hand, there is an overall shift in the L$_2$ main feature towards higher energies as applied potential increases. These spectral changes reflect an increase in the mean oxidation state[247, 258], which can be further linked to structural transformations in the catalyst films at various catalytic stages. Interestingly, changes observed in the XA spectra are reversible and reproducible, as confirmed by measurements carried out with a random sequence of applied potentials, as shown in the Appendix (Figure B.2).

Ex situ TEY-XA spectra were also measured at the Mn L$_{2,3}$-edge for the MnO$_x$ reference samples and the electrodeposited MnO$_x$ catalyst in the as-deposited state and after conditioning at different potentials (Figure 5.6(b and c)) to allow for comparison with the *in situ* results and confirm previous results. The TEY-XA spectra of reference MnO$_x$ samples were used to fit the XA spectra of the biased MnO$_x$ catalyst to establish the effect of potential on the Mn oxidation state of the MnO$_x$ catalyst.
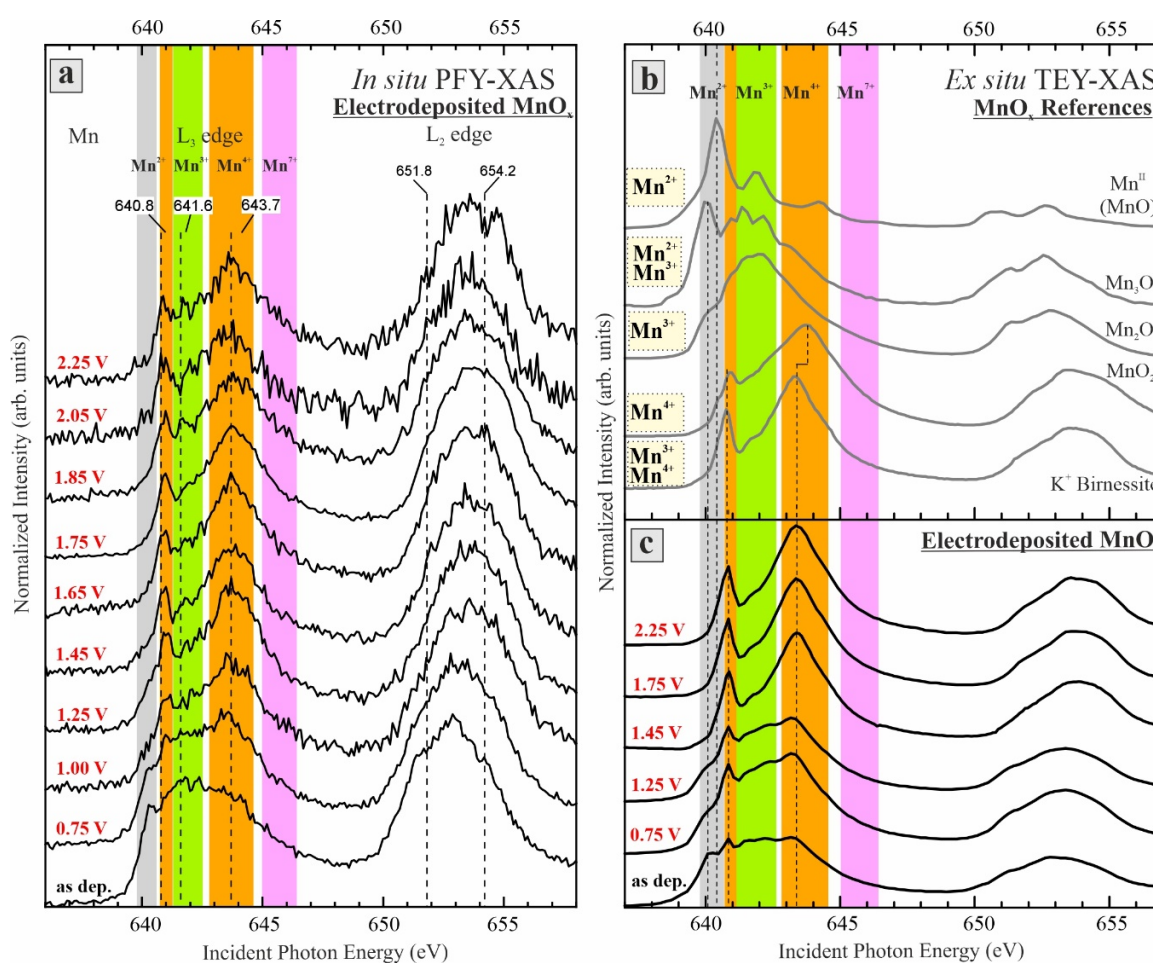
Figure 5.6. Soft XA spectra at the Mn $L_{2,3}$-edge measured (a) *in situ* in the PFY mode
for MnO$_x$ film in contact with 0.1 M borate buffer (pH 9.2) obtained with no potential applied (as dep.
state) and after biasing at specific potentials (values at the dashed *red* lines in the cyclic voltammogram
curve in Figure 5.5). Energies at the dashed lines were used to record the RIXS spectra, (b) *ex situ* in
TEY mode for reference MnO$_x$ materials (Mn$_3$O$_4$, Mn$_2$O$_3$, MnO$_2$, birnessite, and Mn^{II} resembling MnO
[56, 72]), and (c) *ex situ* for the MnO$_x$ in the as-deposited state and after 15 min conditioning at 0.75, 1.25,
1.45, 1.75, and 2.25 V$_{RHE}$ in 0.1 M borate buffer (pH 9.2). Background shading shows the spectral
regions corresponding to a particular Mn oxidation state [258], as identified by the main features of each
MnO$_x$ reference spectra in (b). The spectra are normalized to one at maximum intensity. The oxidation
state of Mn for each reference spectrum is labeled in the *yellow* box. Corresponding current-time
transients recorded during the *in situ* measurements are demonstrated in Figure 5.7.
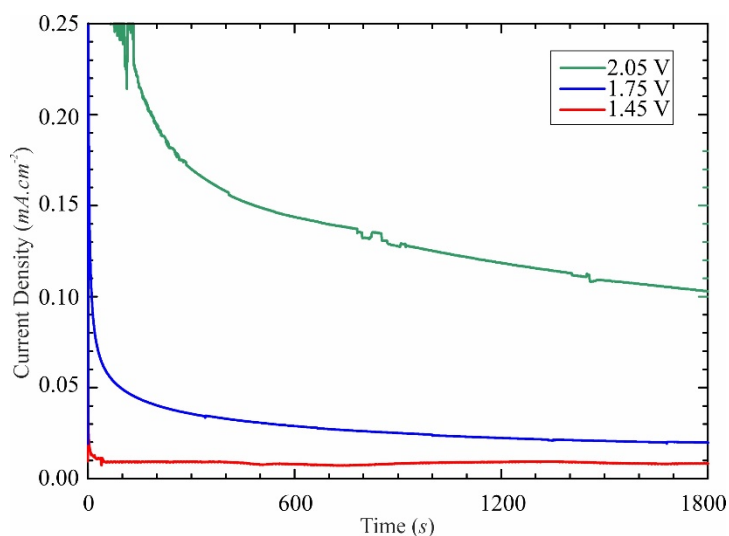
Figure 5.7. Typical water oxidation current-time transients obtained for electrodeposited MnO_x biased at potentials 1.45 (*red*), 1.75 (*blue*), and 2.05 V_{RHE} (*green*). The measurements were undertaken during *in situ* PFY-XAS analysis, while the MnO_x film was in contact with 0.1 M borate buffer electrolyte (pH 9.2).

The fitting results in Figure 5.8 showed that the MnO_x film in the as-deposited state consists of a mixture of almost equal amounts of Mn_3O_4, Mn_2O_3, and birnessite, which oxidize to a film consists predominantly of Mn_2O_3 and birnessite upon biasing the film with 1.25 V_{RHE}. The XA spectra for MnO_x films biased at 1.45 V and 1.75 V are very similar to that measured for a birnessite reference standard with a possible few contents of MnO_2, which is in accordant with the theoretical analysis (*vide infra*) and other studies reported in [39, 73, 113]. At the same time, it should be mentioned that as the TEY measurements were done *ex situ*, it is more likely that the reactive species within catalysts have already been reduced prior to X-ray investigation or possibly experience minor differences. It is also possible that the contribution of MnO_2 in the MnO_x film biased at 1.45 V_{RHE} might be an artifact caused by the similarity of the MnO_2 and birnessite reference spectra.

The potential-induced spectral changes found for the *ex situ* TEY-XA spectra are very similar to the behavior observed in the *in situ* PFY-XA spectra (Figure 5.6(a) *vs.* (c)) except for the well-known intensity amplification of the L_2-edge in the PFY-XA spectra.[169] Furthermore, the negligible changes in the shape and energy positions of the L_3 and L_2 multiplets of the *in situ* PFY-XA spectra when biasing the catalysts at potentials more positive than 1.45 V_{RHE} reflects no fundamental changes in the oxidation state of MnO_x and indicates that the phase formed at positive potentials is predominantly the birnessite phase.
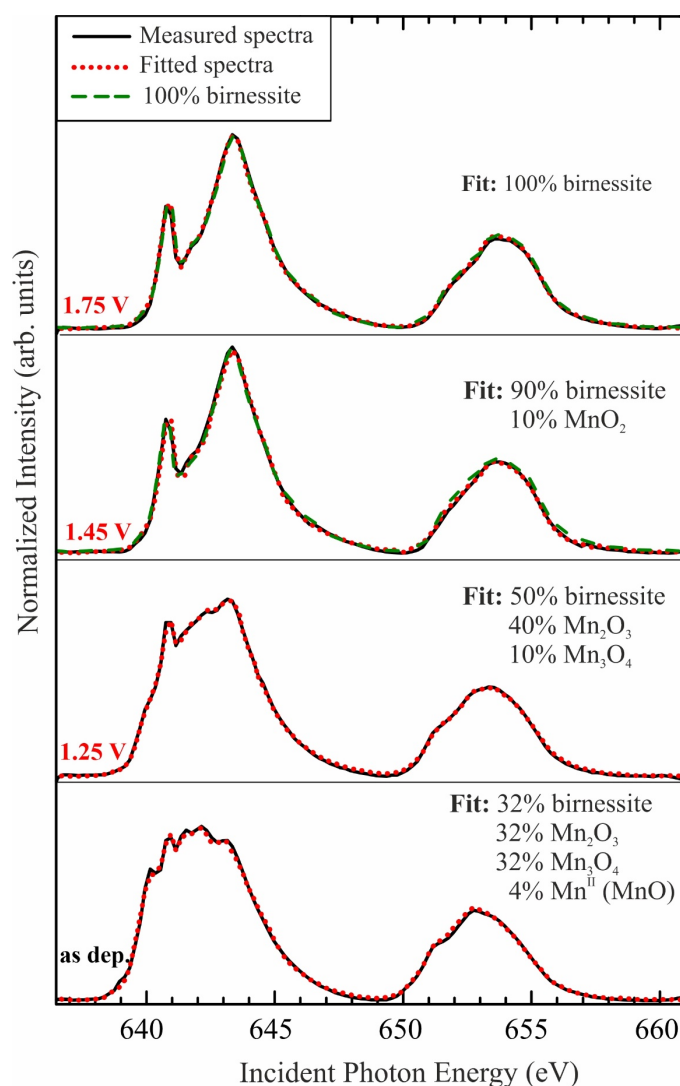
Figure 5.8. Linear combination fitting of the Mn $L_{2,3}$-edge TEY-XA spectra of the well-defined MnO$_x$ species for powder reference samples. The spectra of MnO$_x$ biased at 1.45 and 1.75 V$_{RHE}$ resemble the birnessite reference spectrum, shown in *green*. Note that the fitting is subject to approximately 5-10% uncertainty.

As previously mentioned, the PFY acquisition mode is bulk sensitive (*ca.* 10-100 nm), revealing a structural transformation of the entire MnO$_x$ catalyst into birnessite at more positive than 1.45 V$_{RHE}$. This is in line with the manganese K-edge XAS studies reported in [73]. The catalyst becomes significantly susceptible to the X-ray damage when biased by strongly oxidizing potentials, $\geq$1.75 V$_{RHE}$, revealing the evolution of a highly reactive state of MnO$_x$, which is easily reduced to soluble species by X-ray irradiation. It was shown practically as a MnO$_x$ film peeling off the Au/Si$_3$N$_4$ substrate and spectroscopically as Mn^{II} features in the XA spectrum (Figure 5.4). Indeed the degradation induced by potential simultaneously to X-ray irradiation has been

tackled by decreasing the photon flux (*ca.* 10 times lower) to allow for collecting reliable spectroscopic data as pointed out in detail in the experimental section 5.2.6. Nonetheless, even the L-edge XAS analysis did not offer the sensitivity level required to probe the actual state of this labile MnO_x, which prompted us to carry-out *in situ* RIXS measurements.

5.3.3   *In situ* RIXS measurements of MnO_x films

In situ RIXS measurements were undertaken at different applied potentials (dashed lines of the CV in Figure 5.5) for the MnO_x catalysts, as presented in Figure 5.9. In addition, RIXS spectra were collected at selected energies, which coincide with the most pronounced potential-induced changes in PFY spectra (at the dashed lines in Figure 5.6(a) or Figure 5.10), where significant changes likely occur in the electronic states of the unoccupied $3d$ states. Thus, the RIXS spectra were recorded at the photon energies (640.8, 641.6, and 643.7 eV) at the Mn L_3-edge and (651.8 and 654.2 eV) at the Mn L_2-edge. The energy of 640.2 eV was not considered in the analysis as the signal is not present at high positive potentials. The RIXS spectra are presented as energy loss features of the scattered photons when X-rays of selected energy illuminates the electrode. Therefore, it is possible to probe the inter- and intra- atomic transitions through the amount of energy absorbed in the system.

All the RIXS spectra reveal a peak at 0 eV energy loss, resulting from emitted photons that are scattered with no energy transferred to the system. These elastically scattered photons result from the generated $2p$ core-hole being filled by the excited electron, *i.e.,* photon in = photon out. While other features in the highlighted regions in Figure 5.9 at 1-5 eV and 5-10 eV are related to *d-d* excitations and charge transfer transitions, respectively.[187, 188] Moreover, there are fluorescence features observed in the RIXS spectra at the L_2-edge with energy loss positions that scale linearly with the incident photon energy (Figure 5.10). Details on the RIXS process are reported in section 2.3 and the review [150]. Such spectral features arise when an electron from the occupied $3d$ valence states fills the $2p$ core-hole (photon out $\leq$ photon in), as illustrated in the energy diagram in Figure 5.11.
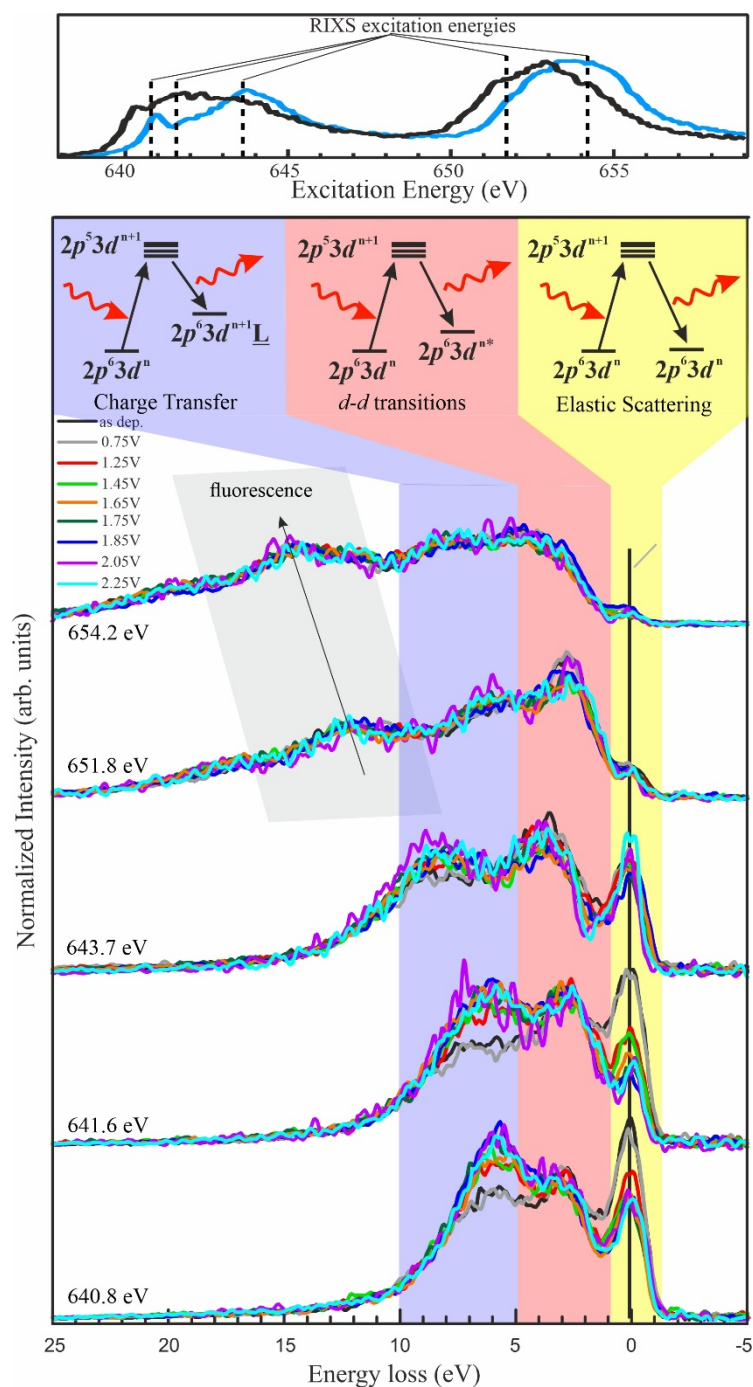
Figure 5.9. *In situ* resonant inelastic X-ray scattering spectra measured as energy loss spectra for MnO_x catalyst in 0.1 M borate buffer (pH 9.2) at 23 ± 2 °C with no potential applied (*black*) and at 0.75 (*gray*), 1.25 (*red*), 1.45 (*light green*), 1.65 (*orange*), 1.75 (*dark green*), 1.85 (*blue*), 2.05 (*violet*) and 2.25 V_{RHE} (*turquoise*). All the spectra were background corrected and normalized to an overall integrated intensity of 1. RIXS spectra are separated vertically according to the PFY-XA energies in the top panel at the *black* dashed lines for MnO_x in the as-deposited state (*black*) and at 1.75 V_{RHE} (*blue*). Highlights in the background describe the different RIXS features with simplified energy diagrams at the top. A 2D RIXS maps for MnO_x in the as-deposited state and at 1.65 V $_{RHE}$ are shown in Figure 5.10.
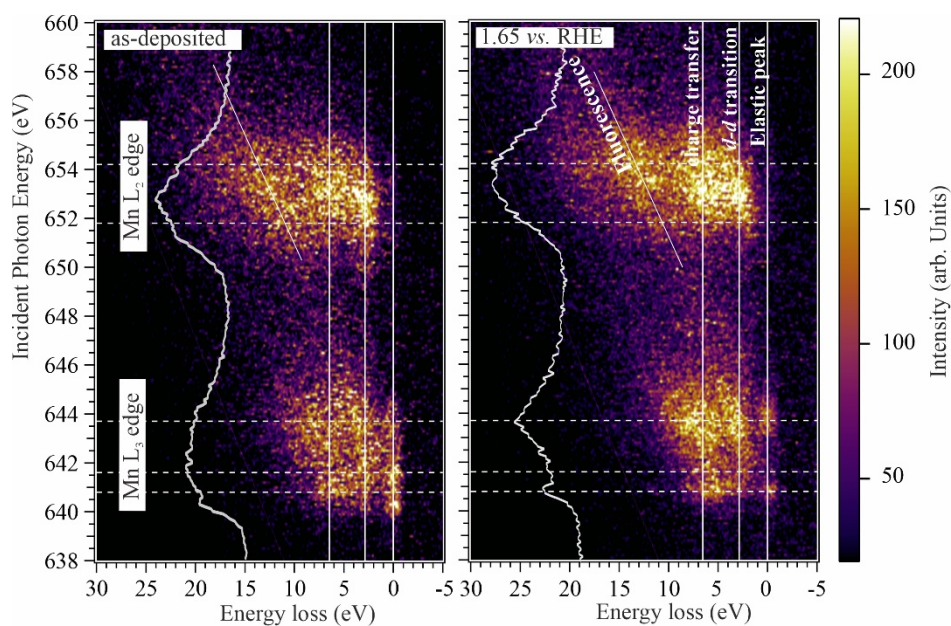
Figure 5.10. 2-D experimental RIXS mapping of the MnO$_x$ catalyst in contact with 0.1 M borate buffer (pH 9.2) in the as-deposited state (left) and at a potential of 1.65 V$_{RHE}$ (right). The map is a plot of the energy-loss of the scattered photons against the incident photon energy. Vertical solid lines indicate the elastically scattered photons at 0 eV energy loss, *d-d* transition, and charge transfer transition peaks; horizontal dashed lines indicate the energies used to collect higher-quality RIXS spectra in Figure 5.9. By integrating the intensity of the emitted photons at each incident photon energy, PFY-XA spectra will be obtained, as showed in white in both images.
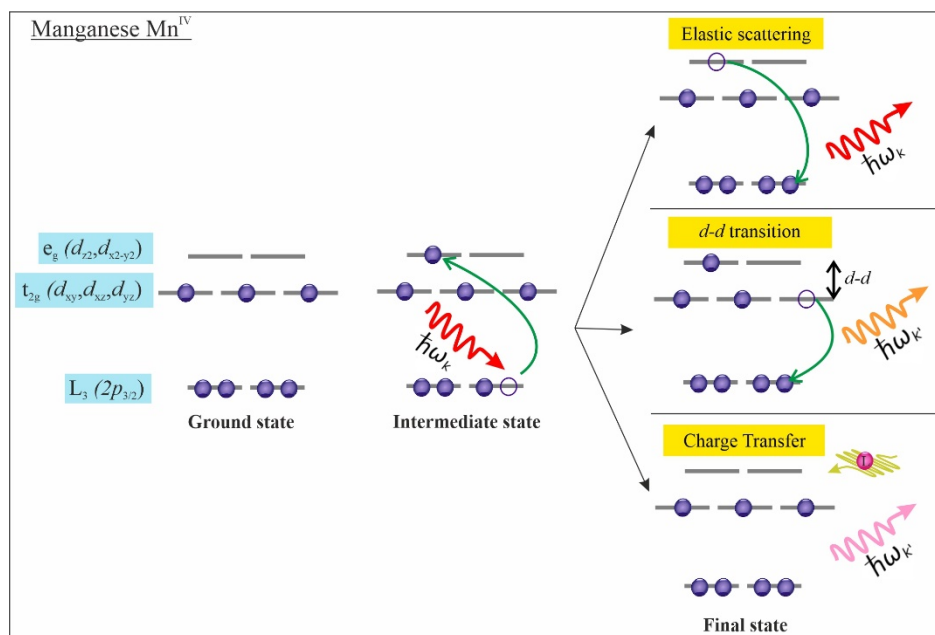
Figure 5.11. The ground, intermediate, and the final electronic state of a typical d^3 transition metal ion (*e.g.,* Mn^{IV}) in octahedral symmetry upon X-ray irradiation, showing transitions at the L$_3$-edge (2p$_{3/2}$). The final state shows the elastic scattering, *d-d* transition, and charge transfer transitions.

The RIXS spectra reveal noticeable features at 3-4 eV and 6-8 eV (Figure 5.9), independent of the excitation energy and assigned to *d-d* transition excitations and CT transitions, respectively. The latter is attributed to electron transfer between the ligand, O, and metal, Mn.[260, 261] The most significant potential-induced changes in the relative peak intensities are found in the RIXS spectra collected at 640.8, 641.6, and 643.7 eV (Figure 5.9). These excitation energies are in the vicinity of the main features for all Mn oxidation states of interest (Mn^{II}, Mn^{III}, Mn^{IV}), as shown in the PFY-XA spectra (Figure 5.6), which allows for a high cross-section of X-rays with these species. Distinctive differences in the RIXS spectra are revealed when the potential is changed.

Interestingly, the applied potential has a negligible change in the energetic positions of the *d-d* transition and CT peaks (Figure 5.9), suggesting that the energies required for those transitions are the same for all Mn oxidation states involved. Furthermore, the fixed energy position of the *d-d* transition peak at *ca.* 3 eV reflects no significant change in the bandgap between the valence and conduction band of the catalyst during water oxidation. Simultaneously and most importantly, by biasing the MnO_x films with different potentials, a significant change in the relative intensities of the RIXS features can be observed. Figure 5.12 shows the relative intensity of the RIXS features associated with elastics scattering (0 eV energy loss), *d-d* transitions (3-4 eV energy loss), and CT transitions (6-7 eV energy loss) as a function of potential applied to the MnO_x film. The intensity of each component was determined by fitting a Gaussian curve then normalized to the intensity of the same feature obtained at the applied potential beyond which the XAS displayed no further change (i.e., 1.45 V_{RHE}).

More concisely, the RIXS data shows that for the MnO_x in the as-deposited state and after biasing with 0.75 V_{RHE}, the most prominent excitation happens is due to the *d-d* transition while the contribution of the CT transition is lower (Figure 5.9). While biasing the MnO_x with more positive potentials than 1.45 V_{RHE}, the CT feature in the RIXS spectra is greatly enhanced, and the elastic peak suppressed while the *d-d* transition feature remained nearly the same (Figure 5.12). These changes in the features are most apparent for RIXS measured at excitation energies of 640.8 and 641.6 eV and saturate at approximately 1.75 V_{RHE}. This can also be observed from the RIXS intensities ratio for the features associated with CT to the *d-d* transitions, which increases with increasing the applied potential at different excitation energies (Figure 5.13). The potential (1.75 V_{RHE}) exceeds the value at which saturation of the XAS spectra is achieved (1.45 V_{RHE}), which implies that further changes regarding the electron transfer between ligand, O, and metal, Mn within the catalyst are happening even after settling the Mn oxidation state. To get a more in-depth insight into understanding this experimentally observed phenomenon, theoretical calculations were applied.
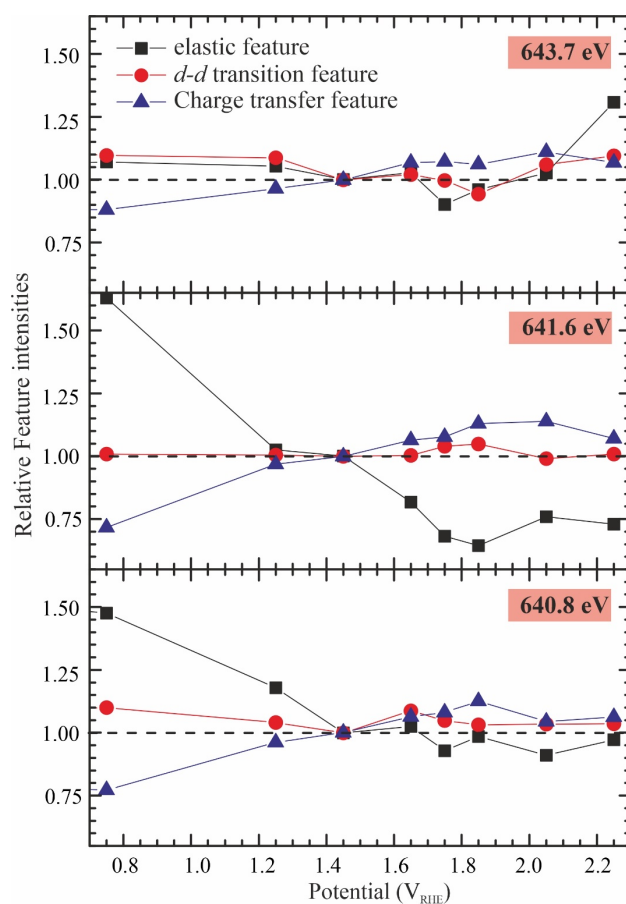
Figure 5.12. Relative peak intensity of the RIXS features assigned due to elastics scattering (*black* squares), *d-d* transitions (*red* circles), and charge transfer transitions (*blue* triangles) obtained for excitation energies of 640.8 (bottom panel), 641.6 (middle panel), and 643.7 (top panel) of the RIXS spectra in Figure 5.9. All values were normalized to the respective feature intensity of the RIXS spectrum at an applied potential of 1.45 V_{RHE}. The dashed lines mark a relative intensity of 1.
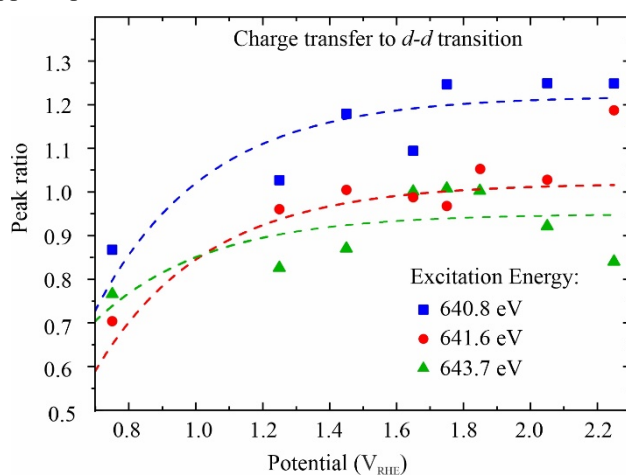
Figure 5.13. The ratio of the RIXS intensities for the features associated with charge transfer (6-7 eV energy loss) and *d-d* transitions (3-4 eV energy loss) measured at the excitation energies of 640.8 (*blue* squares), 641.6 (*red* circles), and 643.7 eV (*green* triangles). Dashed lines serve only as virtual guides for the trend.

5.4   Theoretical Calculations of XA/RIX Spectra

Computation of RIXS and XA spectra in this section was performed by Dr. Travis Jones, from Fritz-Haber-Institute der Max Planck Gesellschaft to confirm and to provide a further explanation of experimental spectra regarding the origins of the apparent increase in the intensity of the CT feature in RIXS spectra with increasing the potential applied to the MnO_x film up to 1.75 V_{RHE} then saturation occurs. RIXS and XA spectra were computed using a standard configuration interaction model within the QUANTY package to take into account hybridization between the metal and its ligands and to control charge transfer energy (Δ), and the Mn-O bond length via the extent of orbital wave function overlap, known as "hopping integral (V_{eg})."[262-264] The calculations were undertaken for Mn^{IV} in a birnessite geometry (octahedral geometry with $3d^3$ Mn electronic configuration), mimicking the obtained experimental results, which showed the full transformation of the MnO_x catalyst to the birnessite phase when biased by positive potentials $\geq$1.45 V_{RHE}. A more detailed theoretical analysis for this study can be found in [148].

The efficiency of charge transfer in first-row transition metal complexes is strongly correlated to orbital hybridization.[265] In particular, this interdependence has been confirmed for lanthanum strontium manganite, where charge transfer is facilitated upon an increase in the hybridization of the Mn $3d$ and O $2p$ orbitals.[266] On this basis, the potential-induced changes in the *in situ* RIXS spectra of MnO_x reported herein can be further rationalized in terms of the enhanced hybridization of the metal and oxygen states at positive potentials. Thus, the theoretical analysis considered varying the hybridization degree of the Mn $3d$ and O $2p$ orbitals. *Dr. Travis Jones* reported that "*this variation can be achieved by altering the energy difference between the two orbitals via the charge transfer energy (Δ), and the Mn—O bond length via the extent of orbital wavefunction overlap (the O—Mn hopping integral, V_{eg}). A decrease in Δ induces greater orbital hybridization, as does an increase in V_{eg}.*"[148] The energy cost associated with a ligand to metal charge transfer, $\Delta = E(d^{(n+1)} L) - E(d^n)$.

By simulating the XA spectrum of Mn^{IV} in a birnessite geometry, all the experimentally attributed features were reproduced when the hybridization between Mn $3d$ and O $2p$ orbital is considered, as clearly indicated in Figure 5.14. When the hybridization was excluded from the model, the resonance peak at the low energy side of the L_3 edge absorption spectrum does not manifest (*gray* curve in Figure 5.14(a)); however, it is captured when hybridization is incorporated in the model. The shape of the calculated absorption spectra is relatively insensitive to the exact values of Δ. Increasing or decreasing Δ by as much as 2 eV only slightly affects the spectral shape (*cf. red, blue*, and *green* curves in Figure 5.14(a)). Notably, the calculated spectra are consistent with the measured TEY-XA spectrum of a birnessite reference sample and the *ex*

situ TEY-XA spectrum and *in situ* PFY-XA spectrum for the electrodeposited MnO$_x$ film biased at 1.75 V$_{RHE}$ as shown in Figure 5.14(b-d).
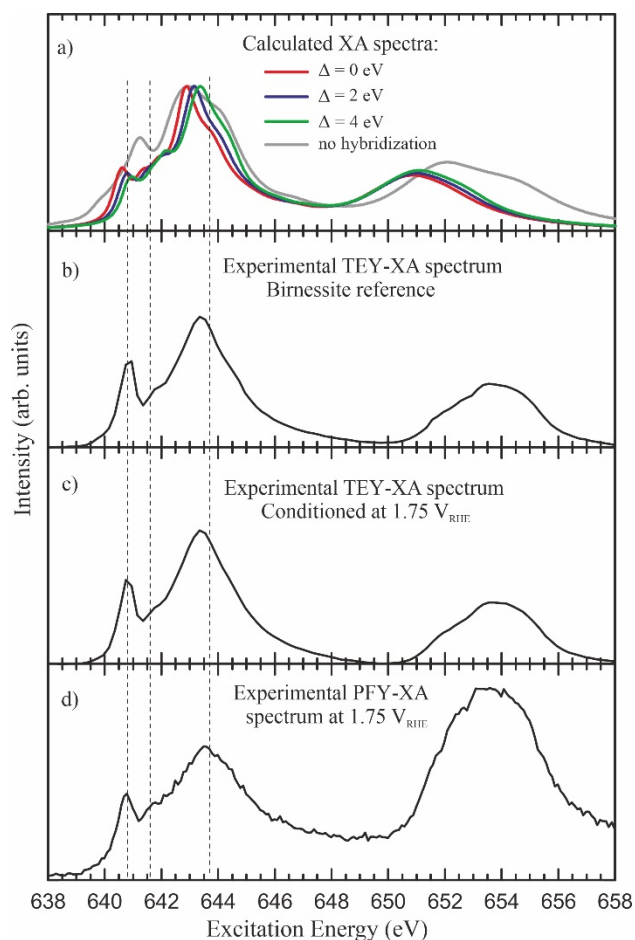

Figure 5.14. Absorption spectra at the Mn L$_{2,3}$-edge. Panel (a) shows calculated XA spectra for Mn^{IV} in birnessite geometry for three different values of the charge transfer energy Δ - controlling the hybridization – and the spectrum in *gray* is calculated with suppressed hybridization. Panel (b) shows an experimental TEY-XA spectrum for a birnessite reference. Panels (c) and (d) present the experimental *ex situ* TEY-XA spectra of the deposited MnO$_x$ film conditioned at 1.75 V$_{RHE}$ and *in situ* PFY-XA spectrum during biasing with a potential of 1.75 V$_{RHE}$, respectively. The dashed lines denote the energies at the Mn L$_3$ edge considered for the experimental and theoretical RIXS spectra.

In contrast to the absorption spectrum, the simulated RIXS spectra can only reproduce the experimental RIXS spectra when hybridization is included in the theoretical model. The RIXS peak positions are susceptible to the hybridization parameters (Δ and V$_{eg}$). Figure 5.15 shows the simulated RIXS spectra calculated at the same excitation energies as for the experimental RIXS spectra (*i.e.,* at 640.8, 641.6, and 643.7 eV) with varying Δ values (*red*, *blue,* and *green* curves in Figure 5.15), which varies the hybridization degree between the Mn and O orbitals. For qualitative comparison to the simulated RIXS spectra, an experimental RIXS spectra (*black*

dashed curves) were added to Figure 5.15 at the three excitation energies, which are an average spectrum of RIXS spectra measured at 1.45, 1.65, 1.75, 1.85, 2.05, and 2.25 V_{RHE}. This was done to improve the signal to noise level of the added experimental spectra.
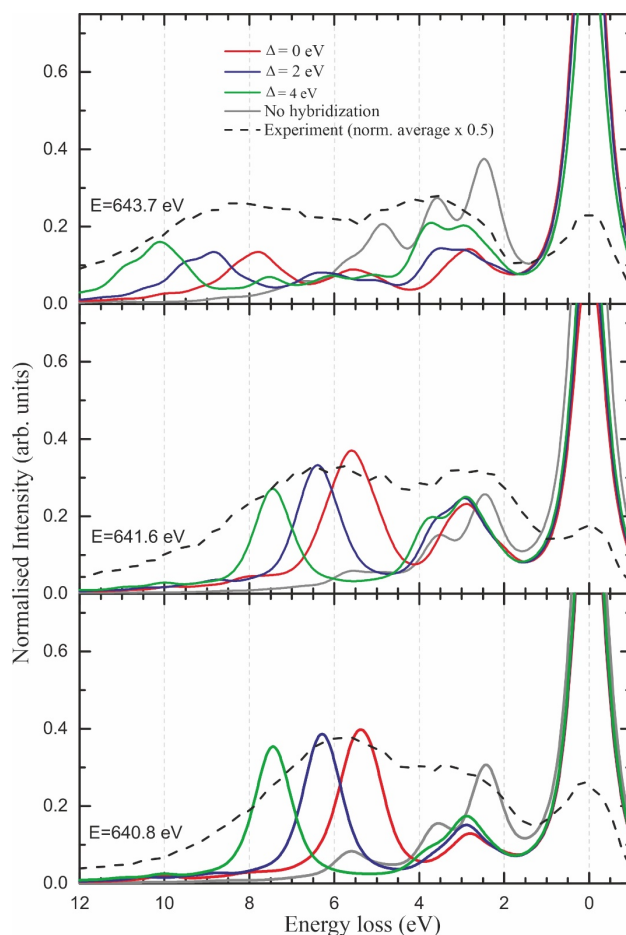

Figure 5.15. Theoretical RIXS spectra (solid lines) calculated with a charge transfer energy of $\Delta = 0$ (*red*), 2 (*blue*), and 4 eV (*green*) with $V_{eg} = 2.6$ eV in all cases, as well as for suppressed hybridization of the Mn and O orbitals (*gray*). Experimental RIXS spectra are overlaid (dashed *black* lines) for excitation energies 640.8, 641.6, and 643.7 eV as specified. All spectra were normalized to an overall integrated intensity of 1.

Importantly, a feature at energy above 5 eV can only pronounce when charge transfer energy Δ is applied and disappeared when the hybridization is excluded (*gray* curves in Figure 5.15), keeping only the elastic feature and a set of features at energies typical of *d-d* transitions (*ca.* 2 to 5.5 eV). The disappearance of the feature above 5 eV when hybridization is suppressed indicates that the experimental feature at *ca.* 6 eV arises from the CT feature (Figure 5.15).

Moreover, there is an absolute shift in the CT feature to *ca.* 8.5 eV energy loss for excitation energy of 643.7 eV, which is concordant with the experimental data. In contrast to experimental RIXS spectra, there is a relative energy shift for the CT feature of the simulated RIXS spectra when the CT energy (Δ) value is changed. Reducing Δ not only increases the intensity of the CT peaks but also shifts the peak position to lower energy loss (Figure 5.15). The energetic position of the CT feature detected experimentally at *ca.* 6 eV for 640.8 or 641.3 eV excitation can be fairly reproduced theoretically with a CT energy between $\Delta = 0$ and 2 eV (*red* and *blue* curves in Figure 5.15), with applying more refinement in the Δ values. Importantly, the energetic position of the *d-d* transition feature is almost the same with varying Δ and located at *ca.* 3 eV energy loss, which is consistent with the experimental spectra. The refinement of the Δ values should be coherent with the observed experimental changes in the intensity of the CT feature. The experimental RIXS spectra show that the relative intensity of the CT feature increased by *ca.* 8-10 % upon increasing the applied bias from +1.45 to +1.75 V_{RHE} (*cf.* Figure 5.9 and Figure 5.12). At the same time, as the intensity of the CT feature increased, the elastic feature subsided while the *d-d* transition feature intensity was only minimally influenced by increasing the potential applied. Such trends are reproduced theoretically by decreasing Δ values along with increasing the hopping integral (V_{eg}). Increasing V_{eg} induces greater hybridization, *viz.* a smaller energy difference between the Mn $3d$ and O $2p$ orbitals along with a contraction in the Mn—O bond length (Figure 5.16).

The simulation started with a value of $V_{eg} = 2.6$ eV for Mn^{IV},[262] together with $\Delta = 1.9$ eV results in an energy position of the CT peak (*ca.* 6 eV energy loss) similar to that obtained experimentally for the MnO_x film biased at 1.45 V_{RHE} which shows the initial birnessite structure. The simulation mimics the experimental spectra when the CT energy is reduced on the order of an electron volt (approximately 0.8 eV, from 1.9 to 1.1 eV), with a slight increase of V_{eg} by a few hundred meV (*ca.* 0.2 eV, from 2.6 to 2.8 eV). This yielded an increase in the relative intensity of the CT peak by 8-10 % as observed experimentally upon changing the applied potential from 1.45 to +1.75 V (Figure 5.9). Hence, the simulated spectra can reproduce all the observed trends of the charge transfer, *d-d* transition, and the elastic feature. Such changes indicate the removal of electron density from the O ligand shell. Crucially, the ligand to metal hybridization or O $2p$ and Mn $3d$ orbital hybridization is strongly correlated with any decrease of Δ and/or increase of V_{eg}. The decrease of Δ is associated with the formation of O $2p$ hole states, which would give rise to a formally O^{I-} species of the oxygen ligand ($d^4\underline{L}^1$), rather than O^{II-} ($d^3\underline{L}^0$), where d^3 is the ionic ground state of the Mn^{IV} ion and $\underline{L}$ is a ligand hole formed by charge transfer to the metal.

The RIXS results reported herein correlate with prominent mechanistic proposals for water

oxidation by the $CaMn_4O_x$ cluster in photosystem II,[267-269] as well as *in situ* XPS and NEXAFS studies on amorphous iridium oxide electrocatalysts, [270] with the generation of O^- species having been suggested to precede the O–O bond formation in both cases.
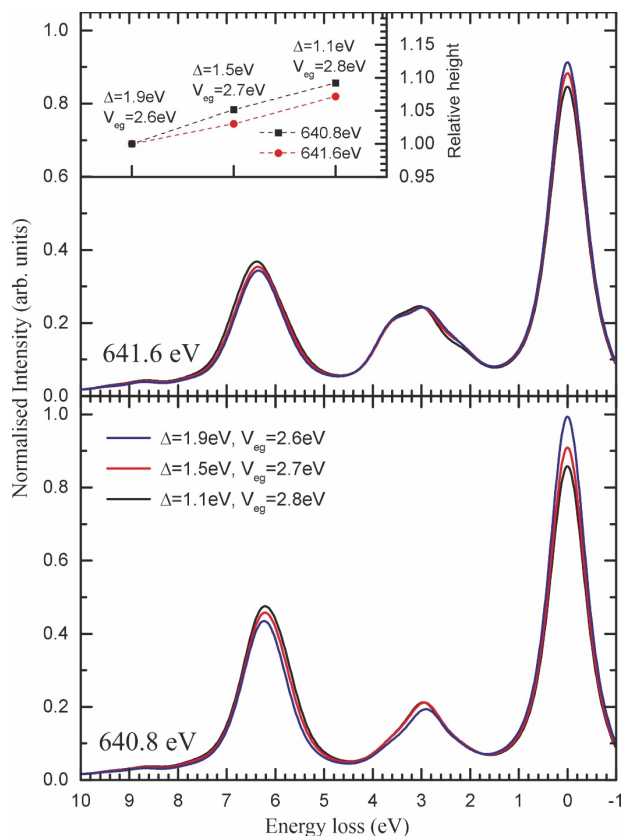

Figure 5.16. Theoretical RIXS spectra calculated for two excitation energies (641.6 eV in the top panel and 640.8 eV in the lower panel) with varying both the charge transfer energy Δ and the hopping integral V_{eg}. The inset in the top panel shows the ratio of the relative increase of the charge transfer feature compared to the calculated feature intensity for Δ = 1.9 eV and V_{eg} = 2.6 eV.

As a result of the refinement of the CT energy and hopping integrals values used to fit the experimental results, the orbital's structure involved in the XAS and RIXS excitations may be interpreted. In the case of XAS, simulations were undertaken by including electronic excitations into either the Mn $3d$ σ (e_g) or π (t_{2g}) orbitals to show precisely to which orbital the electron from Mn $2p$ will be excited. Figure 5.17(a) shows the simulated absorption spectra, where the resonance peak at the low energy side of the L_3 edge in the initial birnessite absorption spectrum (*ca*. 640.8 eV) seems to be related to an electronic transition into the empty $3d^3$ (e_g) - σ orbitals of Mn^{IV} in an octahedral arrangement. Figure 5.17(b) shows that the CT peak at the dashed line observed in the RIXS spectra at the two excitation energies (640.8 and 641.6 eV) is attributed to electron transfer from O-ligand to Mn σ orbitals. Therefore, theory indicates a ligand-to-metal charge transfer from an O $2p$ into an Mn $3d$ orbital. The predominance of the σ orbitals in charge

transfer can be explained by the higher overlap of the Mn and O σ orbitals compared to π orbitals.

Based on the theoretical results reported herein, we conclude that by increasing the potential applied on the MnO_x samples between 1.45 V_{RHE} and *ca.* 1.75 V_{RHE}, the ligand hole character increases. This oxygen hole character appears at potentials 300 mV more positive than the potential required to achieve the full transformation of the MnO_x film into birnessite (*ca.* 1.45 V_{RHE}). Eventually, the Mn $L_{2,3}$-edge RIXS/XAS spectroscopic data can be related directly to the mechanistic electrochemical study controlled by the *in situ* analysis herein.
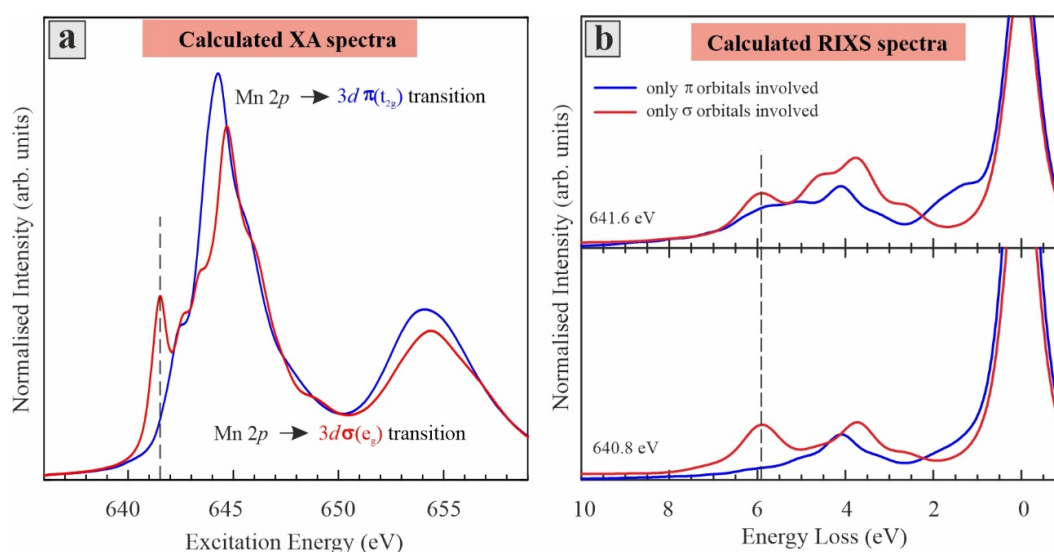
Figure 5.17. Theoretical spectra for Mn^{IV} in birnessite geometry using parameters from literature allowing or disallowing electronic transitions into either π (t_{2g}) (*blue*) or σ (e_g) (*red*) orbitals for (a) Mn $2p \rightarrow 3d$ XAS spectra and (b) RIXS spectra calculated for 641.6 eV (top panel) and 640.8 eV (bottom panel). The first prominent XA feature and the CT feature at the dashed lines in (a) and (b), respectively, can be related to transitions into σ (e_g) orbitals (*red*).

5.5 Conclusion

The *in situ* study pertains to the transformations and electrochemical analysis of the electrodeposited MnO_x water oxidation electrocatalysts induced by conditioning at mild and strongly oxidizing potentials under turnover conditions using *in situ* soft XA and RIX spectroscopy. XAS is highly sensitive to the unoccupied states and was employed to demonstrate the evolution of the Mn oxidation state under applied potentials up to 2.25 V_{RHE}. RIXS is a spectroscopic technique that probes the valence excitations and enables analysis of elementary excitations, like *d-d* excitations and charge transfer transitions, which are not accessible with other techniques. The experimental results are supported by theoretical simulations that converge into an effective, robust modus operandi for probing electrocatalytic mechanisms.

Quantitative analysis of the different MnO_x phases present in each catalyst film as a function of potential reveals that the MnO_x film in the as-deposited state consists of a mixture of almost equal amounts of Mn_3O_4, Mn_2O_3, and birnessite, which oxidize upon biasing the film with 1.25 V_{RHE} to a film which consists predominantly of Mn_2O_3 and birnessite. Importantly, *in situ* PFY-XA spectra revealed a full transformation of the MnO_x film into birnessite state at *ca.* 1.45 V_{RHE}, whereas *in situ* RIXS analysis revealed changes in the electronic state of MnO_x at potentials up to 1.75 V_{RHE}, which could not be detected using XAS alone. RIXS showed that the charge transfer feature intensifies until the MnO_x film biased at 1.75 V_{RHE}. Beyond this potential, a stabilization of the RIXS features occurs, which can be directly coupled to the water oxidation happening in this regime (Figure 5.5). It is worth noting that this stabilization of RIXS data at 1.75 V_{RHE} corresponds well with the water oxidation by MnO_x electrocatalysts in the 1.70-1.75 V_{RHE} range, as studied by *Bonke et al.* in terms of Fourier transformed alternating current voltammetry.[142]

The experimental and theoretical results of the study herein have shown that:

1)   The Mn oxidation state in the MnO_x film increases under applying more positive potential until the film transforms into the birnessite state at *ca.* 1.45 V_{RHE}, then no further change in the Mn oxidation state occurs up to 2.25 V_{RHE}.

2)   No evidence has been seen for including Mn species with higher oxidation states than 4+ in the water oxidation electrocatalysis.

3)   By applying a more positive potential to the MnO_x films, the hybridization degree of Mn 3*d* and O 2*p* orbitals increases (up to 1.75 V_{RHE}).

4)   The continuous change in the RIXS spectra between 1.45 and 1.75 V_{RHE} suggests an extent changes in orbital hybridization between Mn 3*d* and O 2*p*, up to 1.75 V_{RHE}, even after saturating the Mn oxidation state at 4+. It reveals that O-to-Mn charge transfer is needed to bolster fast water oxidation catalyzed by MnO_x achieved at 1.75 V_{RHE} and did not enhance by applying higher potentials (up to 2.25 V_{RHE}). The formation of an O⁻ species associated with ligand-to-metal charge transfer is believed to be of crucial importance for efficient electrocatalytic water oxidation.

As a result, an essential step toward the interaction between an electrocatalyst and water electrooxidation intermediates was experimentally probed. *In situ* soft XAS, together with the RIXS study, consolidate into a powerful spectroscopic tool for advanced analysis of electrocatalytic phenomena, and formation of O⁻ species, play a key role in OER catalysis.
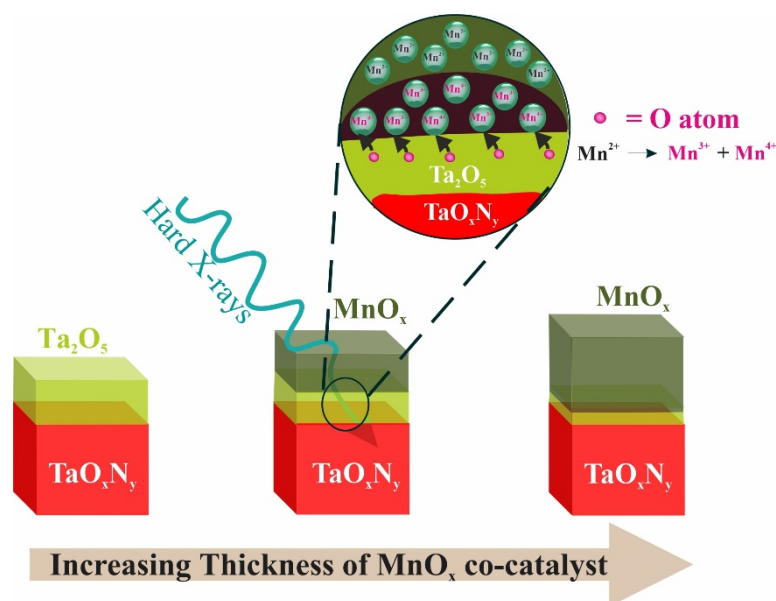
Chapter 6

Chemical Composition and Electronic Structure of the MnO_x/TaO_xN_y Interfaces

Portions of this chapter have been prepared for publication:

"Interfacial Spectroscopic Study of MnO_x/TaO_xN_y Catalytic Films for Water Oxidation analyzed by Hard X-ray Photoelectron Spectroscopic Technique."

Maryam N. Shaker, Marco Favaro, Rowshanak Irani, Paul Plate, Fatwa Abdi, Thomas Götsch, Roel van de Krol, David Starr.

Interfacial spectroscopic study of MnO_x/TaO_xN_y catalytic films by Hard X-ray photoelectron spectroscopy to investigate structural and compositional changes as a function of MnO_x overlayer.

6.1   Introduction

In the last two chapters, manganese oxides have been studied *ex situ* and *in situ* as an independent electrocatalyst for oxygen evolution reaction in an electrochemical cell. Converting an electrochemical cell into a photoelectrochemical cell requires developing photoelectrodes that drive water splitting efficiently under visible light irradiation. As pointed out in section 1.5.4, potential photoanode should have a relatively small bandgap, chemically stable in the dark and under light illumination, suitable band position to straddle for OER, and HER with low overpotential, efficiently transfer charges to the surface of photoelectrodes for water oxidation/reduction, and low cost.[13, 29-31, 34, 37] Many semiconductors, like WO_3, [121, 122] Fe_2O_3, [123] $BiVO_4$,[124, 125] and TaON, [126-133] have been studied as photoanodes for water oxidation. However, they either suffer poor charge separation/ slow rate of charge transfer processes or exhibit low resistance to photo-corrosion under visible light. [121, 123, 134-136] To address these limitations, metal oxide co-catalysts deposited on the semiconducting photoanode surface can enhance the overall water splitting efficiency. On the one hand, the co-catalyst protects the semiconductor surface, so it improves its stability against (photo-)corrosion [34, 130, 137], and on the other hand, it assists in the kinetics of the interfacial charge transfer, *i.e.,* reduces the activation barrier to charge transfer.[14, 34, 138]

In this chapter, manganese oxide is studied as a water oxidation co-catalyst to tantalum oxynitride (TaON), being the semiconducting photoanode material. As pointed out before that, MnO_x is a well-known efficient water oxidation catalyst, which is inexpensive and earth-abundant.[40, 72, 74, 98, 232, 271] While TaON has spurred much attention as a promising photoanode semiconductor for water-splitting devices.[126-133] TaON is an n-type semiconductor of a bandgap of 2.4 eV[272, 273], which makes it an efficient photoabsorber under visible light ($\lambda \leq 500$ nm) irradiation.[274] TaON has an appropriate band edge positions to straddle the OER and HER since the valence band (VB) edge is more positive than the oxidation potential (O_2/H_2O), and the conduction band (CB) edge position is more negative than the reduction potential (H^+/H_2), respectively, as shown in Figure 6.1. So, theoretically, TaON has the potential to produce O_2 and H_2 with no external applied bias.[274-276] On the downside, TaON can suffer self oxidative-deactivation upon irradiation, forming N_2 gas and the inactive Ta_2O_5, which is a poorly visible light absorber because of the large bandgap (E_g =3.9 eV). [130, 135, 275] The formation of an oxide layer (Ta_2O_5) at the TaON surface hinders the transfer of the photogenerated holes from the TaON to the surface at which water oxidation takes place since there is a mismatch in the VB edge levels between Ta_2O_5 and TaON, [130] as illustrated in Figure 6.1. Indeed this limits the photocatalytic activity.
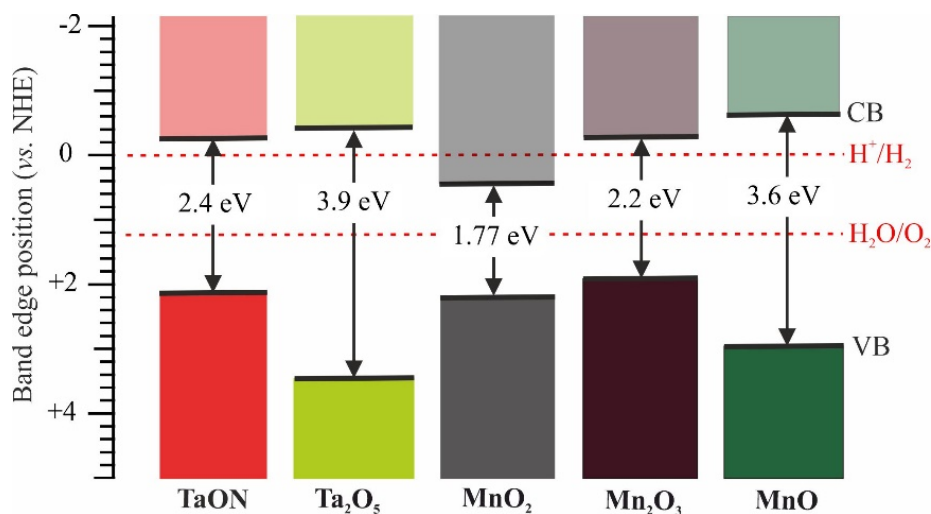
Figure 6.1. The absolute valence and conduction band edge positions of TaON, Ta$_2$O$_5$, MnO$_2$, Mn$_2$O$_3$, and MnO measured with ultraviolet photoelectron spectroscopy in a vacuum state. The dashed *red* lines are hydrogen (H$^+$/H$_2$) and oxygen evolution potentials (H$_2$O/O$_2$). Data on the band-edge values are taken from [36, 275, 277, 278].

Abe et al. reported that the TaON photoanode showed a significant enhancement in the incident photon to current efficiency (IPCE) of *ca.* 76% (at 400 nm at 0.6 V *vs.* Ag|AgCl) after loading of IrO$_2$.nH$_2$O nanoparticles as a co-catalyst for water oxidation.[126] *Higashi et al*. revealed that highly dispersed CoO$_x$ nanoparticles on the TaON photoanode efficiently scavenge the photogenerated holes transfer and suppress the self-oxidative deactivation of the TaON surface, which results in a stable photocurrent and splitting of water at a relatively low applied potential.[135] Furthermore, an improvement in water-splitting performance by electrodepositing MnO$_x$ onto TiO$_2$/TaON films was also reported by *Gujral et al*. [130]. Therein, a 7-fold enhancement in terms of photocatalytic activity was achieved. However, the reason for the catalytic activity improvement is yet not fully understood.

As the VBM of MnO$_x$ is slightly more positive than that of n-type TaON (as schematically shown in Figure 6.1), we hypothesized that by depositing ultrathin MnO$_x$ films (few nms) on TaON, the photo-generated holes could be efficiently utilized to oxidize water, and enhancement of the hole transfer could be achieved, as demonstrated in Figure 6.2. Also, suppression of self-deactivation of TaON might increase with the MnO$_x$ overlayer. Hence, in this chapter, MnO$_x$ layers are uniformly deposited atop the TaON by atomic layer deposition, then a detailed interfacial analysis of the MnO$_x$/TaON is carried out using hard X-ray photoemission

spectroscopy (HAXPES). The chemical composition and the electronic structure changes at the interface between the TaON photoanode and MnO_x overlayer will be investigated as a function of the MnO_x overlayer thickness. Samples are characterized in terms of *voltammetry*, *X-ray diffraction* (XRD), *transmission electron microscopy* (TEM), *energy dispersive X-ray* (EDX). Numerical calculations on a model system of MnO_x/TaON were undertaken to support the experimental results.
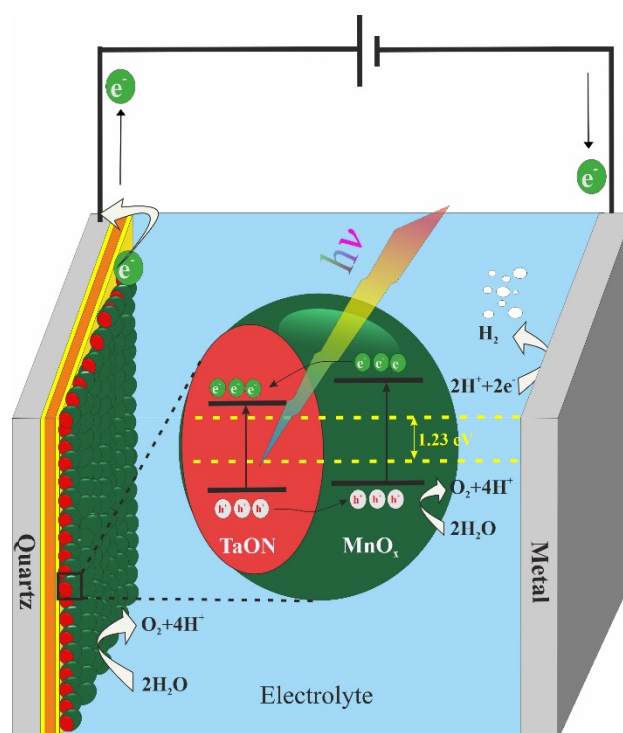

Figure 6.2. A schematic diagram for the possible charge transfer processes during oxygen evolution (O_2/H_2O) happening at the MnO_x overlayer film onto TaON photoanode and hydrogen evolution (H^+/H_2) reactions at a metal cathode.

6.2   Experimental Section

6.2.1   Sample Preparation

All the samples investigated in this study were entirely prepared at the solar fuel institute of the HZB in the form of thin films with the following steps (see Figure 6.3):
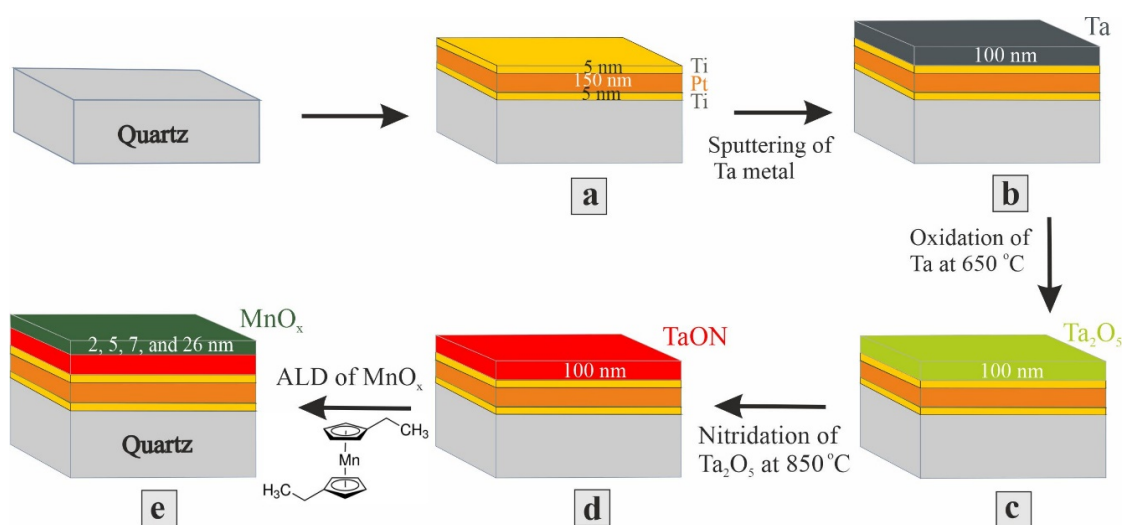
Figure 6.3. Schematic illustration of the sample preparation

(a) Evaporation of the conductive layers of Ti-Pt-Ti on quartz, (b) Sputtering of 100 nm of Tantalum metal (c) Oxidation of Ta at 650 °C, (d) Nitridation of Ta_2O_5 at 850 °C, transforming it into TaON, (e) Atomic layer deposition of MnO_x of different thicknesses (2, 5, 7, and 26 nm) on the TaON photoanode.

6.2.1.1 Tantalum Sputtering

Sputtering of Tantalum (Ta) was done at room temperature using DC magnetron homemade sputtering and evaporation system under high vacuum $6 \cdot 10^{-7}$ mbar.[279] Tantalum metal (99.95% purity) was sputter-coated on 5 nm Titanium – 150 nm platinum – 5 nm Titanium (Ti-Pt-Ti) on a quartz substrate. The conductive layers of Ti-Pt-Ti are necessary to conduct the hard X-ray photoemission spectroscopic measurements. Ti-Pt-Ti layers were deposited first by electron beam evaporation on quartz prior to the sputtering of Ta. Ti was added to assure proper adhesion between Pt with Quartz, as well as Pt with Ta. Sputtering of 100 nm of Ta metal on the Ti (Figure 6.3(b)) was operated at 235 W DC electric power for 67 s.

6.2.1.2 TaON thin film preparation

TaON thin films were prepared according to the recipe of *de Respinis. et al.* [279] As illustrated schematically in Figure 6.3(c-d), Ta is oxidized in a glass tube furnace filled with air at 650 °C for 5 hours to form the Ta_2O_5 film. Followed by nitridation at 850 °C for 22 hours under a flow of ammonia (NH_3), H_2 (g), and H_2O (g) simultaneously to form the β-TaON phase. Based on the phase diagram derived by *Swisher and Read* [280], which shows conditions to reach Ta_2O_5, TaON, and Ta_3N_5 phases, the partial pressure ratio of $P(H_2O)/P(H_2)$ was kept constant at 0.03, while the

partial pressure ratio of $P(NH_3)/P(H_2)^{3/2}$ used is 0.09 at which a pure phase of β-TaON is reached, as confirmed by XRD measurement.

6.2.1.3 Atomic layer deposition of MnOₓ

Atomic layer deposition (ALD) is a deposition method based on the sequential deposition of chemical precursors, layer-by-layer growth.[79, 80] It is generally viewed as an excellent deposition method for producing uniform coating films of a specified thickness on the atomic scale. Here we use ALD to deposit MnO_x catalytic films of controlled thicknesses onto high surface area electrodes.[79, 80] The ultra-thin MnO_x films used in this study were grown on the TaON substrate using a home-built, hot-wall atomic layer deposition reactor setup.[281] In the ALD setup analysis chamber, the TaO_xN_y substrates were mounted on a sample holder attached to a heater. The substrate temperature was kept fixed at 125 °C during the atomic layer deposition of MnO_x onto TaON. The Mn-precursor used for MnO_x film deposition was Bis(ethylcyclopentadienyl) manganese (II) shown in Figure 6.3(e), which was preliminarily stored at 80 °C while the oxidizing agent was Millipore water (18.2 MΩ). The thickness of the MnO_x film depends on the number of deposition cycles. One deposition cycle includes opening the Mn-precursor for 1.5 s followed by pumping to lower pressure 5×10^{-6} mbar, then purging with an Argon pulse for 0.1 s, then flushed with deionized water for 1.5 s.

After MnO_x deposition, *in situ* spectroscopic ellipsometry was used to estimate the MnO_x thickness on a silicon (Si) substrate as a function of deposition cycles. The Si substrate was placed together with the TaO_xN_y substrates during deposition. The thickness growth per cycle of the MnO_x layer was estimated to be 1.3 Å/cycle. However, the exact MnO_x thickness on the TaO_xN_y substrate may differ from that on the Si substrate since different interactions between the MnO_x film with different underlying substrates may lead to different morphologies of the MnO_x film. Nevertheless, reliable MnO_x thicknesses on TaO_xN_y were measured later by the TEM technique.

6.2.2 Experimental Methods

Hard X-ray photoelectron spectroscopy (HAXPES) studies were performed on a series of different thicknesses of MnO_x on TaO_xN_y samples at room temperature and under ultra-high vacuum conditions ($\sim 10^{-9}$ mbar). All HAXPES core levels spectra were measured at two excitation energies, 2003 eV and 4000 eV, to obtain information from different probing depths. For each excitation energy, five investigated samples were measured as a function of MnO_x

thickness at which the 0 nm MnO_x on TaO_xN_y was used as a reference for the underlying TaO_xN_y photoabsorber, and the thick layer of 26 nm MnO_x on TaO_xN_y was used as a reference for the MnO_x overlayer. While the 2, 5, and 7 nm MnO_x thin layers on TaO_xN_y were measured to trends in chemical composition and electronic structure interfacial changes at the TaO_xN_y/MnO_x as a function of MnO_x film thickness.

To assure experimental reproducibility and to test for sample homogeneity, spectra were measured several times at various spots on the same sample. Then upon ascertaining sample homogeneity, all the core levels spectra were measured at the same spot on the sample. All the HAXPES spectra in this study were collected using the HIKE endstation at the KMC-1 beamline at the BESSY II synchrotron facility. Details about the KMC-1 beamline and HIKE endstation are stated in section 3.2.3 & 3.1.2, respectively. The Au foil (reference sample) was attached to the same sample holder as the investigated samples; both had a common ground with the electron energy analyzer. The Au $4f$ core level spectrum was measured before and after collecting a set of HAXPES core levels spectra for every investigated sample at each excitation energy. Hence, for binding energy calibration, peak positions of all HAXPES spectra were calibrated using the Au $4f_{7/2}$ peak (with its binding energy at 84 eV) as a binding energy reference. Before any quantitative analysis, the HAXPES spectra were normalized by the photon flux, the number of sweeps, and acquisition time, which were recorded with each spectrum. A schematic illustration of the HAXPES experimental geometry, which is implemented later in SESSA software for a multi-layered sample of different thicknesses, is shown in Figure 6.4.

Figure 6.4 shows the schematic arrangement of the sample, X-ray direction, and photoelectron direction to the hemispherical electron analyzer (as implemented at BL KMC-1, BESSY II). The synchrotron radiation polarization vector $\vec{\varepsilon}$ (horizontal) and the photoelectron momentum vector $\vec{P}$ lie in the same plane, so the angle φ between the photon momentum vector $\vec{k}$ and the plane containing $\vec{P}$ and $\vec{\varepsilon}$ (as explained precisely in section 2.4) is equal to 0°. Since the photoelectron momentum vector $\vec{P}$ is perpendicular to the photon momentum vector $\vec{k}$, the angle α (angle between $\vec{\varepsilon}$ and $\vec{P}$) is equal to 0°.
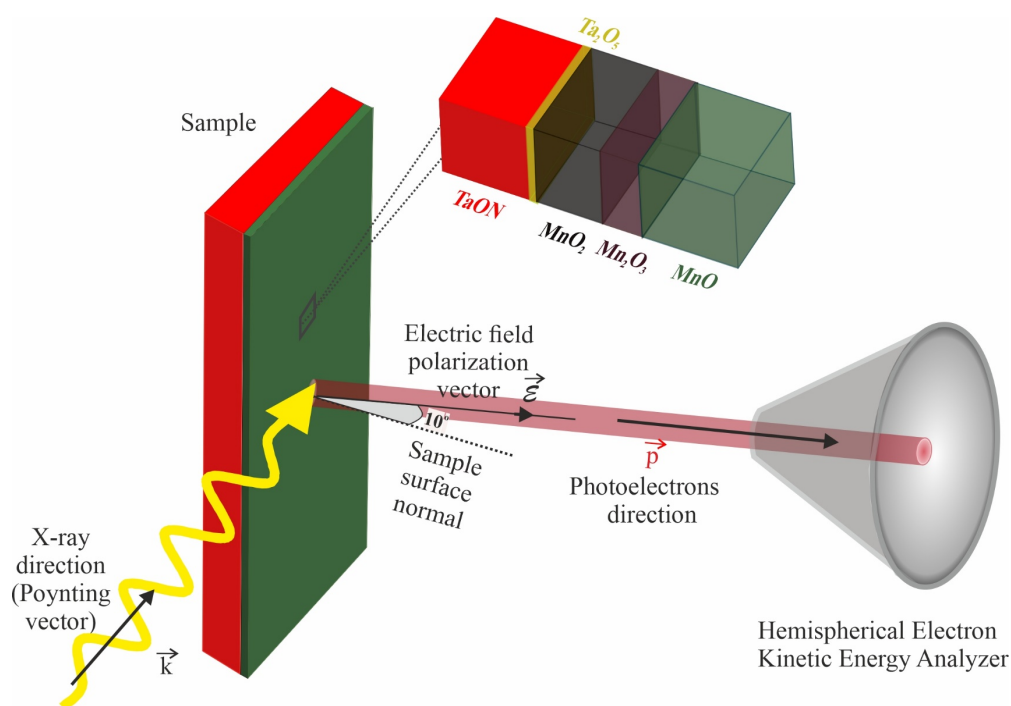
Figure 6.4. Schematic illustration of the hard X-ray photoelectron spectroscopy (HAXPES) experimental geometry. The X-ray source, sample, and hemispherical electron analyzer configuration is designated according to the experimental setup arrangement at BL KMC-1, BESSY II. The angle between the X-ray direction $\vec{k}$ and the analyzer axis (photoelectron direction) $\vec{P}$ is 90º, while the angle between the sample surface normal and the analyzer axis is 10º. This arrangement is implemented in SESSA software for calculation of thicknesses of Ta_2O_5 (*yellow*) at the interface of MnO_x/ TaO_xN_y as well as the thicknesses of the MnO_x layers; MnO_2 (*black*), Mn_2O_3 (*brown*), and MnO (*green*).

6.3   Experimental Results and Discussion

6.3.1   Sample Characterization

6.3.1.1 Photoelectrochemical measurements

PEC measurements were done on bare TaON and MnO_x/TaO_xN_y films in a voltammetric regime (0.1-0.9 V_{RHE}) under chopped AM1.5 light irradiation in potassium borate buffer electrolyte (pH 9). The changes in the photocurrents are shown in Figure 6.5. In the dark, all samples showed negligible oxidative currents. Upon deposition of just an ultra-thin layer (0.5 nm) of MnO_x co-catalyst on the TaO_xN_y photoanode, the photocurrent increased significantly. It increased further slightly up to 5 nm MnO_x thickness with a 5-fold enhancement in photocurrent.
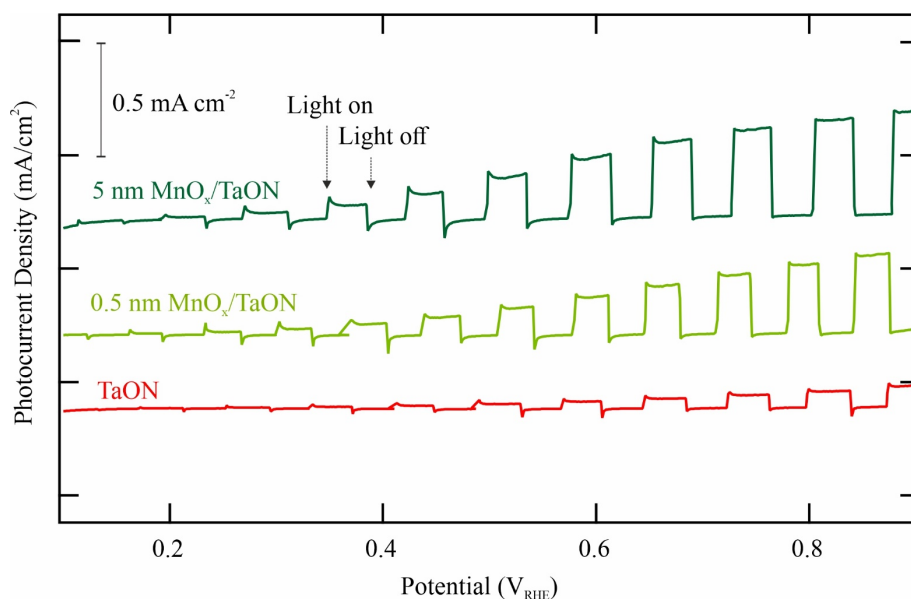
Figure 6.5. Linear sweep voltammetry (LSV) measurements under chopped AM1.5 illumination for bare TaON (*red*), 0.5 nm MnO_x on TaO_xN_y (*light green*), and 5 nm MnO_x on TaO_xN_y (*dark green*) in 0.1 M potassium borate buffer (pH ~ 9) with 0.5 M Na_2SO_4 as a hole scavenger while bubbling Argon.

6.3.1.2 X-ray Diffraction (XRD)

The crystallographic structure of TaO_xN_y film with 0, 2, 7, and 26 nm MnO_x thick overlayers were studied by grazing incidence X-ray diffraction (GIXRD) at room temperature in a Bruker D8 X-ray diffractometer using Cu K_α radiation. The XRD patterns of these samples are displayed in Figure 6.6, at which the XRD pattern of a bare TaON thin film synthesized at 850°C is shown in red, and MnO_x films with different thicknesses on TaO_xN_y are shown in different shades of green. A low incidence angle of 1° was used in order to reduce the signal from the underlying Ti-Pt-Ti layer.

All observed reflections were assigned to a pure β-TaON phase, as shown by Bragg reflections for the monoclinic TaON phase (bottom panel of Figure 6.6) [282, 283] except for two peaks at 40° and 46.5° were assigned to Pt peaks (*, *green*) in the substrate. No change in the XRD patterns was observed for MnO_x films of different thicknesses (up to 26 nm) on TaON, revealing that the MnO_x overlayer films are amorphous. No diffraction peaks arising from any secondary phases can be seen, however, note that XRD may not be able to detect small amounts of amorphous TaO_xN_y, which may still be present in the film.
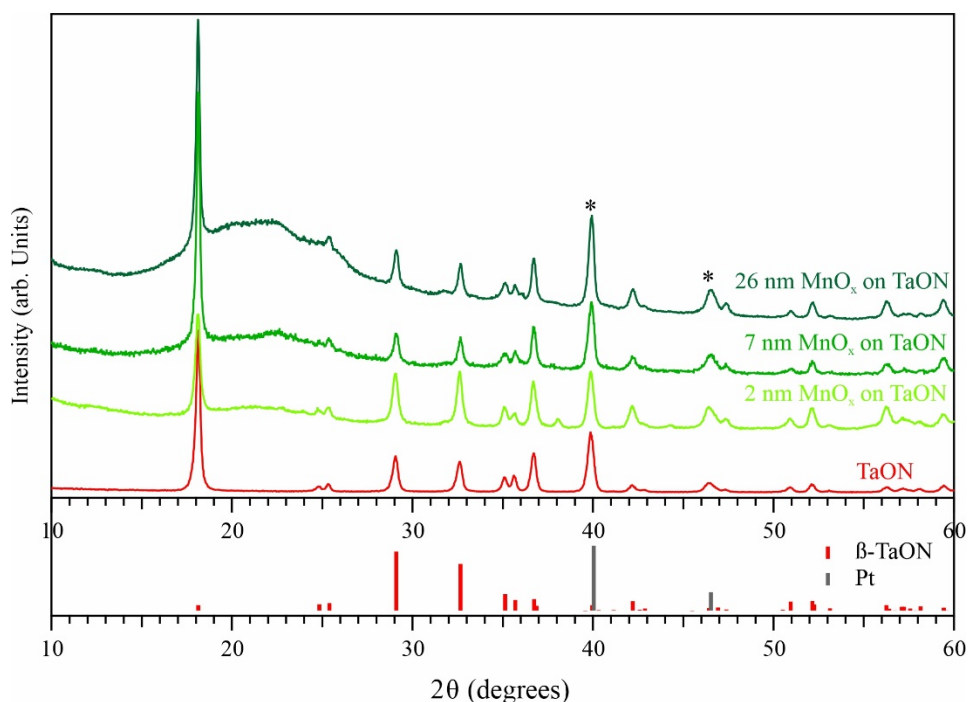
Figure 6.6. X-ray diffraction patterns for TaON (*red*) and MnO$_x$ films with different thicknesses (2, 7, and 26 nm) on TaO$_x$N$_y$ are shown in different shades of *green*. Bragg peaks of the monoclinic β - TaON phase (*red*, PDF # 01-083-4964) and platinum (*gray*, PDF # 00-001-1194) are included in the lower panel for comparison.

6.3.1.3 Transmission Electron Microscopy (TEM)

The cross-sectional *transmission electron microscopy* (TEM) images were conducted at the Fritz-Haber Institute, Berlin, Germany. A cross-sectional TEM image of a 26 nm thick MnO$_x$ film on TaO$_x$N$_y$ is shown in Figure 6.7. Protection layers of platinum/carbon (Pt/C) have been added to minimize sample heating caused by the focused electron beam used during the TEM measurement. The TaO$_x$N$_y$ is found to be very porous, while MnO$_x$ uniformly covers the TaO$_x$N$_y$. The thicknesses of MnO$_x$ were estimated by TEM and are nearly the same as those measured by spectroscopic ellipsometry. The values of MnO$_x$ thicknesses obtained by TEM are tabulated in Table 6.1. Each thickness obtained by TEM is an average value from more than 100 different positions on the sample. A Gauss fit was applied to the generated thickness histograms to provide an average thickness, reported in Table 6.1, with an error ± one standard deviation.
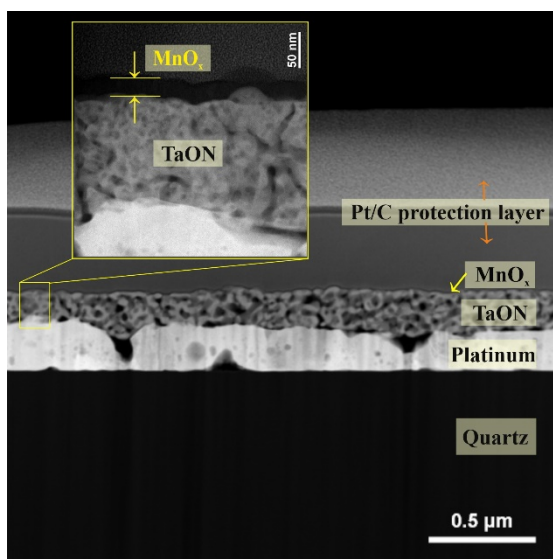
Figure 6.7. Cross-sectional TEM image of the sample layers, including Pt/C protection layers on the top, then 26 nm MnO_x (dark contrast) on porous TaO_xN_y followed by Ti-Pt-Ti on quartz in black at the bottom. The inset shows a magnified area for the formation of a 26 nm MnO_x layer in black on the top of the porous TaO_xN_y.

The roughness of the MnO_x film on TaO_xN_y was also measured by TEM and quantified as the "relative surface roughness" (RSR) factor. The RSR factor is defined here as the cross-sectional length of the surface measured along the tilted surface at the interface (*orange* line in Figure 6.8) divided by the cross-sectional length of the surface projected onto the global surface (*blue* line in Figure 6.8). Table 6.1 includes the RSR values, which reveals that the MnO_x surface's roughness decreases as the MnO_x film thickness increases. These RSR values will be used later in the SESSA simulation of the HAXPES data.

Table 6.1. The average thickness and roughness of MnO_x films.

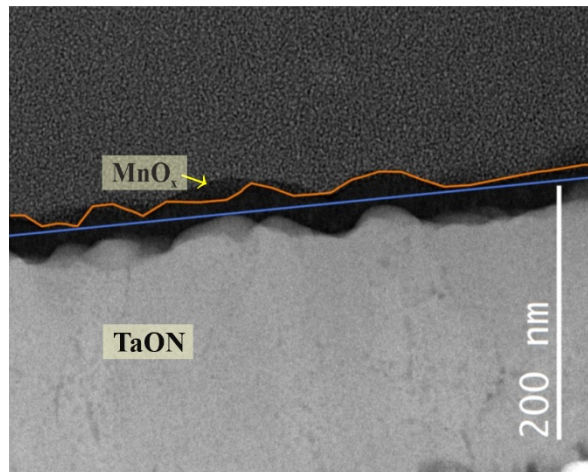| Sample name	Average size of MnO_x films obtained by TEM ± error /nm	Relative Surface Area (RSR)
2 nm MnO_x/TaO_xN_y	2.07 ± 0.051	1.092
5 nm MnO_x/TaO_xN_y	5.25 ± 0.191	1.079
7 nm MnO_x/TaO_xN_y	7.50 ± 0.101	1.049
26 nm MnO_x/TaO_xN_y	26.1 ± 0.327	1.061

Figure 6.8. Cross-sectional TEM image showing the roughness morphology of MnO_x (dark *black*) on the TaON (light *gray*). The *orange* line expresses the length of the surface measured along the tilted surface at the interface, while the length of the surface projected onto the global surface is shown in *blue*.

6.3.1.4 Energy Dispersive X-ray spectroscopy (EDX)

The *energy-dispersive X-ray* (EDX) elemental mapping of MnO_x on TaO_xN_y is shown in Figure 6.9. The TaO_xN_y film is found to be very porous, while MnO_x uniformly covers and generally follows the roughness of the TaO_xN_y film and penetrates its pores.
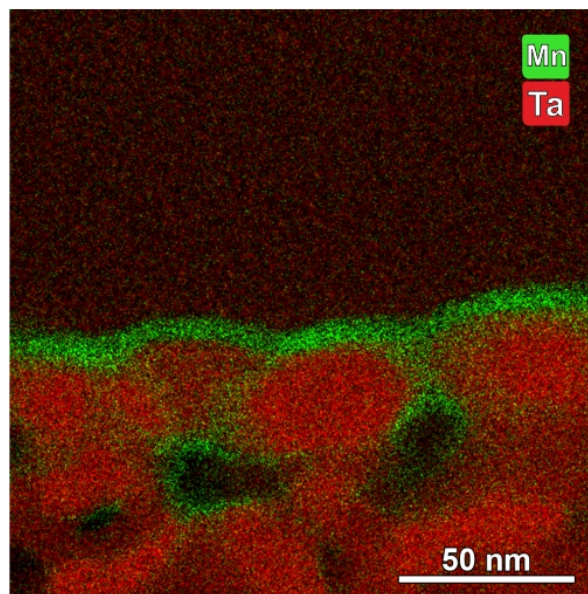
Figure 6.9. EDX elemental mapping of 7 nm MnO_x layer on the top of TaO_xN_y with Mn in *green* and Ta in *red*.

6.3.2   Hard X-ray Photoelectron Spectroscopy (HAXPES) Results

To probe the elemental composition and the chemical state at the MnO_x/TaO_xN_y interface, HAXPES spectra were acquired at two excitation energies 2003 eV and 4000 eV in order to get complementary information for different probing depth. Figure 6.10 shows a survey spectrum for 5 nm MnO_x/TaO_xN_y, which confirms the presence of Ta, O, N, Mn, and C element signals with no trace of impurities. Core levels of Ta 4f, O 2s, Mn 2$p_{3/2}$, Mn 3s, Ta 4$p_{3/2}$, N 1s, C 1s, and the valence band were analyzed and studied herein in detail in order to understand the electronic structure and chemical composition at the interface of MnO_x/TaO_xN_y. The Survey spectra for all the investigated samples are displayed in Figure C.1 in Appendix C.
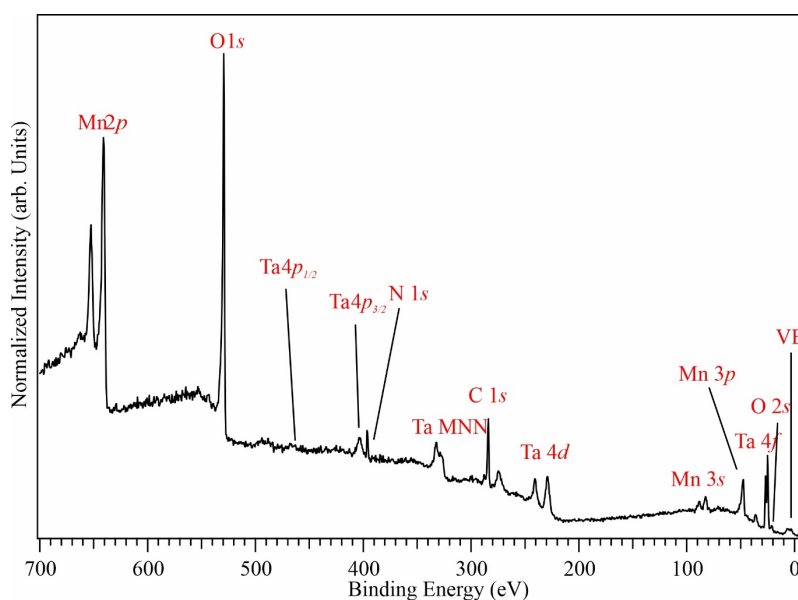
Figure 6.10. The survey spectrum of 5 nm MnO_x/TaO_xN_y sample measured at the 2003 eV excitation energy.

6.3.2.1 Ta 4f + O 2s Core Levels

Ta 4f + O 2s HAXPES spectra in the binding energy range from 17 to 34 eV and 13 to 34 eV measured at the two excitation energies, 2003 eV (left panel) and 4000 eV (right panel), respectively, are shown in Figure 6.11. The spectra were measured at the same spot for both excitation energies, 2003 and 4000 eV, for a fair comparison. The spectra in each panel of Figure 6.11 are separated vertically according to the thickness of the MnO_x overlayer, from 0 nm MnO_x (top), which is used as a reference for the underlying TaO_xN_y photoabsorber, to 26 nm MnO_x (bottommost) used as a reference for the MnO_x overlayer. The Ta_2O_5 reference spectrum

measured at 2003 eV is added to the left panel (topmost) to allow guidance for peak positions assigned to Ta$_2$O$_5$. There is a primary Ta 4f region (red and yellow deconvoluted peaks) in the binding energy range from 24 to 30 eV with a broad overlapping peak originating from O 2s, which extends from 17 eV to 30 eV.
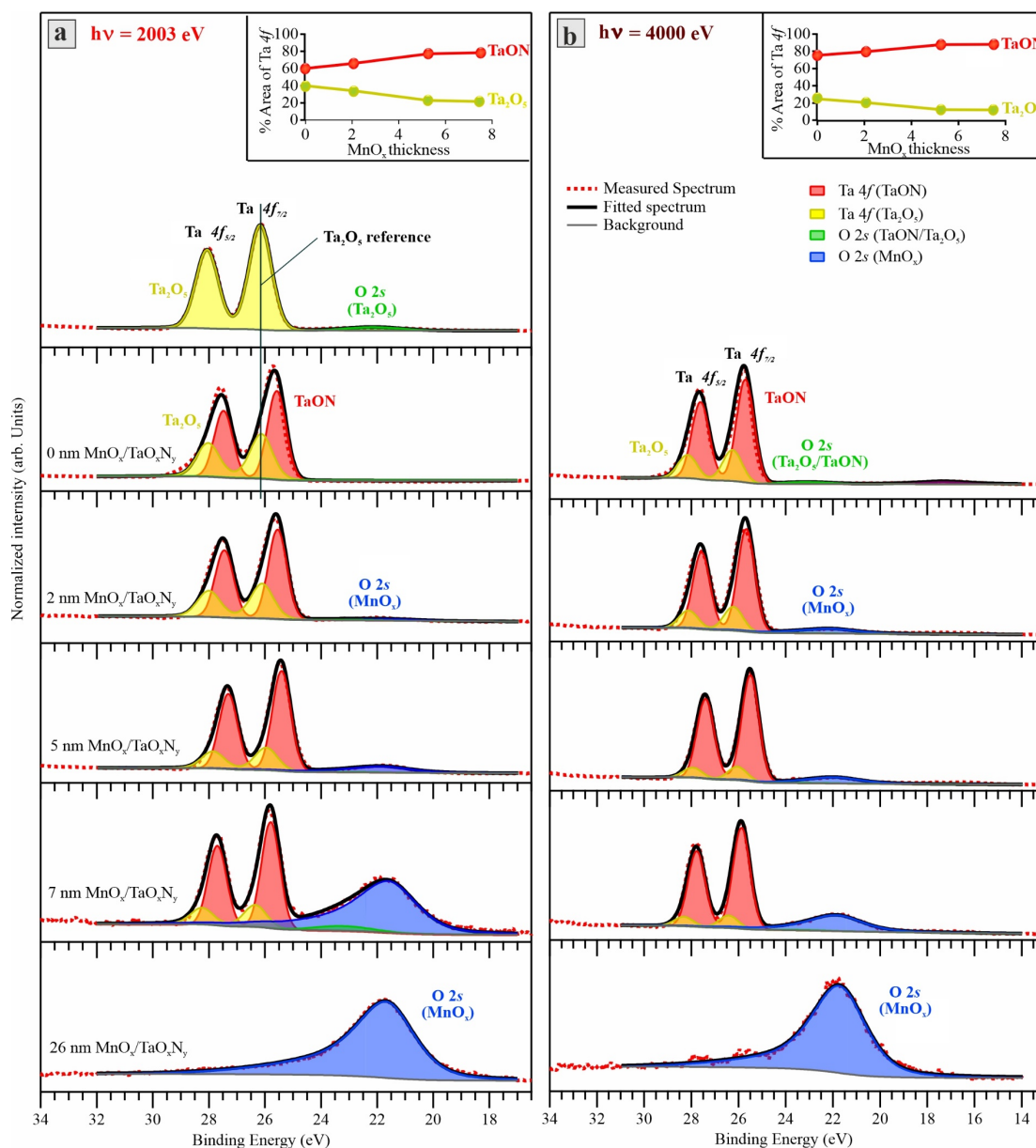

Figure 6.11. Tantalum 4f + Oxygen 2s photoemission spectra for different MnO$_x$ thicknesses on the TaO$_x$N$_y$ photoabsorber substrate. Spectra were collected at two different excitation energies, a) 2003 eV and b) 4000 eV. The MnO$_x$ thickness increases from 0 nm (top spectrum) to 26 nm (bottommost spectrum). The Ta$_2$O$_5$ reference spectrum measured at 2003 eV is added to the left panel (topmost spectrum). The inset figures show the change in the total area percentage of the Ta 4f peak due to TaO$_x$N$_y$ and Ta$_2$O$_5$ as a function of MnO$_x$ thickness.

Two regions for O 2*s* are separated and can be seen in Figure 6.11, one is located in a higher binding energy region of ~ 23-24 eV, indicated by the green peak, and the other region is located at a lower binding energy of 22 eV, which is indicated by the blue peak. The O 2*s* peak at the higher binding energy is assigned to Ta-O[284], as seen for the Ta_2O_5 reference spectrum (at the topmost of the left panel). While the O 2*s* peak in the lower binding energy region increases with increasing MnO_x thickness, which shows that this oxygen species arises from the MnO_x overlayer.[285] Due to a lack of data in the literature and databases about exact binding energies and FWHM of O 2*s* spectra, the asymmetric peak of O 2*s* (blue peak in Figure 6.11) was taken into account which assigned to MnO_x at 21.75 eV with oxygenated carbon species at the tail of the peak. It can be seen that the asymmetry factor is less pronounced for the spectra at 4000 eV since it is less surface sensitive; thus, less sensitive to oxygenated carbon species that arise from surface contamination. These oxygenated carbon species, such as C-O=C and C-O-C, are also confirmed by the C 1*s* spectra (Figure 6.15).

According to literature,[286, 287] the energy difference between the Ta 4*f* peak for TaON and Ta_2O_5 is kept fixed to 0.55 eV, at both excitation energies 2003 and 4000 eV. Interestingly, the relative area of the Ta 4*f* peak attributed to Ta_2O_5 decreases with increasing MnO_x overlayer thickness, as shown by the yellow curve in the insets of Figure 6.11. This was seen at both excitation energies, which probe different depths of the sample; however, this behavior is shown up to 5 nm MnO_x thick film. Using the fact that the spectra collected at 2003 eV are more surface sensitive than that obtained at 4000 eV, it can be deduced that the Ta_2O_5 layer is located at the surface of the TaO_xN_y photoabsorber since the Ta_2O_5 peak area for the bare TaO_xN_y absorber at 2003 eV is higher than that at 4000 eV. The presence of Ta_2O_5 species in all samples is explained by partial surface oxidation of the TaO_xN_y substrate due to exposure to air. From an energy diagram point of view, the presence of the Ta_2O_5 layer on the TaO_xN_y photoabsorber hinders hole transfer since there is an unfavorable mismatch in the valence band-edge levels between Ta_2O_5 and TaON.[273, 275, 279] The reduction in the fractional amount of Ta_2O_5 with the increasing amount of MnO_x implies that part of the role of the MnO_x co-catalyst layer on the TaO_xN_y absorber may be to reduce the amount of Ta_2O_5, thereby facilitating hole transfer. This will be discussed further in the following sections.

6.3.2.2 Mn 2$p_{3/2}$ Core Level

Manganese is a TM characterized by multiplet splitting features in their 2*p* spectra. [155, 288] In general, the multiplet splitting feature arises when an atom contains unpaired electrons in the outer shell. In the photoemission process, the core-electron is ionized upon irradiation, leaving

a core vacancy behind. In such a case, the unpaired core-electron may be coupled to an unpaired electron in the outer shell, creating a number of final states, which appear in the XPS spectrum as multiplet splitting (*i.e.,* several peak components in their 2*p* spectra).[155, 288] Consequently, all Mn oxidation states, including Mn^{II}, Mn^{III}, Mn^{IV}, and Mn^{VI}, give rise to multiplet splitting in their 2*p* spectra except Mn^{VII} species since Mn^{VII} does not have unpaired *d* electrons.[155] For quantitative analysis of the Mn oxidation states from the Mn 2*p* spectra, an adequate analysis of the multiplet splitting was considered. Figure 6.12(a-b) shows HAXPES spectra of the manganese $2p_{3/2}$ collected in the binding energy range of 632-650 eV at excitation energies, 2003 eV and 4000 eV, at the same spot, to obtain a more comprehensive picture of the changes in oxidation states of the MnO_x layers at the surface and the interface as a function of MnO_x thickness.

Biesinger et al. [155] and *Nesbitt et al.* [289] extensively studied XPS structures of Mn $2p_{3/2}$ for manganese oxide references in different oxidation states. They have shown that the XPS spectrum of $Mn^{II}O$ reference has a clear fingerprint of broad and unique shake-up peak at energy ~646 eV [155, 245, 289], which is not present for any other oxidation state. For instance, by comparing the measured Mn $2p_{3/2}$ spectra of the investigated MnO_x on TaO_xN_y samples to that of MnO_x references in literature, it can be seen there is a distinct broad peak at energy ~646 eV, which coincide with the spectral feature of the shake-up peak of the $Mn^{II}O$ reference. [155] This indicates that the investigated samples include a considerable amount of Mn^{II}. The presence of Mn^{II} in the samples is expected since the MnO_x films are atomic layer deposited from Mn^{II} precursor (Bis(ethylcyclopentadienyl) manganese (II)). Although identifying the amount of a particular MnO_x phase is challenging, it is shown that by fitting each XPS spectrum for the investigated samples using peak parameters reported in [155, 289] for MnO_x reference spectra with a well-known structure, the contribution of a single-phase can be determined. To fit the spectra, we used the same relative area and binding energy separation for the multiplet splitting features for MnO and Mn_2O_3 in [155], and the birnessite-like phase (δ-MnO_2) in [289]. The FWHM for all multiplet peaks was constrained to the same values for all samples (close to that in literature). The overall peak positions were allowed to vary within some reasonable bounds (*i.e.,* binding energy position in literature ± 0.2 eV) while keeping the multiplet split component separation the same. All the parameters used for fitting the Mn $2p_{3/2}$ are shown in Appendix C (Table C.1).

These fits are effectively highly constrained fits where the peak shape of the various MnO_x components is kept constant and determined by the relative intensity and splitting of the various multiplet components. The fitting results showed that the MnO_x samples of different thicknesses consist of a mixture of three MnO_x phases: $Mn^{II}O$, $Mn_2^{III}O_3$, and a Birnessite-like phase δ-MnO_2. Similar attempts of fitting with a pure Pyrolusite (β-MnO_2) phase were unsuccessful.
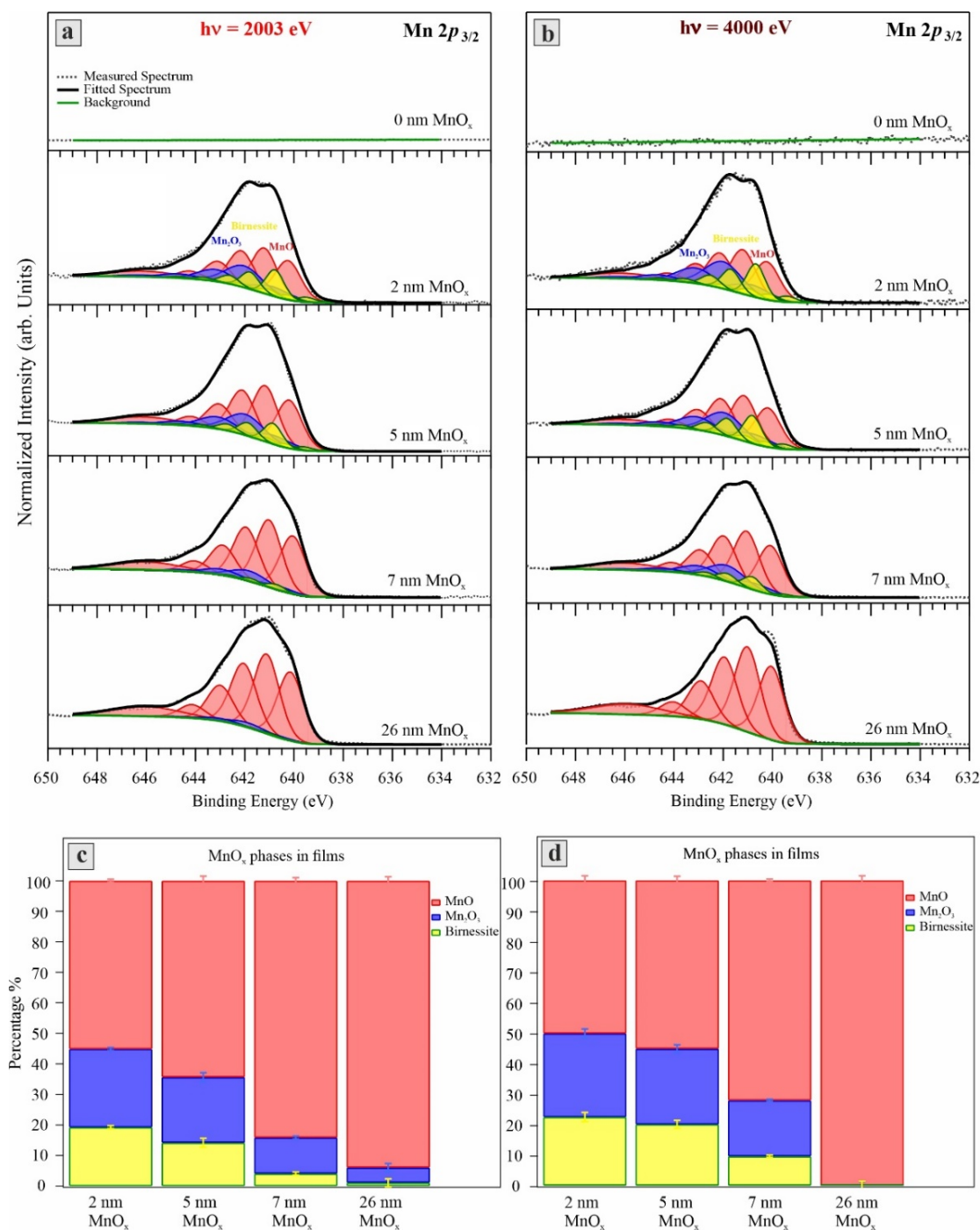
Figure 6.12. HAXPES spectra of manganese $2p_{3/2}$ of different MnO_x thicknesses on TaO_xN_y and their corresponding fittings collected at photon energies (a) 2003 eV and (b) 4000 eV. The MnO_x thickness increases from 0 nm (topmost spectrum) to 26 nm (bottommost spectrum). Mn $2p_{3/2}$ spectra have a significant multiplet splitting for MnO (in *red*), Mn_2O_3 (in *blue*), and birnessite-like phase (in *yellow*). (c) and (d) are the percentages of the total peak area of each MnO_x phase for samples 2, 5, 7, and 26 nm MnO_x measured at excitation energies, 2003 eV, and 4000 eV, respectively. The percentage plotted with error bars of ±1.5 standard deviation. However, the total accuracy is estimated to be approximately ± 5%.

The lower percentages of the Mn_2O_3 and the birnessite-like phase for the 7 nm MnO_x film at 2003 eV compared to that at 4000 eV (Figure 6.12(c-d)) reveals the presence of these oxidized phases mostly at the interface of MnO_x/TaO_xN_y, and a low proportion is existing at the surface since the 4000 eV is less surface sensitive and has larger probing depth than the 2003 eV. For example, the probing depth ($\sim 3\lambda_{IMFP}$) at 4000 eV photon energy (or 3360 eV electron kinetic energy) in MnO is *ca*. 15.0 nm [206] compared to a probing depth of *ca*. 7.3 nm at 2003 eV photon energy.[206, 290] The IMFP values are calculated using the QUASES-IMFP-TPP2M software [206] developed by S. Tougaard based on the Tanuma Powell and Penn algorithm.[290, 291]

This interpretation implies that upon coupling MnO film deposited from the Mn^{II}-precursor to Ta_2O_5/TaO_xN_y substrate, MnO at the interface is oxidized into Mn_2O_3 and a birnessite-like phase. Since the Ta 4*f* spectra in Figure 6.11 showed a reduction of the Ta_2O_5 amount with increasing the MnO_x overlayer thickness, an oxygen source for the oxidation of MnO to Mn_2O_3 and birnessite-like phases could be the Ta_2O_5 layer. That is, during atomic layer deposition, the first MnO_x layers at the interface steal oxygen from Ta_2O_5, leading to a reduction in the Ta_2O_5 amount at the interface and oxidization of MnO to the Mn_2O_3 and birnessite-like phase.

In order to explain these interpretations thermodynamically, several chemical reactions of MnO with Ta_2O_5 have been investigated, whether they are thermodynamically uphill or downhill, as shown below in Table 6.2. By implementing the standard Gibbs free energy (ΔG_f^0) of formation for the Ta_2O_5 and Mn_xO_y compounds from Table 6.3, the standard-state free energy changes for the reaction (ΔG^o) per mole of oxygen is calculated and tabulated in Table 6.2.

Table 6.2. Possible chemical reactions of MnO and Ta_2O_5 with the values of standard-state free energy changes (ΔG^o) per mol oxygen.

Chemical reaction	**standard-state free energy changes (ΔG^o) / [kJ/mol Oxygen]**	**Equation**
$3\ MnO + 2\ Ta_2O_5 \rightarrow Mn_2O_3 + MnO_2 + 4\ TaO_2$	+ 1315	(6.1)
$2\ MnO + Ta_2O_5 \rightarrow Mn_2O_3 + 2\ TaO_2$	+ 1288	(6.2)
$3\ MnO + Ta_2O_5 \rightarrow Mn_3O_4 + 2\ TaO_2$	+ 1250	(6.3)
$10\ MnO + Ta_2O_5 \rightarrow 5\ Mn_2O_3 + 2\ Ta\ (s)$	+ 230	(6.4)

The Gibbs free energies of formation for all these reactions are positive, which indicates an uphill reaction (non-spontaneous), which is thermodynamically unfavorable. Note that all of these values are for bulk materials. Furthermore, there is no spectroscopic evidence that the

chemical reaction (Equ. 6.4) occurs since Ta metal should have a 4*f* peak at 21 eV. The reduction of Ta_2O_5 by MnO_x at the interface despite the reactions being unfavorable in bulk can be explained by differences in the chemical properties of surface atoms from their bulk counterparts since they are on average more coordinatively unsaturated.

Table 6.3. The standard Gibbs free energy of formation (ΔG_f^0) values under conditions (T = 400 K, P= 1 atm.), calculated for Mn_3O_4, Mn_2O_3, MnO_2 according to the literature [292-296]

Compound	Symbol	ΔG_f^0 / [kJ.mol^{-1}]
Tantalum Penta oxide	Ta_2O_5	-2105
Tantalum dioxide	TaO_2	-313
Manganese (II) oxide	MnO	-407
Manganese (II/III) oxide	Mn_3O_4	-1450
Manganese (III) oxide	Mn_2O_3	-1005
Manganese (IV) oxide	MnO_2	-544

6.3.2.3 Mn 3*s* Core Level

To obtain a more comprehensive picture of the changes in the MnO_x electronic structure, additional HAXPES spectra of Mn 3*s* were recorded at two excitation energies 2003 and 4000 eV in the binding energy range of 76-100 eV (Figure 6.13). Two components in the Mn 3*s* spectra can be seen, originating from the exchange coupling between the 3*s* hole with the 3*d* valence electrons.[297] Interestingly, the magnitude of the peak splitting (ΔE) between the Mn 3*s* peaks has been interpreted as arising from the local spin of the 3*d* electrons such that the magnitude of the splitting is proportional to (2S+1), where S is the total spin of the Mn ion in the ground state.[298] *E.g.,* the total spin of Mn^{II} ion (d^5) is 5/2, then $\Delta E \approx 2(5/2)+1= 6$ eV. Hence, ΔE can be used to provide information about the valence state of the Mn ions.

As the oxidation state of manganese increases, the splitting between the two Mn 3*s* components (ΔE) decreases. This correlation was initially reported by *Toupin et al.* [299] and later by *Ilton et al.* [245] for pure MnO_x phases where ΔE for MnO, Mn_2O_3, and MnO_2 is 6.0, 5.4, and 4.4 eV, respectively. The Mn 3*s* spectra for the investigated samples in Figure 6.13 show a shift in the main *blue* peak to lower binding energy (*red* dashed line) while almost no shift for the other peak (*black* dashed line).
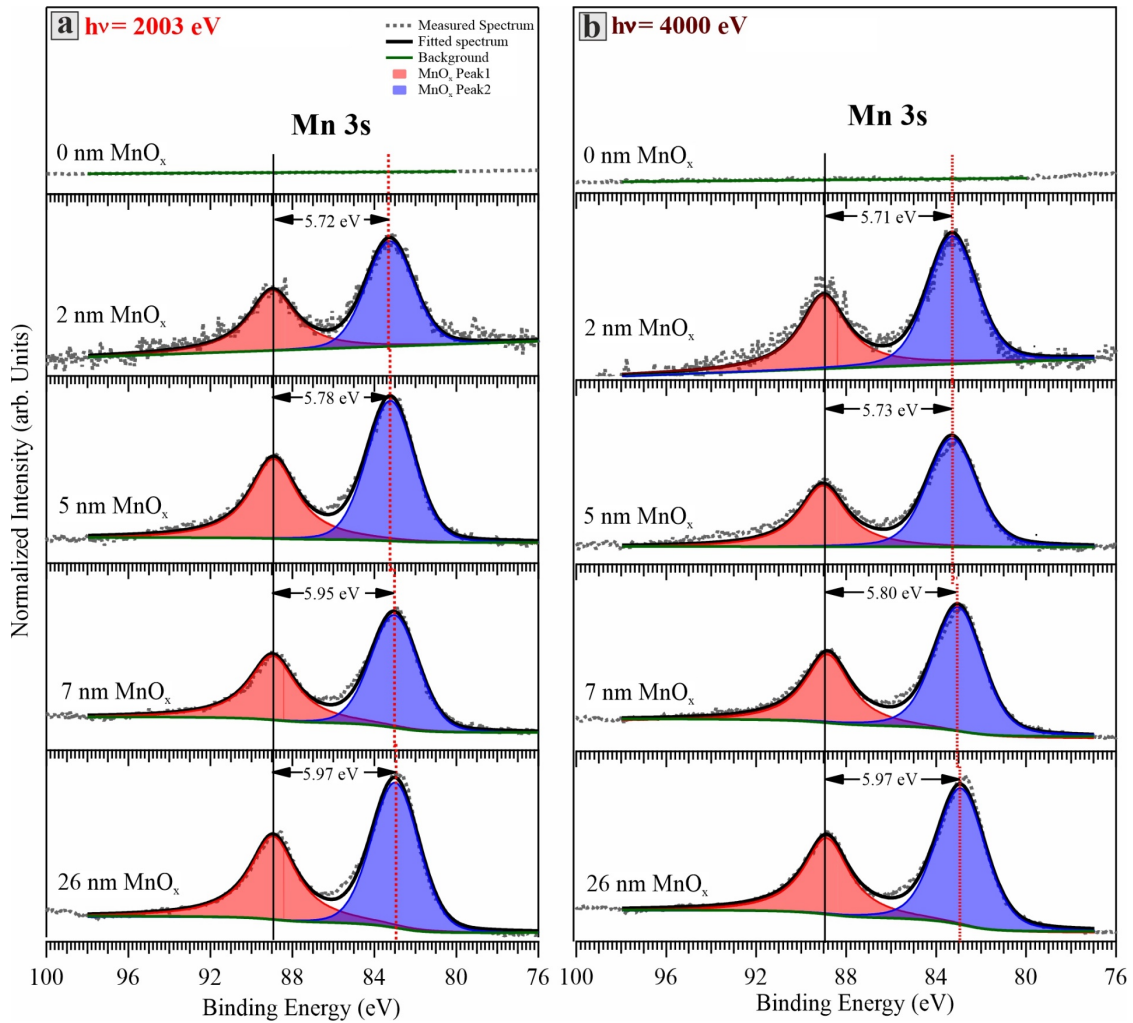
Figure 6.13. HAXPES spectra of manganese 3*s* of the investigated samples of different MnO$_x$ thicknesses and their corresponding fittings. Spectra were collected at photon excitation energies (a) 2003 eV (left panel) (b) 4000 eV (right panel). The MnO$_x$ thickness increases from 0 nm (topmost spectrum) to 26 nm (bottommost spectrum). The splitting value between the two components is indicated for each spectrum.

Furthermore, the separation of the Mn 3*s* peaks increases with increasing the MnO$_x$ thickness, which is consistent with a decrease in the average Mn oxidation state of the film. By looking at the spectra for the same thickness at the two excitation energies (2003 and 4000 eV), it reveals that samples of 2 nm and 5 nm MnO$_x$ are composed of a combination of Mn^{II}, Mn^{III,} and Mn^{IV} since ΔE values are in-between values for MnO, Mn$_2$O$_3$, [245] and Birnessite references while bulk MnO$_x$ samples (26 nm thin film) is mainly composed of Mn^{II}. For the 7 nm MnO$_x$ sample, ΔE is much smaller at excitation energy 4000 eV compared to 2003 eV. Since 4000 eV probes more deeply into the MnO$_x$ film than the 2003 eV measurements, this is consistent with the more

highly oxidized Mn phase being located at the MnO_x/TaO_xN_y interface. These results are consistent with the Mn oxidation state changes obtained from the Mn $2p_{3/2}$ spectra, which confirms the oxidation of Mn^{II} to Mn^{III}/Mn^{IV} at the interface between TaO_xN_y and MnO_x.

6.3.2.4 Ta $4p_{3/2}$ + N 1*s* Core Levels

To further clarify the chemical composition at the MnO_x/TaO_xN_y interface as a function of MnO_x overlayer thicknesses, the HAXPES spectra of Ta $4p_{3/2}$ and N 1*s* core levels were studied and displayed in Figure 6.14(a) at 2003 eV. In this figure, the spectra in the binding energy range from 383 to 419 eV were de-convoluted into two peaks, the main peak (Ta $4p_{3/2}$) at high binding energy (403.8 eV) and a low binding energy peak (N 1*s*) at 397.1 eV similar to that reported in the literature [279, 284], which is assigned to Ta-N bonds. There are two peaks of Ta $4p_{3/2}$, one peak at 404.7 eV assigned to Ta_2O_5, and the other peak at 403.8 eV assigned to TaON. By keeping the binding energy difference between the two components of the Ta $4p_{3/2}$ fixed, it revealed that the relative peak area of Ta $4p_{3/2}$ due to Ta_2O_5 to that for TaON is reduced by increasing the thickness of the MnO_x overlayer, which is in accordance with the results of Ta 4*f* in Figure 6.11. There is no Ta signal for 26 nm MnO_x on TaO_xN_y. Figure 6.14(b) shows relative peak area ratios of the N 1*s* to the Ta $4p_{3/2}$ (TaON) as a function of MnO_x overlayer thickness. This ratio is indicative of the relative amount of nitrogen in the TaO_xN_y. It shows that by depositing MnO_x on TaO_xN_y, the relative peak ratio of N 1*s* to Ta $4p_{3/2}$ decreases, which can be attributed to a loss of N content related to the contaminated carbon species (C-N) in the TaO_xN_y, as revealed by the C 1*s* spectra in Figure 6.15. This also explains the shift of the N 1*s* peak in the bare TaO_xN_y film to lower binding energy upon depositing MnO_x, reflecting a change in the chemical environment on the N in the TaO_xN_y as a result of the loss in the C-N content.
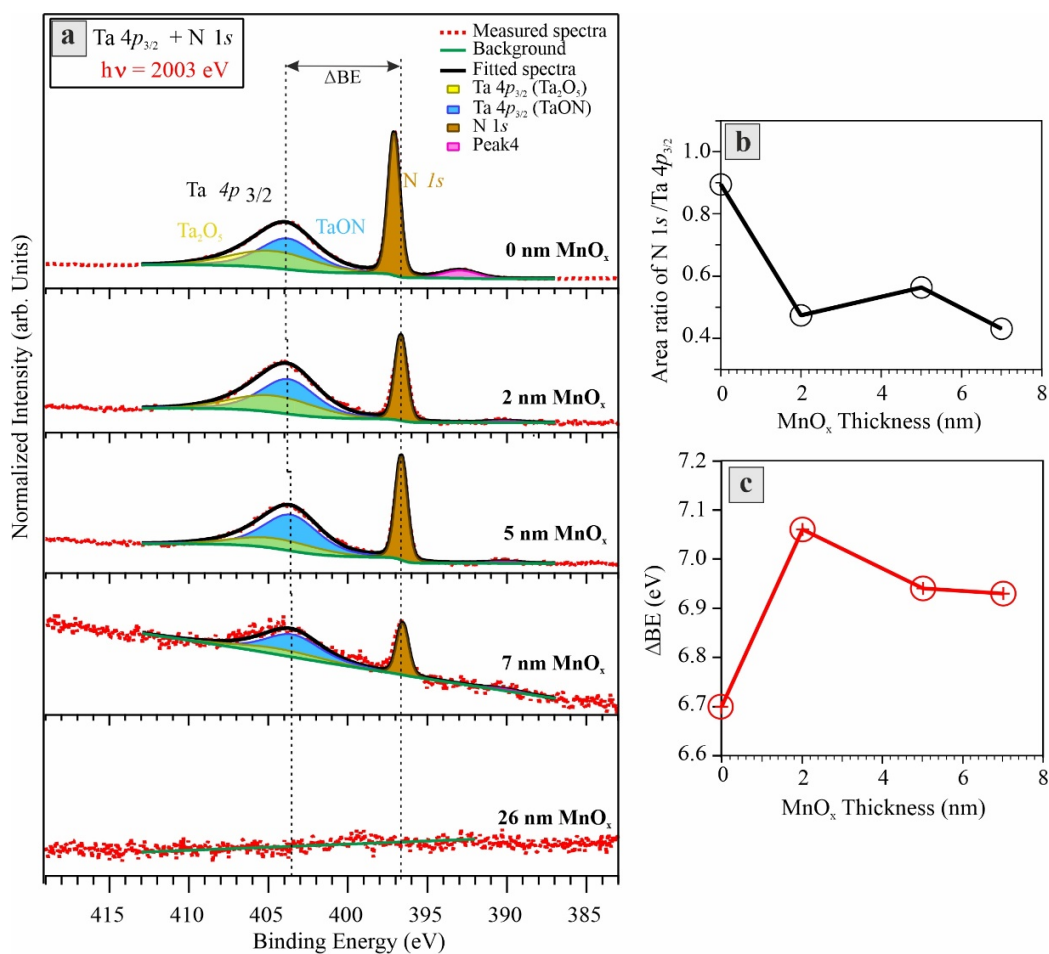
Figure 6.14. a) Ta $4p_{3/2}$ and N $1s$ photoemission spectra for different MnO_x thicknesses on the TaO_xN_y photoabsorber substrate collected at 2003 eV. The MnO_x thickness increases from 0 nm (topmost spectrum) to 26 nm MnO_x (bottommost spectrum). b) The Area ratio of N $1s$ to Ta $4p_{3/2}$, both as a function of MnO_x thickness. c) The change in the binding energy between the main peak of Ta $4p_{3/2}$ and the N $1s$.

6.3.2.5 C 1s Core Level

Since the samples were exposed to air, adventitious carbon contamination is expected. By de-convoluting the C $1s$ core-level spectra reported in Figure 6.15 of the TaO_xN_y bare substrate (*i.e.,* 0 nm MnO_x on TaO_xN_y), three components centered at BE 285.3, 286.2, and 289.75 eV, corresponding to C-N, C–O–C, and O–C=O (oxygenated carbon) type bonds, respectively.[300-302] As the ultra-thin MnO_x films are atomic layer deposited from Bis(ethylcyclopentadienyl) manganese (II) [with the linear formula $Mn(C_5H_4C_2H_5)_2$], the samples after deposition also show carbon species. The C $1s$ core-level spectrum of the 26 nm MnO_x/TaON showed three components at BE 284.8, 286.2, and 288.4 eV, corresponding to C-C, C–O–C, and C–OH type

bonds, respectively.[300-307] By depositing MnO_x layers, there is a decrease in the peak area of the C-N component, which may also explain the reason for the shift in BE of the N 1s peak in Figure 6.13(b), mentioned above.
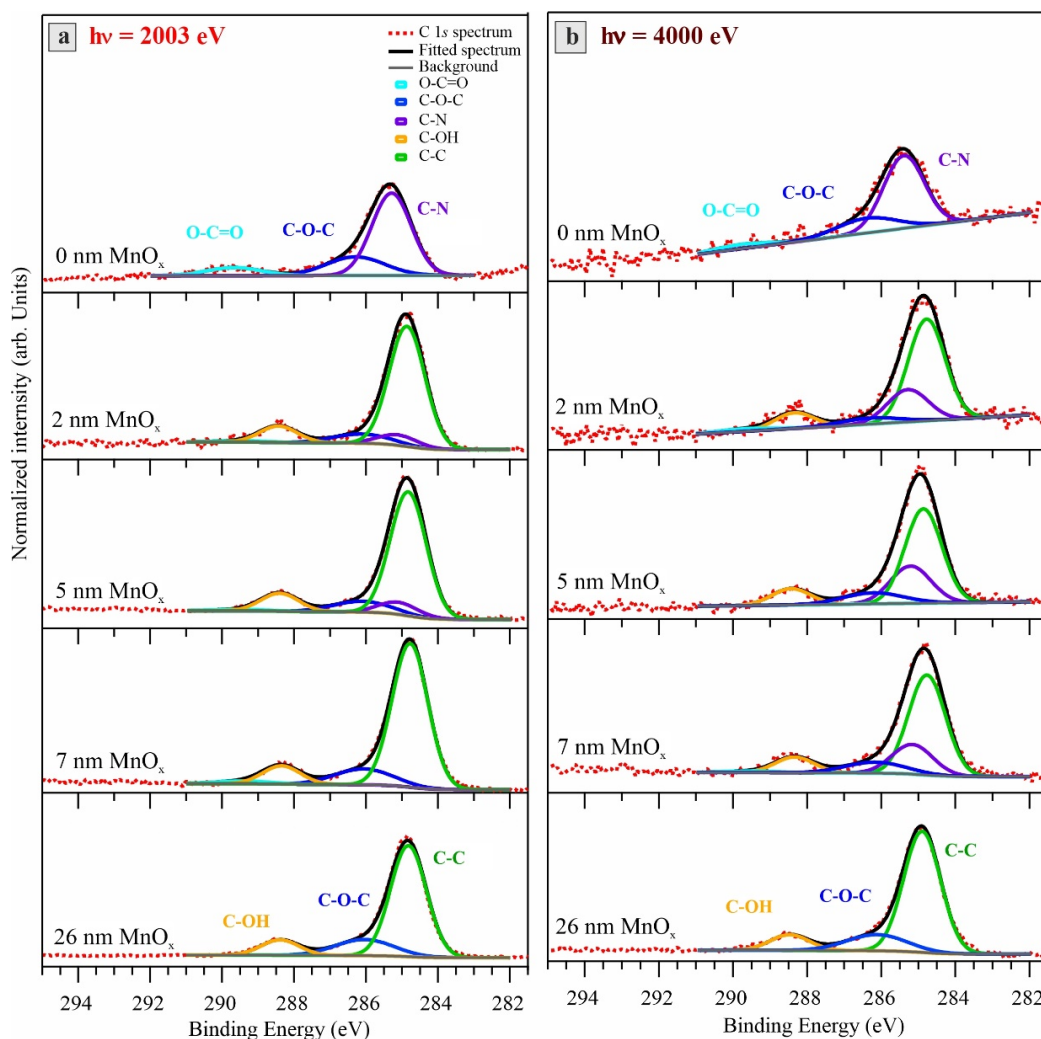

Figure 6.15. Carbon 1s HAXPES spectra for different MnO_x thicknesses on the TaO_xN_y substrate, deconvoluted into 5 components: O–C=O (*turquoise*), C–O–C (*blue*), C–N (*violet*), C–OH (*orange*), and C–C (*green*) type bonds. Spectra were collected at photon excitation energies, (a) 2003 eV , and (b) 4000 eV. The spectra are separated vertically according to the MnO_x thickness from 0 nm (topmost) to 26 nm (bottommost).

6.3.2.6 Valence band of TaON and MnO_x

To investigate the effect of increasing the MnO_x thickness on the valence band (VB) structure, HAXPES measurements were conducted to identify the VB edge position *vs.* the Fermi level. Figure 6.16(a) shows the VB HAXPES spectra of different MnO_x film thicknesses (2, 5, 7, and

26 nm) on TaO_xN_y samples. The VB spectra for Ta_2O_5 bare substrate (light *green*) and TaON photoabsorber substrate (*red*) were also added as references to Figure 6.16 to compare their VB edges with that of the MnO_x/TaO_xN_y films. The valence band maximum (VBM) position for Ta_2O_5 and TaON is found to be 3.9 eV and 2.3 eV *vs.* Fermi level, respectively, which is in line with VBM positions in literature.[272, 273]
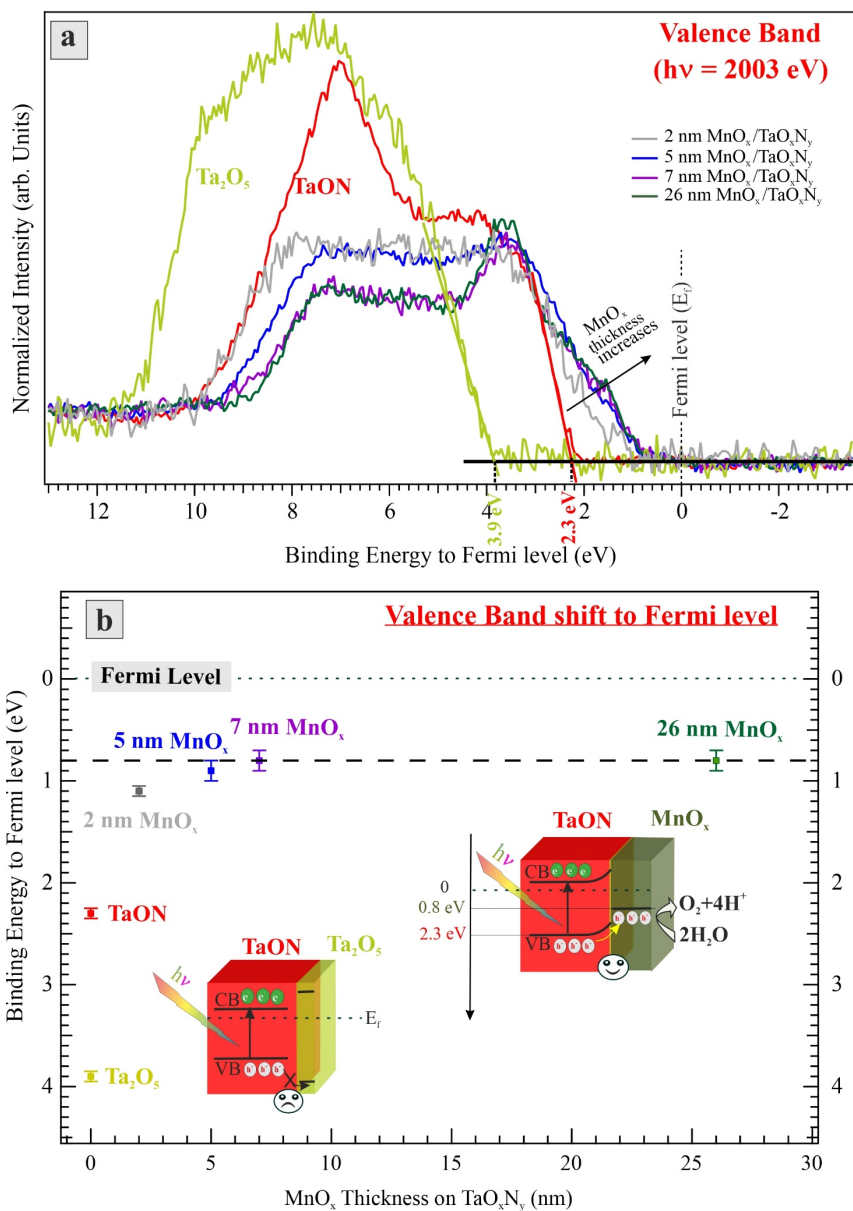

Figure 6.16. (a) HAXPES valence band spectra for different MnO_x thicknesses (5 nm in *blue*, 7 nm in *green*, 26 nm in *violet*) on the TaO_xN_y photoabsorber substrate at 2003 eV photon excitation energy. The valence band spectra for the TaON (*red*) and Ta_2O_5 (light *green*) bare substrates were added as references for comparison. (b) Valence band edge position *vs.* Fermi level as a function of MnO_x thickness. The schematic energy diagram in (b) illustrates the relative valence band edge for TaON with Ta_2O_5 and TaON with MnO_x.

Upon depositing MnO_x layers on the TaON photoabsorber, the VBM shifts to lower binding energy. However, increasing the MnO_x thickness beyond 7 nm does not shift the VBM any further, as shown in Figure 6.16. The VBM position to Fermi level for 2, 5, 7, and 26 nm MnO_x/TaO_xN_y is 1.1 ± 0.05 eV, 0.9 ± 0.1 eV, 0.8 ± 0.1 eV, and 0.8 ± 0.1 eV, respectively. The VBM of MnO, Mn_2O_3, and MnO_2 references is reported as 0.8, 1.2, and 2 eV, respectively.[285] The 26 nm MnO_x valence band spectrum (green) shows an intense feature at ~3.7 eV (Figure 6.16(a)), which is compatible with Mn $3d$ intensity while the high binding energy shoulder at ~7 eV consists largely of O $2p$ character, which is in agreement with features in the calculated valence band obtained from a MnO.[285] This also confirms that the 26 nm MnO_x film is mostly composed of the $Mn^{II}O$ phase. The shift of the VBM upon depositing MnO_x co-catalyst and with increasing the MnO_x thickness can explain the enhanced PEC performance (Figure 6.5). Importantly, the VBM positions of the MnO_x and TaON photoabsorber facilitate transferring holes from the TaON photoabsorber to the MnO_x surface at which water oxidation reaction occurs, as clarified in the schematic illustration in Figure 6.16(b).

The MnO_x co-catalyst in this study showed three advantages: First reduces the inactive and insulating Ta_2O_5 layer at the surface of the TaO_xN_y photoanode. Second, the well-matched valence band at the MnO_x/TaON interface facilitates the transfer of the photogenerated holes from the TaON photoanode to the MnO_x surface for the OER reaction. Third, the oxidation of the MnO_x overlayer at the surface and interface of MnO_x/TaO_xN_y to Mn^{III} and Mn^{IV} oxide species is believed to play a crucial role in enhancing the photoelectrochemical activity of MnO_x as a co-catalyst on TaO_xN_y photoanode. This is in good agreement with our findings in *Chapter 4* and *Chapter 5* and accords with previous studies showing that the $Mn^{III/IV}$ oxide species are active species and function as efficient water oxidation catalysts.[39, 43, 44, 113, 145] However, the experimentally observed phenomenon regarding the oxidation of MnO at the interface in parallel to the reduction of the inactive Ta_2O_5 is still not fully understood of whether the source of oxygen, oxidizing the MnO is Ta_2O_5. Thus, to get a more in-depth insight into understanding this observation, numerical simulations and calculations are applied.

6.4   Numerical Simulation

As a first step to better understand the experimental results regarding the reduction of the Ta_2O_5 layer during MnO_x deposition and oxidation of MnO at the MnO_x/Ta_2O_5-TaO_xN_y interface, the number of oxygen atoms reduced in the Ta_2O_5 layer is calculated and compared to the number of oxygen atoms gained upon oxidizing the MnO to MnO_2 and Mn_2O_3. To do so, simulations of HAXPES data were performed using the "Simulation of Electron Spectra for Surface Analysis

(SESSA)" software.[226, 227] These simulations were made first to calculate thicknesses of the Ta_2O_5 and the MnO_x (*i.e.,* Mn_2O_3 and MnO_2) layers as a function of the deposited MnO layer.

The SESSA application involves the construction of a model of a multi-layered structure, as schematically illustrated in Figure 6.4. The layered structure includes TaON as a substrate, with Ta_2O_5 on the top, followed by 3 MnO_x overlayers arranged according to the Mn $2p_{3/2}$ HAXPES experimental results, in which MnO_2 and Mn_2O_3 are interfaced with Ta_2O_5, then MnO at the very top of the sample. The TaO_xN_y stoichiometry used in the simulation is TaON.

The thickness of the Ta_2O_5 layer at the interface of MnO_x/TaON has been estimated as well as the thicknesses of the MnO_x overlayers using SESSA simulations, as follows: First, I considered a monolayer of Ta_2O_5 with a thickness of ~0.3 nm as a preliminary layer supported on a TaON substrate. Second, the Ta_2O_5 layer thickness is systematically varied until the relative photoelectron intensity ratio of Ta $4f$ (Ta_2O_5) to the Ta $4f$ (TaON) matches the experimentally-determined values reported in Figure 6.11 for the bare substrate. Third, three MnO_x layers atop the Ta_2O_5/TaON sample surface are added, as shown in Figure 6.4, with any preliminary thicknesses such that the total thickness of the three MnO_x overlayers (MnO, Mn_2O_3, and MnO_2) is equal to the average MnO_x thickness determined by cross-sectional TEM in Table 6.1. For example, TEM measurements for the so-called "2 nm MnO_x/TaON" sample showed an average thickness of 2.07 nm MnO_x, so the total thicknesses of the three layers of MnO_2, Mn_2O_3, and MnO should be equal to 2.07 nm.

Fourth, the thicknesses of the three layers of MnO_2, Mn_2O_3, and MnO were systematically varied, keeping the total thickness the same, until the normalized relative integrated photoelectron intensity ratio of Mn $2p_{3/2}$ (MnO_x overlayers) to the Ta $4f$ (Ta_2O_5) match those in the experimental results. In other words, the relative peak area of Ta $4f$ (Ta_2O_5) to Ta $4f$ (TaON), and the relative peak area of Mn $2p_{3/2}$ (MnO_x layers), are identical to those from the experimental results in Figure 6.11 and Figure 6.12(c-d). Simulations were done at the two-photon excitation energies, 2003 eV and 4000 eV, for the four samples, 0, 2, 5, and 7 nm MnO_x/TaON.

Two model systems were considered in the calculations: (1) a model with flat or planar layers, and (2) a model at which the layers has a degree of roughness that is more closely resembling the actual morphology based on data provided by the cross-sectional TEM in Figure 6.7 - 6.8 and Table 6.1. Various aspects of information for the sample, type and energy of the source, experimental geometry, spectrometer settings, and other parameters should be carefully implemented in SESSA software for reliable results.

Firstly, the sample parameters are: The atomic densities (number of atoms per unit volume) of Ta_2O_5 and TaON are equal to 8.6517×10^{22} cm^{-3} [308] and 9.3789×10^{22} cm^{-3} [309], respectively.

While the atomic densities for MnO [310], Mn_2O_3 [311], and MnO_2 [312] are equal to 9.569×10^{22} cm^{-3}, 9.540×10^{22} cm^{-3}, and 1.0754×10^{23} cm^{-3}, respectively. The atomic densities used are for the bulk materials. The energy bandgap between the valence and conduction bands of Ta_2O_5 and TaON was set to 3.9 eV and 2.4 eV, respectively.[36, 272, 273] While the bandgap of MnO, Mn_2O_3, and MnO_2 was set to 3.6 eV, 2.2 eV, and 1.77 eV, respectively.[36, 277, 278, 313, 314]

Secondly, the geometric parameters were implemented in SESSA in a way that resembles the experimental geometry. The orientation of the photon source axis with respect to the sample surface normal, and the analyzer axis, and the photon polarization vector are specified in SESSA in spherical coordinates in a fixed frame of reference using two angles: (1) φ-angle is the angle that rotates counterclockwise around the z-axis starting from the +x-axis, (2) θ-angle is the angle that rotates clockwise around the y-axis starting from +z-axis. Table 6.4 shows the geometric settings used in our simulations based on the HIKE experimental setup using X-ray from beamline KMC-1, BESSY II, Germany.

Table 6.4. Geometric settings implemented in SESSA software according to the experimental arrangement for the investigated MnO_x/TaON samples (see Figure 6.4). The red line in the diagram shows the direction of each orientation axis with respect to spherical coordinates in a fixed frame of reference.

Orientation of	φ-angle	θ-angle	Diagram
sample surface normal	350º	90º	
Analyzer axis ($\vec{P}$)	0º	90º	
Source axis	270º	90º	
Polarization vector ($\vec{\varepsilon}$)	0º	90º	

Furthermore, according to equation (2.13), as the synchrotron photon momentum vector $\vec{k}$ is applied horizontally in the same plane of the photon polarization vector $\vec{\varepsilon}$ and the photoelectron direction $\vec{P}$, the angle φ is equal to $0°$. In our simulations, the angle between the photoelectron direction $\vec{P}$ and the normal n to the sample surface is $10°$.

The estimated thicknesses of the Ta_2O_5 and the MnO_x layers (MnO-Mn_2O_3-MnO_2) resulted from SESSA simulation, at excitation energies, 2003 and 4000 eV, considering planar and rough layers are presented in Figure 6.17(a-d), and values are tabulated in Table C.2 and Table C.3, respectively.
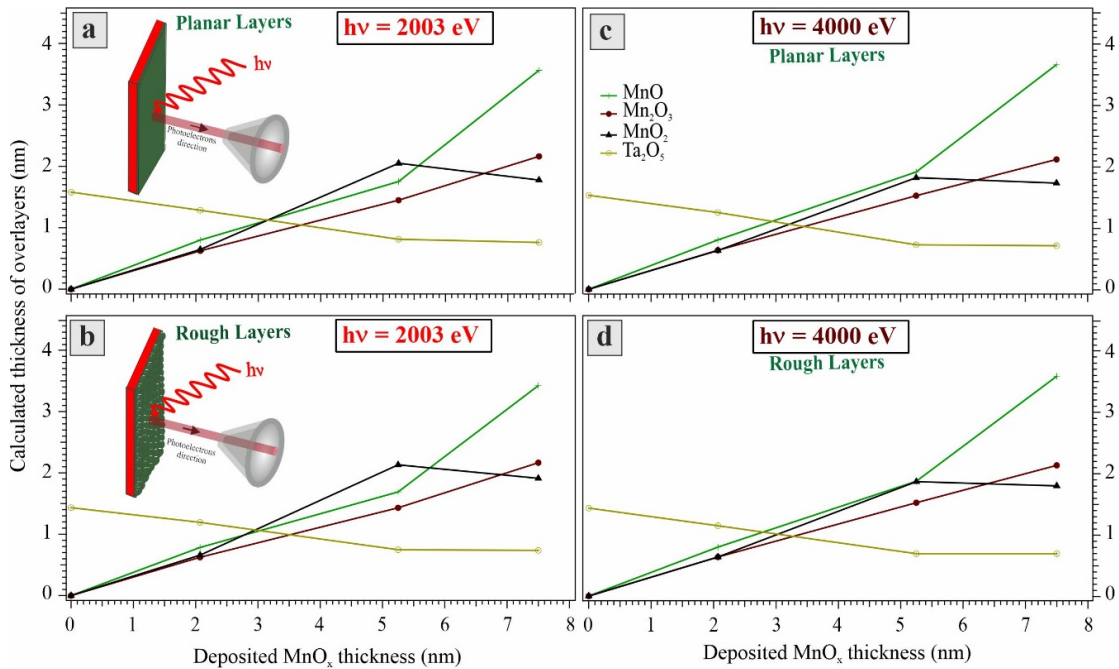
Figure 6.17. SESSA simulations of the thicknesses of Ta_2O_5 and MnO_x overlayers (MnO, Mn_2O_3, and MnO_2) as a function of deposited MnO_x thickness. The calculations were carried out using the photon excitation energy ($h\nu$ = 2003 eV), modeling the layers as (a) planar, and (b) rough, and at $h\nu$ = 4000 eV, assuming (c) planar layers, and (d) rough layers.

Results showed that the calculated thicknesses of Ta_2O_5 and MnO_x layers obtained at the 2003 eV excitation energy are very close to that at 4000 eV, as shown in Figure 6.17(left *vs.* right panel), which is expected since spectra at both excitation energies were collected at the same spot on the sample. Moreover, no significant differences can also be observed for the two different morphological models, the planar and the rough 3D surface, at the two excitation energies (2003 eV and 4000 eV). Simulation results showed that the Ta_2O_5 layer thickness

decreases from 1.58 to 0.76 nm, with MnO_x deposition up to 7.5 nm, with a percentage of 52% (Figure 6.18). The thicknesses of the Mn_2O_3 and MnO_2 layers at the interface increase with increasing the MnO overlayer. An average thickness of Ta_2O_5 and MnO_x layers at 2003 eV and 4000 eV ($d_{average}$) using the planar model was used to estimate the number of O atoms in each layer. Nevertheless, the thicknesses values assuming rough layers at 2003 and 4000 eV are also tabulated in Table C.3 for comparison.
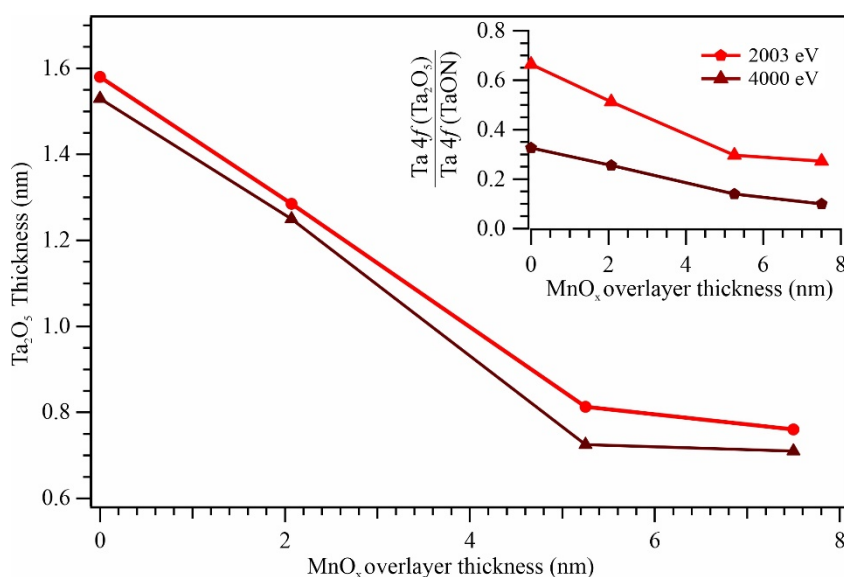
Figure 6.18. The calculated Ta_2O_5 thickness using SESSA as a function of increasing the MnO_x overlayer thickness at photon excitation energy 2003 eV (*red*) and 4000 eV (*brown*). The calculations were undertaken, modeling the TaON as a planar substrate with Ta_2O_5 on the top. The exact Ta_2O_5 thicknesses are tabulated in Table C.2. The inset shows the relative normalized integrated photoelectron intensities ratio of Ta $4f$ (Ta_2O_5) to Ta $4f$ (TaON).

To estimate the amount of oxygen atoms reduced in the Ta_2O_5 layer compared to those oxidizing the MnO to Mn_2O_3 and MnO_2 in each sample, the average thickness for each compound (Ta_2O_5, MnO, Mn_2O_3, and MnO_2) at excitation energies 2003 and 4000 eV (Table C.2 and Table C.3) should be considered as well as knowing the number of O atoms per unit cell for each structure and the unit cell volume, assuming bulk-like densities of layers. Those values were obtained from the crystallography open database[315, 316] and tabulated in Table 6.5.

Table 6.5. The atomic densities, cell volume, and the number of oxygen atoms per unit cell for bulk MnO, Mn_2O_3, MnO_2, and Ta_2O_5 layers.

Layers	Atomic Density (#/cm³)	Cell Volume (cm³)	Number of oxygen atoms/unit cell	References
MnO	9.569×10^{22}	8.360×10^{-23}	4	[310]
Mn_2O_3	9.540×10^{22}	8.386×10^{-22}	48	[311]
MnO_2	1.075×10^{23}	5.579×10^{-23}	4	[312]
Ta_2O_5	8.652×10^{22}	9.709×10^{-22}	62	[308]

The number of oxygen atoms that oxidizes MnO or reduced from Ta_2O_5 for each sample was calculated as follows, taking the 7.5 nm MnO_x planar layers sample as an example:

SESSA simulations showed that the 7.5 nm MnO_x consists of 2.14 nm Mn_2O_3 + 1.75 nm MnO_2 + 3.61 nm MnO on the top of 0.74 nm Ta_2O_5. The number of O atoms added to MnO to oxidize it to Mn_2O_3 and MnO_2 is calculated as follow

1) For 2.14 nm Mn_2O_3

- For 1 cm² area of bulk Mn_2O_3, 48 oxygen atoms exist in Mn_2O_3 of 8.386×10^{-22} cm thickness.[311] So, the total number of O atoms existing in Mn_2O_3 of 2.14×10^{-7} cm thickness is 12.2×10^{15} O atoms.

Based on the oxidation reaction of MnO to Mn_2O_3 [*i.e.,* $2MnO + O \rightarrow Mn_2O_3$], there is only one O atom out of the three O atoms in Mn_2O_3 is added to MnO to oxidize it to Mn_2O_3

Therefore, $\Delta O_{MnO \rightarrow Mn_2O_3}$ (number of O atoms added to MnO to oxidize it to Mn_2O_3) should be one-third of the total number of O atoms in the 2.14 nm Mn_2O_3, which is equal to **4.07×10^{15}** O atoms.

2) For 1.75 nm MnO_2

- For 1 cm² area of MnO_2, 4 O atoms exist in MnO_2 of 5.579×10^{-23} cm thickness.[312] So, the total number of O atoms existing in MnO_2 of 1.75×10^{-7} cm thickness is 12.5×10^{15} O atoms.

Based on the oxidation reaction of MnO to MnO_2 [*i.e.,* $MnO + O \rightarrow MnO_2$], there is one O atom out of the two O atoms in MnO_2 is added to MnO to oxidize it to MnO_2

Therefore, $\Delta O_{MnO \rightarrow MnO_2}$ (number of oxygen atoms added to MnO to oxidize it to MnO_2) should be one-half of the total number of O atoms in the 1.75 nm MnO_2, which is equal to **6.25×10^{15}**

O atoms.

Therefore, the total number of O atoms added to MnO to oxidize it into 2.14 nm Mn_2O_3 and 1.75 nm MnO_2 (ΔO_{MnO}) is

$$\Delta O_{MnO} = \Delta O_{MnO \rightarrow Mn_2O_3} + \Delta O_{MnO \rightarrow MnO_2}$$

$$= (4.07 \times 10^{15}) + (6.25 \times 10^{15}) = \mathbf{10.3 \times 10^{15}} \text{ atoms}$$

3) For 0.74 nm Ta_2O_5

Upon deposition of 7.5 nm MnO_x on Ta_2O_5/TaON, the Ta_2O_5 layer reduced by 0.82 nm, which is the thickness of Ta_2O_5 in the bare substrate (1.56 nm) minus the Ta_2O_5 thickness for 7.5 nm MnO_x sample (0.74 nm), as tabulated in Table C.2. Here, the number of O atoms in 0.82 nm of Ta_2O_5 is calculated the same way as for the previous steps.

- For 1 cm^2 area of Ta_2O_5, 62 oxygen atoms exist in 9.709×10^{-22} cm thickness of Ta_2O_5.[308] Therefore, there are $\mathbf{5.24 \times 10^{15}}$ oxygen atoms ($\Delta O_{Ta_2O_5}$) in Ta_2O_5 of 0.82×10^{-7} cm thickness.

The calculations indicate that the number of O atoms reduced from Ta_2O_5 ($\mathbf{5.24 \times 10^{15}}$ atoms) constitutes almost half (51%) the number of oxygen atoms that oxidize MnO ($\mathbf{10.3 \times 10^{15}}$ atoms) for a 7.5 nm MnO_x sample considering a bulk-like planar layer. The percentages for other samples considering planar and rough layers are tabulated in Table C.2 and Table C.3, respectively. All the numerical results assuming planar or rough layers show that the number of O atoms reduced from Ta_2O_5 represents 43-52% of the number of oxygen atoms that oxidize MnO into Mn_2O_3 and MnO_2.

Three reasons can explain the difference in the number of O atoms that are reduced from Ta_2O_5 to those oxidizing the MnO: The first is due to surface oxidation to samples, shown in the experimental results, and has not been considered in the calculation. The second reason may be due to a possible error in the thicknesses obtained from TEM, which are the basis of the calculated thickness. The third reason is that the atomic densities used in the calculation were for bulk materials that are not in compliance with amorphous MnO_x samples, as confirmed by XRD in Figure 6.6.

In order to prove the suggested factor, further calculations are made, first by correcting the thickness ($\mathbf{d_{corrected}}$) and second by correcting the atomic density ($\Delta \rho$) until the number of oxygen atoms reduced in Ta_2O_5 is equal to the number of oxygen atoms that oxidizes the MnO (*i.e.,* % of $\frac{\Delta O_{MnO}}{\Delta O_{Ta_2O_5}} = 100$ %).

First, the thickness ($d_{average}$) of each layer of MnO, Mn$_2$O$_3$, and MnO$_2$ is reduced by sub nms, *i.e.,* few monolayers, until the number of O atoms reduced in Ta$_2$O$_5$ is equal to the number of oxygen atoms which oxidizes MnO. The corrected thicknesses ($d_{corrected}$) for MnO$_x$ layers are tabulated in Table C.5 in Appendix C. The change in the thicknesses ($d_{average} - d_{corrected}$) are within the standard deviation error bars in Figure 6.19. The total accuracy is estimated to be approximately ± 5 %, which is within the experimental accuracy.
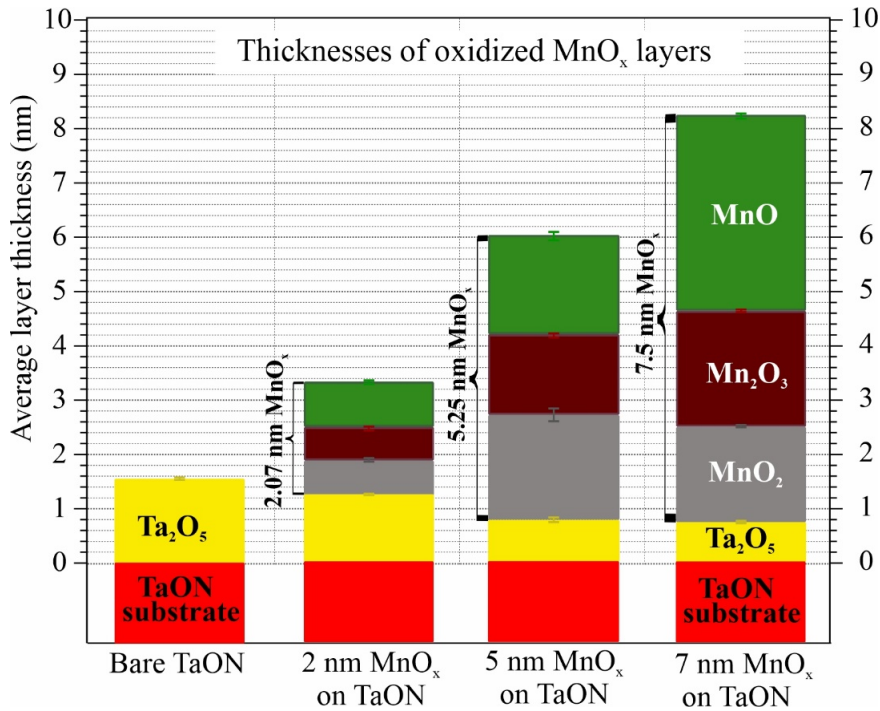
Figure 6.19. Average thicknesses of MnO, Mn$_2$O$_3$, MnO$_2$, and Ta$_2$O$_5$ layers, calculated using SESSA software for the TaON bare substrate, 2, 5, and 7 nm MnO$_x$ on Ta$_2$O$_5$/TaON assuming planar layers. The average layer thickness is the mean thickness at photon excitation energy 2003 eV and 4000 eV. The data are plotted with standard deviation error bars. Tabulated values for the thicknesses are provided in Table C.2.

Second, the amorphization of the MnO$_x$ films is considered to resemble the actual structure of the deposited samples. This was done by reducing the atomic densities of the MnO, Mn$_2$O$_3$, and MnO$_2$ until the number of O atoms reduced in Ta$_2$O$_5$ is equal to those oxidizing MnO. The corrected atomic densities values for MnO$_x$ layers are shown in Figure 6.20 and tabulated in Table C.6 in Appendix C.
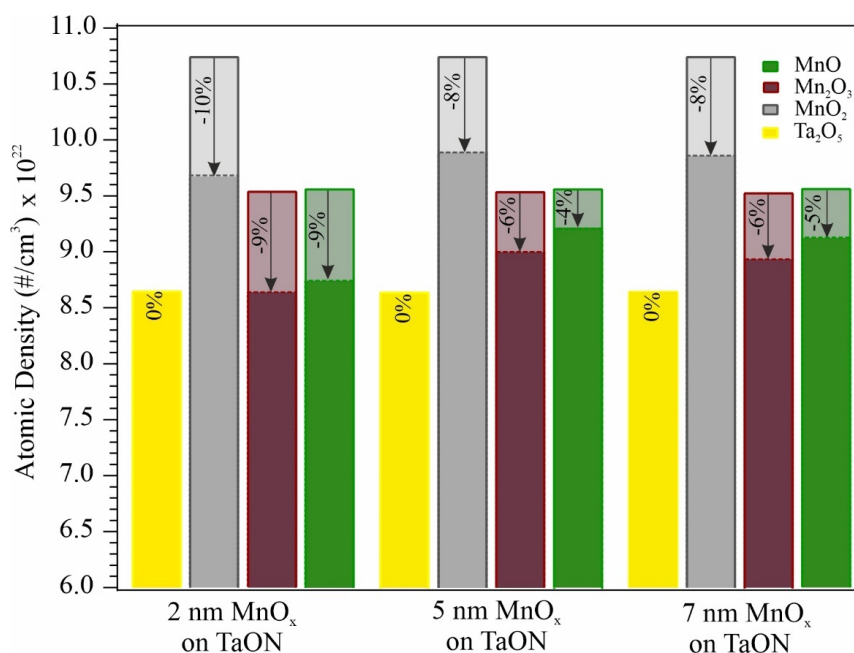
Figure 6.20. Corrected atomic densities for the MnO_x layers: MnO (*green*), Mn_2O_3 (*brown*), MnO_2 (*gray*), at which the amount of O reduced from the Ta_2O_5 is equal to those oxidizing the MnO into Mn_2O_3 and MnO_2. The percentages show the reduction in the atomic densities after considering the amorphization of the MnO_x layers.

6.5   Conclusions

A 5-fold enhancement in the photocurrent was achieved upon the deposition of MnO_x up to 5 nm on the TaON photoanode. The chemical composition and electronic structure changes at the interface between the semiconducting photoanode (TaON) and co-catalyst (MnO_x) systems were then investigated as a function of the thickness of the MnO_x overlayer, aiming to understand the role of MnO_x co-catalyst and the origin of the enhancement in the photocurrent. We employed the HAXPES spectroscopic technique for this purpose using two different excitation energies, 2003 and 4000 eV, to obtain information from different probing depths within the films. The TaON films were first prepared by nitridation of Ta_2O_5 at 850 °C. The phase structure of the prepared TaON films was identified by XRD, which showed the formation of a pure β-TaON monoclinic phase. MnO_x co-catalyst was deposited from Mn^{II} precursor using atomic layer deposition, producing different thicknesses of 2, 5, 7, 26 nm MnO_x films atop the TaON photoabsorber. The structure and morphology of the samples were characterized in terms of XRD, TEM, and EDX. The MnO_x thicknesses were measured by ellipsometry and confirmed

by cross-sectional TEM.

HAXPES studies showed the presence of Ta_2O_5 layers at the surface of all samples, which was explained by partial surface oxidation of the TaON due to exposure to air. This Ta_2O_5 layer hinders hole transfer to the surface at which a water oxidation reaction occurs since there is an unfavorable mismatch in the valence band-edge levels between Ta_2O_5 and TaON. [273, 275, 279] This mismatch is confirmed experimentally from valence band spectra since the valence band maximum positions of Ta_2O_5 and TaON *vs.* the Fermi level are 3.9 eV and 2.3 eV, respectively. Furthermore, it was found that by depositing MnO_x on the TaON photoabsorber, the amount of Ta_2O_5 at the interface reduces with the increasing thickness of MnO_x, which implies part of the role of the MnO_x co-catalyst layer may be to reduce the amount of Ta_2O_5, thereby facilitating hole transfer. In parallel to Ta_2O_5 reduction, there is an oxidation of the deposited MnO once it attaches to the Ta_2O_5 layer. By Fitting Mn $2p_{3/2}$ HAXPES spectra of the investigated samples using Mn $2p_{3/2}$ spectra of MnO_x references of pure phases, it shows the formation of $Mn_2^{III}O_3$ and a Birnessite-like phase δ-MnO_2 ($Mn^{III/IV}$) at the interface. It is interpreted as the MnO at the interface steals oxygen from Ta_2O_5, leading to a reduction of Ta_2O_5 at the interface in parallel to the oxidation of MnO to the Mn_2O_3 and birnessite-like phase.

To confirm our hypothesis, insights from theoretical calculations using SESSA software were performed as a useful aid to better understand the experimental results. SESSA allowed the estimation of the thicknesses of Ta_2O_5, MnO, Mn_2O_3, and MnO_2 layers. Then the calculations showed that the number of O atoms reduced in the Ta_2O_5 layer represents only half that gained by MnO and leads to oxidation of MnO to MnO_2 and Mn_2O_3.

An essential outcome of this study is that the deposition of manganese oxide catalysts on the top of the TaON-based photoanode enhances the water-oxidation activity of the photoanode by reducing the unfavorable Ta_2O_5 layer at the TaON surface. Favorable contact between tantalum oxynitride and transition metal oxide is critical not only to maintain the stability of photoanode but ultimately to achieve efficient transport of photogenerated holes to the surface for the water oxidation reaction.

Chapter 7

Summary and Outlook

My Ph.D. studies reported in this thesis focused on characterizing the chemical composition and electronic structure of the transition metal oxide – MnO_x films as a (co-)catalyst for water oxidation reaction using various synchrotron-based spectroscopic techniques. In this chapter, I summarize the findings based on the measurements shown in *Chapter 4*, *Chapter 5,* and *Chapter 6*. In the outlook section, I briefly highlight my perspectives on future experiments, building on the experience accumulated with MnO_x as a catalyst or co-catalyst to TaO_xN_y photoabsorber systems.

7.1   Summary

One of the milestones in satisfying the steadily increasing energy demand of modern society is to produce energy from sustainable resources rather than using conventional non-renewable resources like fossil fuels, which is also a source of CO_2, responsible for climate change and global warming problems. The efficient conversion of solar energy into chemical energy cleanly and sustainably would allow energy storage as solar fuels. However, achieving this remains one of the greatest challenges for the scientific community. (Photo-)electrochemical water splitting is a process that fulfills key criteria for energy storage and has been the subject of significant attention. An essential requirement for efficient water splitting is the development of catalysts for the mechanistically complex and sluggish water oxidation half-reaction: $2H_2O \rightarrow O_2 + 4H^+ + 4e^-$. In nature, this process is catalyzed within Photosystem II (PS II) by a calcium-manganese oxide complex. One approach to developing water oxidation catalysts is to mimic the natural process. To this end, manganese-based materials have spurred much interest and were chosen to be the specified sample studied in this thesis. MnO_x has many advantageous properties like being non-toxic, innocuous, earth-abundant. It can exist in various oxidation states, 2+, 3+, 4+, 5+, 6+, and 7+, making it highly flexible in carrying charges, charge rearrangement among Mn ions, and versatile to undergo a range of redox reactions. The various composition and structural characteristics of MnO_x-based systems can offer a significant degree of freedom to formulate efficient catalysts. However, at the same time, the pathways to achieving such a goal are challenging. Thus, the thesis goal is to elucidate the electronic structure and the chemical

composition of a catalyst, which are crucial to understanding the water oxidation reaction mechanisms.

Chapter 4 reports the electronic structure of the MnO_x films electrodeposited from Mn^{II} electrolytes at different pH using the LiXEdrom experimental endstation coupled with soft X-ray absorption spectroscopy (XAS). XAS is highly sensitive to the unoccupied states and can be employed to demonstrate the evolution of the Mn oxidation state among a range of MnO_x films. The MnO_x films electrodeposited under different pH showed diversity in their catalytic activity. In this study, seven samples were electrodeposited from electrolytes at different pH, A3, A2, A1, E0, B1, B2, and B3, ordered from highly acidic 'A3' to – neutral 'E0' – to highly basic 'B3' samples. Soft XAS has been performed at the Mn $L_{2,3}$-edge and the O K-edge on these MnO_x films, aiming to understand the influence of compositional changes of different MnO_x phases in correlation with the previously identified catalytic activity of the samples. The XA spectra revealed a gradual increase of the overall mean Mn oxidation state with decreasing pH during the electrodeposition process. Fitting the XA spectra showed that all the MnO_x catalysts include mixtures of Mn_2O_3, Mn_3O_4, and birnessite in different proportions. The amount of Mn_3O_4 is almost the same for the acidic and basic samples. The amount of MnO and MnO_2 present in the samples is minimal (< 10%). The sample with the highest catalytic activity electrodeposited at neutral pH (*i.e.,* E0) showed a composition of nearly equal amounts of the birnessite-like phase and Mn_2O_3. However, the catalytic activity gets worse when any of these phases dominate with less extent of Mn_3O_4. This study did not reveal an isolated single MnO_x structural composition responsible for the optimally achieved catalytic activity, but the interplay of birnessite and Mn_2O_3 could drastically enhance the catalytic activity. Moreover, the findings of this study gave us the knowledge of investigating different MnO_x catalysts and allowed us to control the preparation conditions to create efficient MnO_x films. The study also paved the way toward an extensive *in situ* study of MnO_x film electrodeposited near neutral condition, but under applying potentials under turnover conditions as reported in detail in *Chapter 5*.

Using *in situ* soft XA and RIX spectroscopy, the transformations and electrochemical analysis in the deposited MnO_x electrocatalysts induced by applying oxidizing potentials (0.75 — 2.25 V_{RHE}) was revealed. This potential range is selected to track the electronic structure changes of the MnO_x catalysts before, during, and after the water oxidation reaction. The synergetic coupling of XAS with RIXS techniques allows to directly probe the unoccupied as well as occupied manganese $3d$ electronic valence states, which govern the functionality of the catalysts during water oxidation. [149] XAS was employed to demonstrate the evolution of the Mn oxidation state under applied potentials, while RIXS provided fine details of the electronic structure because the process is element selective and site-specific. In the RIXS process at metal

L-edges, an electron from spatially localized $2p$ orbitals is excited to the $3d$ unoccupied orbitals. This creates a core-hole that can be filled by an electron from the occupied metal $3d$ orbitals, releasing a photon. The energy difference between the incoming and outgoing photons is denoted as a "photon energy loss" and reflects the valence excitations, such as the *d-d* excitations and charge transfer transitions. The *in situ* XAS experimental results revealed that the Mn oxidation state in the MnO_x film increases under applying more positive potential until a full transformation of the MnO_x film into a birnessite state at *ca*. 1.45 V_{RHE} (just before oxidation of water), then no further change in the Mn oxidation state occurs up to 2.25 V_{RHE}. Whereas *in situ* RIXS analysis reveals changes in the electronic state of MnO_x at potentials up to 1.75 V_{RHE}. As confirmed by theoretical calculation, the continuous change in the RIXS spectra between 1.45 and 1.75 V_{RHE} suggests an extent changes in orbital hybridization between Mn $3d$ and O $2p$, up to 1.75 V_{RHE}, even after saturating the Mn oxidation state at 4+. It reveals that charge transfer from O in the ligand to Mn metal is needed to bolster fast water oxidation catalyzed by MnO_x achieved at 1.75 V_{RHE} and did not enhance with the application of higher potentials (up to 2.25 V_{RHE}). No evidence for including manganese species with higher oxidation states than 4+ to the catalytic mechanism. The O^- species associated with the CT is believed to be of crucial importance for efficient electrocatalytic water oxidation.

Based on these findings, my Ph.D. study was extended onto the electronic structure of a more complex system of MnO_x-TaON but efficient for solar water-splitting devices. The MnO_x, as a water oxidation co-catalyst, is coupled to the TaON photoanode to improve the photoanode performance toward OER. The MnO_x film thickness is crucial to the activity, likely due to changes in the chemical and electronic structure at the interface. Analogous to the MnO_x system, *Chapter 6* reports the electronic structure and chemical composition changes at the MnO_x/TaON interface as a function of increasing the thickness of the MnO_x overlayer (2, 5, 7, and 26 nm) using the HIKE experimental endstation coupled with hard X-ray PES (or HAXPES) technique. The MnO_x co-catalyst deposited from Mn^{II} precursor using atomic layer deposition atop the TaON photoabsorber. The samples were characterized in terms of Voltammetry, XRD, TEM, and EDX. The MnO_x thicknesses were measured by cross-sectional TEM. A 5-fold enhancement in the photocurrent is achieved upon the deposition of MnO_x up to 5 nm on the TaO_xN_y photoanode. To understand this enhancement, the chemical composition and electronic structure of the samples were explored by the HAXPES study at two excitation energies, 2003 eV and 4000 eV, to obtain information from different probing depths within the films. The probing depths are ~7.3 nm and ~15.0 nm at the excitation energies, 2003 eV and 4000 eV, respectively. The Ta $4f$ spectra reveal the existence of the Ta_2O_5 layer at the surface of TaON for all the samples (*i.e.,* before depositing MnO_x films on the TaON photoabsorber). This Ta_2O_5 layer is

unfavorable for water oxidation reaction since there is a mismatch in the valence band positions between Ta_2O_5 and TaON, hindering the transfer of photo-generated holes from the TaON to the surface where water oxidation occurs. The Ta 4*f* spectra also show that by depositing a thicker MnO_x overlayer, the Ta_2O_5 at the interface reduces while MnO oxidizes into Mn_2O_3 and birnessite-like phase. These findings are also confirmed by studying the core levels of Mn $2p_{3/2}$, Mn 3*s*, Ta $4p_{3/2}$, N 1*s*, and C 1*s*. Our interpretation suggests that MnO at the interface consumes oxygen from Ta_2O_5, leading to a reduction of Ta_2O_5 and oxidation of Mn^{II} into $Mn^{III/IV}$ oxide. Quantitative analysis using SESSA simulations were then performed to calculate the thicknesses of the Ta_2O_5, MnO, Mn_2O_3, and MnO_2 layers for each sample. Then the number of O atoms transferred from the Ta_2O_5 layer was calculated and estimated to be around half that oxidized the MnO to Mn_2O_3 and MnO_2. An essential outcome of this study is the enhancement of the water-oxidation activity of the TaON-based photoanodes via the coupling of the MnO_x co-catalyst overlayer, reducing the inactive and unfavorable Ta_2O_5 layer, which would facilitate the photogenerated hole transfer process for the water oxidation reaction.

7.2   Outlook

In this section, I am presenting my perspectives and thoughts on future experiments.

Study of MnOx films on TaON in water vapor and bulk liquid

In this dissertation, the interfacial electronic structure and chemical composition of MnO_x co-catalyst on the TaON photoanode is well-studied and investigated in the UHV environment. However, when the photoelectrode is inserted in aqueous electrolytes for water splitting catalysis, it is necessary to understand changes that occur to the surface chemistry when exposed to an electrolyte. For that, I propose an *in situ* and *operando* study of MnO_x co-catalyst on TaON conducted in water vapor using soft X-rays-*Near Ambient Pressure X-ray Photoelectron Spectroscopy* (NAP-XPS). It will help to elucidate how exposure to the aqueous electrolyte affects the surface chemical composition of the MnO_x films (particularly hydroxylation of the film) and the electronic structure of the interface. The results are, in general, relevant to understand modification to the system at the early stages of sample/aqueous electrolyte interface formation. The same measurements can be conducted using tender X-ray photoemission in the presence of a bulk-like electrolyte film. Tender X-rays will probe the manganese oxide films underneath a bulk-like electrolyte film. The interfacial properties can be studied as a function of changing conditions of applied bias and illumination with a solar simulator.

Improving the efficacy of Manganese oxides catalysts - Doping in Nafion

Manganese oxide nanoparticles were demonstrated to be a promising system for water oxidation catalysis.[46] Previous experiments showed that the catalysts exhibited high turnover frequencies for catalytic water oxidation when embedded into a Nafion membrane.[317] For that, the proposed study of Mn_xO_y nanoparticles doped into a hydrophilic Nafion matrix is expected to enhance the stability of MnO_x, allows spatial separation of Mn_xO_y NPs, and sustaining efficient mass-transport of water molecules to the catalytically active sites. This system already showed promising results.[146] However, more insights into the improved system of MnO_x are still required. The size of the MnO_x nanoparticles can be changed by using different manganese precursor complexes doped with Nafion.[46, 146] The catalytic activity strongly depends on the phase of the Mn_xO_y -NP, which can change actively with particle size. The influence of the MnO_x nanoparticle size on the evolution of metal-oxidation states, phase transformation, and the charge transfer transition between the oxygen in the ligand and the metal needs to be explored. For that, an *in situ* characterization using XAS/RIXS techniques would be an effective way to understand the valence excitations in the enhanced version of MnO_x in Nafion.

Appendix A

Supplemental information for *Chapter 4*

Radiation Damage Study
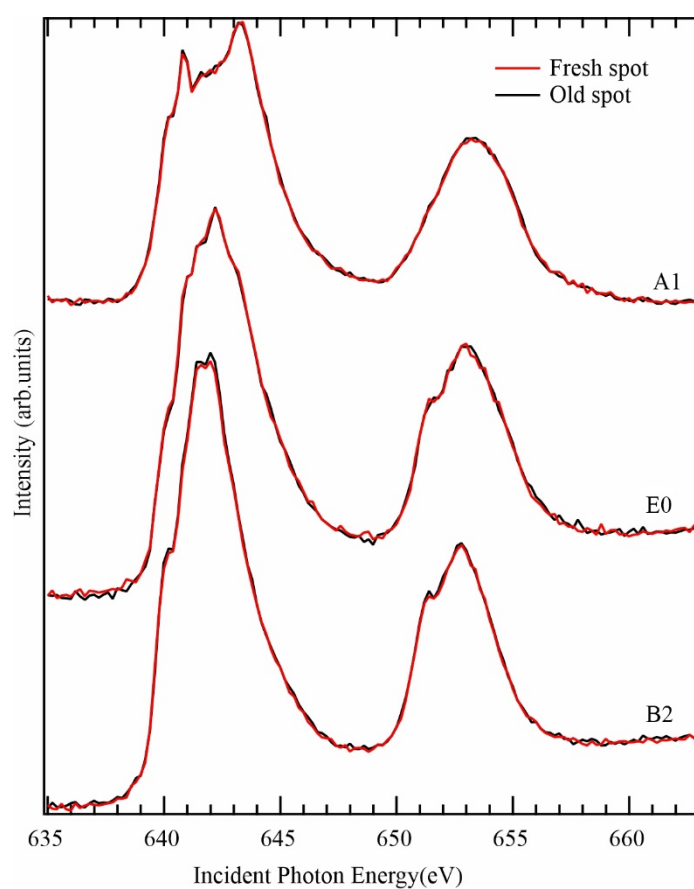
Figure A.1. Radiation damage study showing the Mn $L_{2,3}$-edge TEY-XA spectra of pH treated MnO_x thin films electrodeposited under acidic A1, neutral E0, and Basic B2 conditions. Spectra measured on a fresh spot are in *red*, while subsequent measurements on the same spot are presented in *black*. With the beamline settings used, spectra showed no changes either in the spectral features or the intensity.
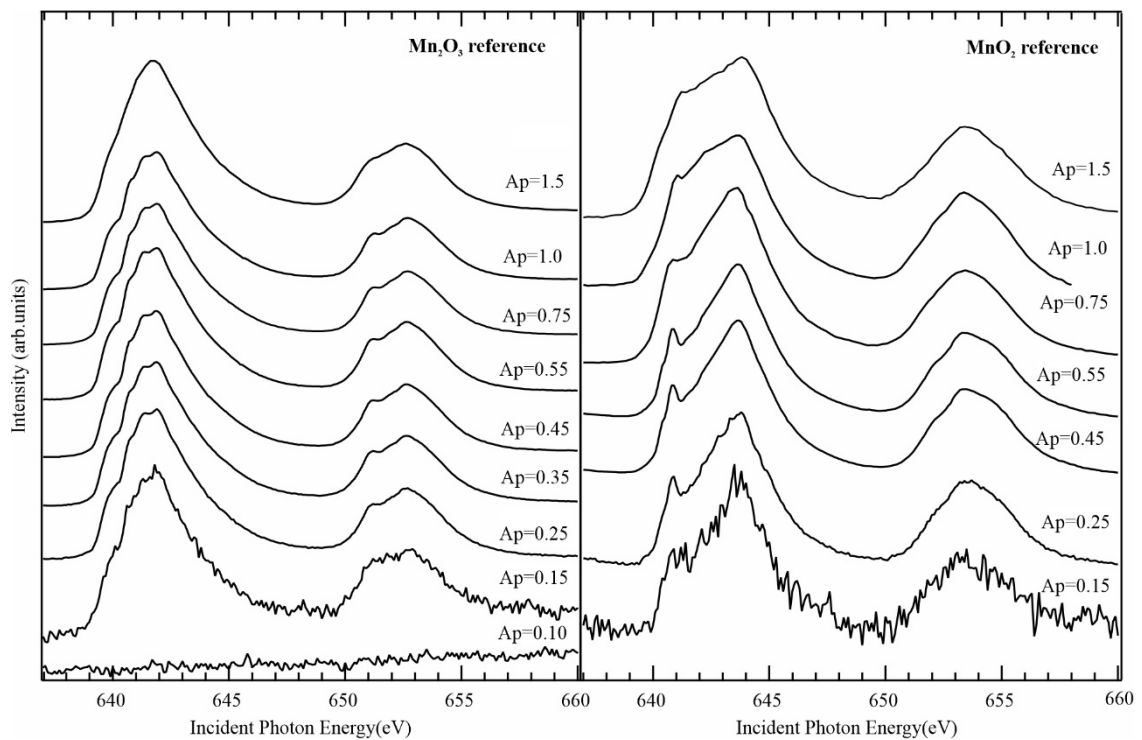
Figure A.2. Radiation damage study showing the Mn $L_{2,3}$-edge TEY-XA spectra of a) Mn_2O_3 and b) MnO_2 oxide powder taken at the same spot, starting with a very low photon flux as determined by opening the primary aperture located directly after the insertion device. The aperture increased from 0.1 mm × 0.1 mm, where no Mn signal was detected, to 1.5 mm × 1.5 mm. The spectra started to change for Mn_2O_3 at an aperture of 1.0, while for MnO_2 at an aperture of 0.75. All the spectra were collected with a beamline slit width of 20 μm.
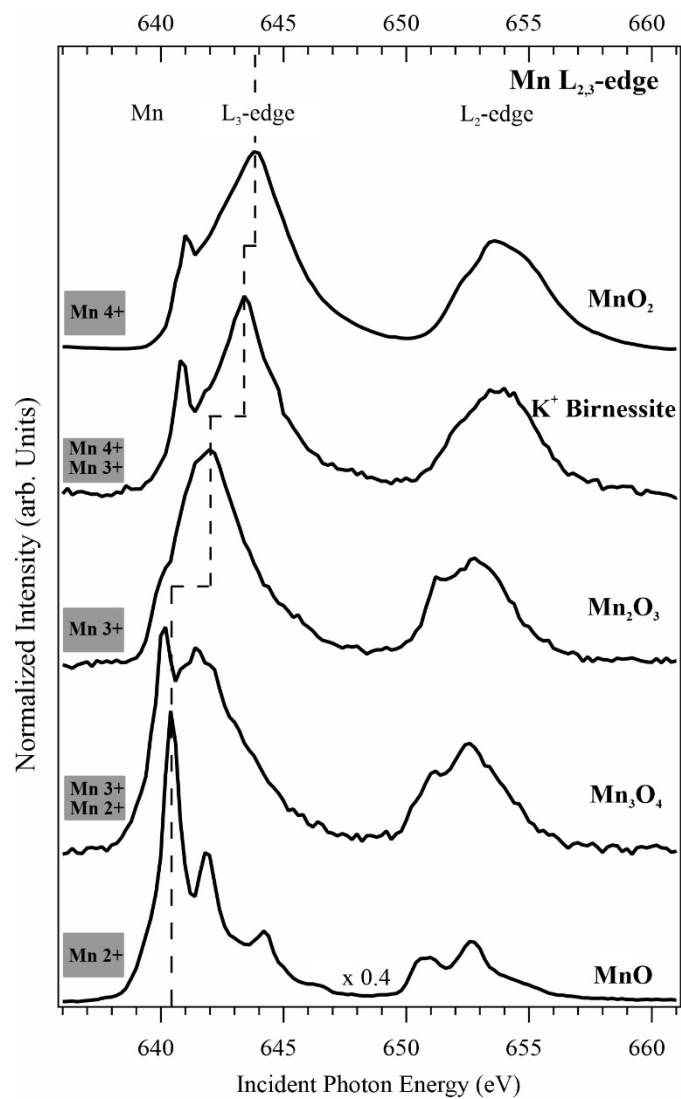
Figure A.3. Mn $L_{2,3}$-edge ($2p \rightarrow 3d$ transition) TEY-XA spectra for reference samples (MnO$_2$, K$^+$ birnessite, Mn$_2$O$_3$, Mn$_3$O$_4$, and Mn^{II} resembling MnO).[56] The oxidation state for each reference spectrum is labeled in the gray box.
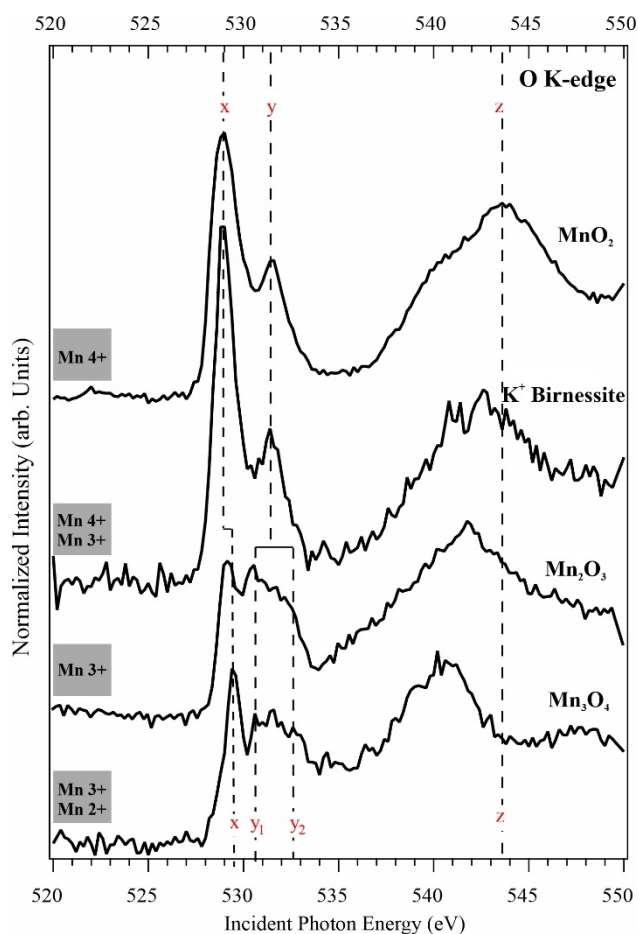
Figure A.4. O K-edge TEY-XA spectra for reference manganese oxide samples (MnO₂, K⁺ birnessite, Mn₂O₃, and Mn₃O₄).[56] The oxidation state for each reference spectrum is labeled in the gray box. MnO spectrum was excluded for the aforementioned reason stated within the text in *Chapter 4*.

Table A.1. The concentration of the H^+ and Ethylamine (EA) added to the Mn-precursor electrolyte used in the electrodeposition MnO_x films.

Catalyst	$[H^+]_{addition}$ mM[a]	$[EA]_{addition}$ mM
A3	20	–
A2	16	–
A1	10	–
E0	(2.7)	–
B1	–	6.3
B2	–	31.5
B3	–	126

[a]   *Values are based on a previously published work* [75]

Table A.2. Contribution of MnO_x phases fitted at the Mn $L_{2,3}$-edge as a linear combination of references of pure phases (MnO-like, Mn_3O_4, Mn_2O_3, MnO_2, and K^+ birnessite) and the calculated error from the fitting algorithm.[b]

Catalyst	MnO-like		Mn_2O_3		Mn_3O_4		MnO_2		K^+ Birnessite	
	α %	Error	β %	Error	γ %	Error	δ %	Error	ε %	Error
A3	3	0.8	0	1.6	32	2.3	7	2.0	58	2.4
A2	3	0.1	0	1.5	31	1.8	4	0.2	62	2.3
A1	2	0.6	2	1.2	33	1.5	3	1.5	60	1.9
E0	0	0.7	67	1.4	4	1.7	2	1.8	27	2.2
B1	0	0.9	57	1.7	29	2.0	0	2.1	14	2.6
B2	0	0.6	79	1.2	21	1.4	0	1.5	0	1.8
B3	0	0.6	75	1.2	25	1.4	0	1.4	0	1.7

[b]   Each parameter is calculated with an error ±1 standard deviation. With a random variation of these parameters by approximately ± 5%, the spectra start to show notable deviations in the feature heights. Although the composition of the samples is only approximated within this error, it is possible to clearly trace the qualitative development of the Mn phases in the MnO_x films as a function of pH.

Table A.3. Contribution of MnO_x phases derived from the fitting of the O K-edge XA spectra as a linear combination of MnO_x phases references (Mn_3O_4, Mn_2O_3, MnO_2, and K^+ birnessite) after applying the parameters used for fitting Mn $L_{2,3}$-edge XA spectra.

Catalyst	Mn_2O_3 %	Mn_3O_4 %	MnO_2 %	K^+ Birnessite %
A3	0	31	7	62
A2	0	32	5	63
A1	5	33	3	59
E0	68	4	2	26
B1	57	29	0	14
B2	78	22	0	0
B3	75	25	0	0

Appendix B

Supplemental information for *Chapter 5*
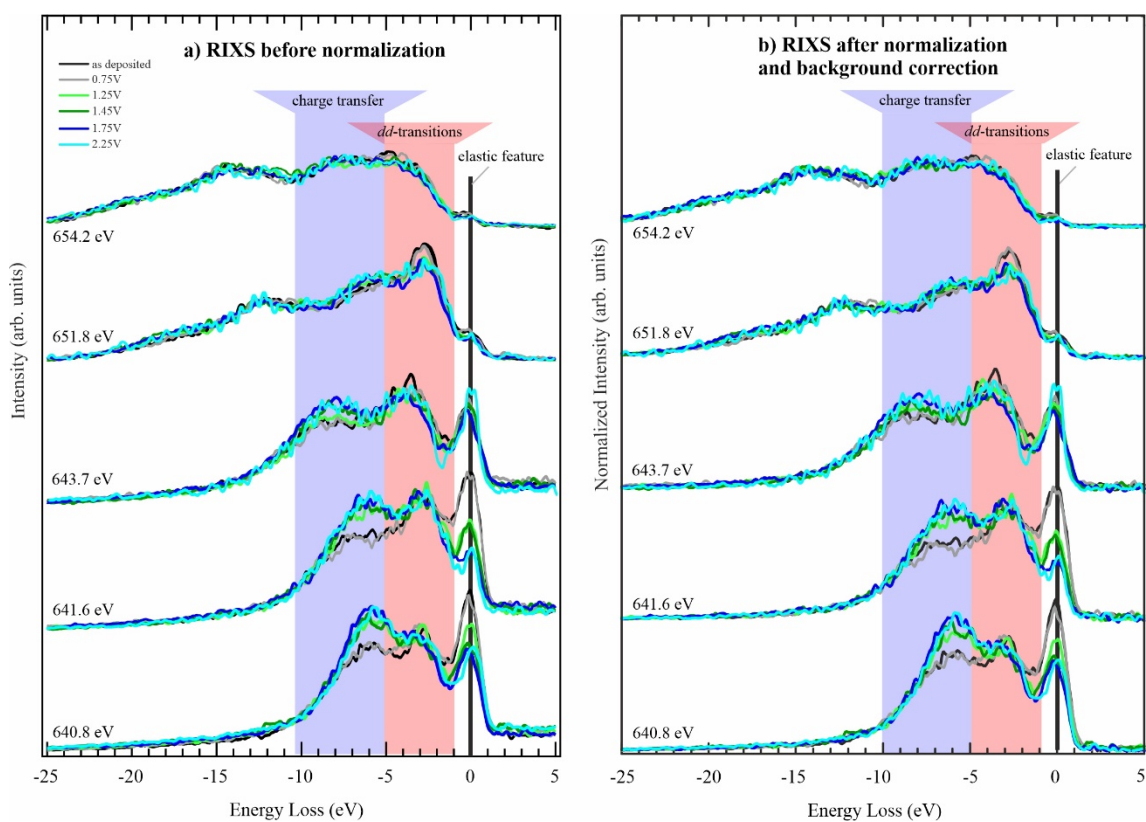
Figure B.1. *In situ* inelastic X-ray scattering a) raw spectra before any normalization
procedure, and b) after background correction due to the noise at the MCP channels and normalization to an
overall integrated intensity of 1. The spectra showed almost no change in the relative intensities of the
elastic peak, *d-d* transition, and the charge transfer peak after normalization and background correction.
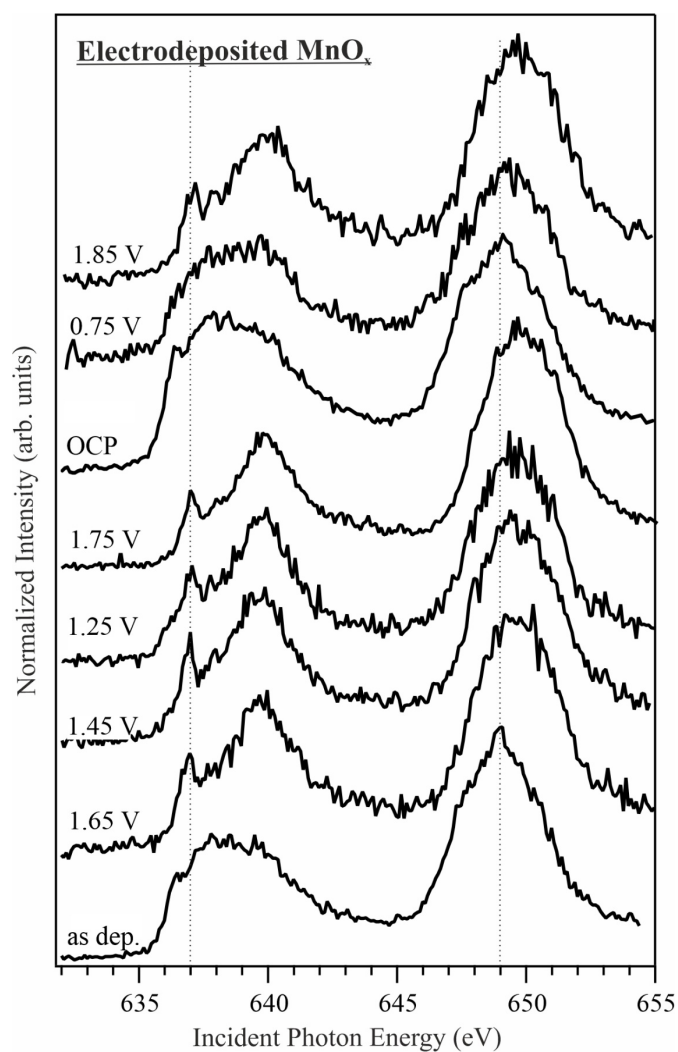
Figure B.2. Soft *in situ* PFY-XA spectra measured at the Mn $L_{2,3}$-edge for MnO_x in 0.1 M borate buffer (pH 9.2). The measurements were carried out after deposition with no potential applied (as dep. state or OCP, open circuit potential), then biasing the films with a random sequence of applied potentials, showing that the XA spectra are reversible and reproducible. The potentials are reported *vs.* reversible hydrogen electrode.

Appendix C

Supplemental information for *Chapter 6*
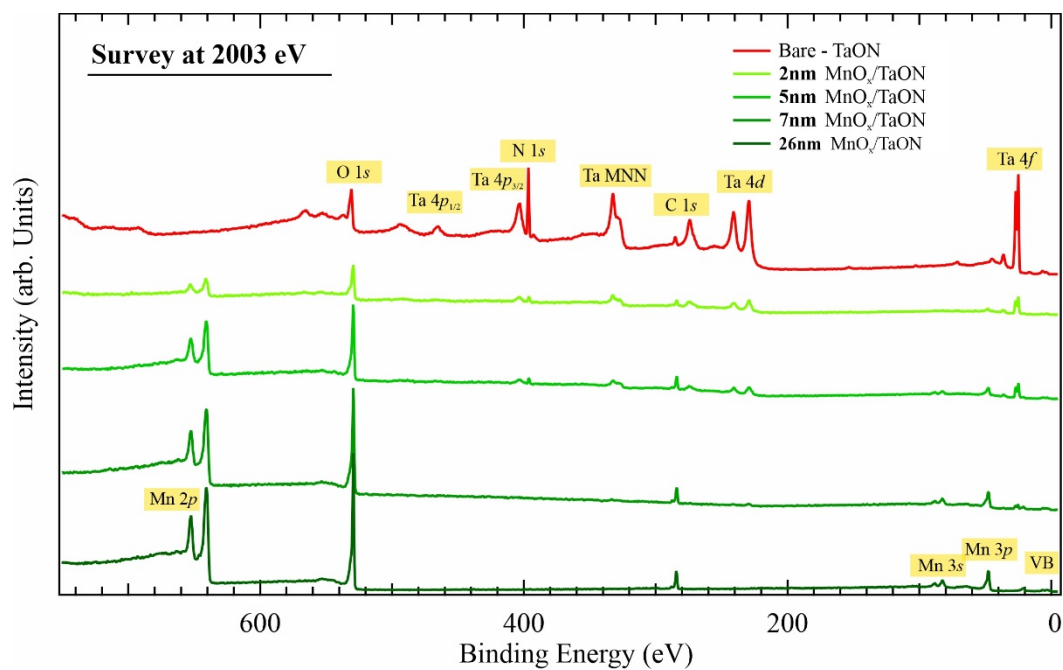
Figure C.1. Survey spectra for bare TaON substrate and 2, 5, 7, and 26 nm MnO_x/TaO_xN_y samples measured at the 2003 eV excitation energy.

Mn 2$p_{3/2}$ HAXPES Fitting

Table C.1. Fitted peak parameters of Mn 2$p_{3/2}$ using MnO, Mn₂O₃, and Birnessite references.

Peak	Peak Position (eV)		FWHM		Peak Area percentage within the total pattern (%)		Comments
	Used in this work	In literature	Used in this work	In literature	Used in this work	In literature	Literature = [155, 289]
Fitted peaks of Mn^{II}O (*red*, Figure 6.12) for **26 nm** MnO$_x$ sample at 4000 eV photon energy							
Mn^{II}O	640.1	640.2	1.15	1.23	24.0	24.0	Multiplet 1
	641.0	641.1	1.15	1.23	27.8	27.8	Multiplet 2
	642.0	642.1	1.15	1.23	22.1	22.1	Multiplet 3
	642.9	643.0	1.15	1.23	12.5	12.5	Multiplet 4
	644.1	644.2	1.15	1.23	4.70	4.70	Multiplet 5
	645.9	645.9	3.30	3.50	9.10	9.10	Satellite
Fitted peaks of Mn₂^{III}O₃ (*blue*, Figure 6.12) for **2 nm** MnO$_x$ sample at 4000 eV photon energy							
Mn₂^{III}O₃	640.8	640.8	1.75	1.75	18.9	18.9	Multiplet 1
	641.9	641.9	1.75	1.75	44.5	44.5	Multiplet 2
	643.1	643.1	1.75	1.75	25.3	25.3	Multiplet 3
	644.6	644.6	1.75	1.75	8.50	8.50	Multiplet 4
	646.2	646.2	1.75	1.75	3.10	3.10	Multiplet 5
Fitted peaks of Birnessite (*yellow*, Figure 6.12) for **2 nm** MnO$_x$ sample at 4000 eV photon energy							
Mn^{II}	638.7	639.75	0.87	0.87	1.80	1.80	Mn^{II} Multiplet 1
	639.9	640.95	0.87	0.87	1.28	1.28	Mn^{II} Multiplet 2
	640.7	641.75	0.87	0.87	0.75	0.75	Mn^{II} Multiplet 3
	641.6	642.65	0.87	0.87	0.54	0.54	Mn^{II} Multiplet 4
	643.1	644.15	0.87	0.87	0.54	0.54	Mn^{II} Multiplet 5
Mn^{III}	639.6	640.65	0.87	0.87	5.92	5.92	Mn^{III} Multiplet 1
	640.3	641.35	0.87	0.87	5.92	5.92	Mn^{III} Multiplet 2
	641.1	642.16	0.87	0.87	6.87	6.87	Mn^{III} Multiplet 3
	642.1	643.18	0.87	0.87	4.32	4.32	Mn^{III} Multiplet 4
	643.5	644.55	0.87	0.87	1.66	1.66	Mn^{III} Multiplet 5
Mn^{IV}	640.9	641.90	0.87	0.87	33.22	33.22	Mn^{IV} Multiplet 1
	641.9	642.92	0.87	0.87	21.26	21.26	Mn^{IV} Multiplet 2
	642.7	643.75	0.87	0.87	10.62	10.62	Mn^{IV} Multiplet 3
	643.7	644.78	0.87	0.87	3.32	3.32	Mn^{IV} Multiplet 4
	644.8	645.80	0.87	0.87	1.99	1.99	Mn^{IV} Multiplet 5

Table C.2. The thicknesses, the percentage of peak intensities due to Ta_2O_5, TaON, MnO, Mn_2O_3, and MnO_2 found in SESSA software, and the calculated number of oxygen atoms which oxidizes MnO layer or reduced in Ta_2O_5, assuming planar layers (model 1) at 2003 eV and 4000 eV excitation energies for the samples, 0, 2, 5, and 7 nm MnO_x/TaON.

Model I: Planar Layers									
Sample	Layer	hv = 2003 eV		hv = 4000 eV		Average Layer thickness		Number of oxygen atoms that		
		% of Ta 4f or Mn $2p_{3/2}$ peak[a]	d_1 (nm)	% of Ta 4f or Mn $2p_{3/2}$ peak	d_2 (nm)	$d_{average} = \frac{d_1+d_2}{2}$ (nm)	St. dev. Error	Oxidizes MnO (ΔO_{MnO}) $\times 10^{15}$ atoms	Reduced from Ta_2O_5 $(\Delta O_{Ta_2O_5})$ $\times 10^{15}$ atoms	% of $\frac{\Delta O_{Ta_2O_5}}{\Delta O_{MnO}}$
bare TaON	Ta_2O_5	39.9	1.58	24.6	1.53	1.56	± 0.03			
2.07 nm MnO_x/TaON	Ta_2O_5	34.0	1.29	20.4	1.25	1.27	± 0.02	3.49	1.83	52 %
	MnO	55.2	0.80	50.1	0.80	0.80	± 0.01			
	Mn_2O_3	25.6	0.62	27.4	0.64	0.63	± 0.01			
	MnO_2	19.2	0.65	22.5	0.63	0.64	± 0.01			
5.25 nm MnO_x/TaON	Ta_2O_5	22.9	0.81	12.3	0.73	0.77	± 0.04	9.76	5.02	51%
	MnO	64.4	1.75	55.2	1.91	1.83	± 0.08			
	Mn_2O_3	21.5	1.45	24.8	1.52	1.48	± 0.04			
	MnO_2	14.1	2.05	20.1	1.82	1.94	± 0.12			
7.5 nm MnO_x/TaON	Ta_2O_5	21.5	0.76	12.0	0.71	0.74	± 0.03	10.3	5.24	51 %
	MnO	84.2	3.56	72.1	3.66	3.61	± 0.05			
	Mn_2O_3	11.7	2.16	18.3	2.11	2.14	± 0.02			
	MnO_2	4.10	1.78	9.6	1.73	1.75	± 0.02			

[a] % of Ta 4f is for Ta_2O_5 while % of Mn $2p_{3/2}$ peak is for MnO, Mn_2O_3, and MnO_2

Table C.3. The thicknesses, the percentage of peak intensities due to Ta_2O_5, TaON, MnO, Mn_2O_3, and MnO_2 found in SESSA software, and the calculated number of oxygen atoms which oxidizes MnO layer or reduced in Ta_2O_5, assuming rough layers resembling real samples (model 2) at 2003 eV and 4000 eV excitation energies for the samples, 0, 2, 5, and 7 nm MnO_x/TaON.

		Model II: Rough Layers								
Sample	Layer	hv = 2003 eV		hv = 4000 eV		Average Layer thickness		Number of oxygen atoms that		% of $\frac{\Delta O_{Ta_2O_5}}{\Delta O_{MnO}}$
		% of Ta 4f or Mn 2$p_{3/2}$ peak	d_1 (nm)	% of Ta 4f or Mn 2$p_{3/2}$ peak	d_2 (nm)	$d_{average} = \frac{d_1+d_2}{2}$ (nm)	St. dev. Error	Oxidizes MnO (ΔO_{MnO}) $\times 10^{15}$ atoms	Reduced from Ta_2O_5 ($\Delta O_{Ta_2O_5}$) $\times 10^{15}$ atoms	
bare TaON	Ta_2O_5	39.9	1.43	24.6	1.43	**1.43**	± 0.002			
2.07 nm MnO_x/TaON (RSR=1.092)	Ta_2O_5	34.0	1.20	20.4	1.15	**1.18**	± 0.025	3.52	1.67	47 %
	MnO	55.2	0.78	50.1	0.80	**0.79**	± 0.007			
	Mn_2O_3	25.6	0.63	27.4	0.63	**0.63**	± 0.005			
	MnO_2	19.2	0.66	22.5	0.64	**0.65**	± 0.012			
5.25 nm MnO_x/TaON (RSR=1.079)	Ta_2O_5	22.9	0.75	12.3	0.69	**0.72**	± 0.029	9.96	4.55	46 %
	MnO	64.4	1.69	55.2	1.87	**1.77**	± 0.090			
	Mn_2O_3	21.5	1.43	24.8	1.52	**1.48**	± 0.045			
	MnO_2	14.1	2.13	20.1	1.86	**2.00**	± 0.135			
7.5 nm MnO_x/TaON (RSR=1.049)	Ta_2O_5	21.5	0.74	12.0	0.69	**0.71**	± 0.023	10.7	4.59	43 %
	MnO	84.2	3.42	72.1	3.58	**3.50**	± 0.078			
	Mn_2O_3	11.7	2.17	18.3	2.13	**2.15**	± 0.019			
	MnO_2	4.1	1.91	9.6	1.79	**1.85**	± 0.059			

[a] % of Ta 4f is for Ta_2O_5 while % of Mn 2$p_{3/2}$ peak is for MnO, Mn_2O_3, and MnO_2

Table C.4. The HAXPES fitting parameters of the core-levels spectra from Figure 6.11 to Figure 6.15 and valence band spectra in Figure 6.16 used for bare TaON and 26 nm MnO_x/TaON (as references for TaON and MnO) at 2003, and 4000 eV excitation energies

		2003 eV		4000 eV	
Peak		**position (eV)**	**FWHM**	**position (eV)**	**FWHM**
Ta 4$f_{7/2}$	TaON	25.58	0.78	25.7	0.78
	Ta_2O_5	26.13	0.95	26.25	0.95
O 2s	MnO_x	21.7	2.37	21.74	2.62
	Ta_2O_5/TaON	23.00	2.37	23.12	2.37
Mn 3s	Peak 1	88.95	2.76	88.87	2.48
	Peak 2	82.98	2.73	82.90	2.58
Ta 4$p_{3/2}$	TaON	403.8	4.11	403.77	4.67
	Ta_2O_5	404.7	6.27	404.67	6.5
N 1s	TaON	397.1	0.86	397.14	0.93
C 1s	O–C=O	289.67	1.78	289.77	1.78
	C–O–C	286.29	1.90	286.39	1.90
	C-N	285.29	1.29	285.39	1.29
	C– OH	288.39	1.23	288.47	1.23
	C-C	284.82	1.17	284.90	1.17

Table C.5. The corrected thicknesses of the planar MnO, Mn_2O_3, and MnO_2 layers (until the amount of O transferred from the Ta_2O_5 is equal to the amount of O oxidizing the MnO into Mn_2O_3 and MnO_2).

Sample	**Layers**	**$d_{average}$ (nm)**	**$d_{corrected}$ (nm)**	**Corrected MnO_x thickness**	**% of Change in thickness**
2.07 nm MnO_x/TaON	MnO	0.80	0.80	2.06	-0.5%
	Mn_2O_3	0.63	0.63		
	MnO_2	0.64	0.63		
	Ta_2O_5	1.27	1.27		
5.25 nm MnO_x/TaON	MnO	1.83	1.75	5.02	-4.4%
	Mn_2O_3	1.48	1.45		
	MnO_2	1.94	1.82		
	Ta_2O_5	0.77	0.77		
7.5 nm MnO_x/TaON	MnO	3.61	3.56	7.40	-1.3%
	Mn_2O_3	2.14	2.11		
	MnO_2	1.75	1.73		
	Ta_2O_5	0.74	0.74		

Table C.6. The corrected atomic densities of the planar MnO, Mn_2O_3, and MnO_2 layers (until the amount of oxygen transferred from the Ta_2O_5 is equal to the amount of oxygen oxidizing the MnO into Mn_2O_3 and MnO_2).

Sample	Layers	Bulk Atomic Density (#/cm³) $\times 10^{22}$	Corrected Atomic Density (#/cm³) $\times 10^{22}$	% of Change in atomic density ($\Delta\rho$)
2.07 nm MnO_x/TaON	MnO	9.57	8.75	- 9 %
	Mn_2O_3	9.54	8.65	- 9 %
	MnO_2	10.8	9.68	- 10 %
	Ta_2O_5	8.65	8.65	0 %
5.25 nm MnO_x/TaON	MnO	9.57	9.23	- 4 %
	Mn_2O_3	9.54	9.01	- 6 %
	MnO_2	10.8	9.90	- 8 %
	Ta_2O_5	8.65	8.65	- 0 %
7.5 nm MnO_x/TaON	MnO	9.57	9.13	- 5 %
	Mn_2O_3	9.54	8.94	- 6 %
	MnO_2	10.8	9.87	- 8 %
	Ta_2O_5	8.65	8.65	0 %

List of Figures

List of Tables

List of Abbreviations

BE	Binding Energy
BESSY	Berliner Elektronenspeicherring-Gesellschaft für Synchrotronstrahlung
CB	Conduction Band
CCD	Charged Couple Device
CV	Cyclic Voltammetry or Cyclic Voltammogram
DFT	Density Functional Theory
EAL	Effective Attenuation Length
EDX	Energy Dispersive X-ray
EXAFS	Extended X-ray Absorption Fine Structure
EY-XAS	Electron Yield - X-ray Absorption Spectrum
FTIR	Fourier Transform Infrared Microscopy
FY-XAS	Fluorescence Yield - X-ray Absorption Spectrum
HAXPES	Hard X-ray Photoelectron Spectroscopy
HER	Hydrogen Evolution Reaction
HIKE	High Kinetic Energy
HOMO	Highest Occupied Molecular Orbital
HZB	Helmholtz-Zentrum Berlin für Materialien und Energie
IMFP	Inelastic Mean Free Path
ID	Information Depth
KE	Kinetic Energy
LUMO	Lowest Unoccupied Molecular Orbital
MCP	Micro-Channel Plate
MED	Mean Escape Depth
MnO$_x$	Manganese Oxide
NEXAFS	Near-Edge X-ray Absorption Fine Structure
NHE	Normal Hydrogen Electrode
NIST	National Institute of Standards and Technology
NP	Nanoparticle
O	Oxygen atom
OEC	Oxygen Evolving Complex
OER	Oxygen Evolution Reaction
PGM	Plane Grating Monochromator
PS II	Photosystem II
PEC	Photo-Electrochemical Cells

PES	Photoelectron Spectroscopy
PFY	Partial Fluorescence Yield
PFY-XAS	X-ray Absorption Spectrum measured in Partial Fluorescence Yield mode
RHE	Reversible Hydrogen Electrode
RIXS	Resonant Inelastic X-ray Scattering
RPES	Resonant Photoemission Spectroscopy
RSR	Relative Surface Roughness
SEM	Scanning Electron Microscopy
SESSA	Simulation of Electron Spectra for Surface Analysis
TEM	Transmission Electron Microscopy
TEY	Total Electron Yield
TEY-XAS	X-ray Absorption Spectrum measured in Total Electron Yield mode
TM	Transition Metal
UHV	Ultra-High Vacuum
VB	Valence Band
WOC	Water Oxidizing Center
XA	X-ray Absorption
XAS	X-ray Absorption Spectroscopy
XP	X-ray Photoemission
XPS	X-ray Photoemission Spectroscopy
XRD	X-ray Diffraction
X-photon	X-ray photon

List of Publications

Parts of this thesis have been published or under preparation as the following articles:

1. "Insight into pH-Dependent Formation of Manganese Oxide Phases in Electrodeposited Catalytic Films Probed by Soft X-ray Absorption Spectroscopy."

Maryam N. Shaker, Shannon A. Bonke, Jie Xiao, Munirah Khan, Rosalie K. Hocking, and Marc F. Tesch. Chempluschem (2018) 83, 721-727. DOI: 10.1002/cplu.201800055

2. "Evolution of Oxygen-Metal Electron Transfer and Metal Electronic States During Manganese Oxide Catalyzed Water Oxidation Revealed with *In Situ* X-ray Spectroscopy."

Marc F. Tesch, Shannon A. Bonke, Jie Xiao, Travis E. Jones, **Maryam N. Shaker**, Jie Xiao, Katarzyna Skorupska, Rik Mom, Jens Melder, Philipp Kurz, Axel Knop-Gericke, Robert Schlögel, Rosalie K. Hocking, Alexander N. Simonov.

Angewandte Chemie International Edition (Internationale Ausgabe) (2019) 58, 3426-3432. DOI: 10.1002/anie.201810825

Angewandte Chemie (Deutsche Ausgabe) (2019), 131, 3464–3470. DOI: 10.1002/ange.201810825

3. "Interfacial Spectroscopic Study of MnO_x/TaON Catalytic Films for Water Oxidation analyzed by Hard X-ray Photo Electron Spectroscopic Technique."

Maryam N. Shaker, Marco Favaro, Rowshanak Irani, Paul Plate, Fatwa Abdi, Thomas Götsch, Roel Van de Krol, and David E. Starr. *In preparation.*

Selected conferences and workshops contributions

- Bunsentagung 115th General Assembly of the German Bunsen Society for physical chemistry, 2016, Rostock, Germany.

  Poster Presentation – Title: "Oxidation state control of MnO_x thin films for water oxidation catalysis by adjustment during the deposition process".

- 8th Joint BER II and BESSY II User Meeting, 2016, Berlin, Germany.

  Poster Presentation – Title: "*In operando* study on MnO_x thin films during electrocatalytic water oxidation using soft X-ray absorption and emission spectroscopy".

- Deutsche Physikalische Gesellschaft (DPG), 2017, Dresden, Germany.

  Oral Presentation – Title: "*In operando* study on MnO_x thin films during electrocatalytic water oxidation using soft X-ray absorption and emission spectroscopy".

- 9th Joint BER II and BESSY II User Meeting, 2017, Berlin, Germany.
  Poster Presentation – Title: "Electronic Structure Study of Manganese Oxide Nanoparticles Catalysts Probed by XAS and RIXS"
- 2nd International Conference on catalysis and chemical engineering (CCE), 2018, Paris, France. ***Oral Presentation*** – Title: "*In situ* study on electrodeposited MnO_x films during electrocatalytic water oxidation using soft X-ray absorption and emission spectroscopy".
- 10th Joint BER II and BESSY II User Meeting, 2018, Berlin, Germany.
  Poster Presentation – Title: "Electronic Structure Study of Manganese Oxide Films on Tantalum Oxynitride Photoanodes Probed by HAXPES and ResPES".

Acknowledgments

I would not have come to this point, and this thesis would not have been conceivable without the support and assistance of many people, especially my supervisors. I was fortunate to have you all on this journey.

First of all, **Prof. Dr. Roel van de Krol**, thank you for being my first supervisor and allowing me to work in this amazing solar fuel department; I like this place with its very motivated and friendly environment. Thanks for always being a strong supporter and advisor. I am very much appreciated for believing in me and your immense support, especially after the bad situations I experienced!

It is also my great honor to have **Prof. Dr. Holger Dau,** and **Prof. Dr. Wolfgang Kuch** from the Freie Universität Berlin, in the doctoral commission of my thesis examination.

My most profound appreciation goes to my Ph.D. mentor, **Dr. David Starr**, the expert scientist of photoelectron spectroscopy. Thanks for the beamtimes, which allowed me to conduct my projects with a large degree of freedom and trust. I appreciate all the support during experiments and research. You are an excellent teacher; thanks for dedicating much time to me and teaching me the principles of photoelectrons. I learned so much from you.

Special thanks to **Prof. Dr. Sebastian Fiechter** from HZB for always keeping his door open for discussion and giving advice.

The challenging experiments with synchrotron radiation presented in this dissertation would not have been achieved without the help and support of two incredible teams at synchrotron beamlines of HZB/BESSY II in Germany and Max IV in Sweden. I would like to thank **Dr. Marco Favaro**, **Dr. Marc Tesch**, **Dr. Ronny Golnak**, **Dr. Jie Xiao, Dr. Tristian Petit**, **Suyun Zhu**, and **Dr. Andrey Shavorskiy**; I am very grateful for your guidance, support, and help not only during the experiments but also during our further scientific discussions. Special thanks to **Marco Favaro,** not only because of helping me with HAXPES experiments but also for discussing results and giving advice on data analysis. "One last thing," thanks Marco, for the Italian cookies and sweets you provided me and for sharing the office in Wannsee for some time. Thanks for always being a very kind person.

I am very grateful to our collaborators from Monash University in Australia, particularly to **Prof. Dr. Leone Spiccia,** for his commitment and collaboration for the manganese oxide research before he passed away in 2016. I would like to thank his group, especially **Dr. Alexander N. Simonov** and **Dr. Shannon Bonke**, for our scientific discussions and for providing us some of the catalysts and references studied in this thesis. Thanks, **Dr. Rosalie Hocking,** from James

Cook University (Australia), for the amazing discussion on my first project.

Curriculum Vitæ

Maryam N. Shaker

For reasons of data protection, the curriculum vitae is not published in the electronic version

Bibliography

[1]   Owusu, P.A., S. Asumadu-Sarkodie, and S. Dubey, A review of renewable energy sources, sustainability issues and climate change mitigation. *Cogent Engineering*, **2016**. 3(1).

[2]   World Population Today, http://www.worldometers.info/world-population/.[10.08.2020]

[3]   World Energy Scenarios Composing energy futures to 2050 https://www.worldenergy.org/publications/entry/world-energy-scenarios-composing-energy-futures-to-2050.[10.07.2020]

[4]   Nehring, R., Traversing the mountaintop: world fossil fuel production to 2050. *Philos Trans R Soc Lond B Biol Sci*, **2009**. 364(1532): p. 3067-79.

[5]   World Reserves of Fossil Fuels, https://knoema.com/smsfgud/bp-world-reserves-of-fossil-fuels. [10.07.2020]

[6]   Demirbas, A., Potential applications of renewable energy sources, biomass combustion problems in boiler power systems and combustion related environmental issues. *Progress in Energy and Combustion Science*, **2005**. 31(2): p. 171-192.

[7]   Wang, W., M.O. Tadé, and Z. Shao, Research progress of perovskite materials in photocatalysis- and photovoltaics-related energy conversion and environmental treatment. *Chem. Soc. Rev.*, **2015**. 44(15): p. 5371-5408.

[8]   Jane H. Hodgkinson, F.D.S., Practical Handbook of Earth Science. **2017**: CRC Press.

[9]   Climate Change: Atmospheric Carbon Dioxide https://www.climate.gov/news-features/understanding-climate/climate-change-atmospheric-carbon-dioxide. [12.07.2020]

[10] CO_2- Earth https://www.co2.earth/co2-acceleration. [12.08.2020]

[11]   Morton, O., Solar energy: a new day dawning? Silicon Valley sunrise. *Nature*, **2006**. 443(7107): p. 19-22.

[12]   Lewis, N.S., and D.G. Nocera, Powering the planet: chemical challenges in solar energy utilization. *Proc. Natl. Acad. Sci. USA*, **2006**. 103(43): p. 15729-35.

[13]   Dunwei Wang, G.C., Nanomaterials for Energy Conversion and Storage. **2017**.

[14]   Roel van de Krol, M.G., Photoelectrochemical Hydrogen Production. Electronic Materials: Science & Technology. **2012**: Springer.

[15]   Kothari, D.P., Renewable Energy Sources and Emerging Technologies. **2008**.

[16]   Dunn, S., Hydrogen futures: toward a sustainable energy system. *Int. J. Hydrog. Energy*, **2002**. 27(3): p. 235-264.

[17]   Graetz, J., New approaches to hydrogen storage. *Chem. Soc. Rev.*, **2009**. 38(1): p. 73-82.

[18]   Holladay, J.D., et al., An overview of hydrogen production technologies. *Catal. Today*, **2009**. 139(4): p. 244-260.

[19]   Gust, D., T.A. Moore, and A.L. Moore, Realizing artificial photosynthesis. *Faraday Discuss.*, **2012**. 155(0): p. 9-26.

[20]   Bard, A.J. and M.A. Fox, Artificial Photosynthesis: Solar Splitting of Water to Hydrogen and Oxygen. *Acc. Chem. Res.*, **1995**. 28(3): p. 141-145.

[21]   Kudo, A. and Y. Miseki, Heterogeneous photocatalyst materials for water splitting. *Chem.*

Soc. Rev., **2009**. 38(1): p. 253-78.

[22]   Wang, C., et al., Controllable incorporation of CdS nanoparticles into TiO_2 nanotubes for highly enhancing the photocatalytic response to visible light. *Sci. China Ser. B: Chemistry*, **2009**. 52(12): p. 2148.

[23]   Hong, W.T., et al., Toward the rational design of non-precious transition metal oxides for oxygen electrocatalysis. *Energy Environ. Sci.*, **2015**. 8(5): p. 1404-1427.

[24]   Suen, N.T., et al., Electrocatalysis for the oxygen evolution reaction: recent development and future perspectives. *Chem. Soc. Rev.*, **2017**. 46(2): p. 337-365.

[25]   Jiao, F. and H. Frei, Nanostructured cobalt and manganese oxide clusters as efficient water oxidation catalysts. *Energy Environ. Sci.*, **2010**. 3(8): p. 1018-1027.

[26]   Matheu, R., et al., The development of molecular water oxidation catalysts. *Nat. Rev. Chem.*, **2019**. 3(5): p. 331-341.

[27]   Park, S., et al., Manganese oxide-based heterogeneous electrocatalysts for water oxidation. *Energy Environ. Sci.*, **2020**. 13(8): p. 2310-2340.

[28]   Kumbhar, V.S., et al., Recent advances in water-splitting electrocatalysts based on manganese oxide. *Carbon Resour. Convers.*, **2019**. 2(3): p. 242-255.

[29]   Fujishima, A. and K. Honda, Electrochemical Photolysis of Water at a Semiconductor Electrode. *Nature*, **1972**. 238(5358): p. 37-38.

[30]   Gersten, S.W., G.J. Samuels, and T.J. Meyer, Catalytic oxidation of water by an oxo-bridged ruthenium dimer. *J. Am. Chem. Soc.*, **1982**. 104(14): p. 4029-4030.

[31]   Pregger, T., et al., Prospects of solar thermal hydrogen production processes. *Int. J. Hydrog. Energy*, **2009**. 34(10): p. 4256-4267.

[32]   Yamada, Y., One chip photovoltaic water electrolysis device. *Int. J. Hydrog. Energy*, **2003**. 28(11): p. 1167-1169.

[33]   Yamasita, D., Recent progress of visible-light-driven heterogeneous photocatalysts for overall water splitting. *Solid State Ion.*, **2004**. 172(1-4): p. 591-595.

[34]   van de Krol, R., Y. Liang, and J. Schoonman, Solar hydrogen production with nanostructured metal oxides. *J. Mater. Chem.*, **2008**. 18(20): p. 2311-2320.

[35]   Fujishima, A. and K. Honda, Electrochemical Evidence for the Mechanism of the Primary Stage of Photosynthesis. *Bull. Chem. Soc. Jpn.*, **1971**. 44(4): p. 1148.

[36]   Park, K.-W. and A.M. Kolpak, Optimal methodology for explicit solvation prediction of band edges of transition metal oxide photocatalysts. *Commun. Chem.*, **2019**. 2(1): p. 79.

[37]   Yang, W., et al., Strategies for enhancing the photocurrent, photovoltage, and stability of photoelectrodes for photoelectrochemical water splitting. *Chem. Soc. Rev.*, **2019**. 48(19): p. 4979-5015.

[38]   Energy Efficiency and Renewable Energy Through Nanotechnology. *Green Energy Environ.*. **2011**.

[39]   Hocking, R.K., et al., Water-oxidation catalysis by manganese in a geochemical-like cycle. *Nat. Chem.*, **2011**. 3(6): p. 461-466.

[40]   Gorlin, Y., et al., In situ X-ray absorption spectroscopy investigation of a bifunctional manganese oxide catalyst with high activity for electrochemical water oxidation and oxygen reduction. *J. Am. Chem. Soc.*, **2013**. 135(23): p. 8525-34.

[41]   Indra, A., et al., Active Mixed-Valent MnO_x Water Oxidation Catalysts through Partial Oxidation (Corrosion) of Nanostructured MnO Particles. *Angew. Chem. Int. Ed.*, **2013**. 52(50): p. 13206-13210.

[42]   Park, J., et al., A new water oxidation catalyst: lithium manganese pyrophosphate with tunable Mn valency. *J. Am. Chem. Soc.*, **2014**. 136(11): p. 4201-11.

[43]   Zaharieva, I., et al., Electrosynthesis, functional, and structural characterization of a water-oxidizing manganese oxide. *Energy Environ. Sci.*, **2012**. 5(5): p. 7081-7089.

[44]   Takashima, T., K. Hashimoto, and R. Nakamura, Mechanisms of pH-dependent activity for water oxidation to molecular oxygen by MnO_2 electrocatalysts. *J. Am. Chem. Soc.*, **2012**. 134(3): p. 1519-27.

[45]   Yano, J., et al., Where water is oxidized to dioxygen: structure of the photosynthetic Mn_4Ca cluster. *Science*, **2006**. 314(5800): p. 821-5.

[46]   Singh, A., et al., Water Oxidation Catalysis by Nanoparticulate Manganese Oxide Thin Films: Probing the Effect of the Manganese Precursors. *Chem. Mater.*, **2013**. 25(7): p. 1098-1108.

[47]   Brimblecombe, R., et al., Sustained water oxidation photocatalysis by a bioinspired manganese cluster. *Angew. Chem. Int. Ed.*, **2008**. 47(38): p. 7335-8.

[48]   Lee, Y., et al., Synthesis and Activities of Rutile IrO_2 and RuO_2 Nanoparticles for Oxygen Evolution in Acid and Alkaline Solutions. *J. Phys. Chem. Lett.*, **2012**. 3(3): p. 399-404.

[49]   Reier, T., M. Oezaslan, and P. Strasser, Electrocatalytic Oxygen Evolution Reaction (OER) on Ru, Ir, and Pt Catalysts: A Comparative Study of Nanoparticles and Bulk Materials. *ACS Catal.*, **2012**. 2(8): p. 1765-1772.

[50]   Smith, R.D.L., et al., Facile Photochemical Preparation of Amorphous Iridium Oxide Films for Water Oxidation Catalysis. *Chem. Mater.*, **2014**. 26(4): p. 1654-1659.

[51]   Shan, J., et al., Regulating Electrocatalysts via Surface and Interface Engineering for Acidic Water Electrooxidation. *ACS Energy Lett.*, **2019**. 4(11): p. 2719-2730.

[52]   Roger, I., M.A. Shipman, and M.D. Symes, Earth-abundant catalysts for electrochemical and photoelectrochemical water splitting. *Nat. Rev. Chem.*, **2017**. 1(1).

[53]   Zhang, B. and L. Sun, Why nature chose the Mn_4CaO_5 cluster as water-splitting catalyst in photosystem II: a new hypothesis for the mechanism of O-O bond formation. *Dalton Trans.,* **2018**. 47(41): p. 14381-14387.

[54]   Post, J.E., Manganese oxide minerals: crystal structures and economic and environmental significance. *Proc. Natl. Acad. Sci. USA*, **1999**. 96(7): p. 3447-54.

[55]   Suib, S.L., Porous Manganese Oxide Octahedral Molecular Sieves and Octahedral Layered Materials. *Acc. Chem. Res.*, **2008**. 41(4): p. 479-487.

[56]   Khan, M., et al., On the Origin of the Improvement of Electrodeposited MnO_x Films in Water Oxidation Catalysis Induced by Heat Treatment. *ChemSusChem*, **2015**. 8(11): p. 1980-5.

[57]   Najafpour, M.M., et al., Water exchange in manganese-based water-oxidizing catalysts in photosynthetic systems: from the water-oxidizing complex in photosystem II to nano-sized manganese oxides. *Biochim Biophys Acta*, **2014**. 1837(9): p. 1395-410.

[58]   Umena, Y., et al., Crystal structure of oxygen-evolving photosystem II at a resolution of 1.9 A. *Nature*, **2011**. 473(7345): p. 55-60.

[59]   Dau, H., et al., The Mechanism of Water Oxidation: From Electrolysis via Homogeneous to Biological Catalysis. *Chemcatchem*, **2010**. 2(7): p. 724-761.

[60]   Indra, A., P.W. Menezes, and M. Driess, Uncovering structure-activity relationships in manganese-oxide-based heterogeneous catalysts for efficient water oxidation. *ChemSusChem*, **2015**. 8(5): p. 776-85.

[61]   Kok, B., B. Forbush, and M. McGloin, Cooperation of charges in photosynthetic O_2 evolution-I. A linear four step mechanism. *Photochem. Photobiol.*, **1970**. 11(6): p. 457-75.

[62]   Schmidt, S.B. and S. Husted, The Biochemical Properties of Manganese in Plants. *Plants*, **2019**. 8(10).

[63]   Lubitz, W., M. Chrysina, and N. Cox, Water oxidation in photosystem II. *Photosynth. Res.*, **2019**. 142(1): p. 105-125.

[64]   Haumann, M., et al., Structural and oxidation state changes of the photosystem II manganese complex in four transitions of the water oxidation cycle ($S_0 \rightarrow S_1$, $S_1 \rightarrow S_2$, $S_2 \rightarrow S_3$, and $S_{3,4} \rightarrow S_0$) characterized by X-ray absorption spectroscopy at 20 K and room temperature. *Biochemistry*, **2005**. 44(6): p. 1894-908.

[65]   Haumann, M., et al., Photosynthetic O_2 formation tracked by time-resolved X-ray experiments. *Science*, **2005**. 310(5750): p. 1019-21.

[66]   Glatzel, P., et al., Electronic structural changes of Mn in the oxygen-evolving complex of photosystem II during the catalytic cycle. *Inorg. Chem.*, **2013**. 52(10): p. 5642-4.

[67]   Glatzel, P., et al., The electronic structure of Mn in oxides, coordination complexes, and the oxygen-evolving complex of photosystem II studied by resonant inelastic X-ray scattering. *J. Am. Chem. Soc.*, **2004**. 126(32): p. 9946-59.

[68]   Wiechen, M., et al., Water oxidation catalysis by manganese oxides: learning from evolution. *Energy Environ. Sci.*, **2014**. 7(7): p. 2203.

[69]   Ferreira, K.N., et al., Architecture of the photosynthetic oxygen-evolving center. *Science*, **2004**. 303(5665): p. 1831-8.

[70]   Barber, J., Photosynthetic energy conversion: natural and artificial. *Chem. Soc. Rev.*, **2009**. 38(1): p. 185-96.

[71]   Ruttinger, W. and G.C. Dismukes, Synthetic Water-Oxidation Catalysts for Artificial Photosynthetic Water Oxidation. *Chem. Rev.,* **1997**. 97(1): p. 1-24.

[72]   Shaker, M.N., et al., Insight into pH-Dependent Formation of Manganese Oxide Phases in Electrodeposited Catalytic Films Probed by Soft X-ray Absorption Spectroscopy. *ChemPlusChem*, **2018**. 83(7): p. 721-727.

[73]   Zaharieva, I., et al., Water oxidation catalysis – role of redox and structural dynamics in biological photosynthesis and inorganic manganese oxides. *Energy Environ. Sci.*, **2016**. 9(7): p. 2433-2443.

[74]   Zhou, F., et al., Improvement of catalytic water oxidation on MnO_x films by heat treatment. *ChemSusChem*, **2013**. 6(4): p. 643-51.

[75]   Zhou, F., et al., Electrodeposited MnO_x Films from Ionic Liquid for Electrocatalytic Water Oxidation. *Adv. Energy Mater.*, **2012**. 2(8): p. 1013-1021.

[76]   Cho, G., et al., Ion exchange: an advanced synthetic method for complex nanoparticles. *Nano Converg.*, **2019**. 6(1): p. 17.

[77]   Najafpour, M.M., et al., Calcium manganese(III) oxides ($CaMn_2O_4.xH_2O$) as biomimetic oxygen-evolving catalysts. *Angew. Chem. Int. Ed.*, **2010**. 49(12): p. 2233-7.

[78]   Najafpour, M.M., et al., Nano-sized manganese oxides as biomimetic catalysts for water oxidation in artificial photosynthesis: a review. *J. R. Soc. Interface*, **2012**. 9(75): p. 2383-95.

[79]   Knoops, H.C.M., et al., Atomic Layer Deposition. **2015**: p. 1101-1134.

[80]   Knoops, H.C.M., et al., Status and prospects of plasma-assisted atomic layer deposition.

J. Vac. Sci. Technol. A, **2019**. 37(3): p. 030902.

[81]   Huynh, M., et al., Nature of Activated Manganese Oxide for Oxygen Evolution. *J. Am. Chem. Soc.*, **2015**. 137(47): p. 14887-904.

[82]   Kuo, C.-H., et al., Robust Mesoporous Manganese Oxide Catalysts for Water Oxidation. *ACS Catal.*, **2015**. 5(3): p. 1693-1699.

[83]   Guan, J., et al., Water oxidation on a mononuclear manganese heterogeneous catalyst. *Nat. Catal.*, **2018**. 1(11): p. 870-877.

[84]   Wang, J. and H.C. Zeng, CoHPi Nanoflakes for Enhanced Oxygen Evolution Reaction. *ACS Appl. Mater. Interfaces*, **2018**. 10(7): p. 6288-6298.

[85]   Chauhan, M., et al., Copper Cobalt Sulfide Nanosheets Realizing a Promising Electrocatalytic Oxygen Evolution Reaction. *ACS Catal.*, **2017**. 7(9): p. 5871-5879.

[86]   Chen, S., et al., Large-area manganese oxide nanorod arrays as efficient electrocatalyst for oxygen evolution reaction. *Int. J. Hydrog. Energy*, **2012**. 37(18): p. 13350-13354.

[87]   Zheng, X., et al., Three-dimensional radial α-MnO_2 synthesized from different redox potential for bifunctional oxygen electrocatalytic activities. *J. Power Sources*, **2017**. 362: p. 332-341.

[88]   Gorlin, Y. and T.F. Jaramillo, A Bifunctional Nonprecious Metal Catalyst for Oxygen Reduction and Water Oxidation. *J. Am. Chem. Soc.*, **2010**. 132(39): p. 13612-13614.

[89]   Jin, K., et al., Partially Oxidized Sub-10 nm MnO Nanocrystals with High Activity for Water Oxidation Catalysis. *Sci. Rep.*, **2015**. 5: p. 10279.

[90]   Jin, K., et al., Mechanistic Investigation of Water Oxidation Catalyzed by Uniform, Assembled MnO Nanoparticles. *J. Am. Chem. Soc.*, **2017**. 139(6): p. 2277-2285.

[91]   Sun, W., et al., Non-equilibrium crystallization pathways of manganese oxides in aqueous solution. *Nat. Commun.*, **2019**. 10(1): p. 573.

[92]   Seidler-Egdal, R.K., et al., High turnover catalysis of water oxidation by Mn(II) complexes of monoanionic pentadentate ligands. *Dalton Trans.*, **2011**. 40(15): p. 3849-3858.

[93]   Faller, P., et al., Rapid formation of the stable tyrosyl radical in photosystem II. *Proc. Natl. Acad. Sci. USA*, **2001**. 98(25): p. 14368-73.

[94]   Kramer, D.M., C.A. Sacksteder, and J.A. Cruz, How acidic is the lumen? *Photosynth. Res.*, **1999**. 60(2): p. 151-163.

[95]   Joliot, P. and G.N. Johnson, Regulation of cyclic and linear electron flow in higher plants. *Proc. Natl. Acad. Sci. USA*, **2011**. 108(32): p. 13317-22.

[96]   Morita, M., C. Iwakura, and H. Tamura, The anodic characteristics of manganese dioxide electrodes prepared by thermal decomposition of manganese nitrate. *Electrochim. Acta*, **1977**. 22(4): p. 325-328.

[97]   Takashima, T., K. Hashimoto, and R. Nakamura, Inhibition of charge disproportionation of MnO_2 electrocatalysts for efficient water oxidation under neutral conditions. *J. Am. Chem. Soc.*, **2012**. 134(44): p. 18153-6.

[98]   Ramírez, A., et al., Evaluation of MnO_x, Mn_2O_3, and Mn_3O_4 Electrodeposited Films for the Oxygen Evolution Reaction of Water. *J. Phys. Chem. C*, **2014**. 118(26): p. 14073-14081.

[99]   Turner, J.A., A realizable renewable energy future. *Science*, **1999**. 285(5428): p. 687-9.

[100]   Bolton, J.R., S.J. Strickler, and J.S. Connolly, Limiting and realizable efficiencies of solar photolysis of water. *Nature*, **1985**. 316(6028): p. 495-500.

[101]   Rajeshwar, K., Hydrogen generation at irradiated oxide semiconductor–solution interfaces. *J. Appl. Electrochem.*, **2007**. 37(7): p. 765-787.

[102]   Walter, M.G., et al., Solar water splitting cells. *Chem. Rev.,* **2010**. 110(11): p. 6446-73.

[103]   Gorlin, Y., et al., Understanding interactions between manganese oxide and gold that lead to enhanced activity for electrocatalytic water oxidation. *J. Am. Chem. Soc.*, **2014**. 136(13): p. 4920-6.

[104]   Meng, Y., et al., Structure-property relationship of bifunctional MnO_2 nanostructures: highly efficient, ultra-stable electrochemical water oxidation and oxygen reduction reaction catalysts identified in alkaline media. *J. Am. Chem. Soc.*, **2014**. 136(32): p. 11452-64.

[105]   Han, G.-Q., et al., Crystallographic Structure and Morphology Transformation of MnO_2 Nanorods as Efficient Electrocatalysts for Oxygen Evolution Reaction. *J. Electrochem. Soc.*, **2015**. 163(2): p. H67-H73.

[106]   Smith, P.F., et al., Coordination Geometry and Oxidation State Requirements of Corner-Sharing MnO_6 Octahedra for Water Oxidation Catalysis: An Investigation of Manganite (γ-MnOOH). *ACS Catal.*, **2016**. 6(3): p. 2089-2099.

[107]   Kölbach, M., et al., Evaluation of electrodeposited α-Mn_2O_3 as a catalyst for the oxygen evolution reaction. *Catal. Today*, **2017**. 290: p. 2-9.

[108]   Simchi, H., et al., Cosputtered Calcium Manganese Oxide Electrodes for Water Oxidation. *Inorg. Chem.*, **2018**. 57(2): p. 785-792.

[109]   Walter, C., et al., Facile Formation of Nanostructured Manganese Oxide Films as High-Performance Catalysts for the Oxygen Evolution Reaction. *ChemSusChem*, **2018**. 11(15): p. 2554-2561.

[110]   Melder, J., et al., Carbon fibre paper coated by a layered manganese oxide: a nano-structured electrocatalyst for water-oxidation with high activity over a very wide pH range. *J. Mater. Chem. A*, **2019**. 7(44): p. 25333-25346.

[111]   Cho, K.H., et al., Uniform, Assembled 4 nm Mn_3O_4 Nanoparticles as Efficient Water Oxidation Electrocatalysts at Neutral pH. *Adv. Funct. Mater.*, **2020**. 30(10).

[112]   Zaharieva, I., et al., Synthetic manganese–calcium oxides mimic the water-oxidizing complex of photosynthesis functionally and structurally. *Energy Environ. Sci.*, **2011**. 4(7): p. 2400-2408.

[113]   Khan, M., et al., Electronic structural insights into efficient MnO_x catalysts. *J. Mater. Chem. A*, **2014**. 2(43): p. 18199-18203.

[114]   Chang, S.L.Y., et al., Nanoscale structural disorder in manganese oxide particles embedded in Nafion. *J. Mater. Chem. A*, **2014**. 2(11): p. 3730-3733.

[115]   Wiechen, M., et al., Layered manganese oxides for water-oxidation: alkaline earth cations influence catalytic activity in a photosystem II-like fashion. *Chem. Sci.*, **2012**. 3(7): p. 2330-2339.

[116]   Robinson, D.M., et al., Photochemical Water Oxidation by Crystalline Polymorphs of Manganese Oxides: Structural Requirements for Catalysis. *J. Am. Chem. Soc.*, **2013**. 135(9): p. 3494-3501.

[117]   Zhao, Y., et al., Structure reinforced birnessite with an extended potential window for supercapacitors. *J. Mater. Chem. A*, **2020**. 8(18): p. 8969-8978.

[118]   Lee, J.M., and S.-J. Hwang, Remarkable influence of the local symmetry of substituted 3d metal ion on bifunctional electrocatalyst performance of α-MnO_2 nanowire. *J. Solid State Chem.*, **2019**. 269: p. 354-360.

[119] Kwon, K.D., K. Refson, and G. Sposito, Defect-Induced Photoconductivity in Layered Manganese Oxides: A Density Functional Theory Study. *Phys. Rev. Lett.*, **2008**. 100(14): p. 146601.

[120] Shibli, S.M.A., P.S. Arun, and A.V. Raj, Exploration of octahedrally shaped $MnCo_2O_4$ catalyst particles for visible light driven photocatalytic water splitting reaction. *RSC Adv.*, **2015**. 5(25): p. 19393-19399.

[121] Gong, H., et al., $Pt@Cu_2O/WO_3$ composite photocatalyst for enhanced photocatalytic water oxidation performance. *Appl. Catal. B Environ.*, **2018**. 237: p. 309-317.

[122] Seabold, J.A., and K.-S. Choi, Effect of a Cobalt-Based Oxygen Evolution Catalyst on the Stability and the Selectivity of Photo-Oxidation Reactions of a WO_3 Photoanode. *Chem. Mater.*, **2011**. 23(5): p. 1105-1112.

[123] Sharma, P., J.W. Jang, and J.S. Lee, Key Strategies to Advance the Photoelectrochemical Water Splitting Performance of α-Fe_2O_3 Photoanode. *ChemCatChem*, **2018**. 11(1): p. 157-179.

[124] Zachäus, C., et al., Photocurrent of $BiVO_4$ is limited by surface recombination, not surface catalysis. *Chem. Sci.*, **2017**. 8(5): p. 3712-3719.

[125] Abdi, F.F., et al., Photocurrent Enhancement by Spontaneous Formation of a p-n Junction in Calcium-Doped Bismuth Vanadate Photoelectrodes. *ChemPlusChem*, **2018**. 83(10): p. 941-946.

[126] Abe, R., M. Higashi, and K. Domen, Facile Fabrication of an Efficient Oxynitride TaON Photoanode for Overall Water Splitting into H_2 and O_2 under Visible Light Irradiation. *J. Am. Chem. Soc.*, **2010**. 132(34): p. 11828-11829.

[127] Fuertes, A., Synthesis and properties of functional oxynitrides – from photocatalysts to CMR materials. *Dalton Trans.*, **2010**. 39(26): p. 5942-5948.

[128] Abe, R., et al., Photocatalytic overall water splitting under visible light by TaON and WO_3 with an IO_3^-/I^- shuttle redox mediator. *ChemComm*, **2005**(30): p. 3829-3831.

[129] Wang, Z., et al., In situ chemical reduction of the Ta_3N_5 quantum dots coupled TaON hollow spheres heterojunction photocatalyst for water oxidation. *J. Mater. Chem.*, **2012**. 22(41): p. 21972-21978.

[130] Singh Gujral, S., et al., Photo-assisted electrodeposition of manganese oxide on TaON anodes: effect on water photooxidation capacity under visible light irradiation. *Catal. Sci. Technol.*, **2016**. 6(11): p. 3745-3757.

[131] Hou, J., et al., Efficient visible-light-driven photocatalytic hydrogen production using CdS@TaON core–shell composites coupled with graphene oxide nanosheets. *J. Mater. Chem.*, **2012**. 22(15): p. 7291-7299.

[132] Wu, Y., et al., First principles high throughput screening of oxynitrides for water-splitting photocatalysts. *Energy Environ. Sci.*, **2013**. 6(1): p. 157-168.

[133] Maeda, K., (Oxy)nitrides with d_0-electronic configuration as photocatalysts and photoanodes that operate under a wide range of visible light for overall water splitting. *Phys. Chem. Chem. Phys.*, **2013**. 15(26): p. 10537-10548.

[134] Toma, F.M., et al., Mechanistic insights into chemical and photochemical transformations of bismuth vanadate photoanodes. *Nat. Commun.*, **2016**. 7(1): p. 12012.

[135] Higashi, M., K. Domen, and R. Abe, Highly Stable Water Splitting on Oxynitride TaON Photoanode System under Visible Light Irradiation. *J. Am. Chem. Soc.*, **2012**. 134(16): p. 6968-6971.

[136] Abdi, F.F., et al., Efficient solar water splitting by enhanced charge separation in a

bismuth vanadate-silicon tandem photoelectrode. *Nat. Commun.*, **2013**. 4: p. 2195.

[137] Kölbach, M., et al., Revealing the Performance-Limiting Factors in α-SnWO$_4$ Photoanodes for Solar Water Splitting. *Chem. Mater.*, **2018**. 30(22): p. 8322-8331.

[138] Zachaus, C., et al., Photocurrent of BiVO$_4$ is limited by surface recombination, not surface catalysis. *Chem. Sci.*, **2017**. 8(5): p. 3712-3719.

[139] Irani, R., et al., The role of ultra-thin MnO$_x$ co-catalysts on the photoelectrochemical properties of BiVO$_4$ photoanodes. *J. Mater. Chem. A*, **2020**. 8(11): p. 5508-5516.

[140] Cao, X., et al., Rationally designed/constructed MnO$_x$/WO$_3$ anode for photoelectrochemical water oxidation. *Chin. Chem. Lett.*, **2018**. 29(6): p. 811-814.

[141] Liu, Y., et al., Operando Investigation of Mn$_3$O$_{4+\delta}$ Co-catalyst on Fe$_2$O$_3$ Photoanode: Manganese-Valency-Determined Enhancement at Varied Potentials. *ACS Appl. Energy Mater.*, **2018**. 1(2): p. 814-821.

[142] Bonke, S.A., et al., Parameterization of Water Electrooxidation Catalyzed by Metal Oxides Using Fourier Transformed Alternating Current Voltammetry. *J. Am. Chem. Soc.*, **2016**. 138(49): p. 16095-16104.

[143] Man, I.C., et al., Universality in Oxygen Evolution Electrocatalysis on Oxide Surfaces. *ChemCatChem*, **2011**. 3(7): p. 1159-1165.

[144] Yoshida, M., et al., In situ observation of carrier transfer in the Mn-oxide/Nb:SrTiO$_3$ photoelectrode by X-ray absorption spectroscopy. *Chem. Commun. (Camb)*, **2013**. 49(71): p. 7848-50.

[145] Yoshida, M., et al., Photoexcited Hole Transfer to a MnO$_x$ Cocatalyst on a SrTiO$_3$ Photoelectrode during Oxygen Evolution Studied by In Situ X-ray Absorption Spectroscopy. *J. Phys. Chem. C*, **2014**. 118(42): p. 24302-24309.

[146] Xiao, J., et al., Enhancing catalytic activity by narrowing local energy gaps-X-ray studies of a manganese water oxidation catalyst. *ChemSusChem*, **2015**. 8(5): p. 872-7.

[147] van Oversteeg, C.H., et al., In situ X-ray absorption spectroscopy of transition metal based water oxidation catalysts. *Chem. Soc. Rev.*, **2017**. 46(1): p. 102-125.

[148] Tesch, M.F., et al., Evolution of oxygen-metal electron transfer and metal electronic states during manganese oxide catalyzed water oxidation revealed with in situ soft X-ray spectroscopy. *Angew. Chem. Int. Ed. Engl*, **2019**. 58(11): p. 3426-3432.

[149] Kubobuchi, K., et al., Mn L$_{2,3}$-edge X-ray absorption spectroscopic studies on charge-discharge mechanism of Li$_2$MnO$_3$. *Appl. Phys. Lett.*, **2014**. 104(5).

[150] Ament, L.J.P., et al., Resonant inelastic X-ray scattering studies of elementary excitations. *Rev. Mod. Phys.*, **2011**. 83(2): p. 705-767.

[151] Willmott, P., An Introduction to Synchrotron Radiation. **2019**.

[152] de Groot, F.M.F., et al., Oxygen 1s X-ray-absorption edges of transition-metal oxides. *Phys. Rev. B*, **1989**. 40(8): p. 5715-5723.

[153] Qiao, R., et al., Spectroscopic fingerprints of valence and spin states in manganese oxides and fluorides. *Curr. Appl. Phys.*, **2013**. 13(3): p. 544-548.

[154] Rez, P., W. Xudong, and M. Hong, The interpretation of near edge structure. *Microsc. Microanal. Microstruct.*, **1991**. 2(2-3): p. 143-151.

[155] Biesinger, M.C., et al., Resolving surface chemical states in XPS analysis of first row transition metals, oxides, and hydroxides: Cr, Mn, Fe, Co, and Ni. *Appl. Surf. Sci.*, **2011**. 257(7): p. 2717-2730.

[156] Röntgen, W.C., Ueber eine neue Art von Strahlen. *Ann Phys.*, **1898**. 300(1): p. 12-17.

[157]   The   Nobel   Prize   in   Physics   1901   at
http://www.nobelprize.org/nobel_prizes/physics/laureates/1901/. [30.07.2020]

[158]   Hahner, G., Near edge X-ray absorption fine structure spectroscopy as a tool to probe
electronic and structural properties of thin organic films and liquids. *Chem. Soc. Rev.*,
2006. 35(12): p. 1244-55.

[159]   F. M. F. de Groot, A.K., Core Level Spectroscopy of Solids. **2008**: CRC Press Taylor &
Francis. 512.

[160]   Golnak, R., et al., Joint Analysis of Radiative and Non-Radiative Electronic Relaxation
Upon X-ray Irradiation of Transition Metal Aqueous Solutions. *Sci. Rep.*, **2016**. 6: p.
24659.

[161]   Rehr, J.J., and R.C. Albers, Theoretical approaches to X-ray absorption fine structure.
Rev. Mod. Phys., **2000**. 72(3): p. 621-654.

[162]   Willmott, P., An Introduction to Synchrotron Radiation: Techniques and Applications.
2011: John Wiley & Sons.

[163]   de Groot, F.M.F., Ligand and metal X-ray absorption in transition metal complexes.
Inorganica Chim. Acta, **2008**. 361(4): p. 850-856.

[164]   van Veenendaal, M., Theory of Inelastic Scattering and Absorption of X-rays. **2015**,
Cambridge: Cambridge University Press.

[165]   de Groot, F.M.F., et al., Differences between L_3 and L_2 x-ray absorption spectra of
transition metal compounds. *J. Chem. Phys.*, **1994**. 101(8): p. 6570-6576.

[166]   Jovic, V., et al., Soft X-ray spectroscopic studies of the electronic structure of $M:BiVO_4$
(M = Mo, W) single crystals. *J. Mater. Chem. A*, **2015**. 3(47): p. 23743-23753.

[167]   Golnak, R., Investigation of the Electronic Structure of Transition Metal-Ions in Solution
from Aqua-Complexes to Porphyrins, *PhD thesis*. **2015**, Freie Universität Berlin.

[168]   Krol, A., et al., X-ray-absorption studies of Y-Ba-Cu-O and Bi-Sr-Ca-Cu-O films at
oxygen K edge by means of fluorescence and total electron yield: A comparison of two
techniques. *Phys. Rev. B Condens. Matter*, **1990**. 42(4): p. 2635-2638.

[169]   de Groot, F.M.F., et al., Fluorescence yield detection: Why it does not measure the X-ray
absorption cross-section. *Solid State Commun.*, **1994**. 92(12): p. 991-995.

[170]   Characterisation   -   X-ray   Absorption   Spectroscopy,
https://www.nffa.eu/offer/characterisation/installation-5/xas/. [02.08.2020]

[171]   Carroll, T.X., et al., Carbon 1s core-hole lifetime in CO_2. *Phys. Rev. A*, **2000**. 61(4): p.
042503.

[172]   Gudat, W. and C. Kunz, Close Similarity between Photoelectric Yield and
Photoabsorption Spectra in the Soft X-ray Range. *Phys. Rev. Lett.*, **1972**. 29(3): p. 169-
172.

[173]   Mangolini, F. and J.B. McClimon, Near Edge X-ray Absorption Fine Structure
Spectroscopy: A Powerful Tool for Investigating the Surface Structure and Chemistry of
Solid Lubricants, in Advanced Analytical Methods in Tribology. **2018**. p. 63-106.

[174]   Ruosi, A., et al., Electron sampling depth and saturation effects in perovskite films
investigated by soft X-ray absorption spectroscopy. *Phys. Rev. B*, **2014**. 90(12): p.
125120.

[175]   Stöhr, J. NEXAFS Spectroscopy. **1992**.

[176]   Eisebitt, S., et al., Determination of absorption coefficients for concentrated samples by
fluorescence detection. *Phys. Rev. B*, **1993**. 47(21): p. 14103-14109.

[177] Krause, M.O., Atomic radiative and radiationless yields for K and L shells. *J. Phys. Chem. Ref. Data*, **1979**. 8(2): p. 307-327.

[178] Attwood, D., Soft X-rays and Extreme Ultraviolet Radiation, Principles and Applications. *Cambridge University Press*. **1999**.

[179] Eisebitt, S., et al., Resonant Inelastic Soft X-ray Scattering as a Bandstructure Probe: A Primer. *Phys. Status Solidi B*, **1999**. 215(1): p. 803-808.

[180] Kotani, A. and S. Shin, Resonant inelastic X-ray scattering spectra for electrons in solids. *Rev. Mod. Phys.*, **2001**. 73(1): p. 203-246.

[181] Rueff, J.-P. and A. Shukla, Inelastic X-ray scattering by electronic excitations under high pressure. *Rev. Mod. Phys.*, **2010**. 82(1): p. 847-896.

[182] Ishii, K., T. Tohyama, and J.i. Mizuki, Inelastic X-ray Scattering Studies of Electronic Excitations. *J. Phys. Soc. Japan*, **2013**. 82(2): p. 021015.

[183] Glatzel, P., et al., Hard X-ray photon-in photon-out spectroscopy. *Catal. Today*, **2009**. 145(3): p. 294-299.

[184] Kramers, H.A. and W. Heisenberg, Über die Streuung von Strahlung durch Atome. *Zeitschrift für Physik*, **1925**. 31(1): p. 681-708.

[185] Rueff, J.P. and A. Shukla, A RIXS cookbook: Five recipes for successful RIXS applications. *J. Electron Spectros. Relat. Phenomena*, **2013**. 188: p. 10-16.

[186] van Schooneveld, M.M., et al., A multispectroscopic study of 3d orbitals in cobalt carboxylates: the high sensitivity of 2p3d resonant X-ray emission spectroscopy to the ligand field. *Angew. Chem. Int. Ed.*, **2013**. 52(4): p. 1170-4.

[187] Ghiringhelli, G., et al., Resonant inelastic X-ray scattering of MnO $L_{2,3}$ edge measurements and assessment of their interpretation. *Phys. Rev. B*, **2006**. 73(3): p. 035111.

[188] Magnuson, M., et al., Large magnetic circular dichroism in resonant inelastic X-ray scattering at the Mn L-edge of Mn-Zn ferrite. *Phys. Rev. B*, **2006**. 74(17): p. 172409.

[189] Einstein, A., Über einen die Erzeugung und Verwandlung des Lichtes betreffenden heuristischen Gesichtspunkt. *Ann Phys.*, **1905**. 322(6): p. 132-148.

[190] Siegbahn, K., Electron spectroscopy for atoms, molecules, and condensed matter. *Rev. Mod. Phys.*, **1982**. 54(3): p. 709-728.

[191] Hüfner, S., Photoelectron Spectroscopy: Principles and Applications. *Springer Series in Solid-State Sciences*. **1996**.

[192] Doh W.H., P.V., Zafeiratos S., Applications of Synchrotron-Based X-ray Photoelectron Spectroscopy in the Characterization of Nanomaterials. In: Kumar C.S.S.R. (eds) Surface Science Tools for Nanomaterials Characterization. *Springer, Berlin, Heidelberg ed.* **2015**.

[193] Kirz, J., C. Jacobsen, and M. Howells, Soft X-ray microscopes and their biological applications. *Q. Rev. Biophys.*, **1995**. 28(1): p. 33-130.

[194] Powell, C.J., and S. Tanuma, Inelastic Mean Free Paths, Mean Escape Depths, Information Depths, and Effective Attenuation Lengths for Hard X-ray Photoelectron Spectroscopy, in Hard X-ray Photoelectron Spectroscopy (HAXPES). **2016**. p. 111-140.

[195] Shirley, D.A., Many-electron and final-state effects: Beyond the one-electron picture. **1978**, *Springer*: Berlin, Heidelberg.

[196] Hüfner, S., et al., Photoemission spectroscopy in metals: band structure-Fermi surface–spectral function. *J. Electron Spectros. Relat. Phenomena*, **1999**. 100: p. 191-213.

[197] Carlson, T.A., Photoelectron and Auger Spectroscopy. **1975**.

[198] Hoffman, S., Auger- and X-ray Photoelectron Spectroscopy in Materials Science. *Springer Series in Surface Sciences*. **2013**.

[199] Favaro, M., et al., Interface Science Using Ambient Pressure Hard X-ray Photoelectron Spectroscopy. *Surfaces*, **2019**. 2(1): p. 78-99.

[200] Cooper, J.W., Multipole corrections to the angular distribution of photoelectrons at low energies. *Phys. Rev. A*, **1990**. 42(11): p. 6942-6945.

[201] Hard X-ray Photoelectron Spectroscopy (HAXPES). Springer Series in Surface Sciences. **2016**.

[202] Powell, C.J., et al., Surface sensitivity of Auger-electron spectroscopy and X-ray photoelectron spectroscopy. *J. Electron Spectros. Relat. Phenomena*, **1999**. 98-99: p. 1-15.

[203] Fadley, C.S., Electron Spectroscopy: Theory, Techniques, and Applications. Vol. 2. **1978**.

[204] Surface Chemical Analysis—Vocabulary—Part 1. General terms and terms used in spectroscopy, *International Organization for Standardization*, Geneva. ISO 18115-1:**2010**.

[205] Powell, C.J., and A. Jablonski, Progress in quantitative surface analysis by X-ray photoelectron spectroscopy: Current status and perspectives. *J. Electron Spectros. Relat. Phenomena*, **2010**. 178-179: p. 331-346.

[206] The QUASES-IMFP-TPP2M software: http://www.quases.com/products/quases-imfp-tpp2m/. [03.08.2020]

[207] Seah, M.P. and W.A. Dench, Quantitative electron spectroscopy of surfaces: A standard data base for electron inelastic mean free paths in solids. *Surf. Interface Anal.*, **1979**. 1(1): p. 2-11.

[208] Helmholtz Zentrum Berlin für Materialien und Energie, LiXEdrom: High Energy Resolution RIXS Station dedicated to Liquid Investigation at BESSY II. *Journal of large-scale research facilities JLSRF*, **2016**. 2.

[209] Seidel, R., S. Thürmer, and B. Winter, Photoelectron Spectroscopy Meets Aqueous Solution: Studies from a Vacuum Liquid Microjet. *J. Phys. Chem. Lett.*, **2011**. 2(6): p. 633-641.

[210] Rowland, H.A., On concave gratings for optical purposes. *Philos. Mag.. 5th series.*, **1883**. 16 (152): p. 197-210.

[211] Gotz, M., Electronic Structure in Solution. Soft X-ray Absorption and Emission for Fe^{2+} in Water. **2012**, Freie Universität Berlin: Germany.

[212] Schwanke, C., et al., Electrochemical flowcell for in-situ investigations by soft X-ray absorption and emission spectroscopy. *Rev. Sci. Instrum.*, **2014**. 85(10): p. 103120.

[213] Gorgoi, M., et al., The high kinetic energy photoelectron spectroscopy facility at BESSY progress and first results. *Nucl. Instrum. Methods. Phys. Res. A: Accelerators, Spectrometers, Detectors and Associated Equipment*, **2009**. 601(1): p. 48-53.

[214] Experimental Facilities at BESSY II and BER II https://www.helmholtz-berlin.de/media/media/user/experimental-facilities-bessy-ii-and-ber-ii.pdf. [05.08.2020]

[215] Zhang, L., et al., Crystal structure of SARS-CoV-2 main protease provides a basis for design of improved alpha-ketoamide inhibitors. *Science*, **2020**. 368(6489): p. 409-412.

[216] Jaeschke, E., BESSY II: A state of the art synchrotron light source for Berlin-Adlershof. Conference Proceedings, 3rd European Particle Accelerator Conference (EPAC 92), **1992**. C920324: p. 43–48.

[217]   Garcia-Diez, R., Characterization of nanoparticles by continuous contrast variation in small-angle X-ray scattering. **2013**.

[218]   Lange, K.M., Structure and Dynamics of Water and Ions in Solution - Soft X-ray Absorption and Emission Studies. **2012**, Freie Universität Berlin.

[219]   Kuske, P., Abo-Bakr, M., Anders, W., Birke, T., Buerkmann, K., Dirsat, M., Dressler, O., Duerr, V., Falkenstern, F., Gericke, W., et al., Preparations of BESSY for Top-Up operation. EPAC08, Genoa, Italy, **2008**: p. 2067.

[220]   Jung, C., et al., First results of the soft X-ray microfocus beamline U41-PGM. *Nucl. Instrum. Methods. Phys. Res. A: Accelerators, Spectrometers, Detectors and Associated Equipment*, **2001**. 467-468: p. 485-487.

[221]   Ch. Jung, F.E., S. Hartlaub, K. Holldack, R. Follath, M. Mast, J.-S. Schmidt, F. Senf, M. R. Weiss, and Zeschke Th, U41-PGM: Commissioning Results.

[222]   Kachel, T., The plane grating monochromator beamline U49-2 PGM-1 at BESSY II. *Journal of large-scale research facilities JLSRF*, **2016**. 2.

[223]   Schaefers, F., M. Mertin, and M. Gorgoi, KMC-1: a high resolution and high flux soft X-ray beamline at BESSY. *Rev. Sci. Instrum.*, **2007**. 78(12): p. 123102.

[224]   KMC-1   beamline   of   BESSY   II   https://helmholtz-berlin.de/pubbin/igama_output?gid=1604&modus=einzel/.

[225]   https://www.ucl.ac.uk/~ucbeoha/Buffer%20Recipes.html#Borate. [06.08.2020]

[226]   Smekal, W., W.S.M. Werner, and C.J. Powell, Simulation of electron spectra for surface analysis (SESSA): a novel software tool for quantitative Auger-electron spectroscopy and X-ray photoelectron spectroscopy. *Surf. Interface Anal.*, **2005**. 37(11): p. 1059-1067.

[227]   Werner, W.S.M., W. Smekal, and C.J. Powell, Simulation of Electron Spectra for Surface Analysis (SESSA) Version 2.1 User's Guide. **2017**.

[228]   Techane, S., D.R. Baer, and D.G. Castner, Simulation and Modeling of Self-Assembled Monolayers of Carboxylic Acid Thiols on Flat and Nanoparticle Gold Surfaces. *Anal. Chem.*, **2011**. 83(17): p. 6704-6712.

[229]   Zhou, F.L., et al., Enhanced photo-electrochemical water oxidation on MnO_x in buffered organic/inorganic electrolytes. *J. Mater. Chem. A*, **2015**. 3(32): p. 16642-16652.

[230]   Pickrahn, K.L., et al., Active MnO_x electrocatalysts prepared by atomic layer deposition for oxygen evolution and oxygen reduction reactions. *Adv. Energy Mater.*, **2012**. 2(10): p. 1269-1277.

[231]   Gaillot, A.-C., et al., Structure of Synthetic K-rich Birnessite Obtained by High-Temperature Decomposition of $KMnO_4$. I. Two-Layer Polytype from 800 °C Experiment. *Chem. Mater.*, **2003**. 15(24): p. 4666-4678.

[232]   Fekete, M., et al., Highly active screen-printed electrocatalysts for water oxidation based on beta-manganese oxide. *Energy Environ. Sci.*, **2013**. 6(7): p. 2222-2232.

[233]   Qiu, G.H., et al., Electrochemical preparation of nanosized manganese dioxides from manganese chloride solutions. *Ionics*, **2011**. 17(3): p. 209-216.

[234]   Lin, Z., et al., Electrodeposited MnO_x/carbon nanofiber composites for use as anode materials in rechargeable lithium-ion batteries. *J. Power Sources*, **2010**. 195(15): p. 5025-5031.

[235]   Adelkhani, H. and M. Ghaemi, Nano-structural tailoring of manganese dioxide by using pulse current electrodeposition. *Solid State Ion.*, **2008**. 179(39): p. 2278-2283.

[236]   Matsumoto, Y., H. Ohmura, and T. Goto, Effect of lanthanide ions on the

electrodeposition of cobalt and manganese oxides. *J. Electroanal. Chem.*, **1995**. 399(1-2): p. 91-96.

[237]   Najafpour, M.M. and M.A. Isaloo, Mechanism of water oxidation by nanolayered manganese oxide: a step forward. *RSC Adv.*, **2014**. 4(13): p. 6375-6378.

[238]   Yamaguchi, A., et al., Regulating proton-coupled electron transfer for efficient water splitting by manganese oxides at neutral pH. *Nat. Commun.*, **2014**. 5(1): p. 4256.

[239]   Izgorodin, A., et al., CdS thin-film electrodeposition from a phosphonium ionic liquid. *Phys. Chem. Chem. Phys.*, **2009**. 11(38): p. 8532-7.

[240]   Gilbert, B., et al., Multiple scattering calculations of bonding and X-ray absorption spectroscopy of manganese oxides. *J. Phys. Chem. A*, **2003**. 107(16): p. 2839-2847.

[241]   Kubin, M., et al., X-ray-induced sample damage at the Mn L-edge: a case study for soft X-ray spectroscopy of transition metal complexes in solution. *Phys. Chem. Chem. Phys.*, **2018**. 20(24): p. 16817-16827.

[242]   Yano, J., et al., X-ray damage to the Mn_4Ca complex in single crystals of photosystem II: a case study for metalloprotein crystallography. *Proc. Natl. Acad. Sci. USA*, **2005**. 102(34): p. 12047-52.

[243]   Kim, S.H., S.J. Kim, and S.M. Oh, Preparation of Layered MnO_2 via Thermal Decomposition of $KMnO_4$ and Its Electrochemical Characterizations. *Chem. Mater.*, **1999**. 11(3): p. 557-563.

[244]   Saratovsky, I., et al., Manganese oxides: Parallels between abiotic and biotic structures. *J. Am. Chem. Soc.*, **2006**. 128(34): p. 11188-11198.

[245]   Ilton, E.S., et al., XPS determination of Mn oxidation states in Mn (hydr)oxides. *Appl. Surf. Sci.*, **2016**. 366: p. 475-485.

[246]   Cui, H., et al., Birnessites with different average manganese oxidation states synthesized, characterized, and transformed to todorokite at atmospheric pressure. *Clays Clay Miner.*, **2009**. 57(6): p. 715-724.

[247]   Cramer, S.P., et al., Ligand field strengths and oxidation states from manganese L-edge spectroscopy. *J. Am. Chem. Soc.*, **1991**. 113(21): p. 7937-7940.

[248]   Yoon, W.S., et al., Investigation of the charge compensation mechanism on the electrochemically Li-ion deintercalated $Li_{1-x}Co_{1/3}Ni_{1/3}Mn_{1/3}O_2$ electrode system by combination of soft and hard X-ray absorption spectroscopy. *J. Am. Chem. Soc.*, **2005**. 127(49): p. 17479-87.

[249]   Frati, F., M.O.J.Y. Hunault, and F.M.F. de Groot, Oxygen K-edge X-ray Absorption Spectra. *Chem. Rev.*, **2020**. 120(9): p. 4056-4110.

[250]   Manceau, A., M.A. Marcus, and S. Grangeon, Determination of Mn valence states in mixed-valent manganates by XANES spectroscopy. *Am. Mineral.*, **2012**. 97(5-6): p. 816-827.

[251]   Maeda, K. and K. Domen, Photocatalytic Water Splitting: Recent Progress and Future Challenges. *J. Phys. Chem. Lett.*, **2010**. 1(18): p. 2655-2661.

[252]   Cox, N., et al., Biological water oxidation. *Acc. Chem. Res.*, **2013**. 46(7): p. 1588-96.

[253]   Yoshida, M., et al., In situ observation of carrier transfer in the Mn-oxide/Nb:$SrTiO_3$ photoelectrode by X-ray absorption spectroscopy. *ChemComm*, **2013**. 49(71): p. 7848-7850.

[254]   Gorlin, Y., et al., In Situ X-ray absorption spectroscopy investigation of a bifunctional manganese oxide catalyst with high activity for electrochemical water oxidation and oxygen reduction. *J. Am. Chem. Soc.*, **2013**. 135(23): p. 8525-8534.

[255] Jaeschke, E.J., et al., Synchrotron Light Sources and Free-Electron Lasers. **2020**.

[256] Dubal, D.P., et al., Conversion of interlocked cube-like Mn_3O_4 into nanoflakes of layered birnessite MnO_2 during supercapacitive studies. *J. Alloys Compd.*, **2010**. 496(1-2): p. 370-375.

[257] Yang, F., et al., A novel hydrothermal synthesis and characterisation of porous Mn_3O_4 for supercapacitors with high rate capability. *RSC Adv.*, **2015**. 5(13): p. 9843-9847.

[258] Garvie, L.A.J. and A.J. Craven, High-resolution parallel electron energy-loss spectroscopy of Mn $L_{2,3}$-edges in inorganic manganese compounds. *Phys. Chem. Miner.*, **1994**. 21(4): p. 191-206.

[259] Diaz-Morales, O., et al., Electrochemical water splitting by gold: evidence for an oxide decomposition mechanism. *Chem. Sci.*, **2013**. 4(6): p. 2334-2343.

[260] Butorin, S.M., et al., Low-energy d-d excitations in MnO studied by resonant X-ray fluorescence spectroscopy. *Phys. Rev. B*, **1996**. 54(7): p. 4405-4408.

[261] Ghiringhelli, G., et al., Resonant inelastic X-ray scattering of MnO:$L_{2,3}$ edge measurements and assessment of their interpretation. *Phys. Rev. B*, **2006**. 73(3): p. 035111.

[262] Bocquet, A.E., et al., Electronic structure of 3d-transition-metal compounds by analysis of the 2p core-level photoemission spectra. *Phys. Rev. B*, **1992**. 46(7): p. 3771-3784.

[263] Haverkort, M.W., M. Zwierzycki, and O.K. Andersen, Multiplet ligand-field theory using Wannier orbitals. *Phys. Rev. B*, **2012**. 85(16): p. 165113.

[264] Lu, Y., et al., Efficient real-frequency solver for dynamical mean-field theory. *Phys. Rev. B*, **2014**. 90(8): p. 085102.

[265] Grisolia, M.N., et al., Hybridization-controlled charge transfer and induced magnetism at correlated oxide interfaces. *Nat. Phys.*, **2016**. 12(5): p. 484-492.

[266] Cui, B., et al., Tuning the entanglement between orbital reconstruction and charge transfer at a film surface. *Sci. Rep.*, **2014**. 4: p. 4206.

[267] Siegbahn, P.E., Structures and energetics for O_2 formation in photosystem II. *Acc. Chem. Res.*, **2009**. 42(12): p. 1871-80.

[268] Rapatskiy, L., et al., Detection of the water-binding sites of the oxygen-evolving complex of Photosystem II using W-band 17O electron-electron double resonance-detected NMR spectroscopy. *J. Am. Chem. Soc.*, **2012**. 134(40): p. 16619-34.

[269] Cox, N., et al., Photosynthesis. Electronic structure of the oxygen-evolving complex in photosystem II prior to O-O bond formation. *Science*, **2014**. 345(6198): p. 804-8.

[270] Pfeifer, V., et al., The electronic structure of iridium oxide electrodes active in water splitting. *Phys. Chem. Chem. Phys.*, **2016**. 18(4): p. 2292-6.

[271] Huynh, M., et al., Nucleation and Growth Mechanisms of an Electrodeposited Manganese Oxide Oxygen Evolution Catalyst. *J. Phys. Chem. C*, **2014**. 118(30): p. 17142-17152.

[272] Xiao, M., et al., Tantalum (Oxy)Nitride: Narrow Bandgap Photocatalysts for Solar Hydrogen Generation. *Engineering*, **2017**. 3(3): p. 365-378.

[273] Maeda, K. and K. Domen, New Non-Oxide Photocatalysts Designed for Overall Water Splitting under Visible Light. *J. Phys. Chem. C*, **2007**. 111(22): p. 7851-7861.

[274] Hitoki, G., et al., An oxynitride, TaON, as an efficient water oxidation photocatalyst under visible light irradiation ($\lambda \leq 500$ nm). *Chem. Commun. (Camb)*, **2002**(16): p. 1698-9.

[275] Chun, W.-J., et al., Conduction and Valence Band Positions of Ta_2O_5, TaON, and Ta_3N_5 by UPS and Electrochemical Methods. *J. Phys. Chem. B*, **2003**. 107(8): p. 1798-1803.

[276] Hara, M., et al., TaON and Ta₃N₅ as new visible light driven photocatalysts. *Catal. Today*, **2003**. 78(1): p. 555-560.

[277] Saravanan, R., et al., Visible light degradation of textile effluent using novel catalyst ZnO/γ-Mn₂O₃. *J. Taiwan Inst. Chem. Eng.*, **2014**. 45(4): p. 1910-1917.

[278] Ma, Q., et al., Fabrication of MnO₂/TiO₂ nano-tube arrays photoelectrode and its enhanced visible light photoelectrocatalytic performance and mechanism. *Separation and Purification Technology*, **2017**. 189: p. 193-203.

[279] de Respinis, M., et al., Oxynitrogenography: Controlled Synthesis of Single-Phase Tantalum Oxynitride Photoabsorbers. *Chem. Mater.*, **2015**. 27(20): p. 7091-7099.

[280] Swisher, J.H. and M.H. Read, Thermodynamic Properties and Electrical Conductivity of Ta₃N₅ and Taon. *Metallurgical Transactions*, **1972**. 3(2): p. 489-494.

[281] Plate, P., Model-system studies on manganese oxide-based water oxidation catalysts made with atomic layer deposition. **2019**, Technische Universität Berlin.

[282] Wang, Z., et al., Hierarchical metastable γ-TaON hollow structures for efficient visible-light water splitting. *Energy Environ. Sci.*, **2013**. 6(7): p. 2134.

[283] Yoon, S., et al., The Influence of the Ammonolysis Temperature on the Photocatalytic Activity of β-TaON. *Int. J. Photoenergy*, **2013**. 2013: p. 1-8.

[284] Cristea, D., et al., Tantalum Oxynitride Thin Films: Assessment of the Photocatalytic Efficiency and Antimicrobial Capacity. *Nanomater. (Basel)*, **2019**. 9(3).

[285] Audi, A.A. and P.M.A. Sherwood, Valence-band X-ray photoelectron spectroscopic studies of manganese and its oxides interpreted by cluster and band structure calculations. *Surf. Interface Anal.*, **2002**. 33(3): p. 274-282.

[286] Xu, J., et al., Reactive-sputter-deposited β-Ta₂O₅ and TaON nanoceramic coatings on Ti–6Al–4V alloy against wear and corrosion damage. *Surf. Coat. Technol.*, **2016**. 296: p. 171-184.

[287] Muraoka, K., et al., Oxygen-Doped Ta₃N₅ Nanoparticles for Enhanced Z-Scheme Carbon Dioxide Reduction with a Binuclear Ruthenium(II) Complex under Visible Light. *ChemPhotoChem*, **2019**. 3(10): p. 1027-1033.

[288] J.F. Moulder, W.F.S., P.E. Sobol, K.D. Bomben, Handbook of X-ray Photoelectron Spectroscopy. **1992**: Perkin-Elmer Corporation, Physical Electronics Division.

[289] Nesbitt, H.W. and D. Banerjee, Interpretation of XPS Mn(2p) spectra of Mn oxyhydroxides and constraints on the mechanism of MnO₂ precipitation. *Am. Mineral.*, **1998**. 83(3-4): p. 305-315.

[290] Tanuma, S., C.J. Powell, and D.R. Penn, Calculation of electron inelastic mean free paths (IMFPs) VII. Reliability of the TPP-2M IMFP predictive equation. *Surf. Interface Anal.*, **2003**. 35(3): p. 268-275.

[291] Tanuma, S., C.J. Powell, and D.R. Penn, Calculations of electron inelastic mean free paths. V. Data for 14 organic compounds over the 50-2000 eV range. *Surf. Interface Anal.*, **1994**. 21(3): p. 165-176.

[292] Rana, A.M., et al., Endurance and Cycle-to-cycle Uniformity Improvement in Tri-Layered CeO₂/Ti/CeO₂ Resistive Switching Devices by Changing Top Electrode Material. *Sci. Rep.*, **2017**. 7: p. 39539.

[293] Elder, S.H., et al., Thermodynamics of ternary nitride formation by ammonolysis: application to lithium molybdenum nitride (LiMoN₂), sodium tungsten nitride (Na₃WN₃), and sodium tungsten oxide nitride (Na₃WO₃N). *Chem. Mater.*, **1993**. 5(10): p. 1545-1553.

[294] Béguin, F. and E. Frąckowiak, Supercapacitors: Materials, Systems, and Applications.

2013.

[295] Jacob, K.T., et al., Thermodynamic Data for Mn_3O_4, Mn_2O_3, and MnO_2. High-Temperature Materials and Processes, **2011**. 30(4-5).

[296] Birkner, N. and A. Navrotsky, Thermodynamics of manganese oxides: Effects of particle size and hydration on oxidation-reduction equilibria among hausmannite, bixbyite, and pyrolusite. *Am. Mineral.*, **2012**. 97(8-9): p. 1291-1298.

[297] Fadley, C.S. and D.A. Shirley, Multiplet Splitting of Metal-Atom Electron Binding Energies. *Phys. Rev. A*, **1970**. 2(4): p. 1109-&.

[298] Galakhov, V.R., et al., Mn3s exchange splitting in mixed-valence manganites. *Phys. Rev. B*, **2002**. 65(11).

[299] Toupin, M., T. Brousse, and D. Bélanger, Influence of Microstructure on the Charge Storage Properties of Chemically Synthesized Manganese Dioxide. *Chem. Mater.*, **2002**. 14(9): p. 3946-3952.

[300] Wang, J., C. Zhang, and F. Kang, Nitrogen-Enriched Porous Carbon Coating for Manganese Oxide Nanostructures toward High-Performance Lithium-Ion Batteries. *ACS Appl. Mater. Interfaces*, **2015**. 7(17): p. 9185-94.

[301] Zhang, K., et al., Synthesis of nitrogen-doped MnO/graphene nanosheets hybrid material for lithium ion batteries. *ACS Appl. Mater. Interfaces*, **2012**. 4(2): p. 658-64.

[302] Gu, X., et al., Coaxial MnO/N-doped carbon nanorods for advanced lithium-ion battery anodes. *J. Mater. Chem. A*, **2015**. 3(3): p. 1037-1041.

[303] Pandi, K., et al., Fabrication of Solid-State Flexible Fiber Supercapacitor Using Agave Americana Derived Activated Carbon and Its Performance Analysis at Different Conditions. *Chemistry Select*, **2016**. 1(21): p. 6713-6725.

[304] Ju, J., et al., Nitrogen-doped graphene quantum dots-based fluorescent probe for the sensitive turn-on detection of glutathione and its cellular imaging. *RSC Adv.*, **2014**. 4(94): p. 52583-52589.

[305] Gong, P., et al., Synthesis of highly luminescent fluorinated graphene quantum dots with tunable fluorine coverage and size. *Mater. Lett.*, **2015**. 143: p. 112-115.

[306] Zheng, Y., et al., Two-step boron and nitrogen doping in graphene for enhanced synergistic catalysis. *Angew. Chem. Int. Ed.*, **2013**. 52(11): p. 3110-6.

[307] Vo, T.-G., H.-M. Liu, and C.-Y. Chiang, Highly conformal deposition of ultrathin cobalt acetate on a bismuth vanadate nanostructure for solar water splitting. *Catal. Sci. Technol.*, **2019**. 9(17): p. 4588-4597.

[308] Stephenson, N.C. and R.S. Roth, Structural systematics in the binary system Ta_2O_5-WO_3. V. The structure of the low-temperature form of tantalum oxide L-Ta_2O_5. *Acta. Crystallogr. B. Struct. Sci.*, **1971**. 27(5): p. 1037-1044.

[309] Weishaupt, V.M. and J. Strahle, Darstellung der Oxidnitride VON, NbON und TaON. Die Kristallstruktur von NbON und TaON. *Z. anorg. allg. Chem.*, **1977**. 429: p. 261-269.

[310] Zhang, J., Room-temperature compressibilities of MnO and CdO: further examination of the role of cation type in bulk modulus systematics. *Phys. Chem. Miner.*, **1999**. 26(8): p. 644-648.

[311] Hase, W., Neutronographische Bestimmung der Kristallstrukturparameter von Dy_2O_3, Tm_2O_3 und α -Mn_2O_3. *Phys. Status Solidi (b)*, **1963**. 3(12): p. K446-K449.

[312] Bolzan, A.A., et al., Powder Neutron-Diffraction Study of Pyrolusite, Beta-MnO_2. *Aust. J. Chem.*, **1993**. 46(6): p. 939-944.

[313] Xu, Y. and M.A.A. Schoonen, The absolute energy positions of conduction and valence bands of selected semiconducting minerals. *Am. Mineral.*, **2000**. 85(3-4): p. 543-556.

[314] Munawar, K., et al., Single-step fabrication of $CuO–MnO–2TiO_2$ composite thin films with improved photoelectrochemical response. *RSC Adv.*, **2017**. 7(26): p. 15885-15893.

[315] Grazulis, S., et al., Crystallography Open Database (COD): an open-access collection of crystal structures and platform for worldwide collaboration. *Nucleic Acids Res.*, **2012**. 40: p. D420-7.

[316] Crystallography Open Database http://www.crystallography.net/cod/. [10.08.2020]

[317] Pang, S.-C., M.A. Anderson, and T.W. Chapman, Novel Electrode Materials for Thin-Film Ultracapacitors: Comparison of Electrochemical Properties of Sol-Gel-Derived and Electrodeposited Manganese Dioxide. *J. Electrochem. Soc.*, **2000**. 147(2): p. 444-450.

Selbständigkeitserklärung

Ich erkläre gegenüber der Freien Universität Berlin, dass ich die vorliegende Dissertation selbstständig und ohne Benutzung anderer als der angegebenen Quellen und Hilfsmittel angefertigt habe. Die vorliegende Arbeit ist frei von Plagiaten. Alle Ausführungen, die wörtlich oder inhaltlich aus anderen Schriften entnommen sind, habe ich als solche kenntlich gemacht. Diese Dissertation wurde in gleicher oder ähnlicher Form noch in keinem früheren Promotionsverfahren eingereicht. Mit einer Prüfung meiner Arbeit durch ein Plagiatsprüfungsprogramm erkläre ich mich einverstanden.

Maryam Shaker

Berlin, den 09.11.2020

Declaration of Authorship

 I declare to the Freie Universität Berlin that I have completed the submitted dissertation independently and without the use of sources and aids other than those indicated. The present thesis is free of plagiarism. I have marked as such all statements that are taken literally or in content from other writings. This dissertation has not been submitted in the same or similar form in any previous doctoral procedure. I agree to have my thesis examined by a plagiarism examination software.

Maryam Shaker

Berlin, 09.11.2020